NANYANG TECHNOLOGICAL UNIVERSITY

DUAL AIR-GAP AXIAL FLUX PERMANENT MAGNET MACHINES FOR FLYWHEEL ENERGY STORAGE SYSTEMS

NGUYEN TRONG DUY

SCHOOL OF ELECTRICAL AND ELECTRONIC ENGINEERING

2012

DUAL AIR-GAP AXIAL FLUX PERMANENT MAGNET MACHINES FOR FLYWHEEL ENERGY STORAGE SYSTEMS

NGUYEN TRONG DUY

SCHOOL OF ELECTRICAL AND ELECTRONIC ENGINEERING

A thesis submitted to the Nanyang Technological University
in partial fulfilment of the requirement for the degree of
Doctor of Philosophy

2012

ACKNOWLEDGMENTS

During the past four years of my Ph.D. study, I am glad to obtain many people's help, care and guidance. They have contributed to help me complete this thesis, both directly, by supplying me with useful suggestions, thoughts and even critical comments, as well as indirectly, by creating a pleasant and motivating working atmosphere. I am not giving a full list of names here, but I am sure that all the people to whom these acknowledgments are addressed are aware of their inclusion. I wish to express my sincere gratitude and appreciation to all of them.

Foremost, I greatly appreciate and would like to express my gratitude to my supervisor Prof. Tseng King Jet who has always guided, encouraged and supported me all throughout my academic life at Nanyang Technological University. Working with Dr. Tseng has been the most rewarding experience in my life. His profound knowledge, constructive suggestions and insights have helped to shape my research skills. His understanding and pleasant personality have carried me on through difficult times. I am deeply indebted to him.

I also want to express my gratitude to all the staff of Power Electronics and Research Laboratory for the support given to me. Especially I wish to thank Ms. Lee-Loh Chin Khim for her dedicated support and selfless helps to me. Whatever my research or daily life, she always supports me kindly and quickly; Ms. Lee-Loh, thank you so much.

Many thanks are also given to my colleagues and university friends. Their help, advice, guidance, encouragement and support are always shining my life. Especially, I wish to thank Hoan Thong Nguyen, Shao Zhang, Dailin Yao, Yen Kheng Tan for the uncountable time they spent with me during my study here.

I also would like to thank my parents and my brother for supporting me not only through my long and adventurous Ph.D. but also through my entire education. And the

most special thanks are given to my wife Truc Phuong Huynh: thank you for your love, support, understanding and patience. It is never easy to be the wife of a Ph.D. student. I am always grateful for everything you have given me. This work is dedicated to you all.

The research scholarship and research fund granted by Nanyang Technological University and AUNSeed-Net is gratefully acknowledged.

SUMMARY

More and more renewable distributed generation (DG) connected to the grid has brought about significant impacts on network system security and reliability. The employment of flywheel energy storage system (FESS) is an effective way to deal with the negative impacts of DG, such as in power smoothing, power leveling, voltage restoring, and energy recycling. Consequently, the research and development of the FESS together with its key-supporting components has become an interesting topic during the last decade.

This thesis has dealt with the efficient and compact dual air-gap axial flux permanent magnet (AFPM) machines for use in the FESS. The key aspects on the design, analysis, implementation and control of the proposed AFPM machine are covered in this thesis in the sequence as follows: (1) Design of the dual air-gap AFPM machine for FESS; (2) Modeling of the proposed AFPM machine; (3) FEM analysis and model verification for the proposed AFPM machine; (4) Development of control system for the proposed AFPM machine; (5) Experimental implementation and analysis of the machine prototypes.

The AFPM machines offer some unique features which have been exploited to employ in FESS applications. In this thesis, an efficient and compact dual air-gap AFPM machine optimized for use in FESS applications is proposed. The conceptual FESS based on the proposed AFPM machine is also briefly presented. The AFPM machine is composed of two separate single air-gap AFPM machines, having two sets of three-phase stator windings but requiring only a single power converter which supplies power for control of both axial force and electromagnetic torque. The application of this machine in FESS is realized by orientating its axial direction vertically and having its double-sided rotor to be the core of the flywheel. In addition, the availability of axial force control helps to minimize the vertical bearing force to improve the efficiency of the FESS.

This thesis has also developed a multi-variable non-linear mathematical model for the proposed AFPM machine. Linearization has been performed to obtain the linear model for this machine and also to facilitate its control system. Three-dimensional finite element analysis have been carried out during the design of the machine and used to verify the machine design together with the effectiveness of its mathematical model. Control strategies under both position sensored and sensorless schemes have also been developed. The effectiveness of the control strategies has been verified by simulations and experimental tests on the fabricated machine prototypes.

TABLE OF CONTENTS

LIST OF FIGURES

LIST OF TABLES

LIST OF ABBREVIATIONS

2D	Two-dimensional
3D	Three-dimensional
AC	Alternating Current
ADC	Analog to Digital Conversion
AFPM	Axial Flux Permanent Magnet
AMB	Active Magnetic Bearing
BESS	Battery Energy Storage System(s)
CEM	Center for Electromechanics, University of Texas
CAES	Compressed Air Energy Storage
DAC	Digital to Analog Conversion
DC	Direct Current
DG	Distributed Generation
DOD	Depth of Discharge
DOF	Degree of Freedom
EMALS	Electromagnetic Aircraft Launch System
EMF	Electromotive Force
ESS	Energy Storage System(s)
FEA	Finite Element Analysis
FEM	Finite Element Method
FESS	Flywheel Energy Storage System(s)
FET	Field Effect Transistor
GCD	Greatest Common Divisor
HCB	Hybrid ceramic bearing(s)
HEV	Hybrid Electric Vehicle
HTS	High-temperature superconductor
IPAC	Infrared Processing and Analysis Center

ISS	International Space Station
IGBT	Insulated Gate Bipolar Transistor(s)
LEO	Low Earth Orbiting
Li-ion	Lithium-ion
LCM	Least Common Multiple
LQG	Linear Quadratic Gaussian
MMF	Magnetomotive Force
MPC	Model Predictive Control
NASA	National Aeronautics Space Administration
PD	Proportional-Derivative
PI	Proportional-Integral
PID	Proportional-Integral-Derivative
PM	Permanent Magnet
PMSM	Permanent Magnet Synchronous Machine
PWM	Pulse Width Modulation
R&D	Research and Development
RFPM	Radial Flux Permanent Magnet
RMS	Root Mean Square
rpm	Revolution(s) per minute
SMES	Super-conducting Magnetic Energy Storage
SPWM	Sinusoidal Pulse Width Modulation
SRM	Switched Reluctance Machine(s)
SVPWM	Space-vector Pulse Width Modulation
SynRM	Synchronous reluctance machine(s)
UPS	Uninterruptible Power Supply
USD	United States Dollar(s)
VSI	Voltage-source Inverter

LIST OF SYMBOLS

α_i	ratio of average to peak air-gap flux density
α-β	stationary reference frame
α_M	magnet span
A_m	peak line current density
A_s	slot rectangular cross-sectional area
B_m	permanent magnet flux density
B_{mg}	peak air-gap flux density
B_{mg1}	peak air-gap flux density in upper machine half
B_{mg2}	peak air-gap flux density in lower machine half
B_{1t}	magnetic flux density in a tooth
B_r	remanent flux density of the permanent magnet
B_{ro}	flux density at operating point
$B_{rot,\,y}$	flux density in the rotor yoke
$B_{s,\,y}$	flux density in the stator yoke
β	coil pitch to pole pitch ratio
d-q	rotor reference frame
δ_i	magnetic skew angle
d_1	height of slot depth - top part
d_2	height of slot depth - inclining part
d_3	height of slot depth - rectangular part
d_{sh}	diameter of the shaft
ΔP	machine total loss
ΔP_{eFe}	stator eddy current loss
ΔP_{fr}	bearing frictional loss
ΔP_{hFe}	stator hysteresis loss
ΔP_{mech}	mechanical loss
ΔP_{PM}	permanent magnet loss
ΔP_{1Fe}	stator core loss
ΔP_{1w}	stator winding loss
ΔP_{2Fe}	rotor core loss
ΔP_{wind}	windage loss
D_i, D_o	inner and outer diameters of the machine
D	average diameter of the machine
$D_{r,o}$	outer diameter of the rim
e_m	specific energy of the flywheel system
E	the stored energy
E_f	phase back electromotive force (EMF)
ε	phase EMF to phase voltage ratio
F_1, F_2, F	upper, lower and total axial forces
g	gravity constant

g_{gr}	gravitational acceleration constant
g'	equivalent air-gap
g_1	air-gap length of upper machine half
g_2	air-gap length of lower machine half
G	gravity of the rotor and its attached rim
G_g	magnetic permeance of the air-gap
G_m	magnetic permeance of the permanent magnet
G_{ml}	magnetic leakage permeance
γ_{Fe}	mass density of rotor
γ_{rim}	mass density of the rim
I_a	line current of phase A
i_a , i_b , i_c	instant currents of phase A, B and C respectively
i_d, i_q	direct and quadrature - axis currents
J	moment of inertia of the flywheel
K	flywheel shape factor
k_C	Carter factor
k_d	ratio of inner to outer diameter; differential coefficient a PID controller
k_i	integral coefficient a PID controller
k_p	proportional coefficient a PID controller
k_{st}	lamination stacking factor
k_ω	fundamental harmonic winding factor
k_{w1}	winding factor
l	constant observer gain
$l_{l,in}$	length of the stator winding inner end connection
$l_{l,out}$	length of the stator winding outer end connection
l_{M1}	permanent magnet axial length of upper machine half
l_{M2}	permanent magnet axial length of lower machine half
l_{rot}	rotor axial length
l_s	length of the stator stack
λ_a, λ_b, λ_c,	linkage flux of phase a, b, and c respectively
λ_d, λ_q	direct and quadrature-axis linkage fluxes
λ_f	rotor linkage flux
λ_{ab}	mutual linkage flux of phase a and b
$\lambda_{l,s}$	coefficient of the slot leakage permeance
$\lambda_{l,ein}$	coefficient of the slot leakage permeance of inner end
$\lambda_{l,eout}$	coefficient of the slot leakage permeance of outer end
L_{aa}, L_{bb}, L_{cc}	self inductances of phase a, b, and c respectively
L_{ab}, L_{bc}, L_{ca}	mutual inductances amongst three phases a, b, and c
L_d, L_q	direct-axis and quadrature-axis inductance
m	number of phases
m_i	modulation index
M	mass of flywheel
MMF	magnetomotive force
μ	dynamic viscosity of the air at 1 atm and 20 ^{o}C

μ_0	permeability of free space
μ_{rrec}	relative recoil magnet permeability
N	number of turns per phase
N_s	equivalent number of turns of a sinusoidally-distributed winding
N_c	number of conductors per coil
N_{cd}	conductor density
N_f	fictitious field winding of the rotor permanent magnet
$N_f i_f$	fictious magnetomotive force of the rotor
N_1 , N_2	number of turns of upper and lower windings
N_{1p}	number of turns in series of each phase
N_m	number of magnet pieces
N_p	number of pole pairs on the rotor
n	speed of the rotor (revolutions per minute)
n_s	speed of the rotor (revolutions per second)
N_{sp}	number of slots per phase
N_{sm}	number of teeth per magnet pole
η	machine efficiency
ω	angular velocity
ω_e	electrical angular velocity
ω_r	mechanical angular velocity
P_{in}	machine input power
P	number of pole pairs
P_{loss}	machine power losses
P_m	machine developed power
P_{out}	machine output power
φ	magnetic flux
φ_{f1}	fundamental component of magnetic flux per pole
φ_d	magnetic flux in d-axis
φ_q	magnetic flux in q-axis
φ_g	air-gap magnetic flux
φ_{lM}	magnetic leakage flux
φ_M	flux of the permanent magnet
φ_r	remanent flux of permanent magnet
Φ_r	angular displacement along the rotor circumference
Φ_s	angular displacement along the stator circumference
Q	number of slots
q	number of lots per pole per phase
R	net reluctance seen by the magnet
r	radius of the flywheel
ρ	mass density of the flywheel
R_g	magnetic reluctance of the air-gap
R_i	inner radius of the machine
R_m	magnetic reluctance of the permanent magnet
R_{ml}	magnetic leakage reluctance

R_o	outer radius of the machine
R_{1dc}	resistance per phase for the direct current
R_r	magnetic reluctance of the rotor
R_s	magnetic reluctance of the stator
S	apparent electromagnetic power
σ_{PM}	electric conductivity of permanent magnet
σ_{lM}	permanent magnet leakage flux coefficient
σ_{min}	minimum tensile strength of material
τ_p	pole pitch
τ_s	slot pitch
$\tau_{s,avg}$	average slot pitch
T_1 , T_2 , T	upper, lower and total electromagnetic torques
$T_{cogging}$	cogging torque
T_m	electromagnetic torque
v_a, v_b, v_c	voltage of phase a, b and c respectively
v_d, v_q	direct-axis and quadrature-axis voltage
θ	position of rotor referring to a winding axis
θ_M	arc-length of a permanent magnet
V	phase voltage
w_{bi}	back iron thickness of the stator
w_M	pole width
w_s	slot opening
w_{sb}	slot bottom width
w_{tbi}	minimum tooth narrow
W	stored magnetic energy
$\hat{x}$	estimated quantities
x^*	reference parameters
X_s	synchronous reactance
X_a	mutual reactance
X_l	stator leakage reactance
z	axial displacement of the flywheel

CHAPTER 1 INTRODUCTION

1.1 Background and Motivation

Grid connection of more and more renewable distributed generation (DG) has significant impacts on network system security and reliability. The use of flywheel energy storage systems (FESS) is an effective way to deal with the negative impacts of DG, such as in power smoothing, power leveling, energy recycling, and voltage restoring [1-4]. An FESS is a kinetic energy storage device which stores energy in a rotating flywheel, with the amount of stored energy dependent on the mass, form, and rotational speed of the flywheel. In the charging mode, the flywheel is speeded up to store the kinetic energy in its rotational motion. The kinetic energy is then maintained in the standby mode. In the discharge mode, the flywheel is slowed down to release the kinetic energy to the load.

Typically an FESS comprises of the motor/generator, bearing system, vacuum chamber, flywheel, power electronics, and other auxiliary items. The motor/generator is the key component responsible for the three aforementioned operation modes: charging, standby and discharge. Therefore the electrical machine of an FESS needs careful considerations during its design. For FESS using permanent magnet machines, the conventional choice has been the radial flux type. However the axial flux permanent magnet (AFPM) configuration has a distinct feature which can be exploited in FESS application: its axial force can be controlled to counter the gravitational force acting on the rotor if the axis of rotation is in the vertical orientation. Theoretically, this can reduce the stress and friction acting on the lower bearing system, thus reducing the bearing losses and therefore the self-discharge of stored energy during the standby mode. This allows the use of conventional ball or advanced ceramic bearings without the complexities and high costs associated with magnetic and superconducting bearings [5-7], or magnetically levitated flywheels.

Due to advances in machine design, AFPM machines can have higher torque, better power density and lower noise compared to radial flux machines [8-11]. It has also been shown that single air-gap axial flux machines [12-15] can generate substantial axial forces which have to be counteracted by the shaft bearings. In the machine proposed for electric vehicle in the literature [12], field control is used to produce a compensating axial force to balance with the attractive (axial) force between the rotor and stator. However this method requires complicated control schemes and efforts in axial force compensation, which may limit the range of electromagnetic torque. Using dual air-gap axial flux machines [11, 16], in which the total axial force is equal to the difference of the two attractive forces of the two air-gaps, one can achieve wider range of field control capability. However these designs have other complications such as requiring one power electronic converter to drive three phase AC currents and another converter to drive a DC field current [11]. In addition, they are not specifically designed for FESS applications.

Considering the pros and cons mentioned above, it is motivated to design a compact and efficient electrical machine for use in FESS applications. This research focuses on the design, analysis, implementation and control of a novel dual air-gap AFPM machine optimized for use in FESS.

1.2 Objectives and contributions of the thesis

The objective of this research is to develop a new dual air-gap AFPM machine optimized for use in FESS applications. This machine has two sets of three-phase stator windings but only requires one power converter which supplies power for control of both axial force and electromagnetic torque, [17]. Its application in FESS is realized by orientating its axial direction vertically and having its double-sided rotor to be the core of the flywheel. The availability of axial force control helps to minimize the vertical bearing force to improve the efficiency of the FESS. The design of the AFPM machine has been optimized for high efficiency, zero fundamental frequency

rotor losses, low cogging torque and improved back-EMF waveforms.

Another objective of this work is to investigate the losses of the proposed AFPM machine. Effects of space harmonics and time harmonics on the machine losses have been respectively analyzed using three-dimensional finite element method. The analysis is validated by comparisons of calculated losses and measured values on a prototype. A solution to reduce eddy-current losses in the magnets for the proposed machine is also suggested.

The contributions of this thesis can be summarized as follows.

- A novel dual air-gap AFPM machine for flywheel energy storage system applications has been presented in this thesis,
- Due to its non-conventional flux distribution, 3D finite element method has been used to analyze the proposed machine,
- Mathematical model for the proposed machine has been derived,
- The control system for the proposed machine has been developed. The position sensorless control scheme for the proposed machine has also been given,
- Implementation of the proposed machine, experimental study of the prototype and comparison between experimental results and simulations has been performed.

1.3 Structure of the Thesis

The study constitutes an overall approach to the design, analysis and control of dual air-gap axial flux permanent magnet machines. In a natural manner, a series of choices and decisions is involved in such an approach. To make a decision, there are some factors imposed at the onset by the requirements and constraints of the system such as

compactness, and efficiency; there are also other factors introduced in due time by the accompanying technical analysis like simplicity, cost effectiveness and reliability. The former are mainly about the configuration and structure of the machine and the latter are more on the details of the machine's parameters and its control, and also additional things such as the power electronic drives.

The study has been performed in sequence as critical review, design, analysis, fabrication, control and followed by the testing and measurement phase. A brief introduction of what is covered in each chapter is given as follows:

First, chapter 2 gives the literature review of the FESS and its related components. The review considers the major research directions in FESS undertaken in both universities and industries. The current status of flywheel energy storage technology, the obstacles faced by FESS industries, the present research and development activities and the potential future applications of FESS are also taken into account. Comparison of FESS with other energy storage systems is presented as well.

A novel dual air-gap axial flux permanent magnet machine for FESS is proposed in Chapter 3. The configuration of the machine is introduced and its basic components are then presented. After that, the detailed design procedure for this machine is summarized and given in section 4 of this chapter. The design specifications and prototypes are presented at the end of this chapter.

Chapter 4 presents the modeling approach for the dual air-gap axial flux permanent magnet machine. Co-energy and decoupling methods have been utilized to obtain the mathematical model for the machine. The nonlinear model is linearized to facilitate the implementation of the control system.

Chapter 5 describes the finite element analysis of the dual air-gap AFPM machine. The analysis is used to check the important parameters of the designed machine such as flux density, electromagnetic torques, cogging torque, axial force, losses and is also used to validate the feasibility of the machine.

Chapter 6 deals with control system design and its implementation for the proposed AFPM machine. Various simulations using Matlab Simulink have been done to test the performance of the machine in both normal operation and short-time over-rated operation. The feasibility of the position-sensorless control system for this machine and its effective performance have also been validated by Matlab Simulink.

The experimental implementation and analysis for the proposed dual air-gap AFPM machine are demonstrated in Chapter 7, where the hardware prototype of the system, control board and DSP-based processor are described. This chapter also presents the measurement and experimental work on the machine prototypes including cogging torque, air-gap flux, inductances, induced voltages, electromagnetic torques, and power losses. Comparisons of dual air-gap AFPM machines with fractional and integral slot per pole are given as well. Lastly, the experimental results obtained from the control performance test of the dual air-gap AFPM machine and the position-sensorless control of the dual air-gap AFPM machine are analyzed and compared with the simulation counterparts.

Finally, Chapter 8 gives the conclusions of this thesis by summarizing the main results and presenting some concluding remarks. Further, some recommendations for future research are included.

CHAPTER 2 LITERATURE REVIEW

2.1 Introduction

Kinetic energy storage in the form of flywheels has been known for centuries. But it has become significant in recent years thanks to the advances in high strength, light weight composite material, high performance magnetic bearings, and power electronics technology. An FESS with very high speed from 20,000 rpm up to above 60,000 rpm is achieved today. Flywheel battery with above 60,000 rpm in operation can generate nearly 10 Whr/kg energy and can supply a depth-of–discharge (DOD) of up to 75% [18-20]. With the development of low-loss bearings, especially magnetic bearings and hybrid ceramic bearings, flywheel batteries become more significant by having low friction losses, contact-free operation, adjustable damping, good stiffness characteristics, and also the fact that no lubricants are required [5, 7, 21-23]. In addition, fast progress in power electronics in recent years, particularly in high-power IGBTs and FETs, underlies higher-power flywheel operation.

Unlike conventional chemical batteries, flywheel batteries operate reliably for many years, up to 20 years [24, 25], with little or even no required maintenance. Flywheel-based energy storage systems, unlike lead-acid batteries, are sustainable "green" technology solutions that do not use hazardous materials for production, nor create them during operation. Due to little harm to the environment, flywheel battery technology is considered as clean and green energy storage technology nowadays.

This chapter presents a general review of the FESS. The fundamentals of FESS will be introduced in Section 2.2. After that the current status of flywheel energy storage technology will be discussed in Section 2.3. Various energy storage systems will be presented and compared with the FESS in Section 2.4.

2.2 Fundamental of FESS

An FESS is a kinetic energy storage device which stores energy in a rotating flywheel, with the amount of stored energy dependent on the mass, form, and rotational speed of the flywheel. In the charging mode, the flywheel is sped up by the input electronic converters and motor to store the kinetic energy in its rotational motion. The kinetic energy is then maintained in the flywheel in the standby mode. In the discharge mode, the flywheel is slowed down to release the kinetic energy to the load by the generator and output electronics. The fundamental components of an FESS are shown in Fig. 2.1. As usual, the motor and the generator are combined into a single machine in many approaches so as to reduce the total system weight and costs.

Fig. 2.1 Flywheel energy storage system fundamental

2.2.1 Configuration of FESS

Typically an FESS comprises of the flywheel, motor/generator, bearing system, vacuum chamber, power electronics, and other auxiliary items. A simplified FESS is illustrated in Fig. 2.2. The main components of an FESS usually include:

- A high speed flywheel attached to the rotor to store the energy;
- Magnetic bearings for minimizing frictional losses;
- A motor/generator which converts electrical energy to mechanical energy and vice versa;
- Mechanical touchdown bearings to support start-up and shut-down, and to protect against magnetic bearing failures;

- A sealed housing to provide structural support for the bearings and vacuum enclosure.
- A power electronic converter to control the power into and out of the windings of the motor/generator;
- A processing unit to provide voltage regulation, machine winding current control, magnetic bearing control, health monitoring, and serial communication for command and telemetry;
- A secondary power supply to furnish low voltage power for the control electronics;
- Magnetic bearing drive amplifiers for driving the magnetic bearing coils;
- An EMI/EMC filter to limit conducted electromagnetic interference;
- Auxiliary bearing actuator electronics

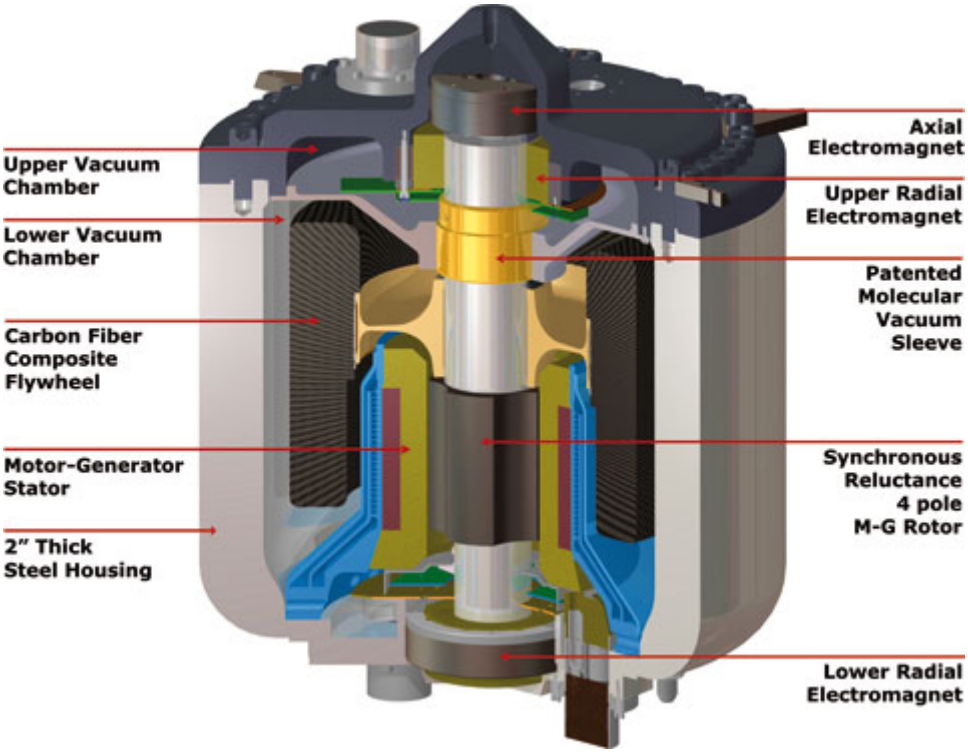

Fig. 2.2 A schematic of an FESS [26]

2.2.2 Materials for the flywheel

It is now possible to construct flywheels with high-strength composite material that can operate at very high speed. Progress in modern bearings makes it suitable for the high-speed flywheel systems due to their contact-free operation, low friction losses, stability and reliability [5, 7, 23, 27-29]. In addition, advance in power electronic devices in recent years underlies higher power FESS operation.

There is a risk that the flywheel may be destroyed when it spins at a very high speed. Therefore in order to prevent them from flying apart, modern high-speed flywheels have complex structures with the use of extremely strong materials like advanced aerospace material, titanium, glass fiber reinforced polymer, carbon fibers, and carbon-nanotube. Air friction losses are addressed by housing the flywheel in evacuated chambers; the level of vacuum being determined by whatever value of air friction loss is tolerable in such particular applications.

The stored energy in a rotating flywheel, in joules, is given by:

$$E = \frac{1}{2} J \omega^2 \tag{2.1}$$

where J is the flywheel moment of inertia and ω is the angular velocity. The moment of inertia is determined by the mass and geometry of the flywheel:

$$J = \int x^2 dm_x \qquad \left[kg.m^2 \right] \tag{2.2}$$

where x is the distance from the axis of rotation to the differential mass dm_x.

Stored energy in the flywheel is proportional to its mass and the square of its speed. Therefore, in order to maximize the energy capacity, the flywheel is designed by increasing its speed rather than its moment of inertia as this approach produces higher specific energy [30, 31]. Hence high or low energy storage can base on high-speed or low-speed systems.

High-speed flywheel systems often have rather small flywheel and can rotate at a few ten thousand revolutions per minute. In this type of FESS, high-strength composite materials are often required to withstand the centrifugal force when operating at very high speed. An example of high-speed flywheel system is shown in Fig. 2.3.

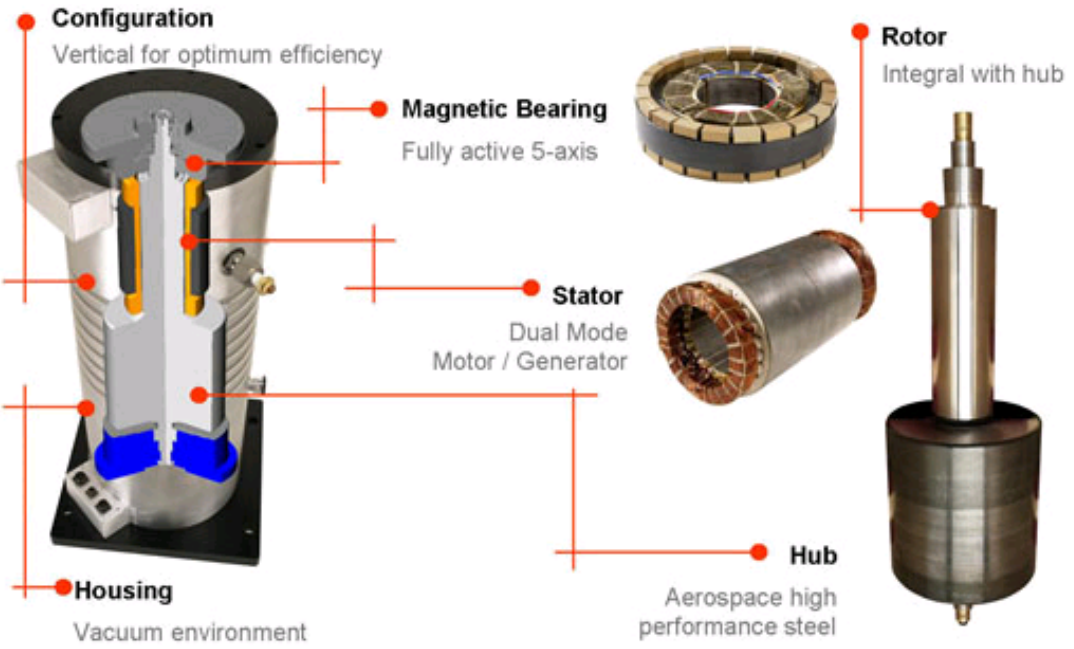

Fig. 2.3 A high-speed FESS [32]

Compared to high-speed FESS, low-speed ones often have bigger flywheel of up to meter or more, spinning at lower speeds of few thousand rpm. For this type, steels are usually used instead of composite material for lower cost and easy manufacture.

Steel flywheels can have high energy density because steel materials are isotropic and have high strength. However due to high mass density, steel flywheel can attain a low specific energy [31]. Fiber-composite flywheel can have higher specific energy than its steel counterpart due to its low mass density. The summary of a comparison between steel and composite flywheel is shown in Table 2.1 - the values in this table are all in per unit (pu).

Table 2.1 A comparison between metal and composite flywheels for the same stored energy [31]

	Composite	Steel
Weight	1 pu	2–5 pu
Volume	2.5–5 pu	1 pu
Circumferential speed	1.5 pu	1 pu
Weight of safety enclosure	0.5 × flywheel weight	2 × flywheel weight

Table 2.1 shows that composite flywheels have an advantage over metal counterparts in term of weight, but the latter are more dominant in term of volume. This means that a steel flywheel can be a heavier system while larger structure is unavoidable for a composite flywheel. However failure during operation is much less destructive in a composite flywheel than in a steel one. In addition, weight of safety enclosure is four times in the steel flywheel system in comparison with its composite counterpart [33]. Circumferential speed index shows that the composite flywheel system has more windage losses than the metal one.

Composite flywheels possess a lightweight and robust structure and have high specific energy but they are bulky, costly and is based on an immature technology. Meanwhile, steel flywheels are of a mature technology with low price; however they are quite heavy and having high losses when used with conventional mechanical bearings. Advantages and disadvantages of the composite flywheels and the steel counterparts are summarized in Tables 2-2 and 2-3 below:

Table 2.2 Advantages and disadvantages of composite flywheel

Advantages	**Disadvantages**
Lightweight and robust	Costly
Low loss during operation	Immature technology
Easy to use with contact-less bearing systems	Higher windage losses than steel flywheel system
High specific energy	Large volume

Table 2.3 Advantages and disadvantages of steel flywheel

Advantages	Disadvantages
Low price	Heavy
Mature technology	High losses when use with mechanical bearing system
Low speed so can use with mechanical bearing system which is mature nowadays	Large containment for safety
Low windage losses	Low specific energy

2.2.3 Bearing technology

In an FESS, the flywheel usually operates at high speed and it uses high performance bearings because the bearings play important role to achieve low losses and to minimize the system maintenance. Different developers and manufacturers have their own special bearings to meet their specific FESS [6, 34-41]. For example, a bearing system consists of a passive magnetic bearing at the top, and a low-loss bearing at the bottom of the vertical axis is utilized in Urenco FESS [35] or a combination of ceramic ball bearings with magnetic levitation bearing is used in Active Power FESS [34] to reduce losses and increase bearing life substantially.

Hybrid ceramic bearings (HCB) have gained great improvements recently [23, 42, 43]. HCB have several advantages over all-steel bearings, such as higher speed and acceleration capability, increased stiffness, higher accuracy, lower friction and heat generation, reduced lubrication requirements, low thermal expansion, and extended operation life. For example, Ringlube Technology bearings have friction energy loss of less than 0.03% per hour, can last over ten years without maintenance and reported to support Tribology Systems Flywheels to coast unpowered for over 4 months [43].

High-temperature superconductor (HTS) bearings with extremely low rotational loss are also utilized in FESS applications [6, 36-41, 44-46]. These bearings have a rotational drag more than two orders of magnitude lower than that of a conventional magnetic bearing and several orders of magnitude lower than that of mechanical

bearings. With HTS bearing, an energy-efficient flywheel could be constructed with a bearing loss of < 2% per day (including parasitic power to cool the HTS). However until the present time, no high-temperature superconducting flywheel in continuous operation is available [6]. Most problems of development are mainly associated with rotor dynamics and rotor stabilization by HTS bearings. It appears that HTS-bearing supported FESSs will not be soon available for use in industry. It requires multidisciplinary skills not only in superconductivity but also in material sciences, magnetics, power electronics, vacuum techniques, and rotor dynamics.

2.2.4 Chamber

A common method of containment for the high speed flywheel at present is the vacuum chamber or helium filled type. Main purposes in advanced design of the chamber are to reduce the aerodynamic losses (windage losses), eliminate rotor stresses and ensure a safe containment for the flywheels. Losses due to windage can be negligible when the chamber pressure is reduced to less than 1 mbar. Currently manufacturers and developers have been working extensively on safety issue as it is also crucial one in the FESS.

2.3 Current status of Flywheel Energy Storage Technology

2.3.1 Manufacturers and developers

More and more manufacturers and developers (M&D) has participated the flywheel storage markets nowadays. Most of them have developed high-speed composite flywheels. Few suppliers manufacture steel flywheels, such as Active Power Inc, and Caterpillar. Almost all of the manufacturers supply standard products targeted at a range of applications, some of them give the design solutions in response to customer-specific requirements. An update of the M&D based on [47] is shown in Table 2.4.

Table 2.4 Brief summary of selected manufactures and developers

	Liebert (Emerson)	**Vycon Flywheel Energy**	**Boeing**	**AFS Trinity**
Product status	XDH series: available FS series: discontinued	Commercial product available	Developed / in test	Commercial
Motor/Gen. type	Synchronous reluctance	Permanent magnet	Permanent magnet brushless	Permanent magnet
Rotor type	Carbon fiber	Aerospace-grade steel	Composite rotor	Carbon fiber composite
Bearing type	5-axis active magnetic levitation systems	5-axis active magnetic bearings	PM lift and HTS bearings	Advanced bearings
Chamber	Not specific: low-loss and extremely safe material	Aluminium, using as vacuum housing to support bearings and the stator	Steel and vacuum	
Power per rotor	200kW	40-1,100 kW	100 kW	100/ 200 kW
Capacity per rotor		833 kWh max.	5 kWh	0.42/ 2.0 kWh
Rotor speed	52,000 rpm	18,500 - 36,000 rpm	22,900 rpm	Up to 40,000 rpm
Applications	UPS	Energy recycling UPS/ Power quality	UPS	UPS, Power quality & management
Efficiency		99.2 – 99.4% at max. power rating		700 W max.
Operating temp. Storage temp.	-20°C to 50°C -20°C to 80°C	-20°C to 40°C		-20°C to 40°C
Lifetime	> 20 years (y)	> 20 y		> 10^5 cycles

	Active Power	**Acumentrics**	**Blueprint Energy**	**Beacon Power**
Product status	Commercial	Commercial	In test/ commercial	Commercial
Rotor type	Solid forged 4340 steel	Composite		Carbon-fiber
Bearing type	Ceramic ball and magnetic lift bearings		Custom bearings	Magnetic bearings
Chamber	Cast iron for vacuum housing and stator	Stainless steel (weatherproof)		Steel
Power per rotor	250kW per rotor	80/ 140/ 200 kW	120 kW	2 - 250 kW
Capacity per rotor	1kWh approx.	0.44/ 0.56/ 0.55 kWh	0.75 kWh	6 - 25 kWh
Rotor speed	2,500 – 7,700 rpm			16, 000 rpm
Applications	UPS	UPS	Transportation applications	Telecomm. UPS & Power quality
Efficiency	99%	>95%	94 – 97%	
Operating temp. Storage temp.	-20°C to 40°C -25°C to 70°C	-20°C to 45°C -50°C to 65°C		0°C to 35°C 20°C to 70°C
Lifetime	> 25 y, $>10^4$ cycles			20 y

	Optimal Energy Systems	**Pentadyne**	**Urenco Power Technologies**	**Tribology Systems Inc.**
Product status	Under development	Commercial	Commercial	Commercial
Motor/Gen. type	Ultra high-speed flywheel module [48]	Synch. reluctance	PM brushless d.c machine	Integrated flywheel motor-generator
Rotor type	Graphite fiber	Carbon fiber	Composite	Composite
Bearing type		Magnetic	Passive magnetic and pivot bearings	Hybrid-ceramic ball bearings
Chamber			800 kg steel	
Power per rotor		120 kW	250 kW max	40kW
Capacity per rotor	0.9 kWh	0.67 kWh	2 - 3 kWh (max)	0.5 kWh
Rotor speed	60,000 rpm	55,000 rpm	18,000- 37,800 rpm	28,000 rpm
Applications	UPS, load levelling, Space, Pulsed power	UPS, Power Quality HEV	Power quality, Traction, Cyclic	Load blancing, Surge power in HEV
Efficiency			91 - 94%	
Operating temp. Storage temp.		-20°C to 50°C -20°C to 80°C	0°C to 40°C 0°C to 70°C	
Lifetime	$2x10^5$ cycles		20 y $0.5 – 10x10^6$ cycles	> 10 y $1x10^5$ cycles

	Flywheel Energy Systems	**Magnet-Motor**	**Piller**	**Rosseta-Technik**
Product status	Rotors developed and system developing	Under development and commercial	Commercial	Under development and commercial
Rotor type	Composite	Carbon fiber composite	Steel disc	Graphite fiber, epoxy resin composite
Bearing type	Mechanical	Bearings, plus magnetic support	Ball bearings, permanent greased	
Chamber			Steel	
Power per rotor	1.5kW (UPS) 50 kW (PQ/HEV)	5MW demonstrator	1,300 kW	100 to 300 kW
Capacity per rotor	1.1kWh (PQ) 1.3kWh (PQ/HEV)	80 MJ (22.2 kWh) prototype	4.6 kWh	2 to 6 kWh
Rotor speed	15,000 – 45,000 rpm		1,800 – 3,400 rpm	10,000 – 25,000 rpm
Applications	UPS, Power Quality, HEV	Urban buses, HEV UPS, Pulsed power	Load-leveling, traction systems	Railway, HEV, Peak load shaving
Efficiency			95%	
Operating temp. Storage temp.			0 to 40°C -30°C to 40°C	
Lifetime	Typ. $1x10^5$ cycles		25 y, $10x10^6$ cycles	20 y, $5 x10^6$ cycles

***There are some blank cells in this Table; it is due to various reasons but mainly is the reason of confidence in research and business of the M&D.**

2.3.2 Applications of FESS

The FESS has attributes that make it attractive for use in both terrestrial and space applications. In terrestrial applications, pulse power supply capability of the FESS is utilized in hybrid and electric vehicles, electric rail, and shipyard crane applications, in renewable energy applications, in distributed generation for power smoothing, power leveling, and voltage restoring. Meanwhile, in space applications, energy storage and attitude control functions of the FESS have been greatly exploited.

2.3.2.1. In Terrestrial applications

A. Power quality

In certain power system, the power consumption varies throughout. The unequal use

of power makes the power system unstable and results in the power quality problems such as instantaneous interruption, voltage sag, lack of reactive power or active power. To retain the quality of power system, uninterruptible power supply (UPS) system is usually considered as one of the best solutions. Ride-through power and voltage stabilization for such power system can be handled by FESS-based UPS which is a more reliable and greener approach to backup power in place of hazardous lead acid based batteries [2-4]. Direct connect FESS-based UPS backup systems also brings unprecedented power capacity for instantaneous and reliable backup power for mission-critical applications nowadays, such as in data centers, hospitals, broadcast studios, casino gaming centers and manufacturing plants [32, 49, 50].

Beside the above-mentioned applications, FESS can also perform fast-response frequency regulation in power system [51, 52]. To ensure a functional and reliable grid, the various regional grids must be maintained their electric frequency very close to 50 hertz (Hz), or cycles per second (60 Hz in the US and elsewhere). Grid frequency is held at a stable level when the supply of electricity matches the demand (or "load"). Therefore, it is necessary to obtain a continuously balance electricity supply with load to maintain the proper frequency. This can be done by directing about one percent of total generation capacity to increase or decrease its power output in response to frequency deviations with the support of the FESS [51-53].

B. Energy recycling

In shipyards and rail yards, a container can be loaded or removed by a mobile crane in about a minute time. Up until now, in that minute the mobile cranes use the fuel and release exhaust fumes for both lift-up and moving-down cycles. Mobile cranes get their power from an on-board diesel generator set, which provides the required voltage and frequency to variable-speed AC motors by way of an inverter. During lift cycles, peak power is drawn from the generator. During lowering and braking, all regenerated power is dissipated in a resistor bank. Instead of burning off the power during down cycles

when significantly less energy is required, the unused energy is stored in the FESS for use during the next up cycle. By utilizing the FESS with the mobile crane, significant savings can be obtained with seamless and instant transitions, such as: improved fuel savings in diesel generator and cranes, reduced exhaust fumes emissions, enhanced system response, and reduced generator set wear and tear [32, 54, 55].

Energy recycling by the FESS has also been applied in hybrid electric vehicles where both internal combustion engine and electric machine are used for propulsion. During climbing hill and acceleration of the vehicles, short bursts of power are taken from an FESS, which is resupplied directly by the engine or by regenerative braking when the vehicle is slowed down. An FESS is a more attractive energy store medium than a chemical battery in the application of electric vehicles [56-58]. Not only it is smaller and lighter than the battery it replaces, but it is also expected to have more than ten times of the lifespan compared to the conventional chemical battery pack.

2.3.2.2. In Space applications

Conventional low earth orbit space satellites require energy storage system and moment gyro attitude reference. High speed FESS can provide energy storage and attitude control at the same time [19, 24, 59-63]. The FESS owns specific attributes which makes it attractive for use on the space station. It fits in roughly the same space and has similar weights of the chemical batteries it would replace, and is likely to last three to ten times longer. NASA's IPAC system shows the advantages of FESS like improved efficiency, reduced space satellite weight and cost. Another NASA's flywheel utilization is to regulate DC bus power of international space station (ISS). During eclipse period of the ISS earth orbit, the FESS provides power to the load.

In spacecraft, another significant benefit can be acquired by combining energy storage with attitude control functions [60]. In this approach the flywheel momentum and torque characteristics are used as an attitude control resource rather than viewed as a potential disturbance source. This reduces the space vehicle bus mass, volume, cost, and maintenances while maintaining or improving the space vehicle performance.

2.3.3 Present research and development activities

Recently, the main R&D activities in FESS have been focusing on reducing the overall cost of the systems, lessening the losses and extending the bearing life. The Composite Manufacturing Technology Center at Pennsylvania State University is working to develop a cost-effective manufacturing and fabrication process for advanced composite rotors. The scope of this research includes the development of a rapid filament winding process for glass and carbon reinforced epoxy and polyurethane matrix rotors, the measurement of strain in high-speed rotors using opto-electronics devices, the determination of fatigue behavior of composite rotor material using coupon tests, and the development of vacuum chamber for testing of rotor up to 14 inches diameter.

The Center for Electromechanics (CEM), University of Texas is involved in Flywheel and Alternator Development for the Advanced Locomotive Propulsion System and is also a pioneer in the US Flywheel Safety and Containment Program. The CEM believe that compact flywheels are feasible with megawatt power and about 500MJ (~140 kWh) stored energy, which are of interest for electric utility line stabilization. The current research at CEM involves in the investigation of high strength materials, rotor dynamics, containment, non-destructive evaluation, and thermal management.

Passive magnetic bearings, which have a long lifetime, do not require maintenance or lubrication, have reduced frictional losses, especially suitable for ultra-high speed flywheel storage systems, and also applicable for other applications have been developed in research centers, such as Department of Mechanical and Aerospace Engineering at the University of Virginia, Lawrence Livermore Laboratory (US). Passive bearings are attractive because they are self-contained, unlike active magnetic bearings that require external electronic circuits and additional power supply. This is one of the current research efforts in reducing the cost of the FESS.

Recent research at NASA Glenn Research Center (US) is aimed to develop a 5-fold

increase in the specific energy of existing spacecraft batteries, and to achieve a 2-fold increase in battery life in low-earth orbit applications. An FESS with full-speed of 60,000 rpm has been achieved at Glenn Center and although this is targeted at spacecraft, it is possible that there will be technology transfer for other applications.

In addition, flywheel for hybrid electric vehicle applications has also received special attentions from many suppliers and centers, such as Alpha Batteries, Ricado, Magnetal AB, and the US Department of Energy HEV program. Combination of the flywheel with a standard engine, to provide assistance during acceleration, and absorb braking energy is one of current research interests. Other noticeable research and development is the continuously variable transmission by advanced kinetic energy recovery systems which is being extensively investigated by Ricado in FLYBUS and KinerStor research projects (partly funded by the UK Government's Technology Strategy Board).

Other research trend is the integration of flywheel systems with other energy storage systems. It seems that a new trend for energy storage in renewable energy systems is to combine several energy storage technologies as what have been done in uninterruptible power system (UPS) application. In this integration, a storage system may compose of compressed-air system, thermal storage unit, and flywheel energy storage, [64].

2.3.4 Potential future applications

Potential applications of FESS in the future include:

- Uninterruptible power supply / Power quality,
- Bridging power until a diesel generating set in a hybrid stand-alone power system,
- Energy recycling for crane and rail applications,

- Power system stability,
- Frequency regulation for power systems,
- Peak power support for power systems,
- Frequency response reserve for power systems,
- Angular instability control to prevent wide-scale blackouts in power systems,
- Reactive power support for power systems,
- Stabilization of distributed generation systems,
- Cloud mitigation for solar photovoltaic,
- Ramp mitigation for wind applications,
- Wind/ diesel generator/ flywheel hybrid systems,
- Integrated solutions for hybrid electric vehicles,
- Voltage support for both existing rail systems and construction of new light rail transit systems.

2.4 Comparison FESS with other Energy Storage Systems

2.4.1 Energy Storage Technologies

Several energy storage technologies have been utilized and introduced in recent years. The selected technologies in this study include electrochemical battery, compressed-air energy storage, pumped hydro storage, superconducting magnetic energy storage, ultra-capacitor energy storage, hydrogen energy storage and flywheel energy storage.

2.4.1.1. Battery Energy Storage System (BESS)

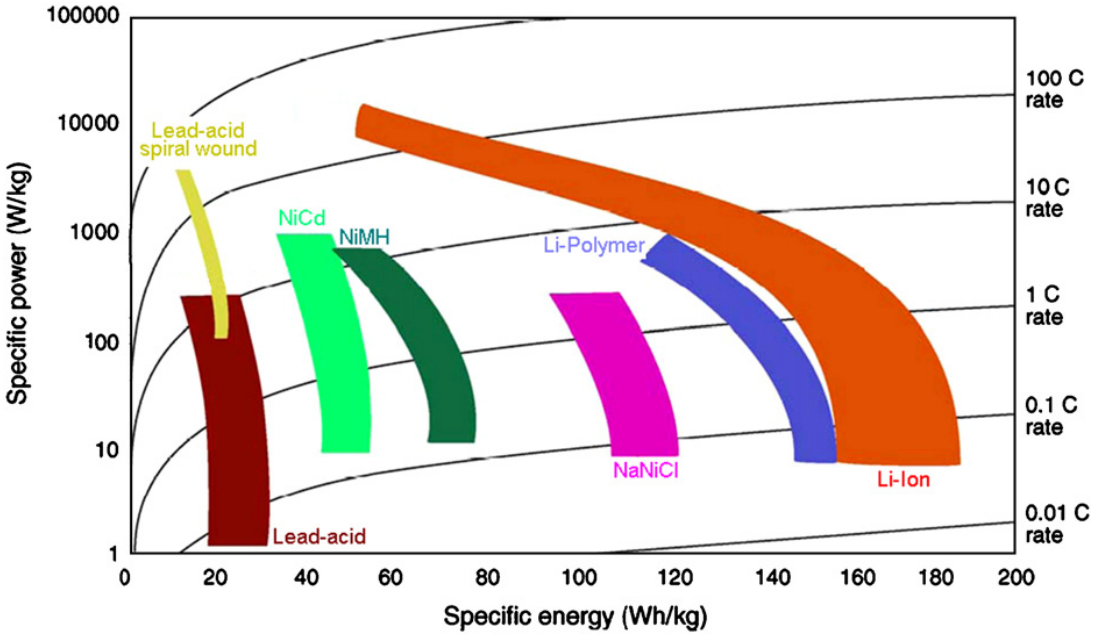

Fig. 2.4 BESS technologies according to their energy densities, their power [65]

A battery stores potential energy through the chemical reactions of its electrochemical components. Charging a battery causes reactions in the compounds which then stores the energy in a chemical form. Upon demand, reverse chemical reactions cause electricity to flow out of the battery and back to the grid. Quick response is one of the battery technology's strong points: some batteries can respond to load changes in about 20 milliseconds. The efficiency of battery modules is in the 60-80% range, depending on how often they are cycled and on the electrochemical types used [66, 67]. BESS is the most common system used until now; its significant characteristics include energy densities (up to 150 and 2,000Wh/kg for lithium), technological maturity (in Fig. 2.4), and the capability to be used in both portable systems and permanent applications. The capital cost for BESS ranges from 300 to 3,000 USD/kW, which much depends on what modern battery technology used. There is a wide range of battery technologies available today: lead–acid, nickel–cadmium, nickel–metal hydride, nickel–iron, zinc–air, iron–air, sodium–sulphur, lithium–ion, lithium–polymer. Most battery technologies are optimized for either power or energy,

but not both [68]. Furthermore, batteries designed for high power often cannot provide the repeated charge/discharge cycles that are required in many energy storage applications. This is the inherent weakness of the BESS.

2.4.1.2. Compressed Air Energy Storage (CAES)

This scheme makes use of a compressor which uses off-peak energy to compress air and store the compressed air at high pressure (typically around 75 bar) in an air reservoir (an aquifer, natural caverns, or mechanically formed caverns). During discharges at peak loads, the compressed air is released to a combustor where the compressed air is mixed with oil or gas driving a gas turbine to create electrical energy. Fig. 2.5 shows an illustration of a CAES. Compared to other technologies, CAES have long cycle life and very large energy density but high installed cost [60, 69]. Typical ratings for a CAES system are in the range of 50-300 MW, with efficiency of about 85% (when properly accounting for thermal and electrical input energies) [67]. Beside large capacity CAES system, there exit smaller ones where the air can be stored in pressurized tanks to reduce the systems' sizes [70, 71]. The world's first commercial 290-MW, 4-hour CAES located in Huntorf, Germany was commissioned in 1978. It has been running for more than 30 years, showing strong performance: 90% availability and 99% starting reliability. Recent research in CAES is devoted to the maximum efficiency point-tracking control [72] or integrated technologies for power-supply applications [72-75]. The main disadvantages of CAES technology include its geographic dependence and high investment cost.

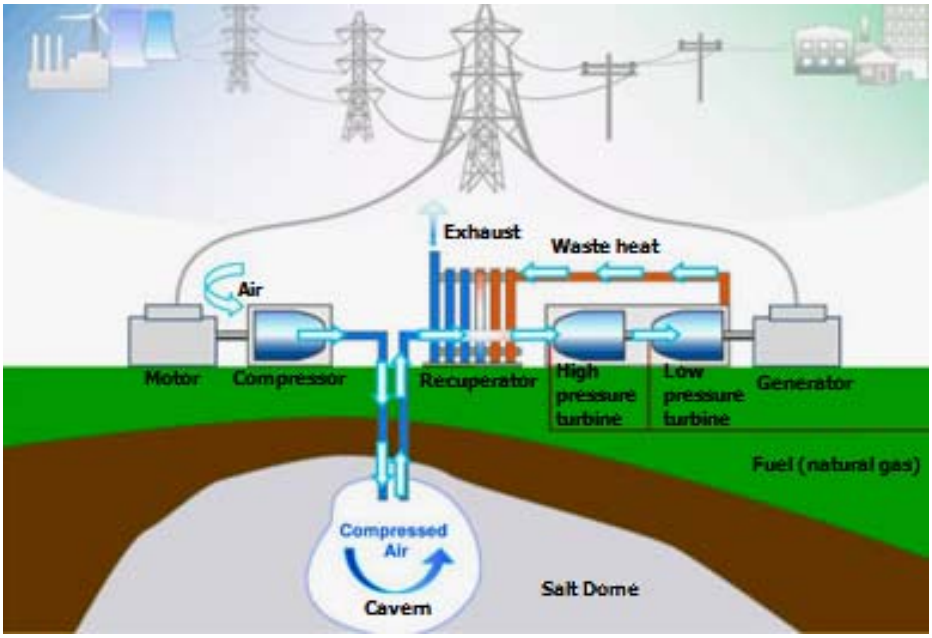

Fig. 2.5 Illustration of compressed-air energy storage [76]

2.4.1.3. Pumped Hydro Energy Storage (PHES)

Pumped hydro was first used in Italy and Switzerland in the 1890's. Since 1930's it has been used as the most widespread ESS on power networks with over 90 GW of pumped storage in operation world wide. Large pumped hydro plants of 1,000MW or above are installed worldwide today. Pumped-hydro plants use off-peak power to pump water uphill to an elevated reservoir. When required, the water flow is reversed to generate electricity by the release of its potential energy [66, 77]. Open sea can also be used as the lower reservoir. An illustration of Pumped-hydro plant is shown in Fig. 2.6. Generally pumped hydro is available at almost any scale, with discharge times ranging from several hours to a few days. Its efficiency is 70-85% depending on plant size, penstock diameter, hydro turbines used, and the height between the upper and lower reservoir [67]. Pumped hydro plant's main applications are for energy management, frequency control and provision of reserve. Current researches are concentrated upon applying modern variable-speed drive techniques in underground pumped hydro storage [78]. These methods have better improvement in efficiency but require very high capital cost of 1,200 - 2,000 USD/kW [79]. Similar to CAES, PHES

technology requires special geographic location and its investment cost is very high.

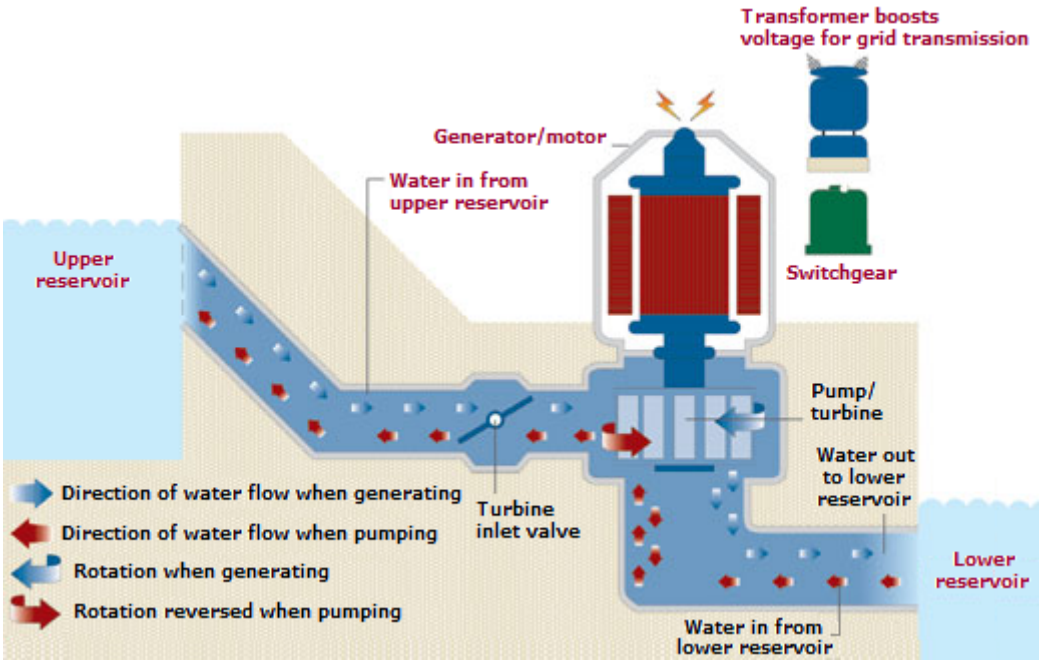

Fig. 2.6 An illustration of pumped hydro storage [80]

2.4.1.4. Superconducting Magnetic Energy Storage (SMES)

A Superconducting Magnetic Energy Storage system stores energy in the magnetic field created by the flow of direct current in a coil of superconducting material [81-83]. A basic structure of SMES is shown in Fig. 2.7. The amount of stored energy is:

$$E = \frac{1}{2} L I^2 \tag{2.3}$$

where I is the direct current flowing in the coil. This current should be maintained as high as possible to store a maximum energy. Non-superconductors cannot be used in this application because of high resistance. Therefore coils made from superconducting material are applied to store significant amounts of energy. To maintain the coil in its superconducting state, the coil is immersed in liquid helium which is contained in a vacuum-insulated cryostat. The energy output of a SMES system is much less dependent on the discharge rate than batteries. SMES systems also have high cycle life and as a result, are suitable for applications that require

constant, full cycling and continuous mode of operation. Although research is being conducted on larger SMES systems in the range of 10-100 MW, recent focus has been on the smaller micro-SMES devices in the range of 1-10 MW for system stability applications [66]. Micro-SMES devices, low temperature cooled by liquid helium types, are available commercially [84] for power quality applications. High temperature SMES cooled by liquid nitrogen is still in the developmental stage and may become a viable commercial ESS in the future [85].

One of the new applications of SMES technology is distributed SMES (D-SMES) system. D-SMES provides cost effective grid stabilization for entire electric utility systems. D-SMES can be used to protect the power grid from voltage dips, load demand variation and switch operation. A D-SMES network from American Superconductor Corporation (AMSC), one of the key developers of SMES, is shown in Fig. 2.8

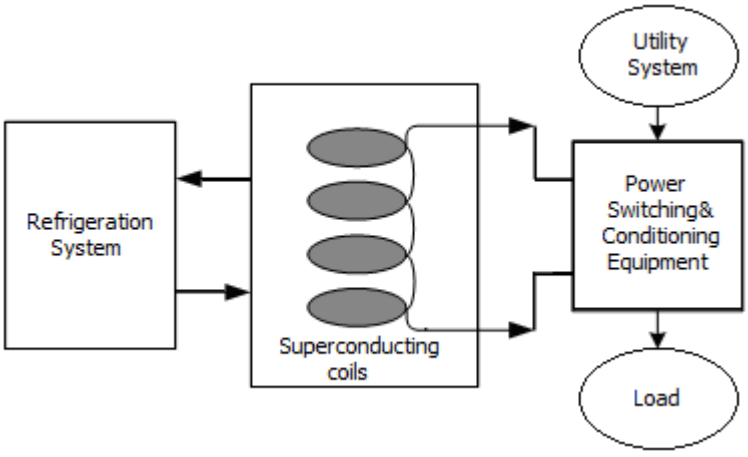

Fig. 2.7 Basic structure of SMES system

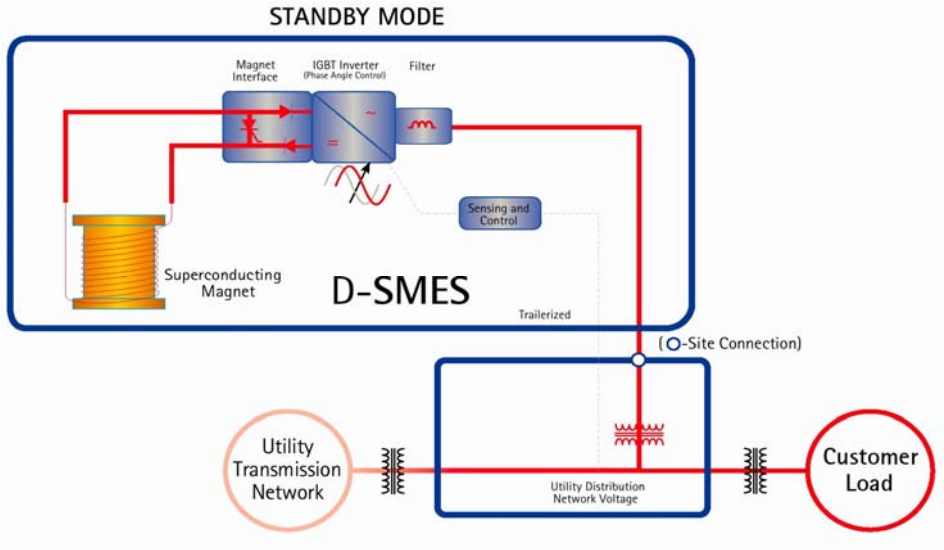

Fig. 2.8 D-SMES Network of AMSC [86]

2.4.1.5. Ultra-capacitor Energy Storage (UCES)

An ultra-capacitor, also known as a double-layer capacitor, polarizes an electrolytic solution to store energy electrostatically. Between the two electrodes there is a dielectric separator used to prevent the charge from moving between the two electrodes. An ultra-capacitor, its modules, and an ultra-capacitor cell are depicted in Fig. 2.9. The capacitance and energy density of these devices are thousands of times larger than electrolytic capacitors.

The energy stored in ultra-capacitors is [87]:

$$E = \frac{1}{2} q V_c = \frac{1}{2} C V_c^2 \tag{2.4}$$

where q (Coulombs) is the charge at each interface, V_c (Volts) the potential difference between two electrodes, and C (Farads) the capacitance of the ultra-capacitor.

Compared to lead-acid batteries, ultra-capacitors have lower energy density of less than 15Wh/kg (60Wh/kg using carbon nanotubes enhanced ultra-capacitors) but they have a very high power density of 4,000 W/Kg, can be cycled tens of thousands of times and have much faster charge and discharge capabilities than batteries [30].

They have considerable promise as replacements for batteries, or use together with batteries in a wide variety of applications. The main drawback of UCES technology is its very high cost which ranges from 100 to 500 USD/kW and reaches up to 10,000 USD/kWh. This prevents UCES technology from popular use in industry at the present time. New trends focus on using ultra-capacitors in power quality applications, covering temporary high peak-power demands, integration with other energy-storage technologies, and development for high-voltage applications [88, 89].

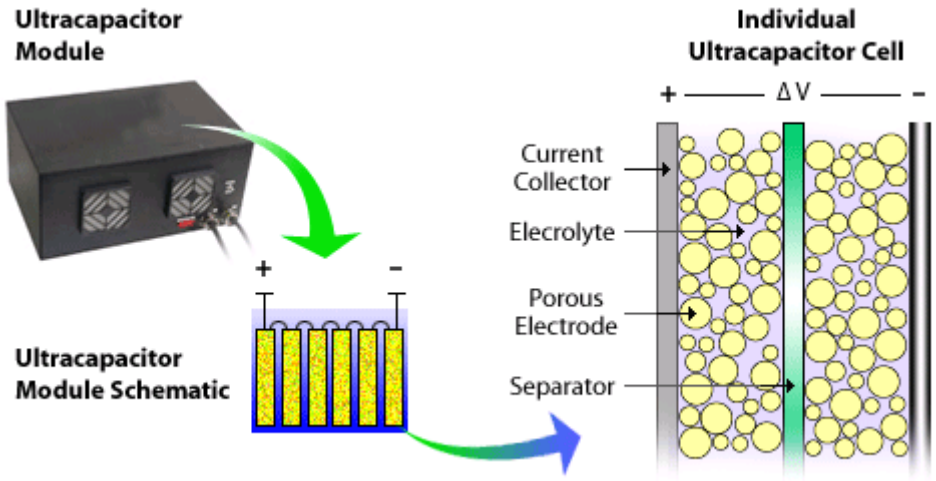

Fig. 2.9 Operation principle in an ultra-capacitor [90]

2.4.1.6. Fuel Cells - Hydrogen Energy Storage

Hydrogen-based energy storage systems are receiving increasing attention recently. Essential element is an electrolyser unit which uses off-peak electricity to produce hydrogen from water. The hydrogen then can be used with oxygen in the air to produce electrical energy at peak time. This means that a bulky storage chamber is needed to store hydrogen. Typical reactants used in a fuel cell are hydrogen on the anode side and oxygen on the cathode side – as shown in Fig. 2.10. Hydrogen fuel is supplied from a gas chamber on the anode side and the oxidant, air or oxygen is supplied from a gas chamber on the cathode side [91]. The anode and cathode are separated by an ion-exchange membrane. This membrane is thin to allow positive hydrogen ions *(H+)* to pass, but thick enough to prevent neutral oxygen *(O_2)* molecules. Electrons are separated from the supplied *$2H_2$* by the catalyst-coated

membrane, in the following chemical reaction:

$$2H_2 = 4H^+ + 4e^- \tag{2.5}$$

In the cathode side, water is combined regarding reaction:

$$O_2 + 4H^+ + 4e^- = 2H_2O \tag{2.6}$$

Electrical energy by an ion-membrane fuel cell is [31]:

$$E = neV_{fc} \tag{2.7}$$

where n is the number of electron, e the electron charge and V_{fc} the cell's electromotive force, 1.23*volts*.

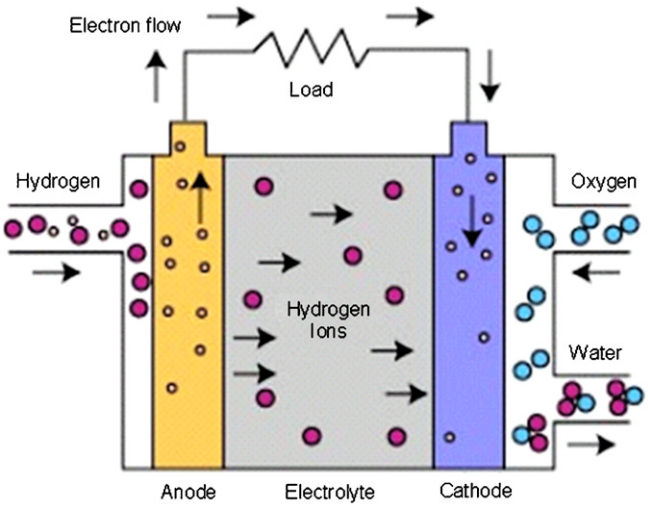

Fig. 2.10 Illustration of a fuel cell [92]

Many types of fuel cells are available, such as: Alkaline Fuel Cell, Polymer Exchange Membrane Fuel Cell, Direct Methanol Fuel Cell, Phosphoric Acid Fuel Cell, Molten Carbonate Fuel Cell, Solid Oxide Fuel Cell. These kinds of batteries differ in electrolyte, operating temperature and field of applications. Its major applications are for electric vehicles and electricity production via fuel cells [93, 94]. Depending on the operating pressure and efficiency of an electrolyzer-fuel cell combination or the operating pressure and efficiency of the reversible fuel cell device,

efficiency is expected to be in the 60-85% range. The main disadvantages of hydrogen-based storage technology include its high cost and limited life expectancy. Recent research and development are focused on new materials and technologies for hydrogen storage. Current applications identify and investigate advanced concepts for energy storage materials that have the potential to achieve the target of 2 kWh/kg and 1.5 kWh/L in upcoming years.

2.4.2 Comparisons amongst energy storage systems

2.4.2.1. Parameters for Comparison Studies

Various energy storage technologies typically have important areas of performance such as energy density and cycle life which can, to a certain extent, be traded against each other. In addition, other non-performance based parameters, for example safety and environment issues are also crucial in the selection process. Therefore to compare the performance of the different storage techniques, a number of parameters often expressed in a wide variety of terms and units need to be considered [30, 31, 66, 95]:

- Storage capacity: the quantity of available energy in the storage system after charging;
- Available power: generally expressed as an average value, as well as a peak value often used to represent maximum power of charge or discharge;
- Depth of discharge;
- Charging and discharging rate;
- Round trip efficiency: the ratio between released and stored energy;
- Durability: cycling capacity;
- Energy density: (kWh/kg or kWh/m^3);

- Power density: (kWh/kg or kWh/m^3);
- Capital cost, operation cost and maintenance cost;
- Feasibility and adaptation to the generating source;
- Service lifetime and cycle life;
- Environmental aspect;
- Operational constrains;
- Maturity of technologies;
- Installation and relocation condition;
- Physical dimensions.

2.4.2.2. Comparison of key features of different storage technologies

Each energy storage technology has some inherent advantages and limitations /disadvantages that make it practical or economical for only a limited range of applications. The key features of various storage technologies are summarized in Table 2.5. As shown in the Table, pumped hydro and CAES have the highest power rating and lifetime however these two energy storage technologies are slow in response time. Battery technology has been the most common type used until now; it has achieved much progress in power rating level, efficiency and lifetime recently. But the weakest characteristic of this technology has always been its lifespan. Meanwhile the relatively new technology SMES has low exposure to power application though it is stated that SMES with up to 100MW capacity has been already installed [96]. This technique can only generate electricity at rated capacity for a few seconds; in addition that, it has strong magnetic fields, and is extremely expensive due to the need for cryogenics to maintain the superconductivity.

Table 2.5 Key features of different storage technologies [74, 79, 92, 96-99]

	Power rating	Discharge duration	Response time	Efficiency	Parasitic losses	Lifetime / cycles	Maturity
Pumped hydro	100 – 4000MW	4 – 12 h	sec - min	0.65 – 0.85	evaporation	30 - 60y	commercial
CAES (in reservoirs)	100 – 300MW	6 – 20 h	sec - min	0.64	-	30 y	commercial
CAES (in vessels)	50 – 100 MW	1 – 4 h	sec - min	0.57	-	30 y	concept
Flywheels (low speed)	250 kW – 2 MW	3 – 120 s	< 1 cycle	0.9	~1%	20 y	commercial products
Flywheels (high speed)	< 20 MW	< 1 h	< 1 cycle	0.93	~3%	20 y	prototypes in testing
Supper-capacitors	< 100 kW	< 1 m	< ¼ cycle	0.84 - 0.95	depends on type: 0.5-40 %	5 -10y	some commercial products
SMES (Micro)	0.1 - 10 MW	1 s – 1 min	< ¼ cycle	0.90 - 0.95	~4%	30 y	Developing/ commercial
SMES	< 100 MW	< 10 s	< ¼ cycle	0.90 - 0.95	~1%	30 y	design concept / in test
Lead-acid battery	< 50 MW	1 m – 8 h	< ¼ cycle	0.65 - 0.85	small	< 2,000 cycles	commercial
NaS battery	< 90 MW	< 8 h	n/a	0.75 – 0.86	5 kW/kWh	< 3,000 cycles	developing
ZnBr flow battery	< 15 MW	3 - 4 h	< ¼ cycle	0.75	small	2,000 cycles	in test / commercial units
V redox flow battery	< 3 MW	< 10 h	n/a	70 – 85	n/a	10 y	in test
Polysulphide Br flow battery	< 15 MW	< 20 h	n/a	60 – 75	n/a	2,000 cycles	in test
Hydrogen (Fuel Cell)	< 250 kW	as needed	< ¼ cycle	0.34 – 0.40	n/a	10 - 20y	in test
Hydrogen (Engine)	< 2 MW	as needed	seconds	0.29 – 0.33	n/a	10 - 20y	available for display

FESS has gained more and more attention due to its significant features such as fast response, high efficiency and long lifetime. Although FESS has not been widely utilized in the power industry, it is slowly penetrating into the market, mostly for UPS,

power conditioning and pulse power. FESS has made tremendous progress in recent years with the highlight of 20MW frequency regulation project of Beacon Power Co. in Stephentown, New York. The plant reached full capacity on June 21, 2011. The 200-unit flywheel matrix is operating and providing commercial frequency regulation services to New York's electricity grid. Approximately 10% of the New York state's overall frequency regulation needs are served by this plan which operates continuously, storing and returning energy to the grid.

A more general view of various storage techniques based on their stored energy and power output is shown in Fig. 2.11. As suggested by [66], for large-scale stationary electrical power storage, the applications can be divided into three major functional categories as power quality, bridging power and energy management. Although some storage technologies can be used in all these three application ranges, it would not be economical and efficient if most options are applied in all of those ranges. Simultaneous combination of technological and economical considerations, such as ratings, volume, weight, capital cost, efficiency and cycle life, and per-cycle cost are essential in the selections of storage mediums [66, 72]. Fig. 2.11 can be used as the preliminary selection of proper storage technology for the three functional application types as mentioned above.

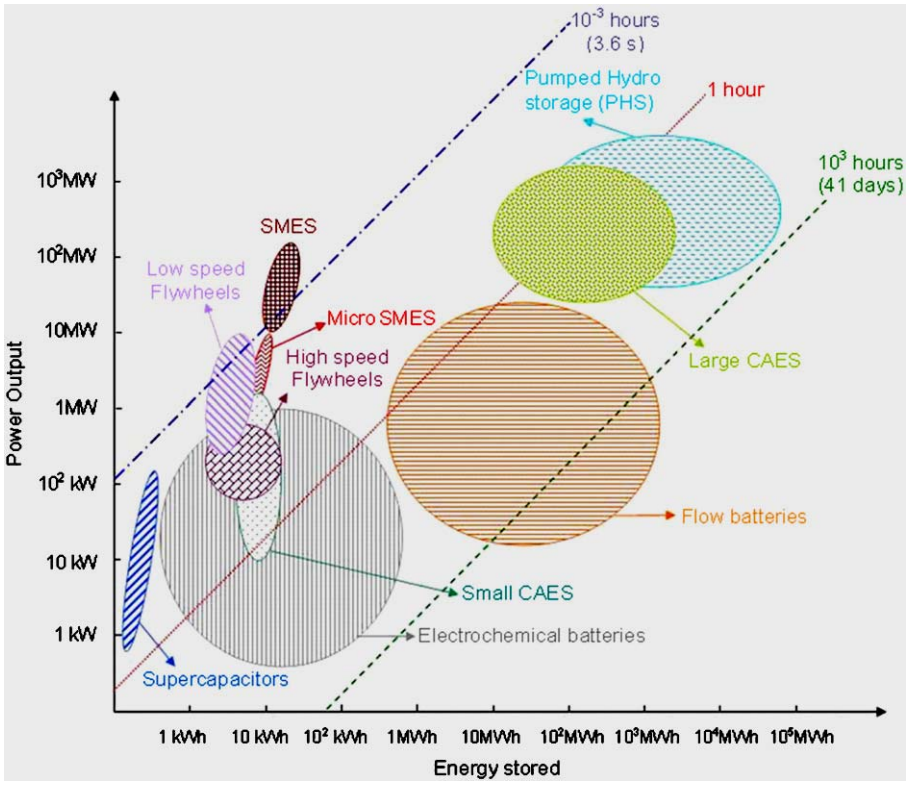

Fig. 2.11 Various storage techniques based on energy stored and power output [100]

2.4.2.3. Comparison of energy density and power density

Energy density is a basic measure of the capability of the storage systems. It refers to how much energy can be stored in a device per unit volume or per unit mass. Similarly, power density is a ratio between rated output power and volume or between rated output power and mass of the storage device. Based on this definition, the power density versus energy density amongst batteries, capacitors, SMES and flywheels are depicted in Fig. 2.12. It is seen that Aluminium electrolytic capacitors have a very high power density but at very low energy densities. Ultra-capacitors do not score high on both axes of this plot. SMES has the highest power density and the third highest energy density. Composite flywheels are worse in term of energy per unit volume than the energy per unit mass. This is because, as shown in Table 2.1, composite flywheels require less mass but more volume for the same amount of stored energy than metal flywheels. Therefore the power density of composite flywheels is relatively worse than that of other technologies in this case. Battery systems have the

highest energy density; meanwhile flywheels have already come quite close to the values achieved by battery technologies.

Recently, it is reported by Boeing Research & Technlogy that the advanced carbon-nanotube flywheel can achieve more than ten times of energy density than its current composite counterpart in the coming years, as shown in Fig. 2.13.

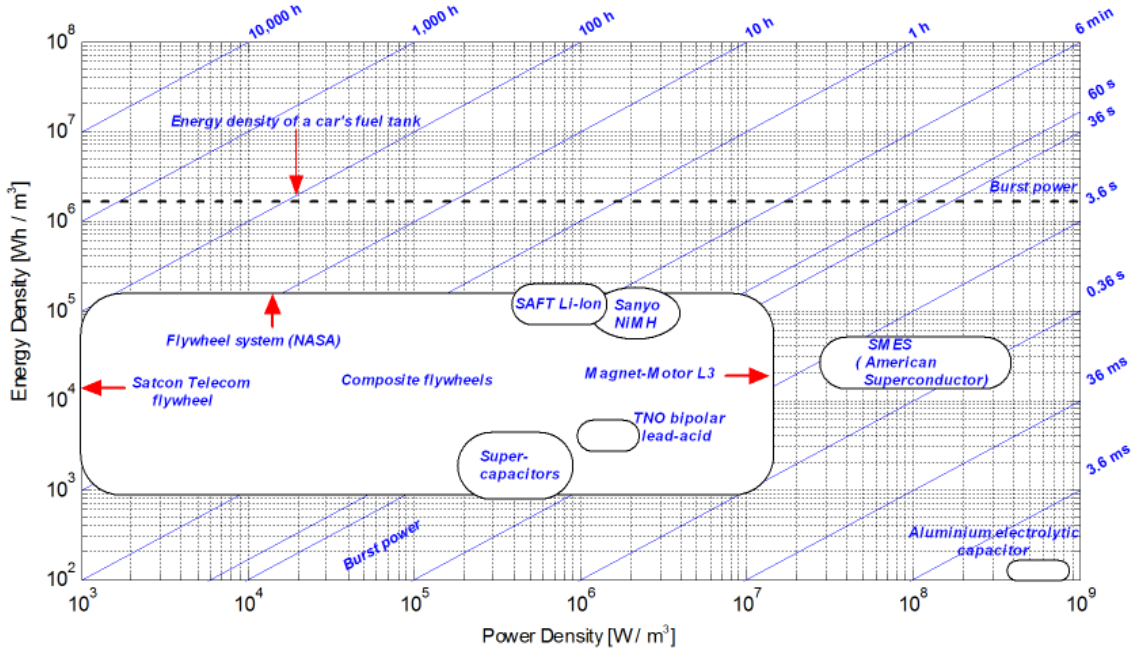

Fig. 2.12. Power density versus energy density [31]

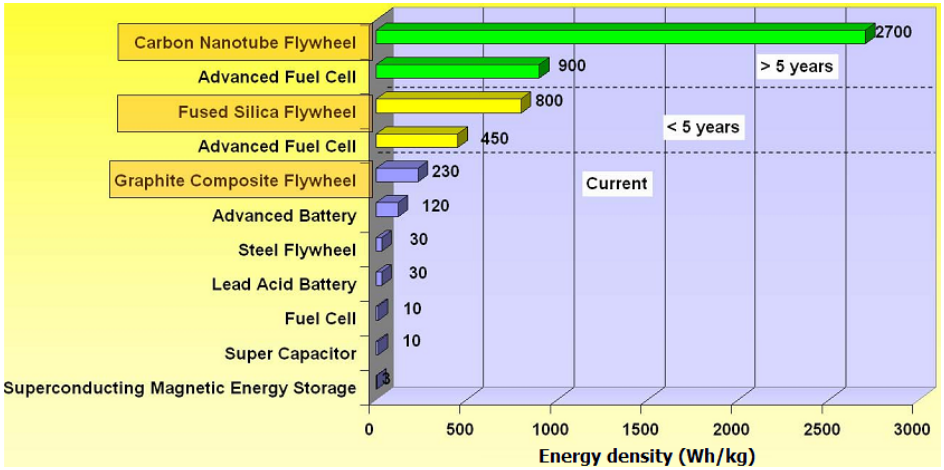

Fig. 2.13. Energy density of selected energy storage technology [101]

2.4.2.4. Comparison of the energy efficiency

Overall costs of a storage system are dependent on the energy efficiency and life the expectancy (maximum number of cycles). Low efficiency increases the effective energy costs since only a small amount of the stored energy can be used. Long life storage system can give a reduction in long-term costs as the storage unit can last longer and have less maintenance or replacement. Fig. 2.14 depicts the characteristics of different storage techniques based on their efficiency and lifetime.

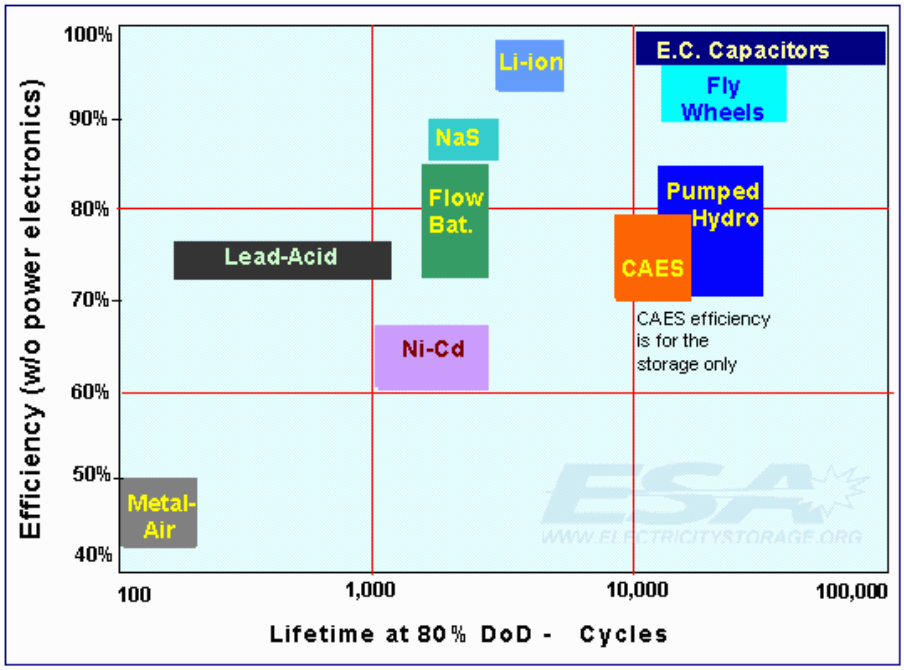

Fig. 2.14 Energy expectancy and life expectancy [66]

2.4.2.5. Comparison of the investment cost

The investment cost is an important economical parameter as it affects the total cost of energy production. Thus, some kinds of storage systems can only be profitable if a certain amount of energy is supplied [92], eg. Lead–acid batteries have low price, but they are not the least expensive option for energy management, due to their relatively low durability. With the assumptions on cost and performance of the selected energy storage technologies as shown in Table 2.6, their latest investment costs are shown in Table 2.7. The cost has been calculated in the first year of 10-year operation scheme.

As seen from Table 2.7, the current cost much varies not only amongst application categories but also amongst technologies. The long-duration and short-duration uses give the clearest difference; this is mainly due to more storage capacity is required for long-duration uses. Although CAES is found to be the least expensive long-duration storage, this technology is hardly used widely because it inherently requires the appropriate geographic location. For some technologies, there are also obvious differences between frequent and infrequent operation. It is more costly for the frequent use because more electricity is utilized for charging and because expensive replacements will be required for some technologies. Therefore the technologies with dominant cycle life such as flywheels, supercapacitors, and advanced batteries are more attractive for applications requiring frequent charge and discharge.

Table 2.6 Cost and performance assumptions

Technology	Power Subsystem Cost (USD/kW)	Energy Storage Subsystem Cost (USD/kWh)	Round-trip Efficiency (%)	Cycles
Advanced Lead-acid Batteries (2000 cycle life)	400	330	80	2,000
Sodium/sulfur Batteries	350	350	75	3,000
Lead-acid Batteries with Carbon-enhanced Electrodes	400	330	75	20,000
Zinc/bromine Batteries	400	400	70	3,000
Vanadium Redox Batteries	400	600	65	5,000
Lithium-ion Batteries (large)	400	600	85	4,000
CAES	700	5	N/A (70)	25,000
Pumped hydro	1,200	75	85	25,000
Flywheels (high speed composite)	600	1,600	95	25,000
Supercapacitors	500	10,000	95	25,000

Table 2.7 Cost of 10-year operation in the first year (USD/kW) [79]

Technology/Use	Long-duration storage, frequent discharge	Long-duration storage, infrequent discharge	Short-duration storage, frequent discharge	Short-duration storage, infrequent discharge
Advanced Lead-acid Battery	2839.26	1620.37	1299.70	704.18
Na/S (7.2 hr)	2527.97	2438.97		
Zn/Br	2518.03	1817.82	905.53	697.78
V-redox	3279.34	2701.41	1459.85	999.78
Lead-acid Battery with Carbon-enhanced Electrodes	2017.87	1559.57	669.85	625.57
Li-ion	2899.41	2442.79	1409.99	960.48
CAES (8 hrs)	1470.10			
Pumped Hydro (8 hrs)	2399.90			
High-speed Flywheel (15 min)			965.73	922.87
Supercapacitor (1 min)			834.62	793.02

Based on the above study and comparisons, the following remarks can be obtained:

- Battery technologies tend to have the highest specific energies; however their specific powers are limited. For low power applications, battery technology, especially lithium-ion is the best candidate but it is still very expensive while lead-acid battery is preferred in larger applications of more than 100 kWh.

- Capacitor technologies have higher specific power than battery technologies because of lower internal impedance but store less energy per kilogram than battery technologies.

In multi megawatt applications (e.g. peak-hour load leveling), pumped hydro and compressed air storage technologies are preferred. With current developed technologies, superconducting magnetic can also be considered as a good candidate for these applications. Flywheel energy storage systems deliver high power per kilogram and can be compared well with the high specific energy of batteries. For the applications concerning power quality and energy savings, burst energy release

capacity and cycling capacity are the key criteria. In this aspect, flywheel storage technology is really a significant candidate compared to current market-available batteries, even the lithium-ion batteries. Ultra-capacitor technology can also be considered as a candidate in this type of application.

2.5 Conclusions

FESS is a viable alternative to traditional battery energy storage systems in the 21st century, the age of clean and green energy systems. Supplementary technologies to support the FESS industry like bearing technology, composite material technology, containment technology, power electronic technology have been intensively researched and promptly developed. This brings a promise of a fruitful FESS technology in energy storage fields. The development trend in FESS technology has been aimed at rotor cost reduction by achieving higher specific energy and reduced rotor mass. Advanced bearings have been actively developed to provide reduced losses, higher efficiency, lessened running costs, and longer bearing life. Both these developments have been particularly significant to the FESS where the rotor and bearing costs usually take the most significant system cost. Successful reduction of losses and costs and improvement of the bearing system would make flywheel systems more and more attractive.

UPS systems, power quality improvement, and traction applications are the main markets for FESS. FESS can be now cost competitive with batteries in some UPS applications. There are more and more applications of high power FESS for power smoothing, power leveling, energy recycling and voltage restoring. These applications are ideally suited to high power cycling capabilities of the FESS. The development of lower loss and reduced cost systems with longer storage times would make the FESS competitive with batteries in the coming years. Therefore it is necessary to improve the energy density and power density, to reduce the complexity of their design and controls, and to lower the costs of production.

CHAPTER 3 PROPOSED DESIGN OF DUAL AIR-GAP AXIAL FLUX PERMAMENT MAGNET MACHINE FOR FESS APPLICATIONS

3.1 Introduction

Design of FESS is a multi-domain project. Various technical disciplines are involved in this research. Numerous issues arising from these disciplines should be taken into consideration during the design of the FESS. This project focuses on the electromagnetic design aspect of the motor/generator for FESS applications, particularly the design of a dual air-gap AFPM machine.

An efficient and compact dual air-gap AFPM machine optimized for use in FESS applications is proposed in [102]. The machine is composed of two separate single air-gap AFPM machines, has two sets of three-phase stator windings but requires only one power converter which supplies power for control of both axial force and electromagnetic torque [17]. The application of the proposed machine in FESS is realized by orientating its axial direction vertically and having its double-sided rotor to be the core of the flywheel. The availability of axial force control helps to minimize the vertical bearing force to improve the efficiency of the FESS.

This chapter is organized as follows: the design issues of the FESS are described in Section 3.2. Overall structure of the FESS and the principle of the AFPM machine used in the FESS are described in Section 3.3. In section 3.4, the detailed design of the AFPM machine is given. Two AFPM machine prototypes with integral and fractional number of slots per pole per phase are designed to confirm the proposed concept; this is presented in Section 3.5.

3.2 Design issues of FESS

3.2.1 Design requirements for FESS

High efficiency is one of the criteria in the design of FESS so that the system can be effective energy storage medium. To achieve that goal, the motor/generator has to be of high efficiency with minimal windage losses and frictional losses. Vacuum housing is a good accommodation to reduce windage losses and the implementation of magnetic bearings or advanced ceramic bearings can further eliminate the influence of frictional losses during the operation.

High energy density is expected in FESS, especially for applications in space station and vehicles. To achieve high energy density, the flywheel has to spin at high speed. The weight of the flywheel should not be excessive to reduce overall system weight. This is the reason high strength and light weight composite material is usually selected to be the rim of the flywheel.

High power density is also required for FESS. It is almost wholly dependent upon the motor/generator. Based on current technology projections, it is possible to expect a power density up to 30 kW/kg [59]. This can be achieved with higher rotational speed and better heat exchangers.

3.2.2 Machine type for the Motor/Generator

As discussed in Chapter 2, the motor/generator is the “heart” of an FESS which is responsible for the three fundamental modes: charging, standby and discharge for the FESS. Therefore selection of electrical machine is crucial in an FESS. Possible types of electrical machines for the motor/generator of the FESS are as follows:

3.2.2.1. Induction Machine

Thanks to the absence of brushes and slip rings, currently induction machines are the

dominant choice for both constant speed and variable speed drives [103]. However, induction machines have their drawbacks such as: rotor resistive losses caused by induction which decrease the efficiency of the machines and cause cooling problems, especially at low power ratings. In addition, rotor parameter variations causing heat produced by rotor losses result in the complexity in field orientation control. Also, the excitation for the induction machines requires reactive power to establish a rotating magnetic field which causes extra conduction losses. Therefore, the induction machines are almost ruled out in FESS applications.

3.2.2.2. Switched Reluctance Machine

Switched Reluctance Machines, or so-called Variable Reluctance Machines have been commonly used in AC drives for years [104, 105]. Their simple and robust rotor structures with concentrated windings reduce manufacture cost. The presence of unidirectional current in its phase windings results in a very simple converter topology. The SRM is now very competitive with induction machines, with its simple structure, high efficiency over wide range of loads and speed, low cost, high reliability and even fault-tolerance. However it has such disadvantages as relatively big torque pulsation and considerable audible noise [106-110]. Also, SRM have the same excitation penalty problems as induction machines do. Considering all the above-mentioned conditions, the switched reluctance machine is not selected in this study.

3.2.2.3. Synchronous Reluctance Machine

Synchronous reluctance machine relies upon the conventional reaction torque rather than reluctance torque of SRM. SynRM typically retains many of the benefits of SRM while at the same time eliminating several of SRM's disadvantages: SynRM has negligible iron stator losses while it is not generating power, has no rotor losses, and overcomes the noise and torque pulsation problems [111-114]. However, it is difficult to construct a synchronous reluctance rotor with high L_d/L_q ratio while maintaining a robust rotor structure. Therefore, a low power factor and an increase of the required VA rating of the drive are unavoidable; this can add significantly to the cost of the

system. According to these considerations, the synchronous reluctance machine is not chosen in this study.

3.2.2.4. Permanent Magnet Machine

Permanent magnet machines offer high torque densities, high efficiency and zero fundamental frequency rotor losses. In addition, PM machines have no field windings hence they have neither drawbacks associated with field windings and slip rings nor external supply to excite the rotor field. Therefore it is also easier to control the PM machines as the electrical excitation is absent. The PMs in the rotor give large magnetic flux which can generate large torque. In spite of having its drawbacks such as low strength, high cost and temperature sensitivity of the PMs, PM machine is still more competitive compared with other machines when implemented in FESS [31, 115]. For this reason, PM synchronous machine is employed in flywheel system.

3.2.2.5. Axial Flux Permanent Magnet Machine

One of the earliest researches on axial flux machines is the synchronous machine developed by Wai-sun Leung and James C. C. Chan in 1980 [116]; with an effort to save the core material, the machine is built as a coreless stator machine with evenly-distributed number of laminated teeth evenly and it is excited by separate field windings. However this machine has extra core and winding in the rotor side, it therefore has increased copper and core losses. Both stator and rotor excitations of this machine are required, so it is inevitable that the machine is large and needs extra supply power for excitations.

With the advance in permanent magnet technology nowadays, permanent magnet has been preferred in developing axial flux synchronous machines. There have been more and more interests in AFPM machine in the recent years, their noticeable applications include: generators for wind systems [117-121], electric vehicles [122-125], pumps, heating gen-sets, machine tools and robots [126-132]. The AFPM machine is an attractive alternative to the conventional radial flux type due to its pancake shape,

compact construction and high power density [8, 9, 133, 134]. Axial flux PM machine have many advantages over radial flux machine such as higher power density, higher torque density, higher efficiency, and especially the unique disc-type structure which make it attractive in the FESS applications. Axial flux PM machines can be designed as double-sided or single-sided machines, with or without armature slots, with internal or external PM rotors and with surface mounted or interior type PM.

A. Single-sided AFPM Machine

Single-sided AFPM machines with stator ferromagnetic cores, as shown in Fig. 3.1, have a single PM rotor disc opposite to a stator unit where the stator windings are wound. The stator ferromagnetic cores can be either slotless or slotted. In case of a slotless stator, the magnets are almost always surface mounted, while in case of a slotted stator with a small air-gap between the rotor and stator core, the magnets can be either mounted on the rotor surface or buried in the rotor disc. Although single-sided construction of an axial flux machine is simple, its produced torque is low. Besides, the bearings used with single-sided AFPM also bear a very large axial attractive force causing high friction losses in operation of the machine [12-15]. This axial force could twist the structure of the machines easily especially the large machines. The axial force can be lessened by special designs such as slotless structures or by active control as in [12]. These are the main drawbacks of single sided AFPM machine which make it almost impossible to be used in FESS.

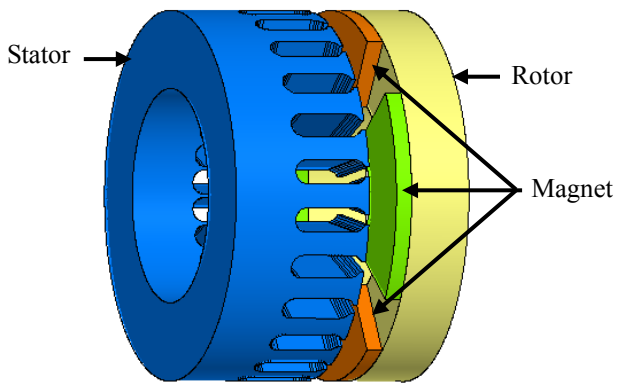

Fig. 3.1 Single-sided AFPM machine

B. Multidisc AFPM Machine

Torque of a single-sided AFPM machine can be increased by enlarging the machine diameter as the torque is a function of the machine diameter. Several configurations of multidisc AFPM machine are available [135-139]. There are factors limiting the single disc design: axial attractive force taken by bearings, the integrity of mechanical joint between the disc and shaft and the disc stiffness. Therefore, for large torque applications, a reasonable solution is double or triple disc machines [140], which are called multidisc AFPM machines, as shown in Fig. 3.2. The number of stacks depends on the required shaft power or torque. This topology is more suitable in low speed high torque applications. It is almost infeasible to be installed with a flywheel, so is not suitable to be used in FESS applications.

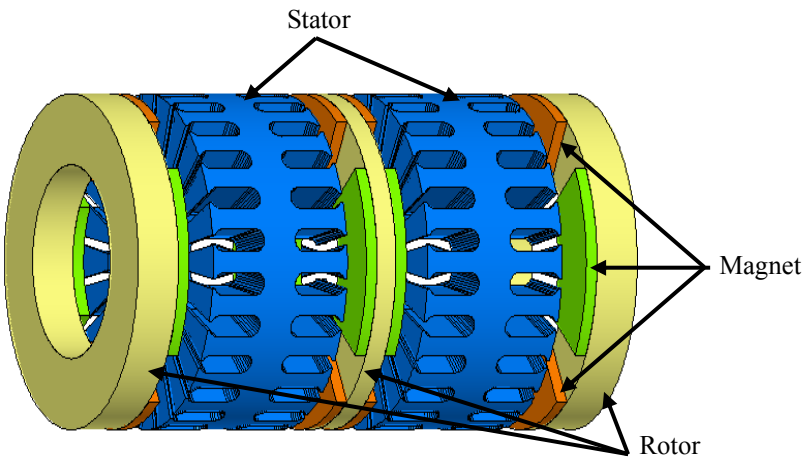

Fig. 3.2 Multidisc AFPM machine

C. Double-sided AFPM Machine

In double-sided AFPM machines with ideal mechanical and magnetic symmetry, the axial attractive forces are balanced with each other. A double sided machine with internal stator, as shown in Fig. 3.3(a), is a compact structure of AFPM machines. The double-sided rotor with permanent magnet is located at two sides of the stator [141-144]. Similar to single-sided AFPM machines the stator ferromagnetic cores can be slotted or slotless, and the rotor magnets can be surface mounted, embedded or

buried. Nevertheless, this topology with external rotating rotors is hard to be installed with the flywheel in FESS applications.

Unlike the AFPM machine with external rotors above, the double-sided machine with internal PM disc rotors, as shown in Fig. 3.3(b), is highly suitable to be used in FESS. The rotors can be attached with composite rim to form the flywheel and sandwiched in between two stators to form a compact FESS structure. In addition that the axial attractive forces of each stator-rotor module are cancelled out with each other, this axial force can also be designed and controlled to balance with the rotating flywheel to reduce friction losses on the bearing system. Double-sided AFPM machine with internal rotors is therefore considered in this study.

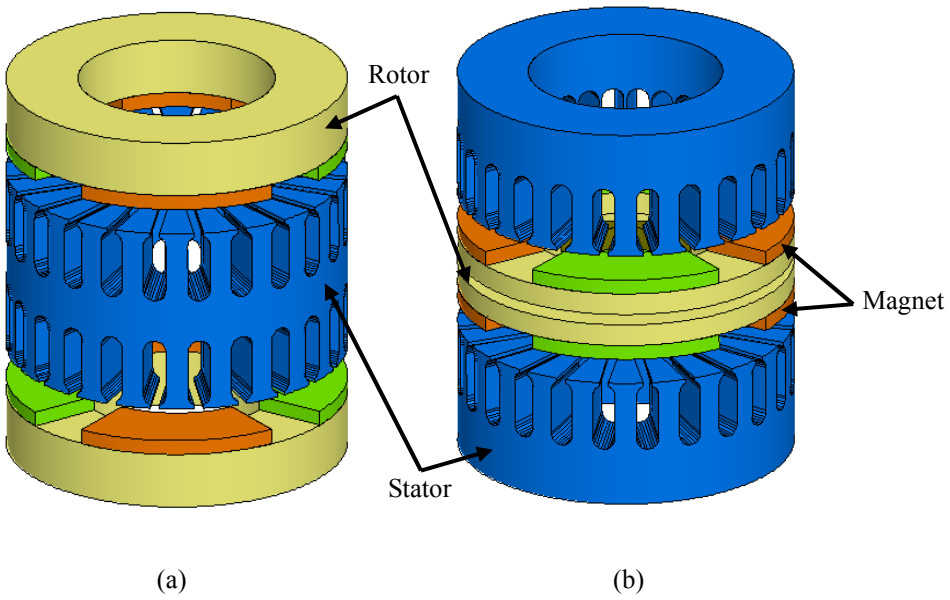

Fig. 3.3 Double-sided AFPM machine (a) internal stator, (b) internal rotor

3.2.3 Concept of the dual air-gap AFPM Machine based FESS

For FESS using permanent magnet machines, the conventional choice has been the radial flux type. However the axial flux permanent magnet configuration has a distinct feature which can be exploited in FESS application: its axial force can be controlled to counter the gravitational force acting on the rotor if the axis of rotation is in the vertical

orientation. Theoretically, this can reduce the stress and friction acting on the lower bearing system, thus reducing the bearing losses and therefore the self-discharge of stored energy during the standby mode. This allows the use of conventional ball or ceramic bearings without the complexities and high costs associated with magnetic and superconducting bearings [5-7], or magnetically levitated flywheels.

From the study in sections above, it has been seen that AFPM machines can have higher torque, better power density and lower noise compared to radial flux machines. It has also been shown that single air-gap axial flux machines [12-15] can generate substantial axial forces which have to be counteracted by the shaft bearings. In the machine proposed for electric vehicle in [12], field control is used to produce a compensating axial force to balance with the attractive force between the rotor and stator. However this method requires complicated control schemes and efforts in axial force compensation, which may limit the range of electromagnetic torque. Using dual air-gap axial flux machines, [11, 16] in which the total axial force is equal to the difference of the two attractive forces of the two air-gaps, can achieve wider range of field control capability. However these designs have other complications such as requiring one power electronic converter to drive three phase AC currents and another converter to drive a DC field current [11]. In addition, they are not specifically designed for FESS applications.

The dual air-gap AFPM machine optimized for use in FESS is introduced in [102]. This machine has two sets of three-phase stator windings but only requires one power converter which supplies power for control of both axial force and electromagnetic torque, [17]. Its application in FESS is realized by orientating its axial direction vertically and having its double-sided rotor to be the core of the flywheel. The availability of axial force control helps to minimize the vertical bearing force to improve the efficiency of the FESS.

3.3 Overall structure of the FESS

This section introduces the conceptual structure of the FESS. Parts of the motor/generator used in this FESS are illustrated. The motor/generator and the composite rim are structurally integrated to form a compact flywheel.

3.3.1 Structure of the FESS

The simplified structure of the FESS is illustrated in Fig. 3.4. Its components are listed in Table I. The core of the FESS is the proposed dual air-gap AFPM machine. It is composed of two separate single air-gap surface-mounted AFPM machines termed as upper and lower machine halves respectively (item 1, 2). Each upper or lower machine half has its own stator, rotor, magnets and windings but their rotors are integrated together by a shaft (11). The two rotors (9, 12) are encircled by a carbon-fiber composite rim which is then attached to the shaft at their center to constitute a compact flywheel. The flywheel is sandwiched in between two disk-type 24-slot stators (4, 16). Each of the upper and lower stators carries a set of three-phase copper windings which are double-layer type with 1.5 or 2 slots per pole per phase [145]. Rotation of the flywheel is supported radially by the two main bearings (5, 17) which can be either based on conventional steel or on advanced ceramic materials [23, 42]. Another set of auxiliary bearings (3, 18) provide axial support. In operation, the flywheel is physically constrained by these two bearing systems. For safety reasons and to reduce windage losses, a vacuum safety chamber (19) would be necessary in the FESS.

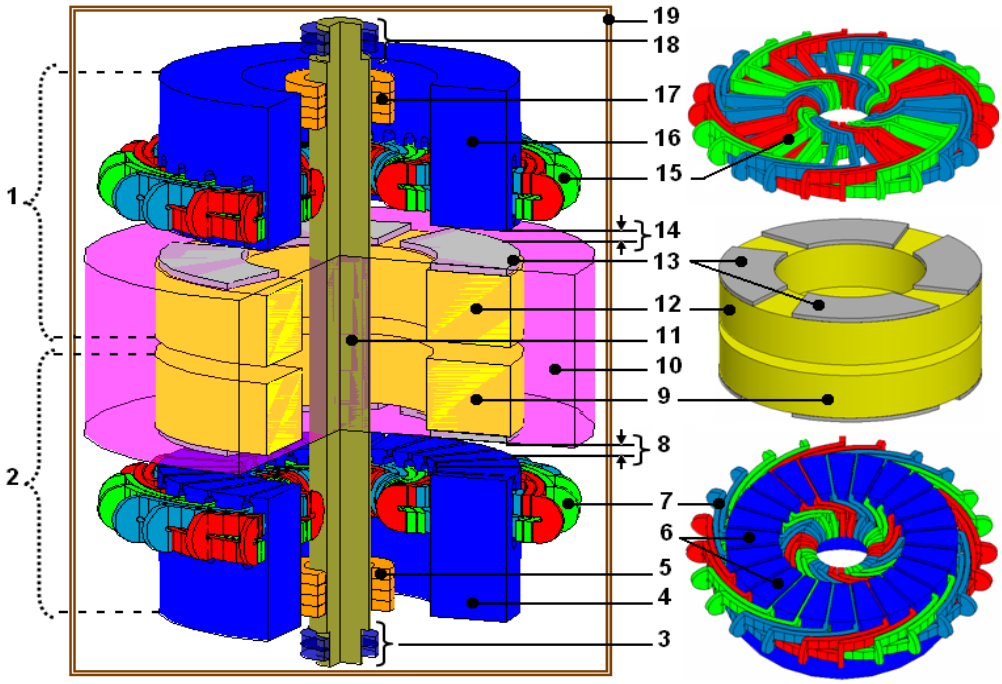

Fig. 3.4 Simplified structure of the FESS

Table 3.1 Components of the FESS

Number of items	Item name
1, 2	upper and lower single-sided machine
3, 18	lower and upper supporting system
4, 16	lower and upper stator
5, 17	lower and upper main bearing
6	stator teeth
7, 15	lower and upper 3-phase stator windings
8, 14	lower and upper air-gap
9, 12	lower and upper rotor
10	rim
11	shaft
13	axially-magnetized permanent magnets
19	vacuum chamber

Maximum energy storage in the FESS is limited by mechanical factors [31]:

$$e_m = K\frac{\sigma_{\min}}{\rho} = Kr^2\omega^2 \quad [Joules/kg] \tag{3.1}$$

It is seen that the specific energy of the FESS, e_m is a function of three mechanical parameters: the flywheel shape factor K, the minimum tensile strength σ_{min} for a given angular velocity ω, and the mass density ρ of the flywheel material. Assuming that mechanical structure of the FESS can support the flywheel at its maximum speed rotation, the theoretical maximum energy storage can be obtained using (3.1).

3.3.2 Principle of the dual air-gap AFPM machine in the FESS

The winding connection diagram and principle of the proposed machine are illustrated in Fig. 3.5. The upper and lower three-phase stator windings (7, 15) are connected in series hence only one single power electronic converter is needed to operate the machine. In general, the power converter works under the pulse width modulation condition to energize the three-phase windings. In operation, for example in the upper air-gap, the rotor flux travels axially from the upper rotor pole to the upper stator and goes back to the rotor. Rotating flux generated by currents in the upper stator windings interacts with rotor flux and then generates electromagnetic torque and axial force, namely T_1, F_1 as illustrated in Fig. 3.5. The torque and axial force of the lower machine half, respectively T_2 and F_2 are derived in the same manner. The net force along the axial axis *(OZ)* is obtained as:

$$F = F_1 - F_2 \tag{3.2}$$

The total electromagnetic torque is written as:

$$T = T_1 + T_2 \tag{3.3}$$

In the proposed machine, the total electromagnetic torque is used to control the rotation of the flywheel, while the net axial force is used to regulate the axial stress on the bearing support.

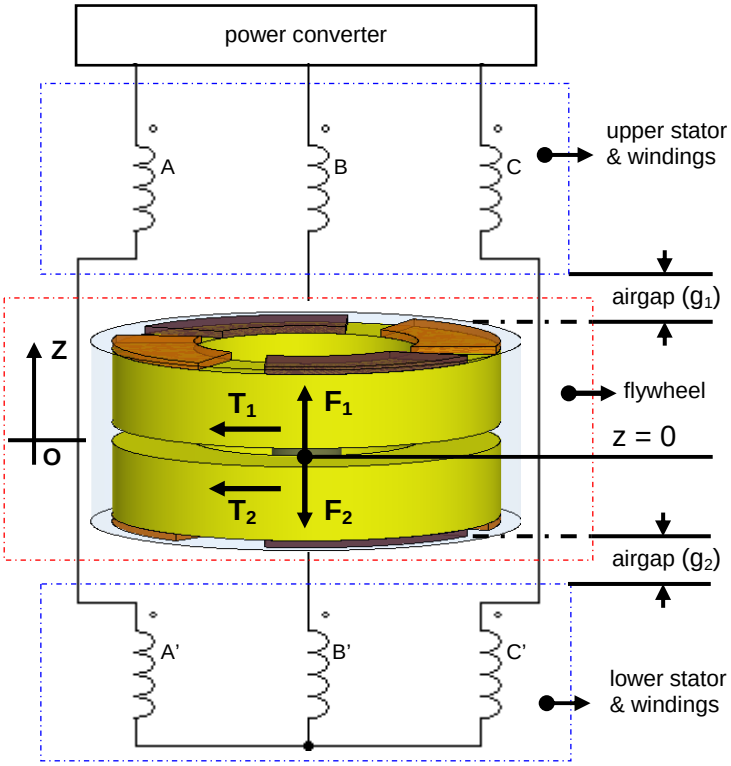

Fig. 3.5 Illustration of the proposed machine principle

To explain the flux distribution of this machine, the coordinate axes of a 2-pole machine is used. The explanation is also valid for a general case, 2*p*-pole machine. The three-phase windings and *dq*-winding layout of the 2-pole AFPM machine are defined in Fig. 3.6(a). The rotating *d*- and *q*-axis windings are in quadrature of each other and their magnetic axes are aligned with the *d*- and *q*-axis of the rotor. The *d*-axis of the rotor is chosen to be aligned with the center lines of the magnets and the *q*-axis between the magnets.

With the alignment of the defined axes, the net air-gap flux over a pole section can be regulated by controlling the magnitude and direction of *d*-axis current. The air-gap flux with positive and negative *d*-axis current are illustrated by 3D-quarter machine models in Fig. 3.6 (b, c). When a positive current i_d is applied, the i_d -generated flux is opposed to the PM flux, the air-gap flux therefore reduces. On the contrary, when a negative current i_d is applied, the i_d -generated flux is added to the PM flux, the air-gap flux therefore increases.

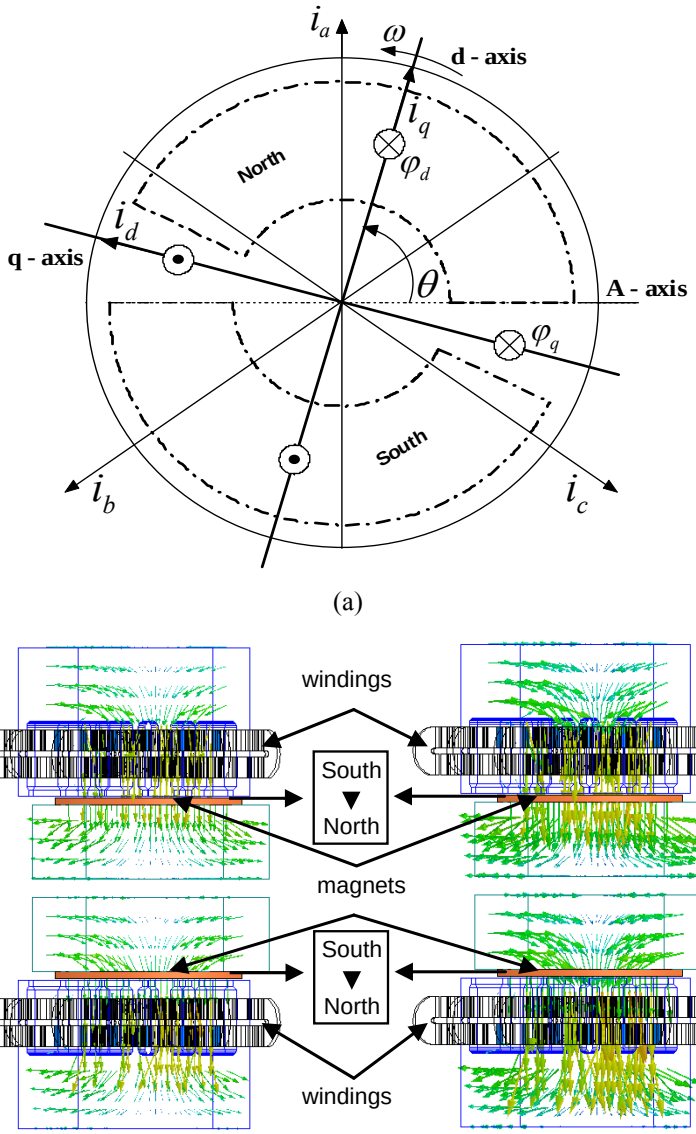

Fig. 3.6 (a) Position of the rotor and *dq*-windings, (b) air-gap flux with positive d-axis current, (c) air-gap flux with negative d-axis current

3.4 Design of the dual air-gap AFPM machine for FESS

3.4.1 Basic magnetic design

3.4.1.1. Magnet shape

Magnetic span

In surface-mounted AFPM machine, the length and span are the two main dimensions of a permanent magnet involving directly to the machine air-gap flux. Magnet shape and magnet-to-magnet distance have a significant effect on machine cogging torque because air-gap flux density at the magnet edges changes as the flux moves from a magnet pole to another. The larger rate of change in flux density, the greater potential increase in the cogging torque is. One of the solutions to decrease that rate of change is to reduce the magnet width or decrease the magnet length. However, for general cases optimum magnet spans are different for various numbers of stator slots and winding configurations. Hence, it should be optimized with the given number of slots and winding configurations.

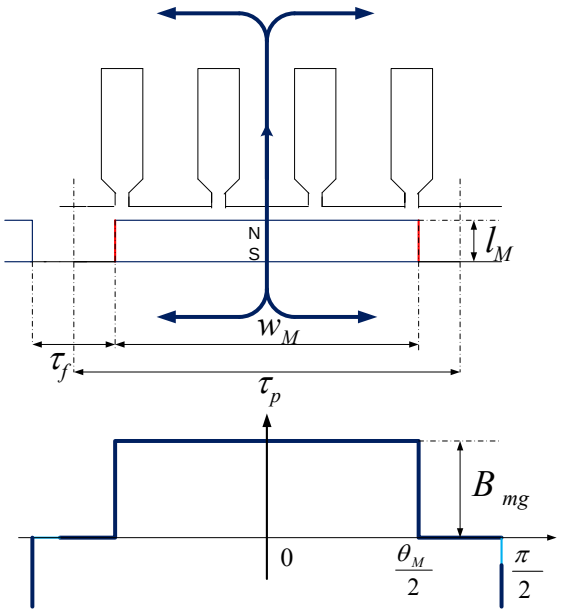

Fig. 3.7 Air-gap flux density waveform.

Surface-mounted AFPM machine has the approximate flux density waveform as shown in Fig. 3.7 if the fringing effects are negligible. It is a symmetric function which can be written in terms of the Fourier series as [145]:

$$B_m(\theta) = \sum_{n=1}^{\infty} \hat{B}_n \cos n\theta \qquad (3.4)$$

where:

$$\hat{B}_n = \frac{B_{mg}}{n\pi}\{\sin(n\frac{\theta_M}{2}) - \sin n(\pi + \frac{\theta_M}{2}) + \sin n(\pi - \frac{\theta_M}{2}) - \sin n(2\pi - \frac{\theta_M}{2})\} \qquad (3.5)$$

The pole pitch $\tau_p(r)$ and the pole width $w_M(r)$ of the AFPM machine are functions of its radius *r*:

$$\tau_p(r) = \frac{2\pi r}{2P} = \frac{\pi r}{P} \qquad (3.6)$$

and

$$w_M(r) = \alpha_M \tau(r) = \alpha_M \frac{\pi r}{P} \qquad (3.7)$$

where:

$$\alpha_M(r) = \frac{w_M(r)}{\tau(r)} = \frac{B_{avg}}{B_{mg}} \qquad (3.8)$$

B_{avg} : average of flux density

B_{mg} : peak value of the air-gap magnetic flux density

P: the number of pole pairs

The amplitude of the first harmonic component is

$$\hat{B}_{g1} = \frac{1}{\pi}\left(\int_{\frac{-\theta_M}{2}}^{\frac{\theta_M}{2}} B_{mg}\cos\theta d\theta + \int_{\pi-\frac{\theta_M}{2}}^{\pi+\frac{\theta_M}{2}} B_{mg}\cos\theta d\theta \right) = \frac{4}{\pi} B_{mg} \sin\frac{\theta_M}{2} \qquad (3.9)$$

Therefore

$$\hat{B}_{g1} = \frac{4}{\pi} B_{mg} \sin\frac{\pi\alpha_M}{2} \qquad (3.10)$$

Magnetic length

Permanent magnet length of the upper machine half is [140]:

$$l_{M1} = \frac{\mu_{rrec} B_{mg1} g'}{B_{ro} - B_{mg1}} \tag{3.11}$$

where μ_{rrec} is the relative recoil magnet permeability at operating temperature,

$g' = k_C . g$ is the equivalent air-gap of the upper machine half,

k_C is the Carter factor,

B_{ro} is the remanent flux density at the operating point.

The normal attractive axial forces induced by permanent magnet in the upper and lower machine half respectively are:

$$F_1 = \frac{1}{2}\frac{B_{mg1}^2}{\mu_0} S_{PM} = \frac{\pi \alpha_M B_{mg1}^2}{8\mu_0}\left(D_o^2 - D_i^2\right)$$
$$F_2 = \frac{1}{2}\frac{B_{mg2}^2}{\mu_0} S_{PM} = \frac{\pi \alpha_M B_{mg2}^2}{8\mu_0}\left(D_o^2 - D_i^2\right) \tag{3.12}$$

To minimize the axial force stress on the bearings in FESS applications, total static axial force produced by rotor permanent magnets has to balance with the flywheel gravity, therefore:

$$F_1 = F_2 + M g_{gr} \tag{3.13}$$

where g_{gr} is the gravitational acceleration constant.

The flux density of the lower air-gap is hence derived in this research as:

$$B_{mg2} = \sqrt{B_{mg1}^2 - \frac{8\mu_0 g_{gr} M}{\pi \alpha_M \left(D_o^2 - D_i^2\right)}} \tag{3.14}$$

Permanent magnet length of lower machine half is:

$$l_{M2} = \frac{\mu_{rrec} B_{mg2} k_C g_2}{B_{ro} - B_{mg2}} \tag{3.15}$$

3.4.1.2. Magnetic circuits

Considering permanent magnets as flux sources, magnetic field can be calculated by means of the magnetic circuit. Two-dimensional magnetic flux loop in the upper machine half is illustrated in Fig. 3.8. The flux from one magnet splits equally and couples to the two magnets next to it.

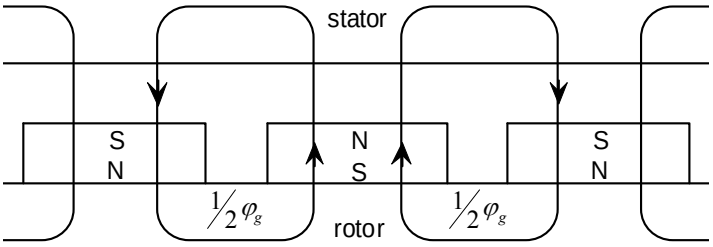

Fig. 3.8 Magnetic flux loop in the upper machine half.

Considering one closed flux loop, the value of flux traveling in each loop equals to the half of air-gap flux. By using the Norton equivalent circuit for the permanent magnet, the equivalent circuit of one flux loop in the upper machine half is described as Fig. 3.9(a). Due to the permeability in the iron is much higher than in the air, R_s and R_r are hence negligible with respect to R_g and R_{ml}. The magnetic circuit is then simplified as depicted in Fig. 3.9(b).

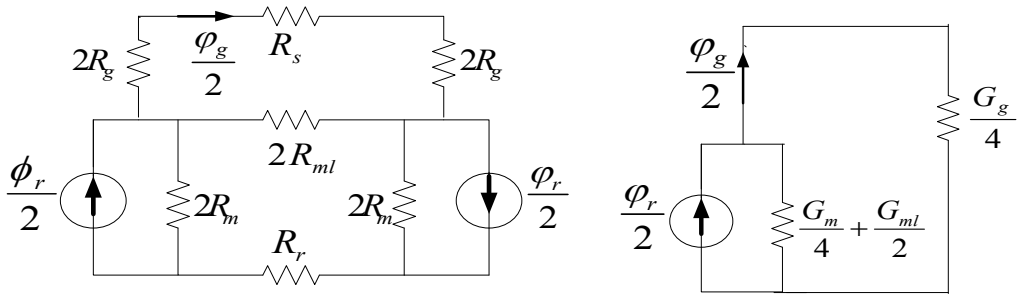

(a) (b)

Fig. 3.9 (a) Magnetic circuit, (b) Simplified magnetic circuit.

The air-gap flux can be expressed in term of remanent flux of permanent magnet as:

$$\phi_g = \frac{G_g}{2G_{ml} + G_m + G_g}\phi_r \tag{3.16}$$

The peak flux density is then obtained as:

$$B_{mg1} = \frac{G_g}{2G_{ml} + G_m + G_g}B_r \tag{3.17}$$

3.4.1.3. The equivalent MMF of the permanent magnet

In order to model the magnet in the later chapter, the equivalent MMF generated by the magnet is calculated in this part. As shown in Fig. 3.8, the PMs mounted on the surfaces of the rotor are shorted by highly permeable iron. The case is illustrated in Fig. 3.10. There is no intensity field when the magnet is shorted, hence the magnet flux density equals to the remanent flux density:

$$B_m = B_r \tag{3.18}$$

The magnet field intensity in the magnet therefore equals to the coercivity H_c:

$$H_c = \frac{B_r}{\mu_r \mu_0} \tag{3.19}$$

Assume that the magnet is no longer magnetized, the flux density B_m can be considered constant; the equivalent magnetomotive force MMF to generate the corresponding B_m can be described as:

$$MMF = H_c l_M + H_i l_i = H_c l_M \tag{3.20}$$

where H_i is the flux intensity in the iron and l_i, l_M are the equivalent magnetic lengths of the iron and magnet respectively.

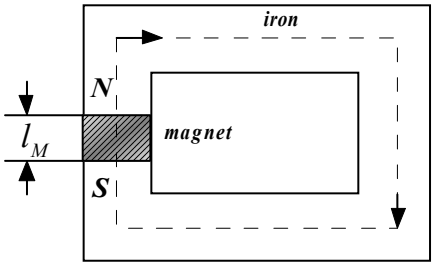

Fig. 3.10 Magnet shorted by highly permeable iron

3.4.1.4. Permeances for main and leakage fluxes

For the computation of the air-gap and flux-leakage permeances, the magnetic field is divided into simple parts as shown in Fig. 3.11.

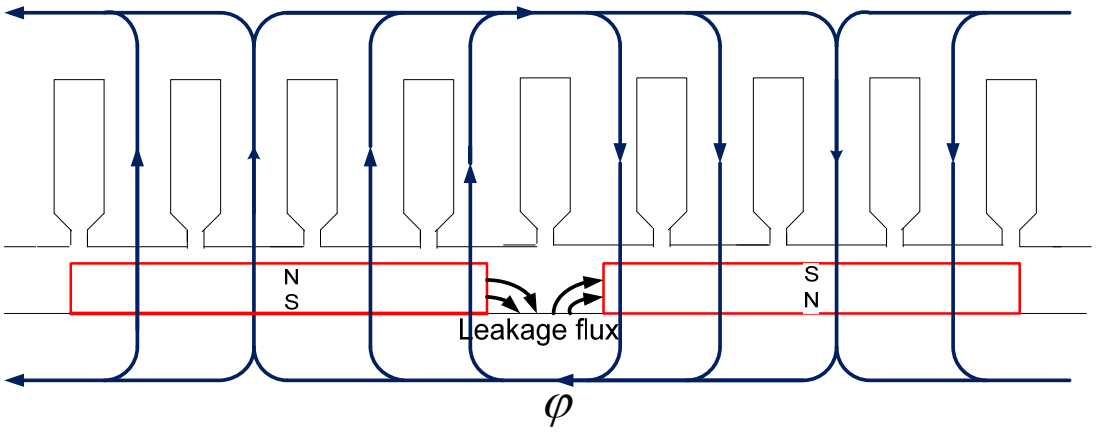

Fig. 3.11 Leakage flux

In case of smooth armature cores (without slots) and surface-mounted PM, the air-gap

permeance, G_g, can be computed from the combination of 17 components as shown in Fig. 3.12 (a):

$$G_g = G_{g1} + 2(G_{g2} + G_{g7}) + G_{g3} + G_{g4} + G_{g5} + G_{g6} + 4(G_{g8} + G_{g9}) \quad (3.21)$$

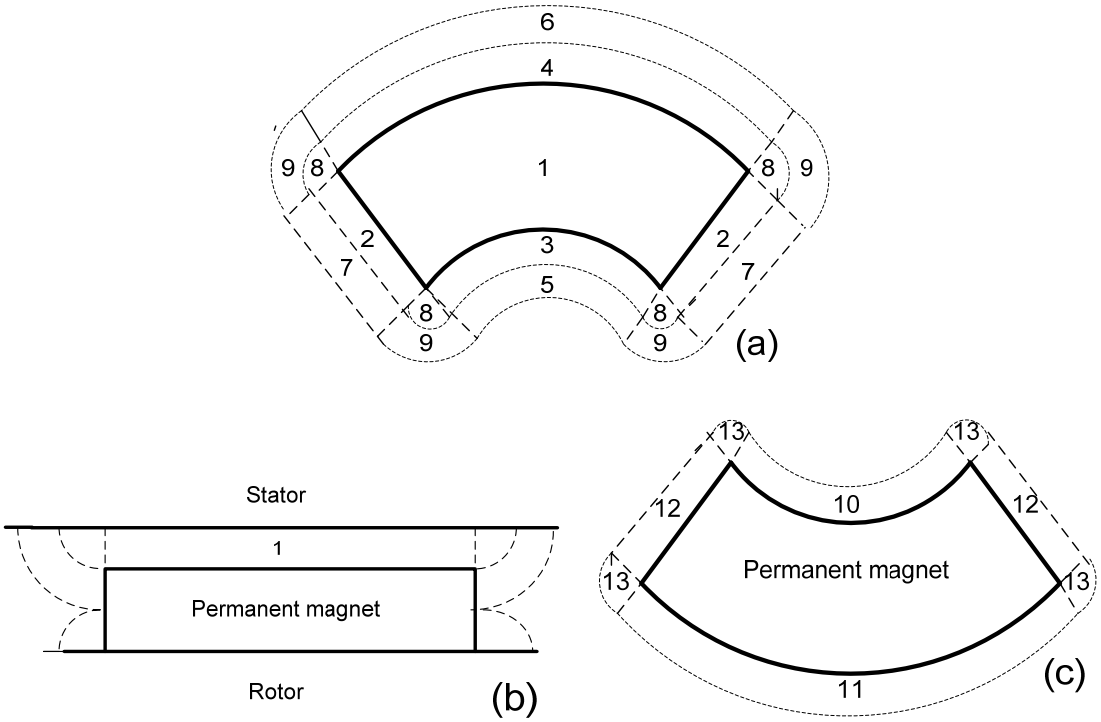

Fig. 3.12 Occupied spaces of the magnet field: (a) in the longitudinal section, (b) the air-gap field, (c) the rotor-PM leakage field

$$G_{g1} = \mu_0 \frac{S_{g1}}{k_C g} = \mu_0 \frac{\pi \alpha_M (D_o^2 - D_i^2)}{8 p k_C g} \quad (3.22)$$

$$G_{g2} = 0.52 \mu_0 \frac{D_o - D_i}{2} \quad (3.23)$$

$$G_{g3} = \frac{3.26 \alpha_M}{2p} \mu_0 \left(\frac{D_i}{2} + \frac{g}{4} \right) \quad (3.24)$$

$$G_{g4} = \frac{3.26 \alpha_M}{2p} \mu_0 \left(\frac{D_o}{2} + \frac{g}{4} \right) \quad (3.25)$$

$$G_{g5} = \frac{2\alpha_M}{2p}\mu_0 \left(D_i + g\right) \ln\left(1 + \frac{l_M}{g}\right) \tag{3.26}$$

$$G_{g6} = \frac{2\alpha_M}{2p}\mu_0 \left(D_o + g\right) \ln\left(1 + \frac{l_M}{g}\right) \tag{3.27}$$

$$G_{g7} = \mu_0 \frac{2\left(D_o - D_i\right)}{2\pi} \ln\left(1 + \frac{l_M}{2g}\right) \tag{3.28}$$

$$G_{g8} = 0.308\mu_0 g \tag{3.29}$$

$$G_{g9} = \mu_0 \frac{l_M}{4} \tag{3.30}$$

where: g is the air-gap length and l_M is the length of the magnet;

Similarly, the leakage-flux permeance of the PM is the sum of 8 components as shown in Fig. 3.12 (c):

$$G_{lM} = G_{10} + G_{11} + 2G_{12} + 4G_{13} \tag{3.31}$$

$$G_{10} = \frac{3.26\alpha_M}{2p}\mu_0 \left(\frac{D_i}{2} + \frac{l_M}{8}\right) \tag{3.32}$$

$$G_{g11} = \frac{3.26\alpha_M}{2p}\mu_0 \left(\frac{D_o}{2} + \frac{l_M}{8}\right) \tag{3.33}$$

$$G_{g12} = 0.52\mu_0 \left(\frac{D_o - D_i}{2}\right) \tag{3.34}$$

$$G_{g13} = 0.308\mu_0 \frac{l_M}{2} \tag{3.35}$$

The PM leakage flux coefficient can be obtained as:

$$\sigma_{lM} = \frac{\varphi_M}{\varphi_g} = 1 + \frac{\varphi_{lM}}{\varphi_g} = 1 + \frac{G_{lM}}{G_g} \tag{3.36}$$

Due to the existence and the difference of the teeth width in machine radius direction, the result of the calculation of the leakage factor can be more accurate by using the approach introduced by [146]. The axial flux machine is divided into a certain number of computation planes. The number of planes depends on which machine parameter is calculated. At a certain computation plane i, the average diameter is written as

$$D_{ave,i} = D_o - j\frac{l_s}{N_{cp}} \tag{3.37}$$

where : $$j = 2i - 1 \tag{3.38}$$

The length of the stator stack is $$l_s = \frac{D_o - D_i}{2} \tag{3.39}$$

Here N_{cp} is the amount of computation planes and $D_{ave,i}$ is the i^{th} average diameter.

The pole pitch for each computation plane of a machine with P pole pair is

$$\tau_{p,i} = \frac{\pi D_{ave,i}}{2P} \tag{3.40}$$

For the machine with the permanent magnet width varying along the radius, the relative magnet width is defined as:

$$\alpha_{M,i} = \frac{w_{M,i}}{\tau_{p,i}} \tag{3.41}$$

where the permanent magnet width $w_{M,i}$ is illustrated in Fig. 3.13.

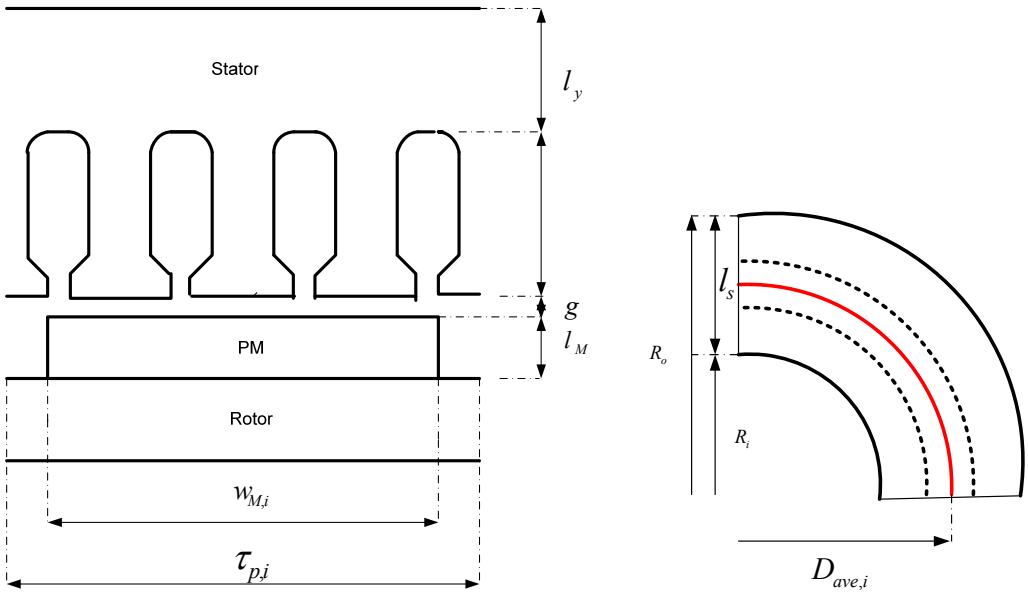

(a) (b)

Fig. 3.13 (a) Cross section at i^{th} computation plane, (b) the average i^{th} diameter

The air-gap flux expressed in terms of the flux induced by the PM is:

$$\varphi_g = k_l \varphi_M \tag{3.42}$$

To estimate the value of leakage coefficient k_l of the permanent magnet flux, the analytical computation method introduced in [147, 148] can be used . This method is useful for computing leakage coefficient of AFPM machine with complex magnet shapes. The k_l for axial flux surface mounted permanent magnet machines is written as:

$$k_l = \frac{\sum_{i=1}^{N} k_{l,i}}{N_{cs}} k_{l,add} \tag{3.43}$$

where N_{cs} is the number of cross sections chosen,

$k_{l,i}$ is the leakage coefficient at i^{th} section,

$k_{l,add}$ is the additional leakage coefficient that stands for the leakage fluxes

occurring between the magnet and the rotor on the inner and outer radii and the leakage fluxes flowing from the magnet pole into the adjacent magnet pole through the slot openings and slots.

The permanent magnet leakage factor k_l includes two leakage components:

- The permanent magnet zigzag leakage,

- The air-gap leakage from the magnet to rotor leakage.

The zigzag leakage factor illustrates the leakage flux through the air-gap and tooth tip from the magnet to the adjacent one. This factor is considered to be present when the distance between two adjacent magnets is less than a slot pitch. The zigzag leakage factor is [148]:

$$k_{l,zz,i} = 1 - \frac{\left[\tau_{slot,i} - (\tau_{p,i} - w_{M,i})\right]^2}{2 w_{M,i} \tau_{slot,i}} \tag{3.44}$$

where $\tau_{slot,i}$ is the slot pitch at each computation plane.

The permanent magnet air-gap leakage coefficient is calculated as:

$$k_{l,ag,i} = \frac{1}{\left(1 + \mu_r \frac{g' w_{M,i}}{l_M (w_{M,i} + 2g')}\right)\left[\frac{2l_M}{\pi \mu_r w_{M,i}} \ln\left(1 + \frac{\pi g'}{l_M}\right) + \frac{4l_M}{\pi \mu_r w_{M,i}} \ln\left(1 + \frac{\pi g'}{\tau_{p,i} - w_{M,i}}\right)\right]} \tag{3.45}$$

3.4.2 Stator

The stator for AFPM machine is either slotted or slot-less type and the corresponding armature windings can be slotted windings or air-gap windings respectively.

Advantages of the slot-less type in comparison with the slotted structure are:

- Slot-less type has almost no cogging torque which reduces the vibration and noise.
- Slot-less structure requires less effort in manufacturing than slotted one.
- Slot-less type requires less axial length of the stator than the slotted type does.
- Due to no slot, slot-less structure has no issue with the teeth saturation.

However, in comparison with slot-less structure, slotted type has numerous advantages:

- Structure of windings in slots is more robust, and with slots the windings are more protected.
- Slotted type has smaller air-gap hence the required length of permanent magnet is smaller.
- With smaller air-gap, the copper losses in the slotted type are less than those in the slot-less structure due to the eddy current induced by the smaller leakage flux.
- Magnets are better protected against the heating from armature winding with high temperature.

Because the robustness and the magnet temperature are amongst the major concerns in the AFPM machine for FESS, the benefits of the slotted stator can totally outweigh its disadvantages.

Combination of slots, poles, and windings is chosen based on the requirement of machine. The rotor has an even number of magnets, N_m, so the number of pole pairs on the rotor is:

$$N_p = \frac{N_m}{2} \tag{3.46}$$

The total number of stator slots equals to a certain even integer times the number of phases. This selection ensures the number of slots per each phase is the same. The total number of slots on stator is:

$$Q = m.N_{sp} \tag{3.47}$$

where N_{sp} is the even integer number of slots per phase,

m is the number of phases.

The selection of the number of poles depends upon many factors such as speed of rotation, mechanical assembly of the rotor and magnets. The large number of poles, the high applied frequency is required. This may cause high switching losses in power devices and high iron losses in the stator. But for a smoother torque, a larger number of poles are required. For very high speed applications, the selection is either two or four pole machine [149].

In addition, as the number of poles increase, stator yoke thickness decreases so two-pole machine not only has a larger iron mass but also a greater susceptibility to magnet unbalance compared with four-pole type. Therefore, four-pole type is selected for the motor/generator of the FESS in this project.

The number of lots per pole per phase is

$$q = \frac{Q}{m.N_m} = \frac{N_{sp}}{N_m} \tag{3.48}$$

q can be either fractional or integral number.

The semi-closed rectangular slot is illustrated in Fig. 3.14. The slot rectangular cross-sectional area is :

$$A_s = w_{sb} d_3 \tag{3.49}$$

where w_{sb} is the slot bottom width,

d_3 is the height of slot depth rectangular part.

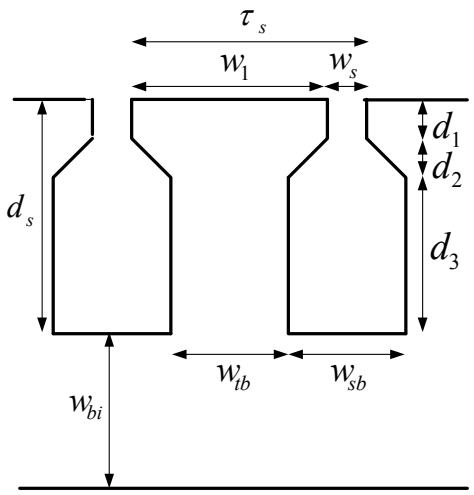

Fig. 3.14 Slot structure of stator

Because the cross sections of slots are uniform, the stator teeth width varies with radius. The air-gap flux increases linearly with radius due to the increase of the magnet width. Thus the total flux crossing the stator back iron also increases with radius.

Consider the different slice of the pole pitch on magnet having width *dr* as shown in Fig. 3.15, the flux induced by the magnet is expressed as:

$$\varphi(r) = \theta_{mp} B_{mg} r dr = \alpha_i \frac{\pi}{p} B_{mg} r dr \qquad (3.50)$$

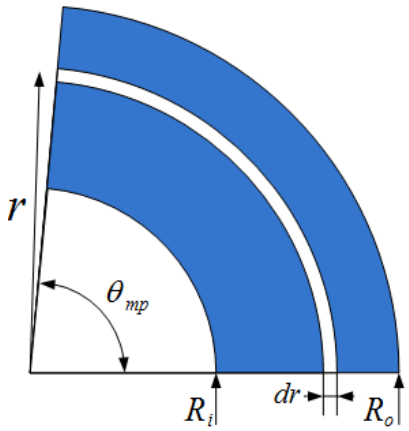

Fig. 3.15 A magnet pole

One half of this flux goes in the back iron, so if the maximum flux density at knee point of electrical steel used in stator is $B_{\max}$, the back iron allowable flux is:

$$\varphi_{bi}(r) = w_{bi} B_{\max} k_{st} dr \tag{3.51}$$

where w_{bi} is the back iron width

k_{st} is the lamination stacking factor.

From (3.50) and (3.51), the required back iron thickness is:

$$w_{bi}(r) = \frac{\alpha_i \pi B_{mg} r}{2pB_{\max} k_{st}} \tag{3.52}$$

Because a stator with a linear increasing back iron width is not practical, the back iron width is constant and equals to the maximum width, as in (3.52). The back iron width is:

$$w_{bi} = \frac{B_{mg} \tau_{po}}{2B_{\max} k_{st}} \tag{3.53}$$

The tooth width can be expressed as:

$$w_{tb}(r) = \frac{2w_{bi}(r)}{N_{sm}} = \frac{\alpha_i \pi B_{mg} r}{pB_{\max} k_{st} N_{sm}} \tag{3.54}$$

The tooth width is minimum at the inside radius of the stator disc, therefore the smallest tooth width is:

$$w_{tbi} = \frac{B_{mg}\tau_{pi}}{B_{\max} k_{st} N_{sm}} \tag{3.55}$$

Since the slot width is constant, the slot bottom width is:

$$w_{sb} = \tau_{si} - w_{tbi} = \frac{2\pi R_i}{Q} - w_{tbi} \tag{3.56}$$

where τ_{si} is the inner slot pitch

R_i is the inner stator radius

3.4.3 Air-gap

The stator surface is with slots so the flux density always decreases at the slot-opening. Thus it is difficult to identify the average flux density between the stator and rotor. A useful solution for this problem was suggested by Carter in 1901. The equivalent air-gap according the Carter principle is larger than its physical length. In case of the rotor is smooth, the approximated equivalent air-gap length is:

$$g' = k_C g_0 \tag{3.57}$$

where k_C is the Carter Factor

g_0 is the physical air-gap

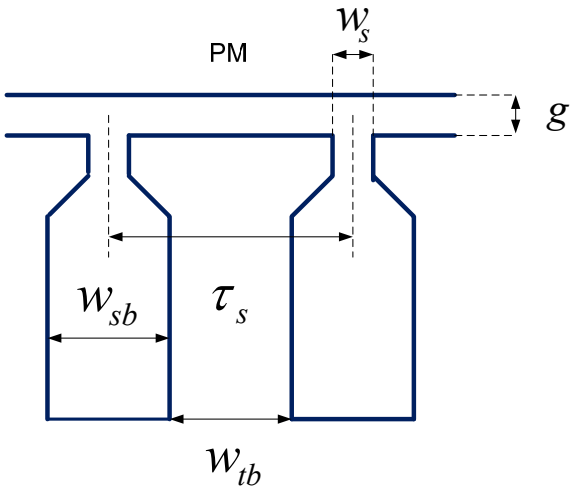

Fig. 3.16 A typical stator slot

The Carter factor depends on the dimensions of slot opening and of physical air-gap.

The Carter factor is [140]:

$$k_C = \frac{\tau_s}{\tau_s - \gamma w_s} \tag{3.58}$$

where τ_s is the slot pitch

w_s is the slot opening

$$\gamma = \frac{4}{\pi}\left[\frac{w_s}{2g}\arctan\frac{w_s}{2g} - \ln\sqrt{1+\left(\frac{w_s}{2g}\right)^2}\right] \tag{3.59}$$

Due to slot pitch changes from inner to outer diameter, Carter factor is calculated based on average slot pitch:

$$\tau_{s,avg} = \frac{\pi D}{Q} = \frac{\pi\left(D_o - D_i\right)}{2Q} \tag{3.60}$$

where D, D_i and D_o is the average, inner and outer diameter of the AFPM machine respectively.

3.4.4 Stator windings

Similar to conventional radial flux machines, the windings of AFPM machine can be either single layer or double layer. Those can also be either full pitch or short. Some parameters of a winding are expressed as follows.

The number of slots per pole is:

$$N_{sm} = \frac{Q}{2P} \tag{3.61}$$

And the number of slots per pole per phase is

$$q = \frac{Q}{2Pm} \tag{3.62}$$

where q is an integer or fraction for integral or fractional slot windings.

For a double-layer winding, the number of conductors per coil can be calculated as:

$$N_C = \frac{N_{1p}}{2pq} = \frac{mN_{1p}}{Q} \tag{3.63}$$

where N_{1p} is the number of turns in series of each phase.

The number of conductors per slot is

$$N_{sl} = \frac{N_{1p}}{pq} = \frac{N_{1p}m}{Q} \tag{3.64}$$

For full pitch winding, the coil pitch in the number of slots is

$$y_1 = N_{sm} \tag{3.65}$$

For short pitch winding, the coil pitch is expressed as:

$$y_1 = \frac{w_c(r)}{\tau(r)} N_{sm} \tag{3.66}$$

where $w_c(r)$ is the coil pitch measured in units of length at a given radius r and $\tau(r)$ is the pole pitch at the same radius.

The coil pitch-to-pole pitch ratio is

$$\beta = \frac{w_c(r)}{\tau(r)} \tag{3.67}$$

The winding factor is

$$k_{w1} = k_{d1} k_{p1} \tag{3.68}$$

Here, k_{d1} is the distribution factor:

$$k_{d1} = \frac{\sin(\pi / 2m)}{q \sin\left[\pi / (2mq)\right]} \quad \text{for integral number of slots,}$$

$$k_{d1} = \frac{\sin(\pi / 6)}{M \sin(\pi / 6M)} \quad \text{for fractional number of slots,} \tag{3.69}$$

$$q = \frac{M}{d}, \ (M \text{ and } d \text{ have no common divisor}) \tag{3.70}$$

$$k_{p1} = \sin\left(\beta \frac{\pi}{2}\right) \text{ is the pitch factor.} \tag{3.71}$$

Two types of windings are considered for the AFPM machine in our FESS. They are double-layer windings with fractional slot ($Q = 18$) and integral slot ($Q = 24$) respectively, as shown in Fig. 3.17. In these two double layer windings, the slot is divided into an upper and a lower part, and each part conduct a winding coil. The winding coil at the bottom of the slot belongs to the bottom layer of the slot, and the

winding coil adjacent to the air-gap belongs to the upper layer as illustrated in the figure.

The arrangement of connections has a significant influence on the space requirements for the windings, the amount of copper and their manufacturing costs. It also affects on certain electrical properties, such as the leakage flux of the windings. Short-pitch winding is selected for the two machines because the end-coil is shorter, and the copper material used is thus reduced. Furthermore, short pitching also influences the harmonics content of the flux density of the air-gap. A proper short-pitch winding produces a more sinusoidal current linkage distribution than a full pitch winding [145].

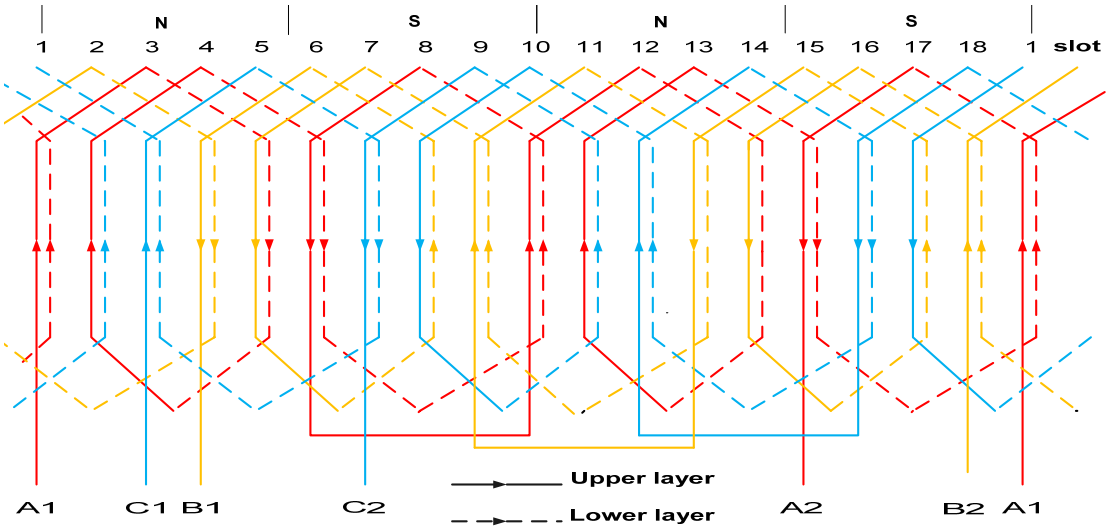

(a)

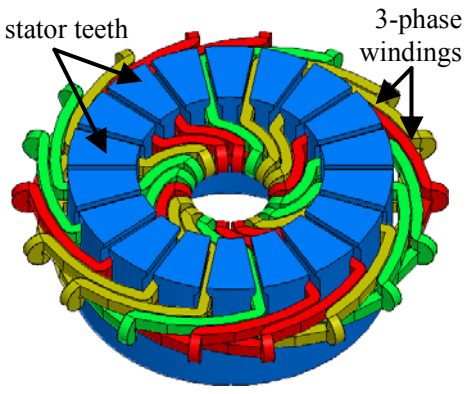

(b)

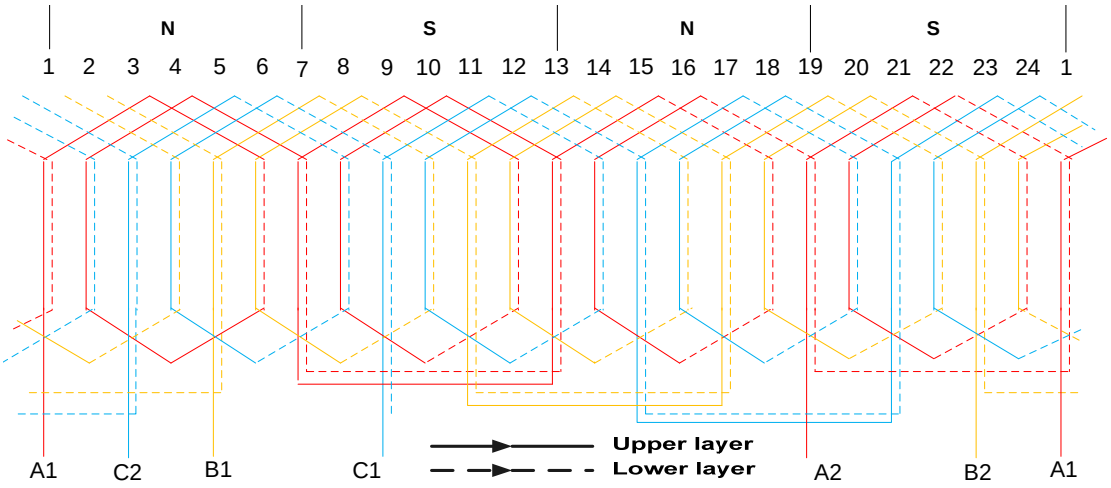

(c)

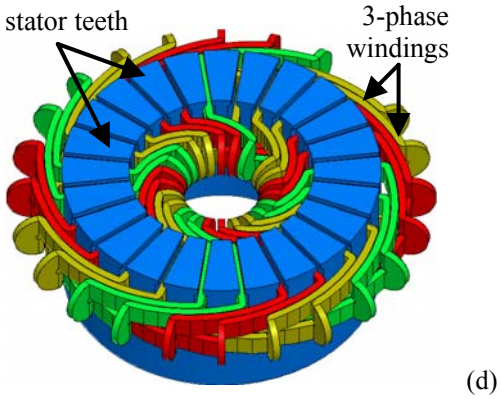

(d)

Fig. 3.17 (a) Windings with *q* = *1.5* slots/pole/phase, (b) Stator and windings with *q* = *1.5*, (c) Windings with *q* = *2*, and (d) Stator and windings with *q* = *2*.

3.4.5 EMF

For a non-sinusoidal magnetic flux density waveform, the amplitude of the first harmonic component of the magnetic flux per pole induced by a permanent magnet is [140]:

$$\varphi_{f1} = \int_{R_i}^{R_o} \frac{4}{\pi} \alpha_M B_{mg} \sin\left(\frac{\alpha_M \pi}{2}\right) * \frac{2\pi}{2p} rdr = \frac{2}{p} \alpha_M B_{mg} \sin\left(\frac{\alpha_M \pi}{2}\right)\left(R_o^2 - R_i^2\right)$$

$$= \frac{1}{2p} \alpha_M B_{mg} \sin\left(\frac{\alpha_M \pi}{2}\right) D_o^2 \left(1 - k_d^2\right) \qquad (3.72)$$

The EMF at no load can be found by:

$$e_f = N_1 k_{w1} \frac{d\varphi_{f1}}{dt} = N_1 k_{w1} \frac{d\varphi_f \sin \omega t}{dt}$$
$$= N_1 k_{w1} \omega \varphi_f \frac{d \sin \omega t}{d \omega t} = 2\pi f N_1 k_{w1} \varphi_f \cos \omega t \qquad (3.73)$$

The RMS value of EMF is then obtained as:

$$E_f = \sqrt{2}\pi f N_1 k_{w1} \varphi_f = \sqrt{2}\pi p n_s N_1 k_{w1} \varphi_f \qquad (3.74)$$

where $n_s = pf$ is the velocity of rotor [*in revolutions per second - rps*]

The number of turns per phase is:

$$N_1 = \frac{E_f}{\sqrt{2}\pi p n_s k_{w1} \varphi_f} \qquad (3.75)$$

From (3.72) and (3.74):

$$E_f = \frac{\pi}{\sqrt{2}} n_s N_1 k_{w1} \alpha_M B_{mg} D_o^2 \left(1 - k^2{}_d\right) \sin\left(\frac{\alpha_M \pi}{2}\right) \qquad (3.76)$$

where the inner-to-outer PM radius $k_d = \frac{R_i}{R_o} = \frac{D_i}{D_o}$

For maximum electromagnet torque k_d can be chosen as [140]:

$$k_d = \frac{1}{\sqrt{3}} \approx 0.58$$

3.4.6 Sizing equation

The average diameter of the AFPM machine is given by:

$$D = 0.5(D_o + D_i) = 0.5D_o(1 + k_d) \tag{3.77}$$

The peak line current density per stator is:

$$A_m = \frac{\sqrt{2} I_a N_1 m}{\pi D / 2} = \frac{4\sqrt{2} m I_a N_1}{\pi D_o (1 + k_d)} \tag{3.78}$$

In the proposed machine, the upper and lower stator windings are connected in series, hence apparent electromagnetic power is:

$$S = 2mE_f I_a \tag{3.79}$$

Sizing equation for this machine is expressed as:

$$S = \frac{\pi^2}{4} n_s k_{w1} \alpha_M B_{mg} A_m D_o^3 (1 + k_d)(1 - k^2{}_d) \sin\left(\frac{\alpha_M \pi}{2}\right) \tag{3.80}$$

The electromagnetic power expressed in terms of active output power is

$$S = \varepsilon \frac{P_{out}}{\eta \cos\varphi} \tag{3.81}$$

where the phase EMF-to phase voltage ratio is

$$\varepsilon = \frac{E_f}{V_1} \tag{3.82}$$

A_m is the peak value of the stator line current density, amplitude of the stator line current density ranges from 10,000 A/m for small motor to 55,000 A/m for medium power motors [140].

From sizing equation, the outer diameter of stator core can be obtained as:

$$D_o = \sqrt[3]{\frac{4\varepsilon P_{out}}{\pi^2 \eta \cos\varphi n_s k_{w1} \alpha_M B_{mg} A_m (1+k_d)(1-k^2{}_d) \sin\left(\frac{\alpha_M \pi}{2}\right)}} \qquad (3.83)$$

or

$$D_o = \sqrt[3]{\frac{4\varepsilon S}{\pi^2 n_s k_{w1} \alpha_M B_{mg} A_m (1+k_d)(1-k^2{}_d) \sin\left(\frac{\alpha_M \pi}{2}\right)}} \qquad (3.84)$$

3.4.7 Shaft

Diameter of the shaft is determined by considerations of stiffness i.e. ability to resist deflection due to weight of rotor or unbalanced magnet pull rather than strength to transmit power. The shaft designed properly has to satisfy the following requirements:

- The shaft must be strong enough throughout its section to withstand all loads without causing residual strain.
- The shaft must have enough rigidity satisfying that the deflection of shaft under operation of machine does not cause crashing of the stator and rotor.
- Critical speeds of rotation must be different from the machine operating speed.

The diameter of the shaft can be calculated by using a convenient formula [145]:

$$d_{sh}[m] = 0.0055 \sqrt[3]{\frac{P_{out}[W]}{n_s[rpm]}} \qquad (3.85)$$

3.4.8 Electrical parameters

3.4.8.1. Reactance:

In surface-mounted AFPM machines, the synchronous reactance, X_s is approximated as the sum of the mutual reactance X_a, and stator leakage reactance X_l:

$$X_s = X_a + X_l \tag{3.86}$$

The mutual reactance can be expressed as [140]:

$$X_a = m_1 \mu_0 f \left(\frac{N_1 k_{w1}}{p} \right)^2 \frac{\left(D_o^2 - D_i^2 \right)}{2 g_{eq}} \tag{3.87}$$

where g_{eq} is the equivalent air gap length [150] $\quad g_{eq} = g_0 k_C + \dfrac{l_{M1}}{\mu_{rrec}}$

At the fundamental frequency, the stator leakage reactance is the combination of two components namely slot leakage reactance and the end connection leakage reactance:

$$X_l = X_{ls} + X_{le} = 4\pi f \mu_0 \frac{N_1^2}{pq} \left[\frac{\left(D_o - D_i \right)}{2} \lambda_{ls} + l_{l,in} \lambda_{l,ein} + l_{l,out} \lambda_{l,eout} \right] \tag{3.88}$$

where $\lambda_{l,s}$ is the coefficient of the slot leakage permeance

$\lambda_{l,ein}$ is the coefficient of the leakage permeance of inner end.

$\lambda_{l,eout}$ is the coefficient of the leakage permeance of outer end

$l_{l,in}$ is the length of the stator winding inner end connection.

$l_{l,out}$ is the length of the stator winding outer end connection.

For the AFPM machine with rectangular semi-open slots and double-layer windings in this study, the coefficient of the slot leakage permeance is:

$$\lambda_{l,s} = \frac{3\beta + 1}{4} \left(\frac{d_3}{3 w_{sb}} + \frac{2 d_2}{w_s + w_{sb}} + \frac{d_1}{w_s} \right) \tag{3.89}$$

where β is the coil pitch-to-pole pitch ratio, according to (3.67)

The specific leakage permeances of inner and outer end connections are estimated on the basic of experiments. For double-layer, low voltage and small machines those are:

$$\lambda_{l,ein} \approx 0.17q\left(1-\frac{2w_{cin}}{\pi l_{l,in}}\right) \tag{3.90}$$

and

$$\lambda_{l,eout} \approx 0.17q\left(1-\frac{2w_{cout}}{\pi l_{l,out}}\right) \tag{3.91}$$

In practice, [140]

$$\frac{w_{e,in}}{l_{l,in}} \approx \frac{w_{e,out}}{l_l} \approx 0.64 \tag{3.92}$$

Therefore,

$$\lambda_{l,ein} = \lambda_{l,eout} = 0.1q \tag{3.93}$$

The length of inner connection of each turn is

$$l_{l,in} = 0.9\frac{\pi D_i}{2}\sin\left(\frac{\beta\pi}{p}\right) \tag{3.94}$$

Similarly, the length of outer connection of each turn is

$$l_{l,out} = 0.9\frac{\pi D_o}{2}\sin\left(\frac{\beta\pi}{p}\right) \tag{3.95}$$

3.4.8.2. Resistance

The armature winding resistance per phase for the d.c. current [150]:

$$R_{1dc} = \frac{N_1 l_{1av}}{a_p a_w s_a}\rho_{,1} \tag{3.96}$$

where a_p : the number of parallel paths

a_w : the number of parallel conductors

s_a [m^2] the conductor cross section

$\rho_{,1}$ [Ωm]: is resistivity of the armature conductor at operating temperature.

For copper material.

$$\rho_{cu,1} = \rho_{cu,20}\left[1 + \alpha_{cu20}\left(\vartheta_1 - 20\right)\right] \tag{3.97}$$

here $\rho_{cu,20} = 0.01724 * 10^{-6}$ resistivity of copper at $20^0 C$

$$\alpha_{cu} = 0.00393 \quad [1/^0 C]$$

l_{1av} [m] is the average length of turn

$$l_{1av} = 2L_i + l_{1in} + l_{1out} \tag{3.98}$$

where l_{1in} : the length of the inner end connection,

l_{1out} : the length of the outer end connection,

L_i is the effective length of the stack

$$L_i = \frac{D_o - D_i}{2} \tag{3.99}$$

Therefore

$$l_{1av} = D_o - D_i + l_{1in} + l_{1out} \tag{3.100}$$

The AC resistance is larger than the DC register due to the effects caused by the skin effect and proximity effect. Furthermore, eddy currents induced by leakage fluxes through the slots cause additional loss to the conductors. Because of these phenomena, the phase resistance can be approximated as [150]

$$R_1 = R_{1,dc}\left[1+\frac{1}{9}\left(\frac{d_3 d_{st}}{\chi^2}\right)^2\right] \tag{3.101}$$

where d_3 is the depth of the slot

d_{st} is the diameter of single conductor

χ is the skin depth of the conductor in free space

$$\chi = \sqrt{\frac{2}{\omega\mu_0\sigma_1}} = \sqrt{\frac{\rho_1}{\pi f_1 \mu_0}} \tag{3.102}$$

3.4.9 Losses and Efficiency

3.4.9.1. Stator losses

a. Stator core losses

The AFPM machine in the FESS is usually fed from power converters. The armature current under PWM mode contains harmonic components which contribute to the stator core losses. Theoretically, the stator core losses are:

$$\Delta P_{1Fe} = \Delta P_{eFe} + \Delta P_{hFe} \tag{3.103}$$

where ΔP_{eFe} is the eddy current loss,

ΔP_{hFe} is the hysteresis loss.

The equations for calculating ΔP_{eFe} and ΔP_{hFe} give the results which are usually lower than those obtained from measurements. If the specific core losses are known, the stator core losses can be obtained by [140]:

$$\Delta P_{1Fe} = \Delta p_{1/50} (\frac{f}{50})^{4/3} (k_{adt} B_{1t}^2 m_{1t} + k_{ady} B_{1y}^2 m_{1y}) \qquad (3.104)$$

where $k_{adt} = 1.7 \to 2$

$k_{ady} = 2.4 \to 4$

$\Delta P_{1/50}$ is the specific core loss in W/kg at 1 T and 50 Hg

B_{1t} is the magnet flux density in a tooth

B_{1y} is the magnet flux density in the yoke

m_{1t} is the mass of the teeth and m_{1y} is the mass of the yoke.

Due to the dimensions of the teeth do not vary. The mass of the teeth can be expressed as:

$$\begin{aligned} m_{1r} &= \gamma_{Fe} \left[\frac{\pi (D_o^2 - D_i^2)}{4} (d_1 + d_2 + d_3) - Q w_{sb} (d_1 + d_2 + d_3) \frac{D_o - D_i}{2} \right] \\ &= \gamma_{Fe} (d_1 + d_2 + d_3) \left[\frac{\pi (D_o^2 - D_i^2)}{4} - Q w_{sb} \frac{D_o - D_i}{2} \right] \end{aligned} \qquad (3.105)$$

The total area of the teeth:

$$S_{\Sigma,t} = \left[\frac{\pi (D_o^2 - D_i^2)}{4} - Q w_{sb} \frac{D_o - D_i}{2} \right] \qquad (3.106)$$

The mass of the stator yoke:

$$m_{1y} = \gamma_{Fe} w_{bi} \frac{\pi \left(D_o^2 - D_i^2 \right)}{4} \qquad (3.107)$$

The magnet flux density in a tooth:

$$B_{1r} = \frac{2p\varphi_{f1}}{S_{\Sigma,t}} \tag{3.108}$$

The magnet flux density in the yoke

$$B_{1y} = \frac{\varphi_{f1}}{w_{bi}\left(D_o - D_i\right)} \tag{3.109}$$

b. Stator winding losses

Stator winding losses are the sum of losses due to both armature current and eddy current. In case of the AFPM machine with slotted stator, the stator winding losses can be approximated using conventional equation ignoring eddy current effect as follow:

$$\Delta P_{1w} = mI_a^2 R_1 \tag{3.110}$$

where I_a is the phase current and R_1 the approximated phase resistance as in (3.101).

3.4.9.2. Permanent magnet losses

The losses in permanent magnet due to high harmonics produced by armature current in stator cannot be neglected because the electric conductivity of rare-earth permanent magnet is only 4 to 9 times lower than that of a copper conductor. The power losses in permanent magnet can be expressed as [140]:

$$\Delta P_{PM} = \frac{1}{2} a_R k_z \frac{\left|\alpha_1\right|^2}{\beta_1^2}\left(\frac{B_{sl}}{\mu_0 \mu_{rrec}}\right)^2 \frac{k}{\sigma_{PM}} \alpha_M \frac{\pi}{4}\left(D_o^2 - D_i^2\right) \tag{3.111}$$

where σ_{PM} is the electric conductivity of permanent magnet,

$$a_R = \frac{1}{\sqrt{2}}\sqrt{\sqrt{4+\left(\frac{\beta_1}{k}\right)^4} + \left(\frac{\beta_1}{k}\right)^2} \tag{3.112}$$

$$k_z = 1 + \frac{\tau_{sl,avg}}{(D_o - D_i)} = 1 + \frac{\pi(D_o + D_i)}{2Q(D_o - D_i)} \tag{3.113}$$

$$\alpha_1 = (1 + j)k \tag{3.114}$$

$$\beta_1 = \frac{\pi}{\tau_s} = \frac{2Q}{D} = \frac{4Q}{D_o + D_i} \tag{3.115}$$

$$k = \sqrt{\frac{\omega \mu_0 \mu_{rrec} \sigma_{PM}}{2}} = \sqrt{\frac{2\pi f_{sl} \mu_0 \mu_{rrec} \sigma_{PM}}{2}} \tag{3.116}$$

3.4.9.3. Rotor losses

The rotor core losses in the solid steel can be expressed as [140]:

$$\Delta P_{2Fe} = \frac{1}{2} a_{RFe} k_Z \frac{|\alpha_1|^2}{\beta_1^2} \left(\frac{B_{sl}}{\mu_0 \mu_r} \right)^2 \frac{k}{\sigma_{Fe}} S_{Fe} \tag{3.117}$$

where σ_{Fe} is the steel electric conductivity

μ_r is the relative magnetic permeability of the rotor steel

S_{Fe} is the surface of the rotor disc, $S_{Fe} = \frac{\pi}{4}\left(D_o^2 - D_i^2\right)$ (3.118)

$$a_{RFe} = \left[\sqrt{4a_R^2 a_X^2 + \left(a_R^2 - a_X^2 + \frac{\beta_1^2}{k^2} \right)^2} + a_R^2 - a_X^2 + \frac{\beta_1^2}{k^2} \right]^{1/2} \tag{3.119}$$

where a_R = 1.4 to 1.5 and a_X = 0.8 to 0.9.

3.4.9.4. Mechanical losses

Mechanical losses or rotation losses in AFPM can be divided into two parts beings;

- Bearing losses
- Windage losses

3.4.9.5. Bearing frictional loss

The bearing loss depends on the loads of the bearing. This loss can be evaluated by using approximate formula as follows [140]:

$$\Delta P_{fr} = 0.06 k_{fb} (m_r + m_{sh}) n \qquad (3.120)$$

where $k_{fb} = 1$ to 3 $[\frac{m^2}{s^2}]$

m_r : the mass of rotor [kg]

m_{sh} : the mass of shaft [kg]

n : the speed of rotor [rpm]

Mass of shaft $$m_{sh} \approx \frac{\pi d_{sh}^2}{4} l_{sh} \gamma_{Fe} \qquad (3.121)$$

d_{sh} : the diameter of rotor shaft [m]

l_{sh} : the length of rotor shaft [m]

γ_{Fe} : density of rotor shaft [kg/m^3].

Mass of the rotor is:

$$m_r = 2\frac{\pi\left(D_o^2 - D_i^2\right)}{4} l_{rot} \gamma_{Fe} + \frac{\pi \gamma_{rim}}{4}\left[(D_i^2 - d_{sh}^2) + (D_{r,o}^2 - D_o^2)\right] \qquad (3.122)$$

where l_{rot} is the length of rotor [m],

$D_{r,o}$ is the outer diameter of the rim [m]

γ_{rim} is the mass density of the rim [kg/m^3].

3.4.9.6. Windage loss

The friction caused by the air with a rotating rotor brings about the windage losses which can be calculated based on the friction factor similar to that used in rotating enclosed discs in [147]. The windage loss in AFPM machine can be written as:

$$\Delta P_{wind} = \frac{1}{2} c_f \rho (2\pi n)^3 \left[\left(\frac{D_{r,o}}{2} \right)^5 - \left(\frac{d_{sh}}{2} \right)^5 \right] \tag{3.123}$$

where ρ is the specific density of the cooling medium and c_f is the coefficient of drag for turbulent flow:

$$c_f = \frac{3.87}{\sqrt{\frac{2\pi\rho n D_{r,o}^2}{4\mu}}} \tag{3.124}$$

where $\mu = 1.8 * 10^{-5}$ Pa: dynamic viscosity of the air at 1 atm and $20\,^o C$.

The mechanical loss is:

$$\Delta P_{mech} = \Delta P_{fr} + \Delta P_{wind} \tag{3.125}$$

The total losses in the AFPM machine is:

$$\Delta P = \Delta P_{mech} + \Delta P_{1w} + \Delta P_{1Fe} + \Delta P_{2,Fe} + \Delta P_{PM} \tag{3.126}$$

The electromagnetic torque of the machine is:

$$T_m = 2 p m_1 N_1 k_{w1} \varphi_{f1} I_a \tag{3.127}$$

The developed power of the machine is:

$$P_m = T_m \omega_s = 2\pi n_s T_m \tag{3.128}$$

Output power is then expressed as:

$$P_{out} = P_m - (\Delta P_{mech} + \Delta P_{2,Fe} + \Delta P_{PM}) \tag{3.129}$$

The efficiency of the machine can be obtained as:

$$\eta = \frac{P_{out}}{P_{out} + \Delta P} \tag{3.130}$$

3.4.10 Design procedure

In operation, the FESS works in the standby mode most of the time. Therefore reducing losses during standby mode of the FESS is one of the main concerns during the design. In our design, the motor/generator is required to have high efficiency, low rotor losses, low THD of back EMF, low cogging torque, no demagnetization and minimum axial force stress on the FESS bearings for low losses in the standby mode. To fulfill the mentioned requirements, the machine is designed by analytical equations and then verified by 3D-FEM respectively. At first, based on design requirements, tentative machine dimensions are obtained: air-gap length, stator outer diameter (using (3.83), and ratio of the inner and outer diameters of the stator. Specifications of magnet material, dimensions of the stator, dimensions of magnet and stator yoke are then determined. After that, losses, efficiency, torque and force of machine are checked analytically. Once these are analytically satisfied, the machine dimensions are further examined by 3D-FEM. At this stage, losses, efficiency, magnet demagnetization, EMF, cogging torque and static axial force of the machine are investigated by 3D-FEM. The procedure is then repeated until the desired requirements are fulfilled. The step-by-step design procedure is illustrated in Fig. 3.18.

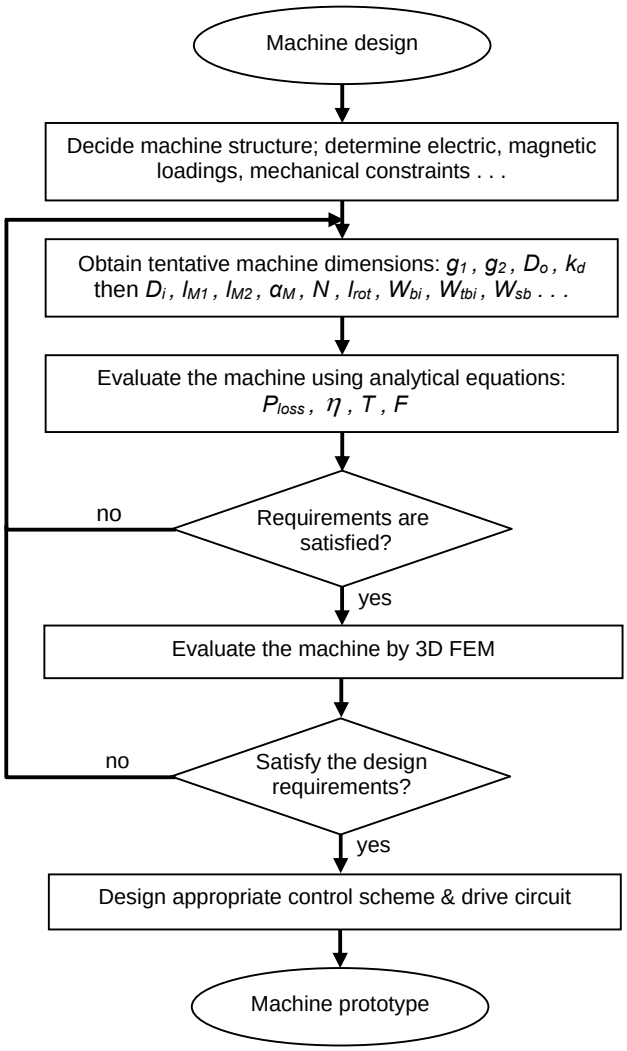

Fig. 3.18 Design procedure

3.5 Design specifications and prototypes

For the reason of safety in the experiments together with the consideration of duration, technique and cost for the construction of the FESS, a low speed AFPM machine is designed and developed. The components of this machine: stators and rotors are shown in Fig. 3.4, but the composite material rim is not included in the flywheel. The rated speed of this machine is selected to be 6,000 rpm as the main purpose is to verify the feasibility of the system and the accuracy of the mathematical model.

The specifications of the machine are listed in Table 3.2. Based on the design method and procedure described in the sections 3.4, the design results for two AFPM machine

prototypes with integral and fractional number of slot per pole per phase has been obtained as shown in Table 3.3.

Table 3.2 Design specification of the dual air-gap AFPM machine in the FESS

Rated power	1 kVA
Number of phases	3
Number of poles	4
Rated current	1.66 A
Rated speed	6,000 rpm
Frequency at full speed	200 Hz
Power factor	0.9
Efficiency	0.9
Magnet type	NdFeB
Remanent flux density	1.23 T
Magnet recoil permeability	1.1

Table 3.3 Dimensions of the 4-pole AFPM machine prototypes with fractional and integral number of slots per pole per phase

Parameter		**Machine 1**	**Machine 2**
Upper stator winding turns		210	208
Lower stator winding turns		210	208
Stator outer diameter		90 mm	90 mm
Stator inner diameter		52 mm	52 mm
Air-gap length		0.9 mm	0.9 mm
Number of slots		18	24
Number of slots per pole per phase		1.5	2
Permanent magnet length of upper rotor		2.0 mm	2.0 mm
Permanent magnet length of lower rotor		1.87 mm	1.87 mm
Stator yoke thickness		20 mm	20 mm
Rotor core thickness		20 mm	20 mm
Rectangular semi-opening slot dimensions, as shown in Fig 3.14	w_{sb}	5 mm	3.5 mm
	w_s	2 mm	1.5 mm
	d_1	2 mm	1.5 mm
	d_2	2 mm	1.5 mm
	d_3	18 mm	20 mm

3.6 Conclusions

This chapter has presented the design approach of the dual air-gap AFPM machine for FESS. A compact FESS structure based on the proposed machine has also been presented. The proposed machine has dual functions of motoring functionality and acting as axial magnetic bearings in the FESS. This distinct feature has been exploited in FESS application where either conventional ball or ceramic bearings can be used without the complexities and high costs associated with magnetic and superconducting bearings [5-7], or magnetically levitated flywheels.

Two 4-pole machines with fractional and integral number of slot per pole per phase respectively have been designed. They are used in the FEM analysis, mathematical model verification, control system design and experimental implementation in the later chapters.

CHAPTER 4 MODELING OF THE DUAL AIR-GAP AFPM MACHINES

4.1 Introduction

The motor/generator is one of the most important components in the flywheel energy storage system. The proposed dual air-gap AFPM machine, used as the motor/generator in FESS, performs both motoring functionality and axial magnetic bearings. Therefore, an accurate mathematical model of this machine is necessary to control its electromagnetic torque and axial force. Based on that, the rotor speed can be controlled to meet with the requirements of energy and the availability of axial force control ensures the rotor can operate at the optimum position.

The permanent magnet synchronous machine is a type of synchronous machine, where the field magnet motive force is provided by permanent magnets. It can be treated as a conventional synchronous motor by assuming that the rotor field is excited by a field current of constant value i_f with winding number N_f, and that the machine inductances can be calculated based on the effective permeability of the permanent magnet rotor [151].

Mathematical model for the AFPM machine can be derived based on the basic principle of AC machine. Therefore the modeling of the AFPM machine is quite similar to the conventional radial-flux PM type. However, different with the conventional type, the air-gap of the AFPM machine is in its axial direction. More attention should be paid as the proposed AFPM machine has dual air-gaps and the length of the air-gaps is not constant. Therefore the inductances, electromagnetic torques and axial forces, which are functions of air-gap length, thus vary versus the

physical operation point of the rotor. Co-energy method has been used to derive the electromagnetic torque and axial force equations for the upper and lower machine half respectively; and the total force and torque has been then achieved.

4.2 Modeling of the Dual Air-gap AFPM Machines

In this section, the flux linkages and co-energy of the dual air-gap AFPM Machines are obtained from the stator and rotor inductances. After that, the electromagnetic torque, axial force and voltage equations are acquired. To facilitate the control system implementation, the machine equations are then presented in rotor-reference frame (*d-q*) based on the Park transformation.

4.2.1 Derivation of winding inductances

The modeling of the proposed AFPM machine shown in Fig. 3.4 & 3.5 is presented in this part. The full machine is composing of two halves. So, firstly one half of the machine is analyzed and then extended to the model of the full machine. Permanent magnets are mounted on the surface of the disk-type rotor, as shown in Fig. 4.1, hence the proposed machine can be analyzed as a non-salient-rotor machine. The rotor is allowed to rotate around z-axis and also displace along this axial. Meanwhile the rotor is constrained in x- and y-axis by mechanical bearings.

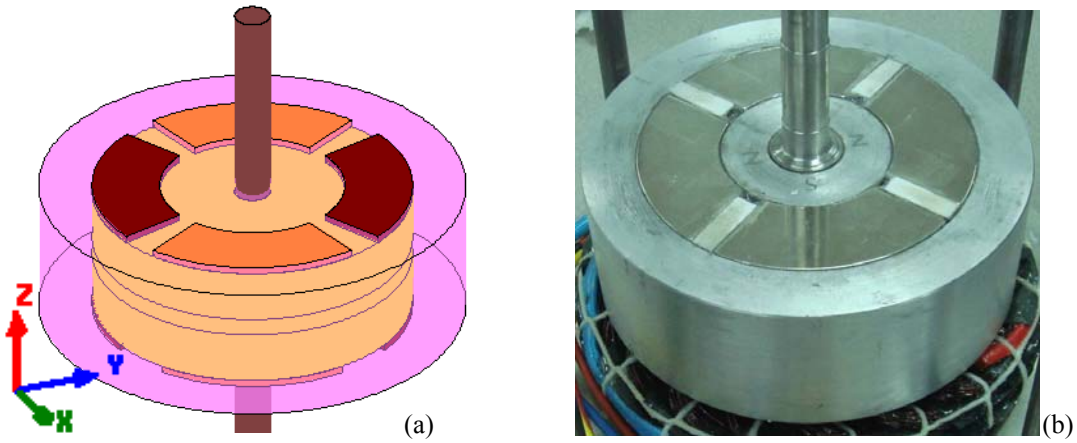

(a) (b)

Fig. 4.1 Surface-mounted PM on the rotors, (a) rotor model, (b) rotor prototype

For the sake of modeling, schematic of the proposed AFPM machine and the coordinate axes of a 2-pole AFPM machine are illustrated in Fig. 4.2. The obtained results from a 2-pole machine then can be extended for a general case, 2*P*-pole machine. For the upper half, the rotating flux generated by currents in the upper stator windings interacts with rotor flux and then generates electromagnetic torques and axial forces, namely T_1, F_1 and similarly T_2, F_2 for the lower half. Three-phase *a, b* and *c*, winding, and *dq*-winding layout are defined in Fig. 4.2. The rotating *d*- and *q*-axis windings are in quadrature of each other and their magnetic axes are aligned with the *d*- and *q*-axis of the rotor. The *d*-axis of the rotor is chosen to be aligned with the centre lines of the magnets and the *q*-axis between the magnets. The angular displacement of the rotor is defined as θ. ϕ_s, ϕ_r respectively are angular displacements along the stator and rotor circumference, which yield to:

$$\phi_s = \phi_r + \theta \tag{4.1}$$

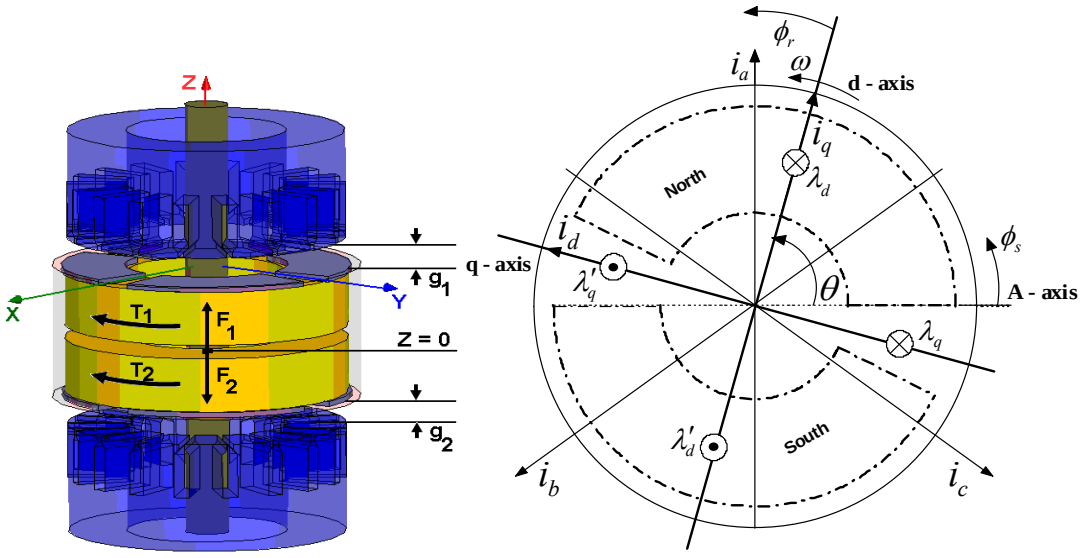

Fig. 4.2 (a) The machine schematic, (b) position of the rotor and windings

The distribution of three phase windings is written as [152]:

$$
\begin{aligned}
N_{as} &= -\frac{N_s}{2}\sin P\phi_s \\
N_{bs} &= -\frac{N_s}{2}\sin(P\phi_s - \frac{2}{3}\pi) \\
N_{cs} &= -\frac{N_s}{2}\sin(P\phi_s + \frac{2}{3}\pi)
\end{aligned}
\tag{4.2}
$$

As each of three phase windings has the same number of turns, the equivalent number of turns of a sinusoidally-distributed winding N_s is obtained by integrating N_{as} over an electrical pole-pitch π/P:

$$
N_s = P.\int_0^{\pi/P} \frac{N_{cd}}{2}\sin(P\phi_s)d\phi_s \tag{4.3}
$$

where N_{cd} is the conductor density expressed in turns per radian.

Assume that the rotor permanent magnet is expressed by a fictitious field winding with N_f equivalent turns, which is also sinusoidally distributed:

$$
N_{fr} = \frac{N_f}{2}\sin P\phi_r \tag{4.4}
$$

Then the air-gap MMFs due to currents in the equivalent stator and field windings can be approximated as sinusoidal waveforms as:

$$
\begin{aligned}
MMF_{as} &= \frac{N_s}{2P} i_{as}\cos P\phi_s \\
MMF_{bs} &= \frac{N_s}{2P} i_{bs}\cos(P\phi_s - \frac{2}{3}\pi) \\
MMF_{cs} &= \frac{N_s}{2P} i_{cs}\cos(P\phi_s + \frac{2}{3}\pi) \\
MMF_{f} &= -\frac{N_f}{2P} i_{f}\cos P\phi_r
\end{aligned}
\tag{4.5}
$$

where P is number of pole pairs.

The number of turns for the fundamental components of a distributed winding can be derived as [151]:

$$N_s = k_{w1} N_1 \tag{4.6}$$

where, N_1 is the number of turns in each phase of the stator windings and k_{w1} is the fundamental harmonic winding factor calculated according to (3.65).

The maximum equivalent magnetomotive force produced by the permanent magnets is obtained according to (3.20) as:

$$MMF_{fm} = \frac{N_f i_f}{2P} = H_m l_m \tag{4.7}$$

where l_m and H_m denote the magnet length and the magnetic field intensity of the magnet. Then the value of $N_f i_f$ can be derived as:

$$N_f i_f = 2P \frac{B_r l_m}{\mu_r \mu_0} \tag{4.8}$$

where B_r is the remanent flux density of the PMs, μ_r is the relative permeability, and μ_0 is the magnetic permeability of the air with the value of $4\pi \times 10^{-7}$ H/m.

The effective air-gap length between the surfaces of the stator and rotor is defined as *g*, the magnetic flux density *B* is expressed below [151]:

$$B(\phi_s, \theta_r) = \mu_0 \frac{MMF(\phi_s)}{g} \tag{4.9}$$

The flux is determined by performing a surface integral over the open surface of a single turn as follows:

$$\phi(\phi_s,\phi_r)=\int_{\phi_s}^{\phi_s+\pi/P} Br(\xi,\theta_r)\,rld\xi \tag{4.10}$$

The total flux linkage due to current flowing in a phase winding, for example phase *a*, can be derived as:

$$\begin{aligned}\lambda_{as} &= \int N_{as}(\phi_s)\phi_{as}(\phi_s)d\phi_s + L_{ls}i_{as}\\ &= -\frac{PN_s}{2}\int_0^{\pi/P}\sin P\phi_s.\left\{\int_{\phi_s}^{\phi_s+\pi/P}\left\{\frac{\mu_0 N_s(R_o^2-R_i^2)}{4gP}\right\}ias\cos P\xi d\xi\right\}d\phi_s + L_{ls}i_{as}\\ &= \frac{\mu_0\pi(R_o^2-R_i^2)N_s^2}{8P^2g}i_{as}+L_{ls}i_{as}\end{aligned} \tag{4.11}$$

In (4.11) L_{ls} is the stator leakage inductance due mainly to leakage flux at the end turns. In general, this inductance accounts for 5% to 10% of the maximum self-inductance. The self-inductance of phase *a* winding is obtained by diving (4.11) by i_{as}, thus:

$$L_{aa}=\frac{\mu_0\pi(R_o^2-R_i^2)N_s^2}{8P^2g}+L_{ls}=L_s+L_{ls} \tag{4.12}$$

Similarly, by ignoring the leakage inductances, the self-inductances of other phase windings can be obtained:

$$\begin{aligned}L_{aa}&=L_{bb}=L_{cc}=L_s\\ L_{ff}&=\frac{\mu_0\pi(R_o^2-R_i^2)N_f^2}{8gP^2}=L_f\end{aligned} \tag{4.13}$$

In a similar method, the mutual flux linkage in phase *a* winding due to current in phase *b* winding can be found, for this case, the flux linkage can be obtained as:

$$\begin{aligned}\lambda_{ab} &= \int N_{as}(\phi_s)\phi_{bs}(\phi_s)d\phi_s\\ &= -\frac{\mu_0\pi(R_o^2-R_i^2)N_s^2}{16gP^2}i_{bs}\end{aligned} \tag{4.14}$$

Thus the mutual inductance L_{ab} can be found by diving (4.14) by $i_{bs,}$ thus:

$$L_{ab} = -\frac{\mu_0 \pi (R_o^2 - R_i^2) N_s^2}{16 g P^2} \tag{4.15}$$

The other mutual inductances can be obtained as in a similar manner as:

$$L_{bc} = L_{ca} = L_{ab} = -\frac{\mu_0 \pi (R_o^2 - R_i^2) N_s^2}{16 g P^2} \tag{4.16}$$

By the same method mentioned above, the mutual inductances between stator windings and field winding can be achieved as:

$$\begin{aligned} L_{af} &= \frac{\mu_0 \pi (R_o^2 - R_i^2) N_s N_f}{8 P^2 g} \cos(P\theta) = L_m \cos(P\theta) \\ L_{bf} &= \frac{\mu_0 \pi (R_o^2 - R_i^2) N_s N_f}{8 P^2 g} \cos(P\theta - \frac{2}{3}\pi) = L_m \cos(P\theta - \frac{2}{3}\pi) \\ L_{cf} &= \frac{\mu_0 \pi (R_o^2 - R_i^2) N_s N_f}{8 P^2 g} \cos(P\theta + \frac{2}{3}\pi) = L_m \cos(P\theta + \frac{2}{3}\pi) \end{aligned} \tag{4.17}$$

To summarize, the inductances can be written in matrix form as follow:

$$L = \begin{bmatrix} L_{ff} & L_{fa} & L_{fb} & L_{fc} \\ L_{af} & L_{aa} & L_{ab} & L_{ac} \\ L_{bf} & L_{ba} & L_{bb} & L_{bc} \\ L_{cf} & L_{ca} & L_{cb} & L_{cc} \end{bmatrix} \tag{4.18}$$

where,

$$\begin{cases} L_{aa} = L_{bb} = L_{cc} \\ L_{ff} = L_f \\ L_{ab} = L_{ba}; L_{bc} = L_{cb}; L_{ca} = L_{ac} \\ L_{af} = L_{af}; L_{bf} = L_{fb}; L_{cf} = L_{fc} \end{cases}$$

4.2.2 Voltage equations

The flux linkage in any winding is the summation of its self inductances and mutual inductances caused by other currents. Expression of the flux linkages in phases *a, b,*

and *c* respectively is:

$$\begin{cases} \lambda_f = L_{ff} i_f + L_{fa} i_a + L_{fb} i_b + L_{fc} i_c \\ \lambda_a = L_{af} i_f + L_{aa} i_a + L_{ab} i_b + L_{ac} i_c \\ \lambda_b = L_{bf} i_f + L_{ba} i_a + L_{bb} i_b + L_{bc} i_c \\ \lambda_c = L_{cf} i_f + L_{ca} i_a + L_{cb} i_b + L_{cc} i_c \end{cases} \tag{4.19}$$

In matrix form, these equations can be expressed as:

$$\begin{aligned} \lambda &= Li \\ \lambda &= \begin{pmatrix} \lambda_f & \lambda_a & \lambda_b & \lambda_c \end{pmatrix}^T \\ i &= \begin{pmatrix} i_f & i_a & i_b & i_c \end{pmatrix}^T \end{aligned} \tag{4.20}$$

Then the voltage equations for the axial-flux machine can be written as:

$$\begin{aligned} v_a &= R_s i_a + \frac{d\lambda_a}{dt} \\ v_b &= R_s i_b + \frac{d\lambda_b}{dt} \\ v_c &= R_s i_c + \frac{d\lambda_c}{dt} \end{aligned} \tag{4.21}$$

4.2.3 Machine equations in *d-q* reference frame

Generally, 3-phase variables, such as voltages, currents or fluxes, in any reference frame can be transformed into the orthogonal components as follow [152]:

$$[x_{dq0}] = C[x_{abc}] \tag{4.22}$$

where :

$$C = \begin{bmatrix} \cos\theta & \cos(\theta - \frac{2\pi}{3}) & \cos(\theta + \frac{2\pi}{3}) \\ -\sin\theta & -\sin(\theta - \frac{2\pi}{3}) & -\sin(\theta + \frac{2\pi}{3}) \\ \frac{1}{2} & \frac{1}{2} & \frac{1}{2} \end{bmatrix},$$

and *x* is amongst the variables mentioned above.

Applying the transformation in (4.22), the flux linkages equations in (4.20) are transformed into:

$$\begin{bmatrix} \lambda_f \\ \lambda_d \\ \lambda_q \end{bmatrix} = \begin{bmatrix} L_f & 3/2L_m & 0 \\ L_m & 3/2L_s & 0 \\ 0 & 0 & 3/2L_s \end{bmatrix} \begin{bmatrix} i_f \\ i_d \\ i_q \end{bmatrix} \tag{4.23}$$

where i_d and i_q are the direct and quadrature currents in the *d-q* reference frame.

Ignoring the leakage inductances, the direct axis inductance L_d and the quadrature axis inductance L_q are obtained as:

$$L_d = L_q = \frac{3}{2} L_s = \frac{3\mu_0 \pi (R_o^2 - R_i^2) N_s^2}{16 g P^2} \tag{4.24}$$

The amplitude of the flux induced by the permanent magnets of the rotor in the stator phases is:

$$\lambda_m = L_m i_f = \frac{\mu_0 \pi (R_o^2 - R_i^2) N_s N_f}{8 P^2 g} i_f \tag{4.25}$$

and therefore the flux linkages in *d-q* reference frame can be expressed as:

$$\begin{aligned} \lambda_d &= L_d i_d + \lambda_m \\ \lambda_q &= L_q i_q \end{aligned} \tag{4.26}$$

The voltage equations can be transformed into:

$$\begin{aligned} v_d &= R_s i_d + \frac{d}{dt}\lambda_d - \omega_e \lambda_q \\ v_q &= R_s i_q + \frac{d}{dt}\lambda_q + \omega_e \lambda_d \end{aligned} \tag{4.27}$$

where ω_e is the electrical speed of the rotor. From (4.23), (4.26) and (4.27), the following equation is obtained:

$$\begin{aligned}\frac{d}{dt}i_d &= \frac{1}{L_d}v_d - \frac{R_s}{L_d}i_d + \frac{L_q}{L_d}P\omega_r i_q \\ \frac{d}{dt}i_q &= \frac{1}{L_q}v_q - \frac{R_s}{L_q}i_q - \frac{L_d}{L_q}P\omega_r i_d - \frac{L_m}{L_q}P\omega_r\end{aligned} \tag{4.28}$$

4.2.4 Equations of axial forces

The axial force can be derived by the co-energy method. The stored magnetic energy is expressed as [152]:

$$W = \frac{1}{2}\lambda_f i_f + \frac{1}{2}\lambda_d i_d + \frac{1}{2}\lambda_q i_q \tag{4.29}$$

The axial force F can be obtained as:

$$\begin{aligned}F &= -\frac{\partial W}{\partial g} \\ &= \frac{\mu_0 \pi (R_o^2 - R_i^2)}{16P^2 g^2}\left[N_f^2 i_f^2 + \frac{5}{2}N_s N_f i_d i_f + \frac{3}{2}N_s^2(i_d^2 + i_q^2)\right]\end{aligned} \tag{4.30}$$

where the air-gap between the surfaces of the stator and the PMs at the equilibrium point is defined as l_{gap}, so the effective air-gap between the stator and rotor at the equilibrium point can be obtained as (3.57):

$$g_0 = k_C(l_{gap} + \frac{l_M}{\mu_r}) \tag{4.31}$$

Therefore, the effective air-gap of the upper and lower machine half can be expressed respectively as:

$$\begin{aligned}g_{10} &= k_C(l_{gap1} + \frac{l_{M1}}{\mu_r}) \\ g_{20} &= k_C(l_{gap2} + \frac{l_{M2}}{\mu_r})\end{aligned} \tag{4.32}$$

Then the forces F_1 and F_2 which are generated by the upper and lower machine half

respectively can be calculated by substituting the corresponding values of g, i_d, i_q and $N_f i_f$ into (4.30). The total axial force F can be expressed as:

$$F = F_1 - F_2 = \frac{\mu_0 \pi (R_o^2 - R_i^2)}{16P^2} \left\{ \begin{array}{l} \dfrac{N_{f1}^2 i_{f1}^2 + \dfrac{5}{2} N_s N_{f1} i_{d1} i_{f1} + \dfrac{3}{2} N_s^2 (i_{d1}^2 + i_{q1}^2)}{(g_{10} - z)^2} \\ -\dfrac{N_{f2}^2 i_{f2}^2 + \dfrac{5}{2} N_s N_{f2} i_{d2} i_{f2} + \dfrac{3}{2} N_s^2 (i_{d2}^2 + i_{q2}^2)}{(g_{20} + z)^2} \end{array} \right\} \quad (4.33)$$

The stator windings of the upper and lower machine half are connected in series together, therefore the axial can be obtained as:

$$F = \frac{\mu_0 \pi (R_o^2 - R_i^2)}{16P^2} \left\{ \begin{array}{l} \dfrac{1}{(g_{10} - z)^2} \left(N_{f1}^2 i_{f1}^2 + \dfrac{5}{2} N_s N_{f1} i_{f1} i_d + \dfrac{3}{2} N_s^2 (i_d^2 + i_q^2) \right) \\ -\dfrac{1}{(g_{20} + z)^2} \left(N_{f2}^2 i_{f2}^2 + \dfrac{5}{2} N_s N_{f2} i_{f2} i_d + \dfrac{3}{2} N_s^2 (i_d^2 + i_q^2) \right) \end{array} \right\} \quad (4.34)$$

4.2.5 Equations of electromagnetic torques

The electromagnetic torque T in term of rotor-reference frame variables can be written as [152]:

$$\begin{aligned} T &= \frac{3}{2} P[\lambda_m i_q + (L_d - L_q) i_d i_q] \\ &= \frac{3}{2} P[(L_d i_d + \lambda_m) i_q - L_q i_d i_q] \\ &= \frac{3}{2} P(\lambda_d i_q - \lambda_q i_d) = \frac{3\mu_0 \pi (R_o^2 - R_i^2)}{16Pg} N_s N_f i_f i_q \end{aligned} \quad (4.35)$$

The total electromagnetic torque of the proposed machine is the summation of the torque from the upper and lower machine half respectively, this can be obtained as:

$$T_e = T_1 + T_2 = \frac{3\mu_0 \pi (R_o^2 - R_i^2) N_s}{16P} \left[\frac{N_{f1} i_{f1} i_{q1}}{g_{10} - z} + \frac{N_{f2} i_{f2} i_{q2}}{g_{20} + z} \right] \quad (4.36)$$

The stator windings of the upper and lower machine half are connected in series together, thus the total torque can be obtained as:

$$T_e = \frac{3\mu_0\pi(R_o^2 - R_i^2)N_s}{16P}\left[\frac{N_{f1}i_{f1}}{g_{10} - z} + \frac{N_{f2}i_{f2}}{g_{20} + z}\right] \times i_q \tag{4.37}$$

4.2.6 Equations of axial position

For the control purpose, it is necessary to simplify the axial force equation in (4.34). The following relationship is defined:

$$i_d = I_{d0} + i_{cd} \tag{4.38}$$

where I_{d0} is a constant offset, and i_{cd} is a control variable.

Linearizing the force equation about the point where z = 0 and $i_d = I_{d0}$, then expanding it into Taylor series to the first order term:

$$F(z, i_d) \approx F_{(z_0, I_{d0})} + \frac{\partial F_{(z_0, I_{d0})}}{\partial z}.(z - z_0) + \frac{\partial F_{(z_0, I_{d0})}}{\partial i_d}.(i_d - I_{d0}) \tag{4.39}$$

Therefore, the force equation can be derived in this research as follows:

$$F(z, i_d) \approx F_{(z_0, I_{d0})} + \frac{\partial F_{(z_0, I_{d0})}}{\partial z}.z + \frac{\partial F_{(z_0, I_{d0})}}{\partial i_d}.i_{cd} \tag{4.40}$$

where

$$F_{(z_0, I_{d0})} = K \times \left\{ \begin{array}{l} \frac{1}{g_{10}^2}\left(N_{f1}^2 i_{f1}^2 + \frac{5}{2}N_s N_{f1} i_{f1} I_{d0} + \frac{3}{2}N_s^2(I_{d0}^2 + i_q^2)\right) \\ -\frac{1}{g_{20}^2}\left(N_{f2}^2 i_{f2}^2 + \frac{5}{2}N_s N_{f2} i_{f2} I_{d0} + \frac{3}{2}N_s^2(I_{d0}^2 + i_q^2)\right) \end{array} \right\} \tag{4.41}$$

$$\frac{\partial F_{(z_0,I_{d0})}}{\partial z} = -K \times \left\{ \begin{array}{l} \frac{1}{g_{10}^3}\left(N_{f1}^2 i_{f1}^2 + \frac{5}{2} N_s N_{f1} i_{f1} I_{d0} + \frac{3}{2} N_s^2 (I_{d0}^2 + i_q^2) \right) \\ + \frac{1}{g_{20}^3}\left(N_{f2}^2 i_{f2}^2 + \frac{5}{2} N_s N_{f2} i_{f2} I_{d0} + \frac{3}{2} N_s^2 (I_{d0}^2 + i_q^2) \right) \end{array} \right\} \tag{4.42}$$

$$\frac{\partial F_{(z_0,I_{d0})}}{\partial i_d} = K \times \left\{ \begin{array}{l} \frac{1}{g_{10}^2}\left(\frac{5}{2} N_s N_{f1} i_{f1} + 3 N_s^2 I_{d0} \right) \\ - \frac{1}{g_{20}^2}\left(\frac{5}{2} N_s N_{f2} i_{f2} + 3 N_s^2 I_{d0} \right) \end{array} \right\} \tag{4.43}$$

$$K = \frac{\mu_0 \pi (R_o^2 - R_i^2)}{16 P^2} \tag{4.44}$$

The force equation then can be obtained as:

$$F = K_1 + K_2 z + K_3 i_{cd} \tag{4.45}$$

where $$K_1 = F_{(z_0,I_{d0})}, K_2 = \frac{\partial F_{(z_0,I_{d0})}}{\partial z}, K_3 = \frac{\partial F_{(z_0,I_{d0})}}{\partial i_d}$$

Here, in the steady state of the machine, K_1 is a constant which is around the gravity of the rotor. The term $K_2 z$ is about zero at the equilibrium point $z = 0$. The dynamic term $K_3 i_{cd}$ is the variable which is used to control the levitation of the rotor.

Assume that radial motion of the rotor is constrained by passive mechanical or passive magnetic bearings; hence the axial motion of the rotor is independent from its radial motion, The dynamic equation of the rotor in axial direction can be expressed as:

$$m \frac{d^2 z}{d^2 t} = F - G = K_1 + K_2 z + K_3 i_{cd} - G \tag{4.46}$$

where G is the gravity of the rotor and its attached rim.

Let $I_{cd0} = (K_1 - G) / K_3$, the above equation can be transformed into:

$$m\frac{d^2z}{d^2t} = K_2 z + K_3(i_{cd} + I_{cd0}) \tag{4.47}$$

The dynamic equation of the rotor now can be expressed as:

$$m\frac{d^2z}{d^2t} = K_2 z + K_3\tilde{i}_{cd} \tag{4.48}$$

where

$$\tilde{i}_{cd} = i_{cd} + I_{cd0} \tag{4.49}$$

4.2.7 Equations of rotational speed

It can be seen from (4.37) that the electromagnetic torque only depends on quadrature current i_q and is independent of the direct current i_d. As z is far smaller than g_{10} and g_{20}, this can be transformed into:

$$T_e = \frac{3\mu_0\pi(R_o^2 - R_i^2)N_s}{16P} \times \left(\frac{N_{f1}i_{f1}}{g_{10}} + \frac{N_{f2}i_{f2}}{g_{20}} \right) \times i_q = K_T i_q \tag{4.50}$$

where

$$K_T = \frac{3\mu_0\pi(R_o^2 - R_i^2)N_s}{16P} \times \left(\frac{N_{f1}i_{f1}}{g_{10}} + \frac{N_{f2}i_{f2}}{g_{20}} \right) \tag{4.51}$$

This is the torque constant defined as the torque per ampere generated by the current i_q. The speed equation is rewritten as follows:

$$\frac{d\omega}{dt} = \frac{1}{J}T_e = \frac{K_T}{J}i_q \tag{4.52}$$

From above equation, it is seen that T_e is positive in the motoring mode; it is when the machine is sped up to store the kinetic energy. When the machine is in generating

mode, T_e is negative. These can be obtained by controlling the i_q.

4.2.8 The entire mathematical model

From the derivations shown above, the entire mathematical model can be written as follow:

$$\begin{aligned} \lambda_{d1} &= L_{d1} i_{d1} + L_{f1} i_{f1} \\ \lambda_{q1} &= L_{q1} i_{q1} \end{aligned} \tag{4.53}$$

$$\begin{aligned} v_{d1} &= R_s i_{d1} + \frac{d}{dt}\lambda_{d1} - \omega\lambda_{q1} \\ v_{q1} &= R_s i_{q1} + \frac{d}{dt}\lambda_{q1} + \omega\lambda_{d1} \end{aligned} \tag{4.54}$$

$$F_1 = \frac{\mu_0 \pi (R_o^2 - R_i^2)}{16 P^2 {g_1}^2} \left[N_{f1}^2 i_{f1}^2 + \frac{5}{2} N_s N_{f1} i_{d1} i_{f1} + \frac{3}{2} N_s^2 (i_{d1}^2 + i_{q1}^2) \right] \tag{4.55}$$

$$T_{e1} = \frac{3}{2} P(\lambda_{d1} i_{q1} - \lambda_{q1} i_{d1}) \tag{4.56}$$

$$\begin{aligned} \lambda_{d2} &= L_{d2} i_{d2} + L_{f2} i_{f2} \\ \lambda_{q2} &= L_{q2} i_{q2} \end{aligned} \tag{4.57}$$

$$\begin{aligned} v_{d2} &= R_s i_{d2} + \frac{d}{dt}\lambda_{d2} - \omega\lambda_{q2} \\ v_{q2} &= R_s i_{q2} + \frac{d}{dt}\lambda_{q2} + \omega\lambda_{d2} \end{aligned} \tag{4.58}$$

$$F_2 = \frac{\mu_0 \pi (R_o^2 - R_i^2)}{16 P^2 {g_2}^2} \left[N_{f2}^2 i_{f2}^2 + \frac{5}{2} N_s N_{f2} i_{d2} i_{f2} + \frac{3}{2} N_s^2 (i_{d2}^2 + i_{q2}^2) \right] \tag{4.59}$$

$$T_{e2} = \frac{3}{2} P(\lambda_{d2} i_{q2} - \lambda_{q2} i_{d2}) \tag{4.60}$$

$$F = \frac{\mu_0 \pi (R_o^2 - R_i^2)}{16P^2} \left\{ \begin{array}{l} \dfrac{N_{f1}^2 i_{f1}^2 + \dfrac{5}{2} N_s N_{f1} i_{f1} i_d + \dfrac{3}{2} N_s^2 (i_d^2 + i_q^2)}{(g_{10} - z)^2} \\ - \dfrac{N_{f2}^2 i_{f2}^2 + \dfrac{5}{2} N_s N_{f2} i_{f2} i_d + \dfrac{3}{2} N_s^2 (i_d^2 + i_q^2)}{(g_{20} + z)^2} \end{array} \right\} \tag{4.61}$$

$$T_e = \frac{3\mu_0 \pi (R_o^2 - R_i^2) N_s}{16P} \left[\frac{N_{f1} i_{f1}}{g_{10} - z} + \frac{N_{f2} i_{f2}}{g_{20} + z} \right] \times i_q \tag{4.62}$$

4.3 Conclusions

In order to control the electromagnetic torque and axial force for the proposed dual air-gap AFPM machine as well as its speed and axial displacement, the mathematical model for this machine has been developed in this chapter. Modeling of this special machine has been built based on the basic theory of AC electrical machines. The machine equations are also obtained in rotor-reference frame to facilitate its control implementation which will be presented in Chapter 6. The electromagnetic torques and axial forces have been derived based on co-energy method. After that the equations of speed and axial displacement of the rotor are obtained. As the model is a non-linear multi-variable system, linearization has been used to facilitate the control system implementation. Verification of this linearized model by Matlab simulations, by 3D-finite element method and on machine prototypes will be presented respectively in the following chapters.

CHAPTER 5 FINITE ELEMENT ANALYSIS OF PROPOSED AFPM MACHINES

5.1 Introduction

The finite element method (FEM) is a numerical method for solving the complex electromagnetic field problems and circuit parameters. For problems with non-linear material characteristics and complex structure, FEM has been especially powerful and useful since its first introduction in the 1940s [153].

The method involves dividing the machine into smaller areas or volumes. The variation of the magnetic potential in the machine is expressed by non-linear differential equations which are derived from Maxwell equations. These equations are written in terms of vector potential in which the significant field quantities such as flux, field density and direction can be determined. The finite element method can accurately analyze the models involving permanent magnets of any shape and material. It is not necessary to calculate the reluctances, inductances, leakage factor, the operating point on the magnetic recoil line or torques using circuit type analytical methods since these values can simply be extracted from the finite element analysis. One important advantage of FEM analysis over other approaches in analysing of electric machines is the ability to calculate accurately the cogging torque, armature reaction effects, electromagnetic force and torque [154, 155].

In this chapter, the finite element analysis of the machines designed in Chapter 3 is presented. The underlying theory is given in section 5.2. In section 5.3, the analysis method and results of the FEA on the two machines with $q = 2$ and $q = 1.5$ slots/pole/phase are respectively presented. Three-dimensional (3D) finite element method is employed for the design and analysis of these machines, including their electromagnetic torque and axial force performances. Effects of rotor PM skew angle

on the cogging torque and the axial force are also studied. Finally, the performance study of the machine is presented in section 5.4.

5.2 Relevant theory

The traditional two-dimensional (2D) FEA used for radial flux machines is not suitable for the proposed dual air-gap AFPM machine due to its unconventional flux distribution. Therefore three-dimensional finite element method is employed for the design and analysis of the proposed machine.

5.2.1 Flux density and field intensity

The most important parameters in the analysis of an electrical machine are the magnitude and the distribution of flux density $\vec{B}$ and the magnetic field intensity or magnetizing force $\vec{H}$. These quantities are solved by FEM in terms of potentials: scalar magnetic potential Ω, which is expressed in ampere-turns and magnetic vector potential $\vec{A}$, in terms of Wb/m [153].

The relevant field formulation can be obtained from Maxwell's Equations. In three dimensional analysis:

$$\nabla.\vec{B} = 0 \tag{5.1}$$

$$\nabla \times \vec{H} = \vec{J} \tag{5.2}$$

where $\vec{H}$ is the field intensity vector, $\vec{J}$ is the current density vector, and $\vec{B}$ is the magnetic flux density vector.

In scalar form (5.1) can be expressed as:

$$\frac{\partial B_x}{\partial x} + \frac{\partial B_y}{\partial y} + \frac{\partial B_z}{\partial z} = 0 \tag{5.3}$$

Besides, the magnetic vector potential $\vec{A}$ satisfies the following relation:

$$\vec{B} = \nabla \times \vec{A} \tag{5.4}$$

where

$$B_x = \frac{\partial A_z}{\partial y} - \frac{\partial A_y}{\partial z} \tag{5.5}$$

$$B_y = \frac{\partial A_x}{\partial z} - \frac{\partial A_z}{\partial x} \tag{5.6}$$

$$B_z = \frac{\partial A_y}{\partial x} - \frac{\partial A_x}{\partial y} \tag{5.7}$$

where A_x, A_y, and A_z are the x, y, and z components of vector A in the Cartesian Coordinate System respectively.

Current density vector in (5.2) can be expressed as:

$$\frac{\partial H_z}{\partial y} - \frac{\partial H_y}{\partial z} = J_x \tag{5.8}$$

$$\frac{\partial H_x}{\partial z} - \frac{\partial H_z}{\partial x} = J_y \tag{5.9}$$

$$\frac{\partial H_y}{\partial x} - \frac{\partial H_x}{\partial y} = J_z \tag{5.10}$$

Since

$$\vec{B} = \mu_0 \mu_r \vec{H} \tag{5.11}$$

From (5.2) and (5.4), the following equation is derived:

$$\nabla \times \left(\frac{1}{\mu_0 \mu_r} \nabla \times \vec{A} \right) = \vec{J} \tag{5.12}$$

Considering A_x and A_y are constant, B_x and B_y can be obtained as:

$$B_x = \frac{\partial A_z}{\partial y} \tag{5.13}$$

$$B_y = -\frac{\partial A_z}{\partial x} \tag{5.14}$$

Using (5.12) and assuming isotropy, the following equation is obtained:

$$\frac{1}{\mu_0 \mu_r}\left[\frac{\partial}{\partial x}\left(\frac{\partial A_z}{\partial x}\right)+\frac{\partial}{\partial y}\left(\frac{\partial A_z}{\partial y}\right)\right] = -J_z \tag{5.15}$$

which yields to:

$$\frac{\partial}{\partial x}\left(\frac{\partial A_z}{\partial x}\right)+\frac{\partial}{\partial y}\left(\frac{\partial A_z}{\partial y}\right) = -\mu_0 \mu_r J_z \tag{5.16}$$

This is called Poisson's equation where the flux density vector components depend only on the gradients of the magnetic vector potential components.

5.2.2 Force and torque by co-energy method

The law of conservation of energy in electrical machines can be derived from Maxwell's equations. The net electrical input active power can be expressed as [153]:

$$\begin{aligned} P_{in} &= \int_v \sigma \vec{E}^2 dv \\ &= \int_v \vec{E}.\vec{J} dv \\ &= \int_l \int_S \left(\vec{J}.d\vec{S}\right).\vec{E}d\vec{l} \end{aligned} \tag{5.17}$$

The EMF can be expressed as:

$$\begin{aligned} e &= \int_l \vec{E}.d\vec{J} \\ &= -\frac{\partial}{\partial t}\int_S \vec{B}.d\vec{S} \end{aligned} \tag{5.18}$$

From Ampere's law, the current enclosed can be written as:

$$\begin{aligned} I &= \int_s \vec{J} d\vec{S} \\ &= \oint_l \vec{H}.d\vec{l} \end{aligned} \tag{5.19}$$

From (5.17), (5.18) and (5.19), the net electrical input power can be derived as:

$$\begin{aligned} P_{in} &= \oint_l \vec{H}.d\vec{l} \left[-\frac{\partial}{\partial t} \int_s \vec{B}.d\vec{S} \right] \\ &= -\int_v \vec{H} \cdot \frac{\partial \vec{B}}{\partial t} dv \\ &= -\frac{\partial}{\partial t} \int_v \left[\int_0^B \vec{H} \cdot d\vec{B} \right] dv \end{aligned} \tag{5.20}$$

The stored magnetic co-energy is:

$$W_{co} = \int_v \left[\int_0^B \vec{H}.d\vec{B} \right] dv \tag{5.21}$$

The force and torque can be calculated as the derivative of the stored magnetic co-energy with respect to a small corresponding displacement. Then the component of instantaneous force F_z toward the displacement direction *z* is [151]:

$$F_z = \frac{W_{co}}{dz} \tag{5.22}$$

The instant torque T_θ with a small angular displacement θ is:

$$T_\theta = \left. \frac{W_{co}(i,\theta)}{d\theta} \right|_{i=const} \tag{5.23}$$

5.3 Finite Element Analysis

5.3.1 Finite element mesh and accuracy

The three important things needing to be considered in FEA of an electrical machine are the size of mesh, the desired level of accuracy, and the amount of available computing resources. A trade-off amongst these three things is necessary for an acceptable solution within reasonable computing time. The size of the individual elements (tetrahedra) of a studied model directly affects the accuracy of the obtained results: solutions based on meshes using thousands of elements are more accurate than solutions based on coarse meshes using relatively few elements. Therefore, in order to generate a precise description of a field quantity in higher field-gradient regions with the problem space, each element must occupy a region that is small enough for the field to be adequately interpolated from the nodal values. Nevertheless, solving the field problems is based on manipulating the matrix with the size of approximately as many elements as the number of tetrahedra nodes. Significant amount of computing power and memory is required for the meshes with large number of elements. Therefore, it is desirable to use the mesh that is fine enough to obtain the accurate field solution but not so tiny that it overwhelms the available computer memory and processing power.

5.3.2 FEA of the dual air-gap AFPM machine with $q = 2$ slots/pole/phase

The machine has symmetrical structure so its 3D quarter model is analyzed to reduce the simulation time, as illustrated in Fig. 5.1 (a). According to the principles described above, the mesh shape of the analysis model is obtained as illustrated in Fig. 5.1 (b). The mesh numbers in tetrahedra are shown in Table 5.1.

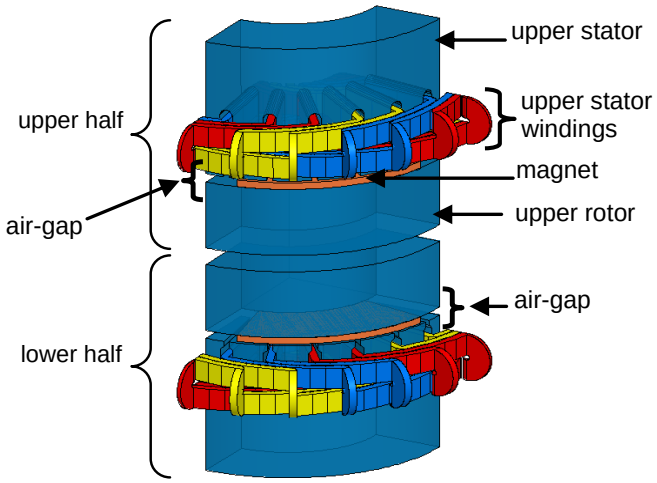

(a)

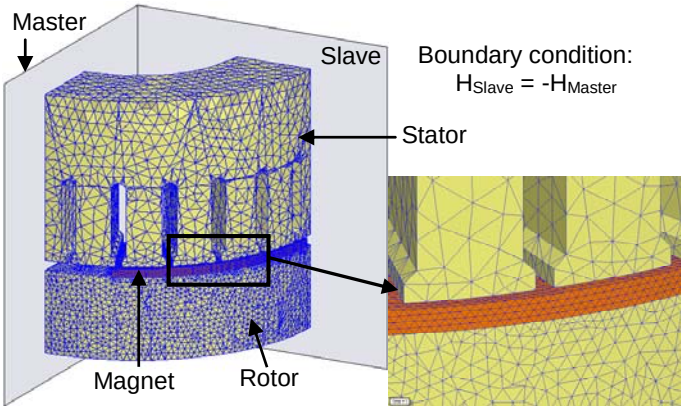

(b)

Fig. 5.1 3D-quarter machine model, (b) Mesh of 3D-quarter of the upper half.

Table 5.1 Mesh number of the machine components

Component name	Mesh numbers
Stator	28361
Rotor	34906
Coils	24674
Magnet	41971

5.3.2.1. Flux density

The air-gap flux density of the machine operating at the no load condition is shown in Fig. 5.2(a). From the figure, it can be seen that the air-gap flux density is about 0.65 T. Based on the principle of the operation of the proposed machine, the magnetization directions of the magnets are set and the direction of the magnet flux density are illustrated in Fig. 5.2(b). The flux directions and flux density of the full machine are shown in Fig. 5.3.

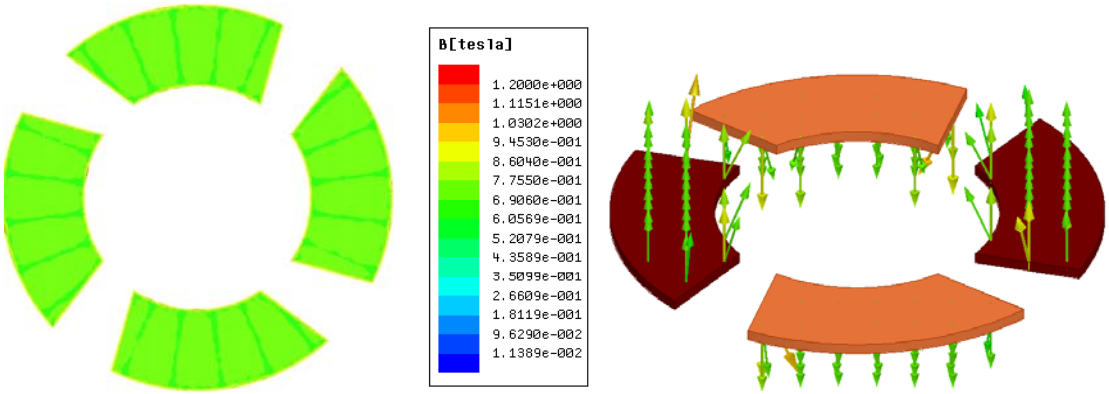

(a) (b)

Fig. 5.2 (a) Air-gap flux density, (b) magnetization direction of the magnets

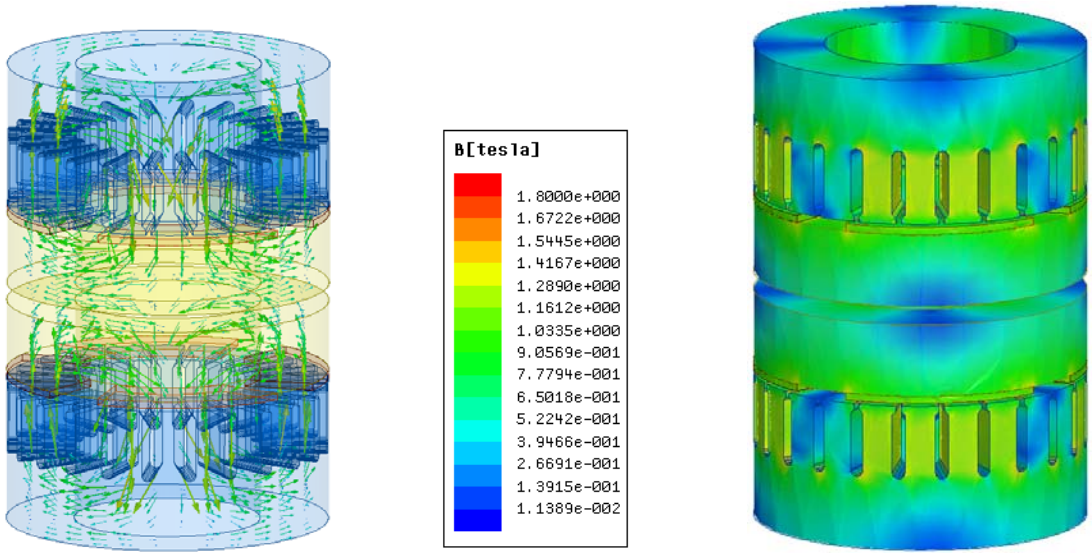

(a) (b)

Fig. 5.3 (a) The flux directions, (b) flux density of the full machine

The quarter model of the machine is studied for less computational time and the obtained simulation results are shown in Fig. 5.4. The flux directions and flux density of the machine are respectively illustrated in Fig. 5.4(a, b). Zoomed-in area of the teeth, magnet and rotor is shown in Fig. 5.4(c). It can also be seen that the maximum flux density on the stator is roughly 1.6 T and the air-gap flux density is about 0.65T.

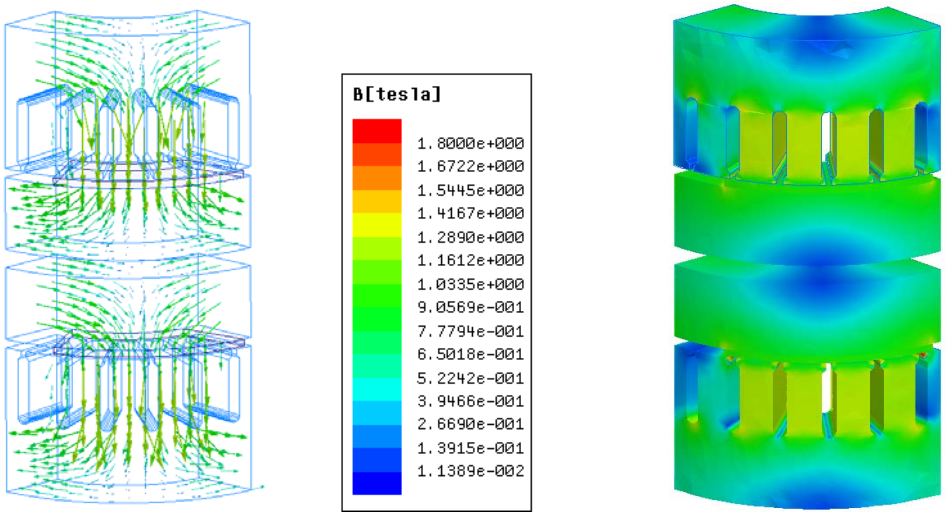

(a) (b)

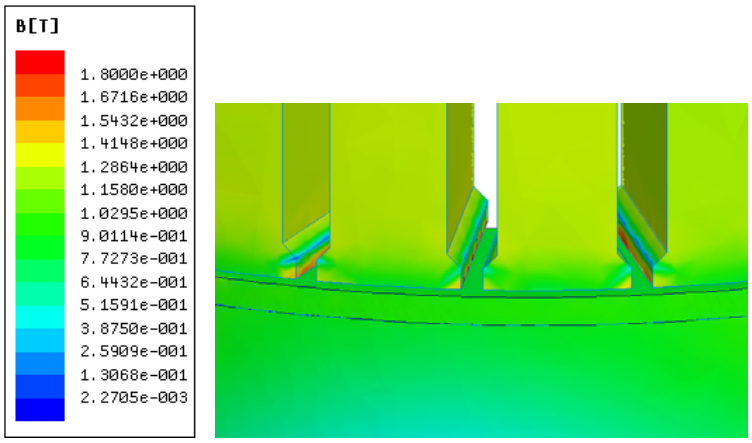

(c)

Fig. 5.4 (a) The flux directions, (b) flux density, (c) zoomed-in of tootth-magnet-rotor area

The air-gap flux density at the average diameter *D* over one pole is also obtained and illustrated in Fig. 5.5. It can be seen from the plot that there exist the gaps in the air-gap flux density waveform between the stator slots and the rotor caused by the sudden changes of the air-gap permeance.

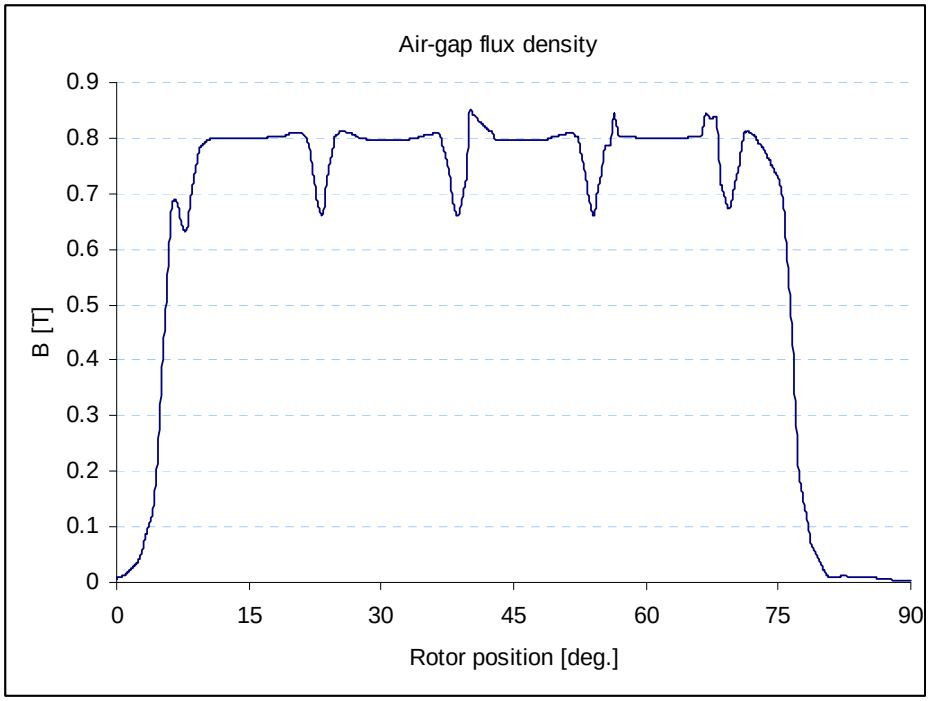

Fig. 5.5 Air-gap flux density at the average diameter *D*.

5.3.2.2. Torques and forces

Cogging torque is one of the main sources of torque pulsations in permanent magnet machines. It is generated by the interaction between stator teeth and rotor magnets. The proposed dual air-gap AFPM machine has cogging torque contributed from both upper and lower stators. The cogging torque is proportional to the magnet flux and reluctance variation as [150]:

$$T_{cogging} = \frac{1}{2}\phi_r^2 \frac{dR}{d\theta} \tag{5.24}$$

The cogging torque can be lessened by various techniques, such as auxiliary teeth and slots, optimal magnet pole-arc, skewing of slots and/or magnets, [156]. Magnetic skew technique is simpler to use with the axial flux machine than with traditional radial flux type. Therefore magnetic skew technique is used to reduce the cogging torque component for the proposed machine. The principle of this technique is to skew the magnet with respect to the stator teeth by a skew angle δ_i to reduce

reluctance variation $dR/d\theta$ when the rotor rotates. Permanent magnets with zero and non-zero skew angle are shown in Fig. 5.6.

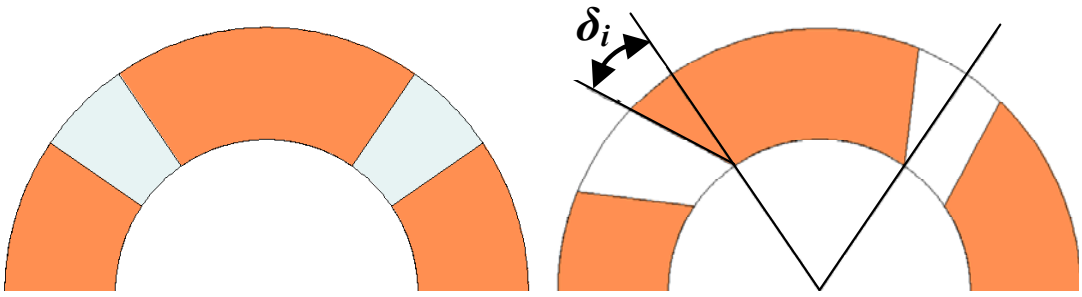

(a) (b)

Fig. 5.6 Rotor PM skew: (a) Non-skewed, (b) Skewed by δ_i degree

Taking the rated torque as the base value, the cogging torque in per unit at different rotor positions are presented in Fig. 5.7 for various skew angles. The peak amplitudes of the cogging torque for each different skew angle are plotted in Fig. 5.8. It is seen that the peak cogging torque reduces with the increase of skew angle and is minimized at around 18 to 20 degrees.

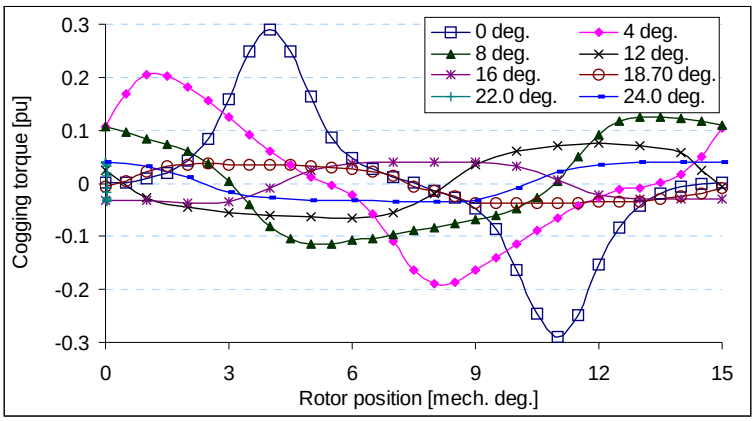

Fig. 5.7 Cogging torque against rotor position for various skew angles

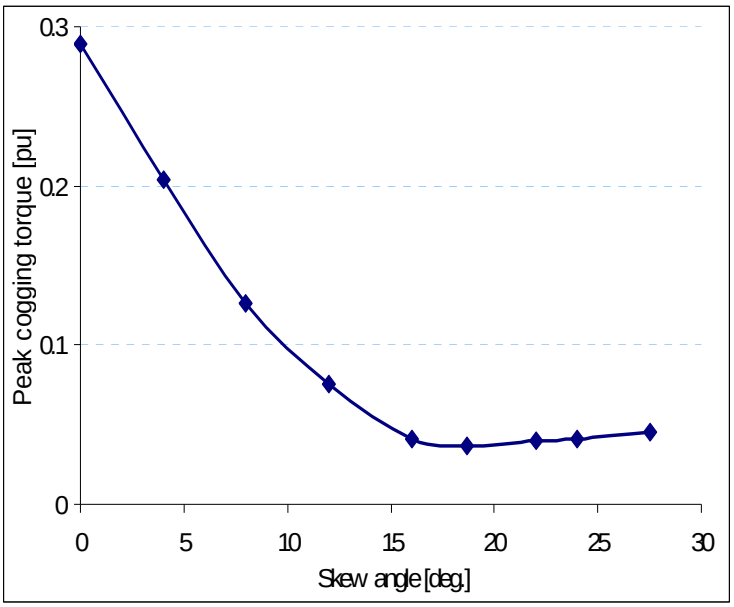

Fig. 5.8 Peak cogging torque against skew angle

A ripple torque analysis for this machine was carried out for the rated load case. In order to the ripple torque variation of the machine, the MMF generated by the rotor and the MMF created by the 3-phase stator windings are rotated in such a manner that the angle between the two MMFs is kept constant. The angle between the rotor MMF and the stator MMF is chosen at the condition that the torque is maximum. At the chosen angle, the two MMFs were rotated to realize the total torque and ripple torque. By using this approach, finite element calculations are obtained. The total torque of the machine at the rated torque condition is shown in Fig 5.9. It is seen from the plots that the ripple torque is roughly 0.581 pu for non-skewed PM rotor case. When the rotor magnets are skewed by 18.7 degrees, the peak-to-peak torque ripple is reduced to 0.070 pu as shown in Fig. 5.9(b).

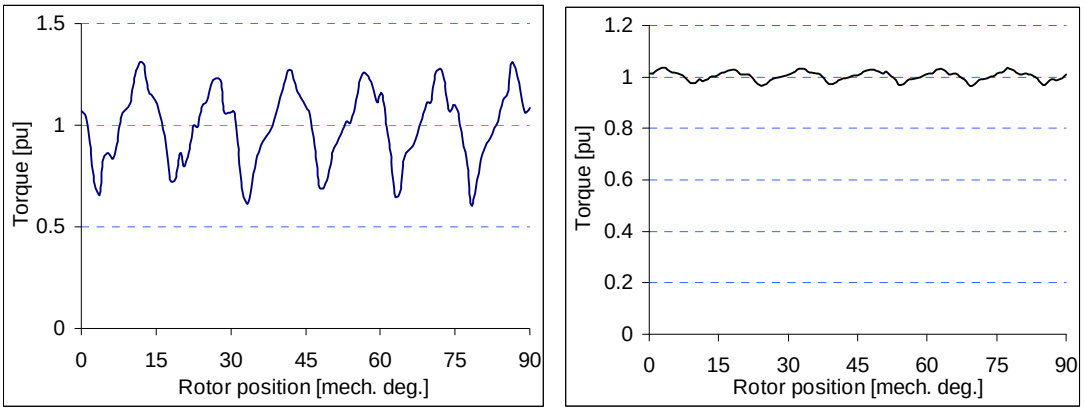

(a) (b)

Fig. 5.9 Total torque at rated load (a) without and (b) skewed rotor magnets

Fig. 5.10 respectively shows the static axial forces in the upper air-gap, the lower air-gap and the net static axial force of the machine for rotor PM skew angles of zero and 18.7 degrees. It is seen that each of the air-gaps (upper or lower) contributes very significant axial forces, up to 1,000 N, but in opposite directions. These axial forces are the major disturbances in the control and operation of single air-gap machines. They give rise to large axial stress on their bearings which certainly contributes to power losses and decreases the bearing lifespan. It is also seen that the rotor PM skew reduces the absolute static axial forces in upper and lower air-gaps, but the net static axial force is relatively unchanged. Using the design procedure described in Chapter 3, the net static axial force is designed to counter the weight of the rotor-flywheel assembly. Minimum axial stress on the bearings of the FESS can therefore be attained.

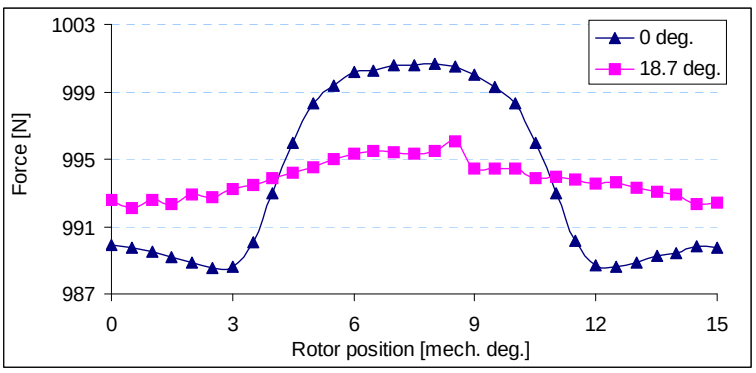

(a)

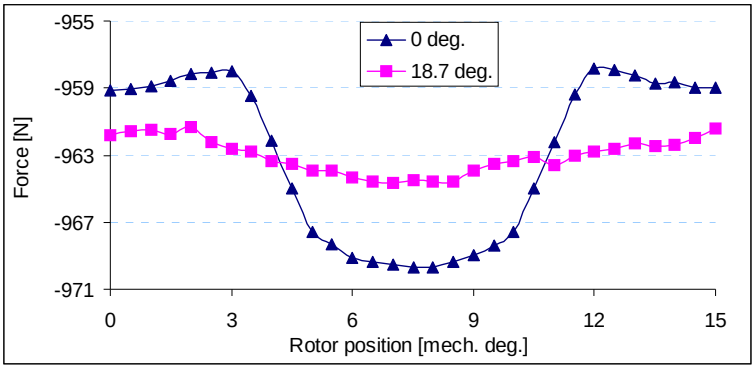

(b)

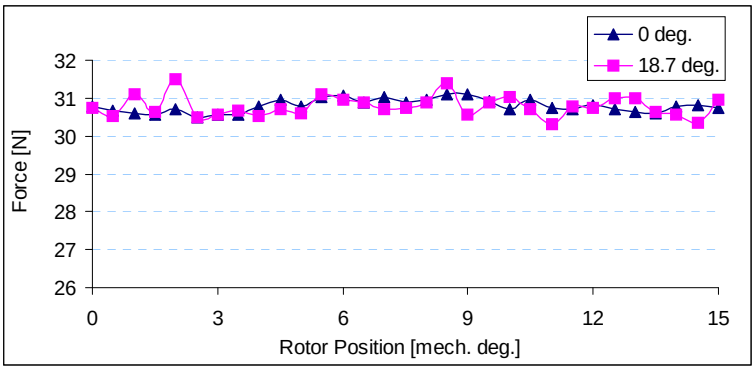

(c)

Fig. 5.10 Static axial force against rotor position for non-skewed and skewed PM: (a) upper air-gap; (b) lower air-gap; (c) net force of both air-gaps

5.3.2.3. Losses

Losses on rotor of the PM machine are generated by high-order stator slot and magnet harmonics and also by time-harmonic components in supply voltages in case of supply with square voltage waveforms generated by pulse width modulation [157-159]. In this part, the 3D FEM is used in analysis of this AFPM machine where effect of core losses on field and edge effect on magnets are included. Losses on iron-core and permanent magnets caused by both space harmonics (magnet harmonics and stator slot harmonics) and time harmonics are respectively analyzed. Effect of magnetic skew on machine losses is also taken into study. A solution to reduce eddy-current losses in magnets for this machine is also presented.

A. Analysis Method

At first the machine is experimentally controlled with vector control method to operate in the speed range of 1,500 to 3,000 rpm at rated torque. The PWM switching frequency is set at 1.5 KHz. After that, the voltages are measured and a power analyzer is used to measure the significant time-harmonic components of the PWM voltage, as shown in Fig. 5.11. The harmonic order in the PWM waveform, Fig. 5.11b yields the following equation [160]:

$$h = j\left(\frac{f_{sw}}{f_1}\right) \pm k \tag{5.25}$$

where f_{sw} is the switching frequency

f_1 is the fundamental frequency

j and k are integer (1, 2, 3,…);

In (5.25), for odd values of j the harmonics exists only for even values of k; And for even values of j the harmonics exists only for even values of k. In case of $\frac{f_{sw}}{f_1}$=15, the orders of the main harmonics are: 15 ± 2, 15 ± 4, 30 ± 1, 30 ± 3, 30 ± 5 … The obtained harmonics agree well with equation (5.25). The largest harmonics in this case are 29th and 31st respectively.

The obtained harmonics are then put into analysis by the 3D-FEM software. By this method, effect of both space and time harmonics on machine losses can be acquired.

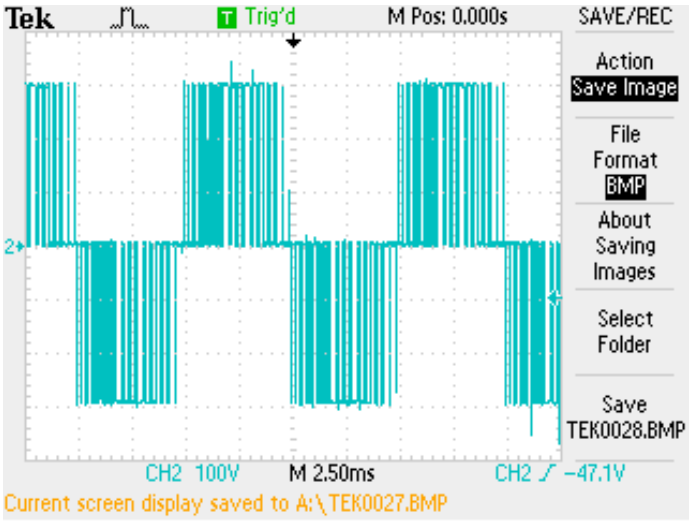

(a)

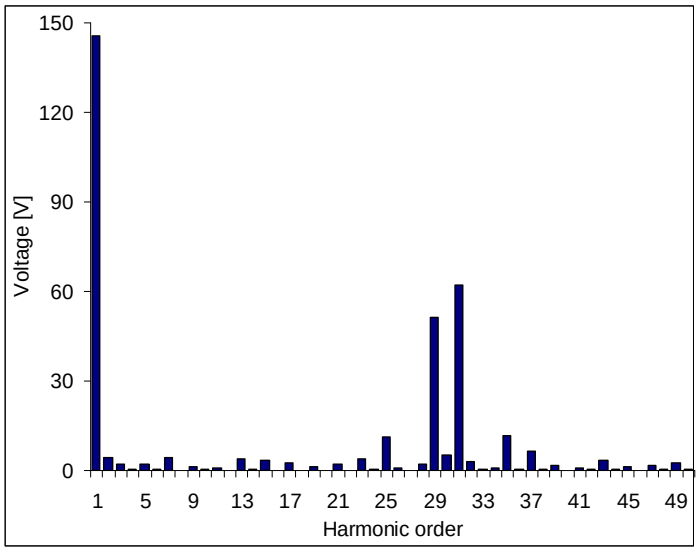

(b)

Fig. 5.11 (a) Measured voltage, (b) harmonic components

B. Loss Analysis

In order to study the effect of space harmonics on machine losses, the model is studied by only activating the PM magnets while setting the input voltages to zero. Core losses and PM losses caused by space harmonics are studied at various skew angles (0, 18.70, 30 deg). The obtained results are shown in Fig. 5.12. It is found that space harmonics give much greater loss contribution in the core than in the magnet and that magnetic skew can reduce core losses about 6% to 17% compared with non-skewed magnet case. It is also seen that when operating frequency increase both magnet losses and core losses increase significantly, as shown in Fig. 5.13.

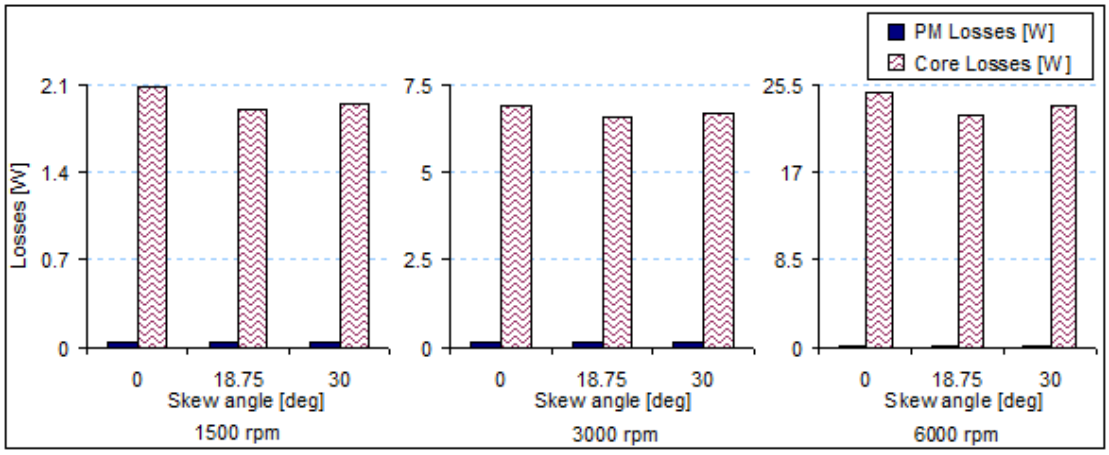

Fig. 5.12 Core and PM Losses caused by space harmonics vs skew angle at various speeds

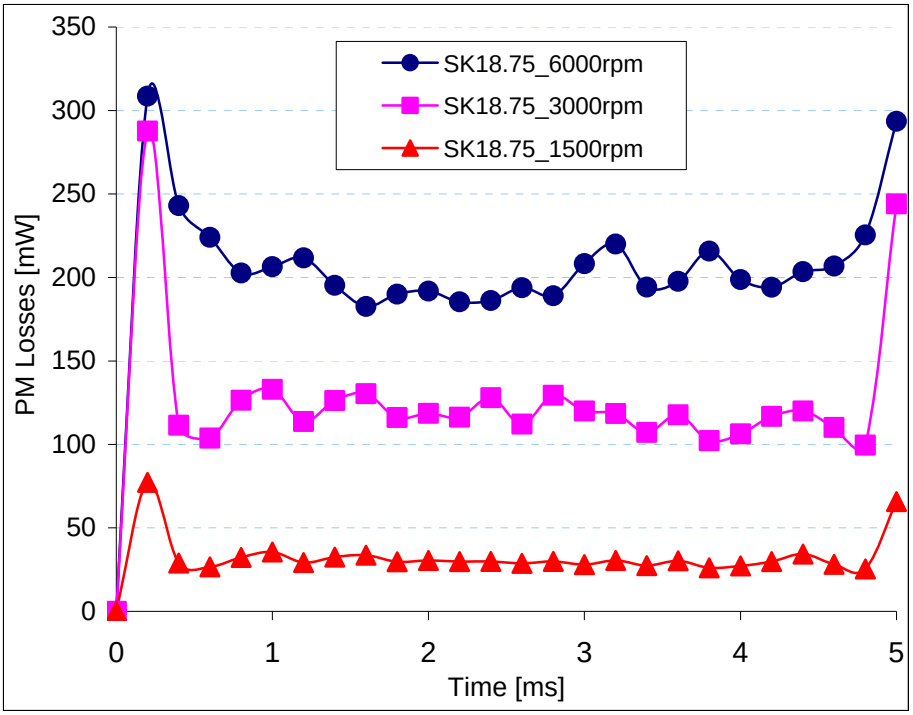

(a)

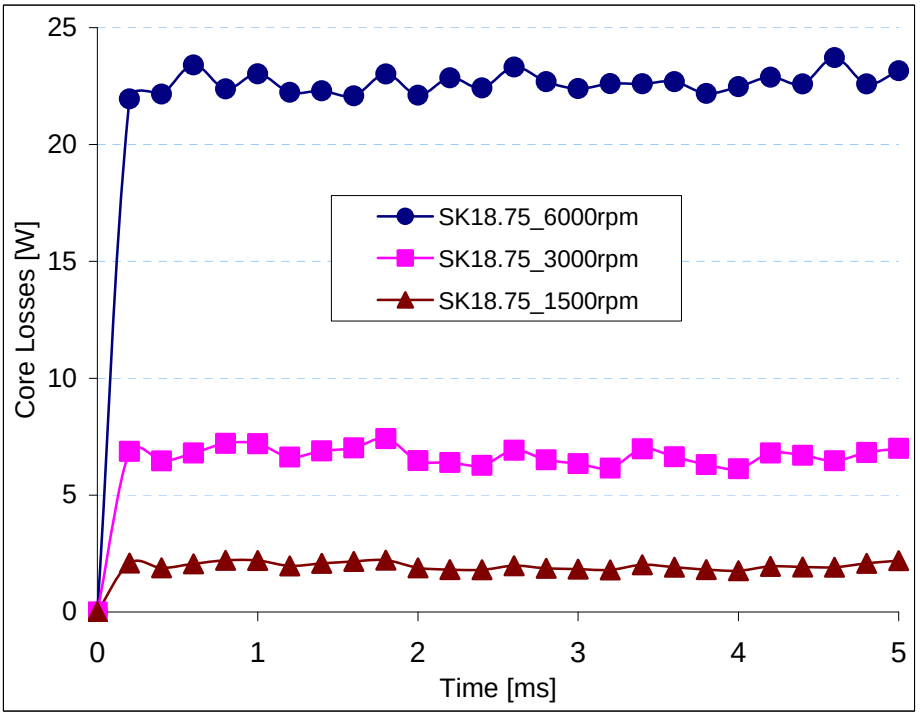

(b)

Fig. 5.13 (a) PM losses caused by space harmonics, (b) Core losses caused by space harmonics

Core and magnet losses caused by both space and time harmonics over skew angle at

various speeds are shown in Fig. 5.14. The plot reveals that the magnet losses are mainly caused by time-harmonics and contribute a considerable part to the machine losses and the iron-core losses increase with frequency which yields to conventional equation (3.103).

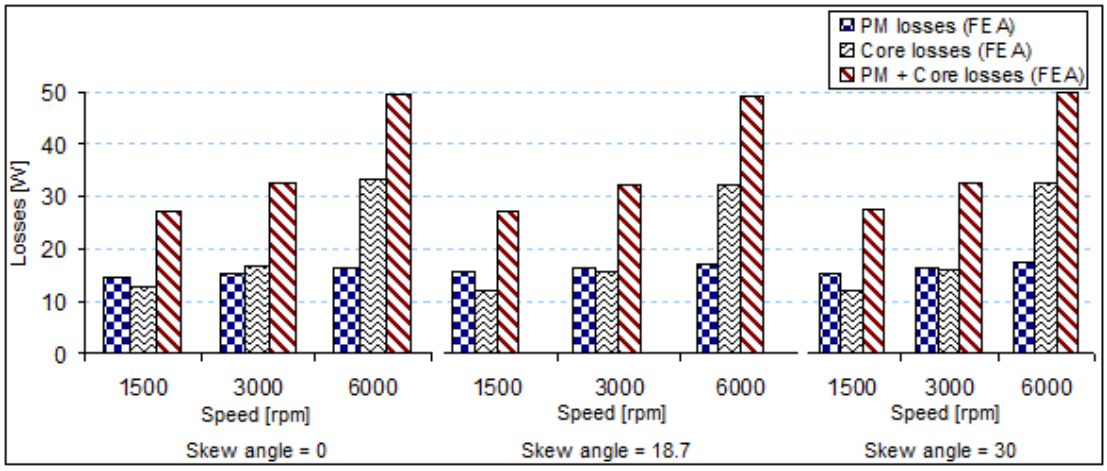

Fig. 5.14 Core and PM Losses caused by both space and time harmonics vs skew angle at various speeds

Distributions of eddy-current caused by both space and time harmonics in the non-skewed and skewed-magnet are shown in Fig. 5.15 (a, b) respectively. It is seen that eddy-currents in the magnets tend to distribute at the magnet side due to the skin effect. Eddy-current circulates in the path along the magnet side. As the eddy-current path is proportional to magnet resistance, eddy-current losses in the magnets can be reduced by increasing its circulating path length. The method to lessen these eddy-current losses in the magnets is presented in the following section.

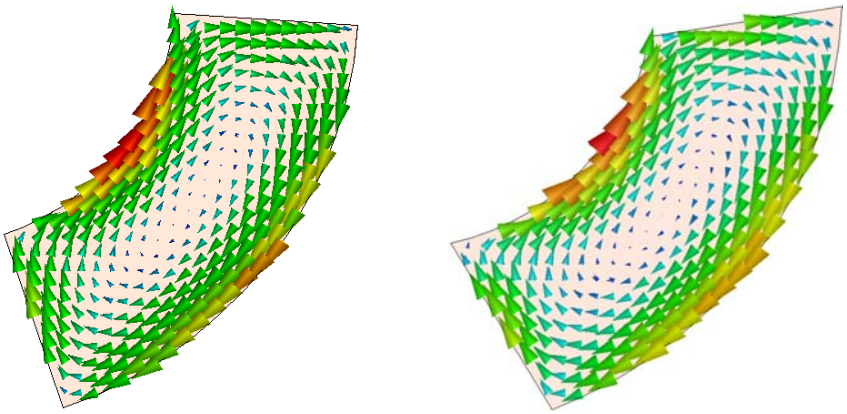

(a) (b)

Fig. 5.15 Eddy current distribution in (a) Non-skewed and (b) skewed-magnet

C. Magnet loss reduction by segmentations

It is seen from the analysis above, the magnet losses of this machine are mainly caused by time-harmonics. Eddy-currents flow in the magnets and they have tendency to distribute at the magnet side because of the skin effect. In order to reduce the eddy-current losses in the magnets, the magnets can be divided into small segments in both circumferential and radial directions. Fig. 5.16 shows the skewed magnet which is segmented in both circumferential and radial direction.

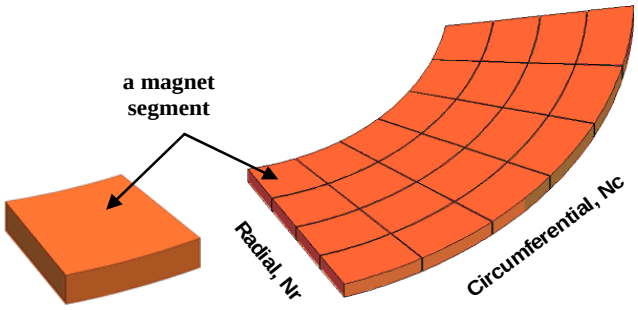

Fig. 5.16 Magnet segmentations in radial and circumferential direction

The magnet losses versus number of segments are obtained from the FEA and shown in Fig. 5.17. It is seen that both circumferential and radial segmentation give effective magnet loss reductions. The distributions of the eddy-current in the 1, 6 and 36 segment-magnet are shown in Fig. 5.18. The eddy-current density reduces

significantly with the increase of both radial and circumferential segmentation numbers; and the radial segmentation is more effective than circumferential segmentation.

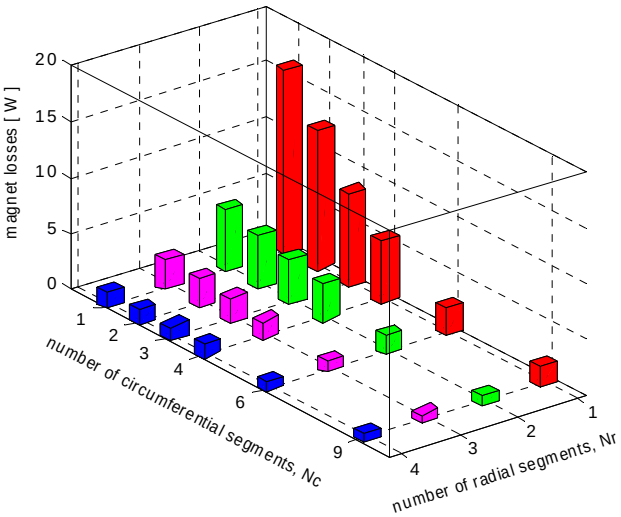

Fig. 5.17 Magnet losses versus number of segments

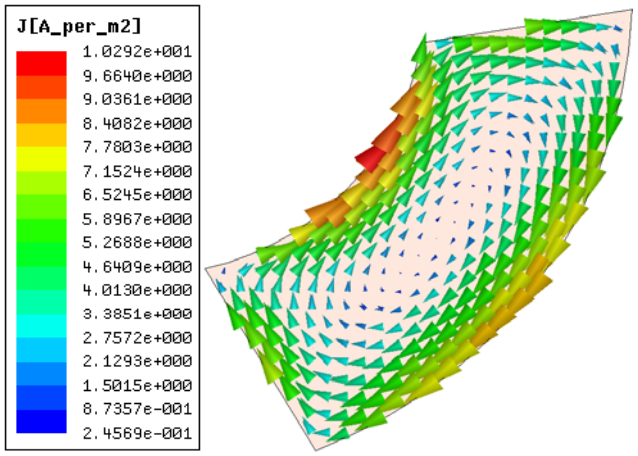

(a)

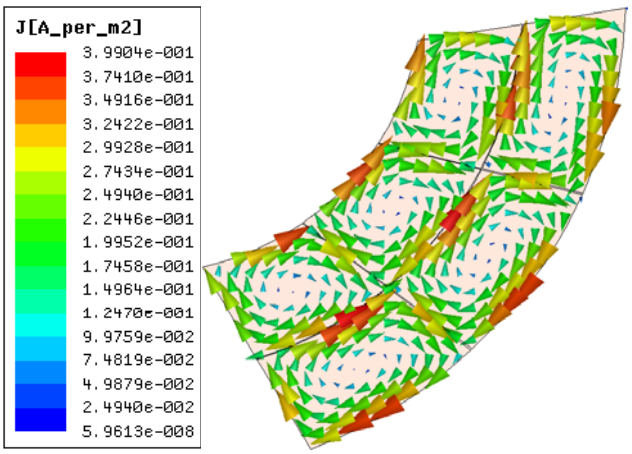

(b)

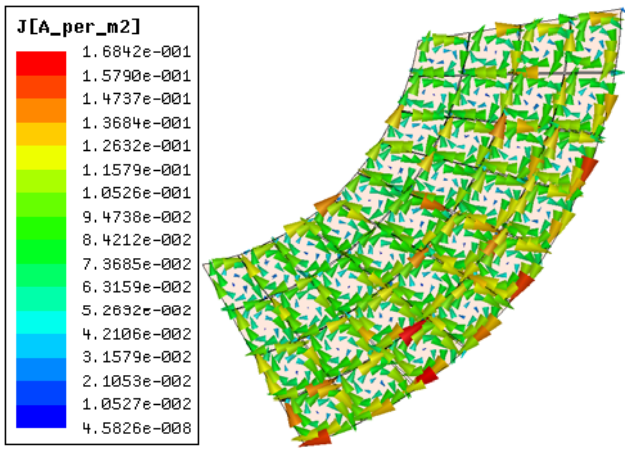

(c)

Fig. 5.18 Eddy-current distribution in the permanent magnets of: (a) 1 monolithic segment (N_r x N_C= *1* x *1*), (b) 6 segments (N_r x N_C= *2* x *3*), (c) 36 segments (N_r x N_C= *4* x *9*).

5.3.3 FEA of the dual air-gap AFPM machine with *q* = *1.5* slots/pole/phase

5.3.3.1. Flux density

The AFPM machine with $q = 1.5$ slots/pole/phase described in Chapter 3 has been analysed by the 3D FEM. The flux directions and flux density of the full machine are shown in Fig. 5.19. Fig. 5.20(a) shows the air-gap flux density of the machine at no load condition. It can be seen from the plot that the maximum air-gap flux density is about 0.65 *T*. Based on the principle of the operation of the proposed machine, the

magnetization directions of the magnets are set and the directions of the air-gap flux density are illustrated in Fig. 5.20 (b).

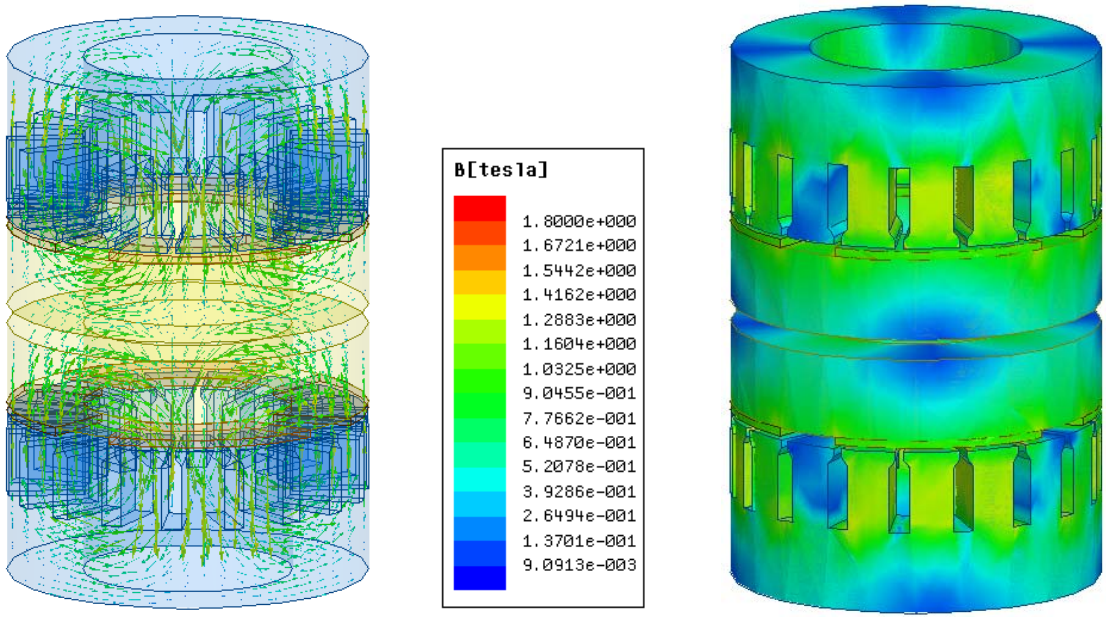

(a) (b)

Fig. 5.19 (a) The flux directions, (b) flux density of the full machine (*q = 1.5* slots/pole/phase)

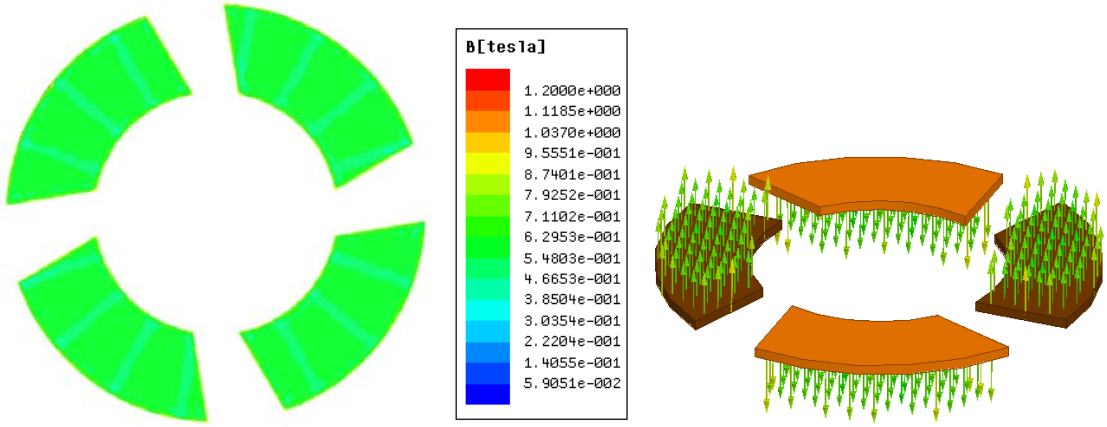

(a) (b)

Fig. 5.20 (a) Air-gap flux density, (b) magnetization direction of the magnets

5.3.3.2. Torques and forces

The analysis of the machine with $q = 1.5$ slots/pole/phase has been performed for two types of rotor structures: non-skewed and skewed PM rotor. The resultant plots are given in Fig. 5. 21. It can be seen from the plot that the peak-to-peak cogging torque of the machine with non-skewed PM rotor is roughly 0.44 pu. When the rotor magnets are skewed by 20 degrees, the optimum skew angle, the cogging torque is reduced to 0.074 pu. Skewing the rotor magnets can lessen the cogging torque by about 83% in this case.

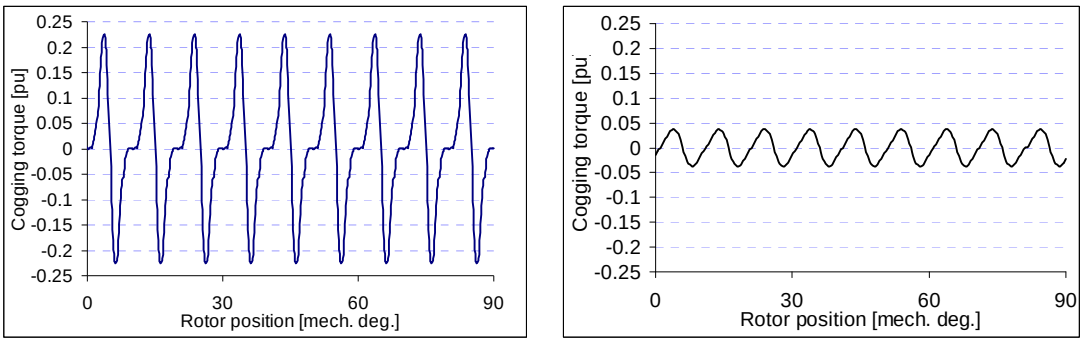

(a) (b)

Fig. 5.21 Cogging torque of the machine with (a) non-skewed, (b) skewed PM rotor

Using the same method described in previous section, the pulsating torques of the machine with non-skewed and skewed PM rotor have been analysed. Fig. 5.22. shows the ripple torque of the two rotor structures. The ripple torque is 0.334 pu peak-to-peak for the non-skewed rotor magnet and it is 0.072 peak-to-peak for the skewed magnet rotor case. The ripple torque has been reduced by roughly 78% by skewing the permanent magnets.

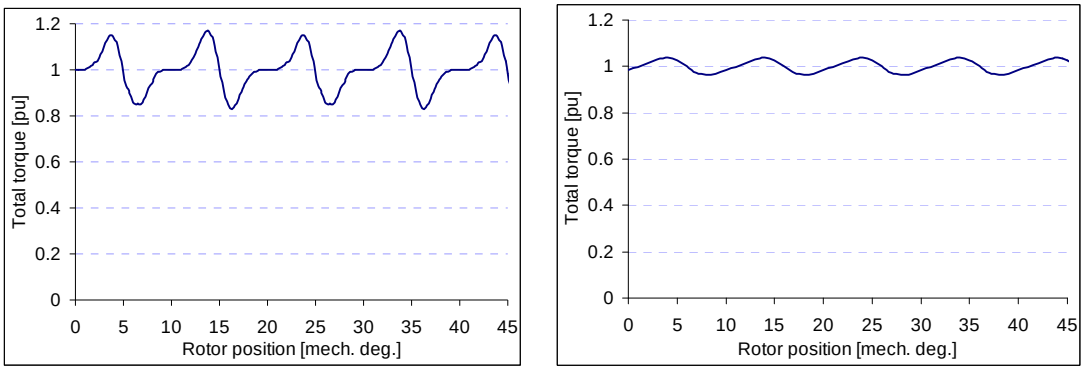

(a) (b)

Fig. 5.22 Total torque of the machine with (a) non-skewed, (b) skewed PM rotor

The static axial forces of the machine with the two rotor configurations have been obtained as shown in Fig. 5.23. The rotor PM skew gives a slight reduction by roughly 5% in the peak-to-peak magnitude of net static axial forces.

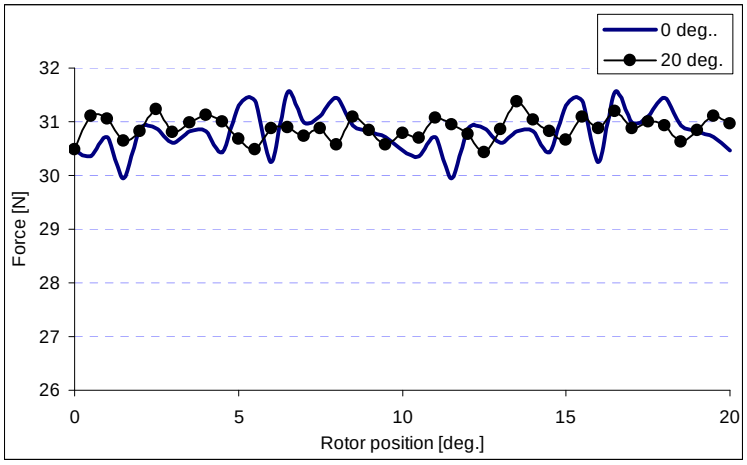

Fig. 5.23 Net static axial forces of the machine with non-skewed and skewed PM rotor

5.3.3.3. Losses

Loss analysis has also been done with this machine with non-skewed and skewed PM rotor. The core losses and PM losses caused by both space and time harmonics versus the change of skew angles (0, 20, 30 degrees) are shown in Fig. 5.24. It is seen that the magnet losses are comparable with the iron-core losses in this machine; and the machine loss is found to be minimal at the optimum skew angle of 20 degrees.

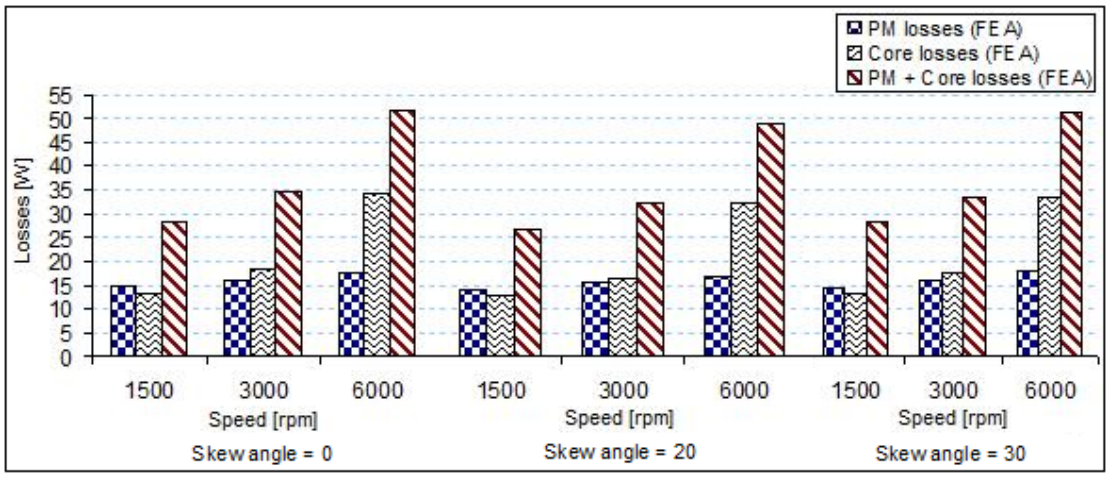

Fig. 5.24 Core and PM Losses caused by both space and time harmonics vs skew angle at various speeds

5.4 Time-stepping Finite Element Analysis

The machines with $q = 2$ slots/pole/phase are further studied with time-stepping FEM for rotating torque and dynamic axial force performance. The two rotor configurations with non-skewed and with 18.7-degree-skewed magnets are analysed. The performance of the machines is obtained by applying i_d, i_q to stator windings respectively.

The three phase currents can be decoupled into *d*- and *q*-axis components as follows [151]:

$$\begin{aligned} i_a &= i_d \cos(\theta) - i_q \sin(\theta) \\ i_b &= i_d \cos(\theta - 120^0) - i_q \sin(\theta - 120^0) \\ i_c &= i_d \cos(\theta - 240^0) - i_q \sin(\theta - 240^0) \end{aligned} \tag{5.26}$$

By assigning $i_d = 0$ and varying i_q, torque versus i_q profile is obtained as shown in Fig. 5. 25. Force versus i_d is obtained by keeping $i_q = 0$ and varying i_d, as shown in Fig. 5.26. It is seen that the electromagnetic torque and the axial force are minimally affected by any magnetic skew. This is because the currents assigned to the machine are actively controlled. It can also be seen that the force and torque are relatively

linear with i_d and i_q respectively. This agrees well with the linearized equations of torque and force (4.45) and (4.50) in Chapter 4.

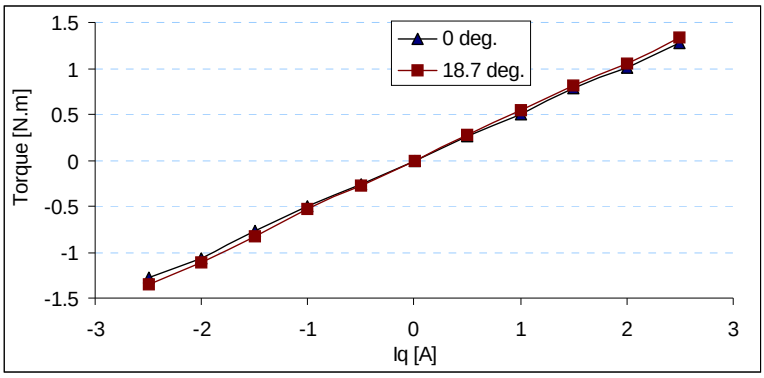

Fig. 5.25 Torque vs i_q

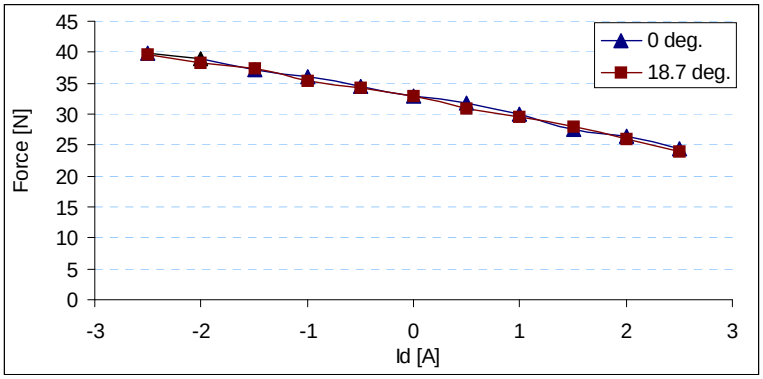

Fig. 5.26 Force vs i_d

5.5 Conclusions

This chapter has presented the finite element analysis of the dual air-gap axial flux permanent magnets machines with $q = 2$ and $q = 1.5$ slots/pole/phase respectively. Due to the special geometry of the machines, the 3D FEA using Ansoft Maxwell [161] has been employed for the design and analysis, including their electromagnetic torques, axial forces and losses of the machines. Effects of rotor PM skew angle on the torque and the axial force have been studied. It is found that an optimum skew angle is effective in reducing the overall cogging torque with negligible effect on the static axial force. The latter is crucial and it is exploited to minimize axial bearing

stress in the FESS application described in Chapter 3. The performance of the machine has also been studied and verified with experimental tests on the machine prototype in Chapter 7.

CHAPTER 6 DEVELOPMENT OF CONTROL SYSTEM FOR PROPOSED AFPM MACHINE

6.1 Introduction

As presented in Chapter 3, the proposed AFPM machine can be energized by a single power converter which supplies space-vector pulse width modulation voltage. The power converter hence needs to be controlled to feed the currents to the machine. And as described in the same chapter, the proposed machine supplies both the rotation and the levitation for the flywheel assembly. So the flywheel needs to be actively controlled for its rotation and levitation simultaneously. Therefore the control system design plays an important role in operating this AFPM machine. The control system for the proposed machine is designed in this chapter based on linearized equations presented in Chapter 4. First the control strategy for this AFPM machine is discussed. After that, the current and speed regulators of the drive are dealt with. Next, the position sensorless control for this machine is demonstrated. Simulations to study the feasibility of the proposed machine are presented finally.

6.2 Control Strategy

The entire model of the machine as shown in Chapter 4 is the nonlinear model especially, the torque and force equations. The characteristics of the two machine halves are respectively expounded in the voltage equations in (4.54) and (4.58). To facilitate the control of this AFPM machine, the linearized equations have been derived. Based on this, the two-loop control scheme shown in Fig. 6.1 is implemented to control the machine. The outer loop is the axial position and angular speed control based on equations (4.48) and (4.52). In this loop, the command currents $\tilde{i}_{cd}^{*}$ and i_q^* are generated by the axial position and angular speed controller where criteria to

minimize the errors of $\omega_r^* - \omega_r$ and $z^* - z$ are performed. The inner loop is for the current control where the currents i_d and i_q are regulated to track their commands i_d^* and i_q^*. The current control in rotor-reference frame as shown in Fig. 6.2 can be employed to make the currents track their commands. The advantage of this regulation scheme is that it performs on DC quantities and therefore can achieve zero steady state error for the regulated currents. It is well suitable with this machine drive where sinusoidal currents and voltages are required. These control approaches are well-known and popularly used in electrical machine drive [162-167], therefore will not be further presented here.

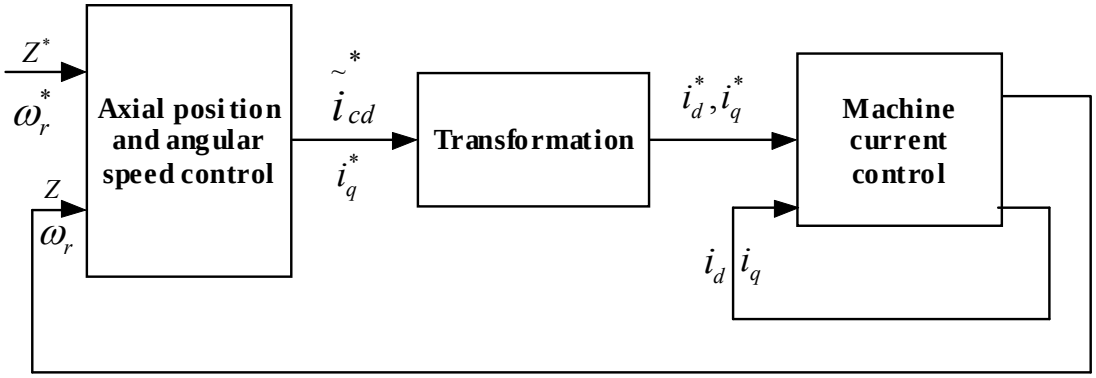

Fig. 6.1 Two-loop control scheme for the AFPM machine

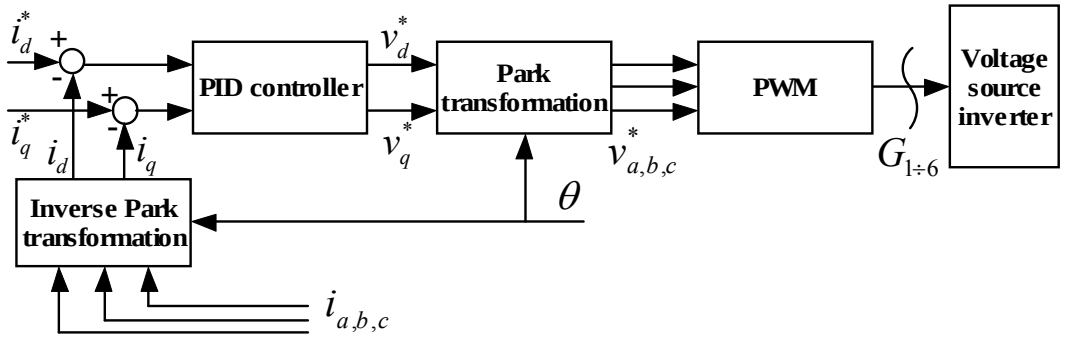

Fig. 6.2 Current regulation scheme for the AFPM machine

6.3 Control of the dual air-gap AFPM machine

PID control method has the advantages of simple algorithm, stable properties and facilitation in implementation. Therefore the control schemes based on PID method are designed for this AFPM machine.

6.3.1 Axial position displacement control

Using the Laplace transformation, equation (4.46) can be transformed into:

$$ms^2 z(s) = K_2 z(s) + K_3 i_{cd}(s) + \frac{K_1 - G}{s} \tag{6.1}$$

$$z(s) = \frac{K_3}{ms^2 - K_2} i_{cd}(s) + \frac{K_1 - G}{ms^3 - K_2 s} \tag{6.2}$$

It is seen that K_2 is positive, thus the system is unstable. A proportional integral derivative controller (PID) can be used to stabilize the displacement. The transfer function of a PID controller can be written as:

$$G_c(s) = K_p + \frac{K_i}{s} + K_d s \tag{6.3}$$

where K_p, K_i and K_d are the proportional, integral and differential coefficients, respectively.

The control structure is drawn as illustrated in Fig. 6.3. The characteristic polynomial of the system can be written as:

$$\begin{aligned} & ms^3 + K_3 K_d s^2 + (K_3 K_p - K_2)s + K_3 K_i = 0 \\ \Leftrightarrow\ & s^3 + \frac{K_3 K_d}{m} s^2 + \frac{(K_3 K_p - K_2)}{m} s + \frac{K_3 K_i}{m} = 0 \end{aligned} \tag{6.4}$$

From Routh criteria, when $K_3 K_d > 0$, $K_3 K_i > 0$ and $K_3 K_p > K_2 + \frac{m K_i}{K_d}$, the system is stable.

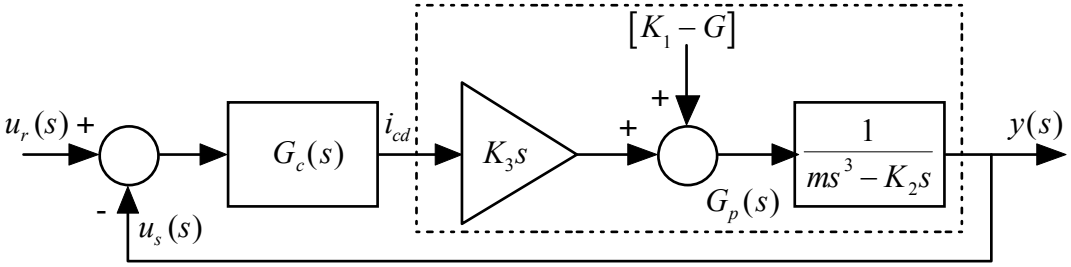

Fig. 6.3 Diagram of axial displacement control using PID controller

A suitable closed-loop characteristic equation for a third-order system is:

$$(s+a)(s^2+2\xi\omega_n s+\omega_n^2)=0 \tag{6.5}$$

where ξ is damping coefficient and ω_n is natural frequency.

By identifying the characteristic polynomial with (6.5), K_p, K_i and K_d are obtained.

6.3.2 Rotational speed control

By using the Laplace transformation and ignoring the friction and external disturbance torque in (4.52), the rotational speed equation can be written as:

$$\theta(s)=\frac{1}{s}\omega(s) \tag{6.6}$$

$$\omega(s)=\frac{K_T}{J.s}i_q(s) \tag{6.7}$$

So the angle velocity can be controlled by a PI controller.

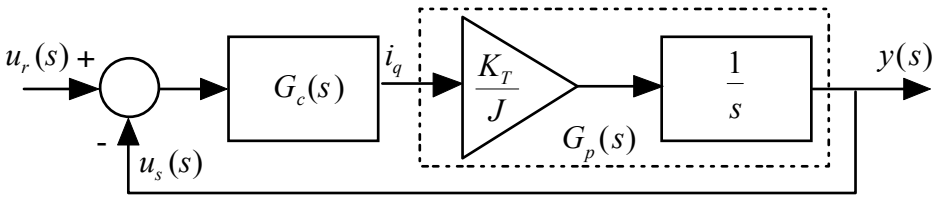

Fig. 6.4 Diagram of speed control using PI controller

As shown in Fig. 6.4, a PI controller is used to control the velocity of the machine, and the feedback control is employed in the velocity control system. The controller is expressed as

$$G_c(s) = K_{p1} + \frac{K_{i1}}{s} \tag{6.8}$$

The transfer function of the close-loop system is

$$\frac{Y(s)}{U(s)} = \frac{K_T K_{p1} s + K_T K_{i1}}{Js^2 + K_T K_{p1} s + K_T K_{i1}} \tag{6.9}$$

Because J, K_T, K_{p1}, K_{i1} are all positive, the system will be stable with the PI controller.

6.3.3 Control scheme for the dual air-gap AFPM machine

It has been derived as shown in (4.45) and (4.50) that axial force and electromagnetic torque of this AFPM machine can be controlled directly by i_d (or i_{cd}) and i_q respectively. Referring to (4.48) and (4.52), it is seen that the position displacement along the z axis and the rotational speed of the rotor can be controlled by the i_d and i_q respectively. Therefore the control system for this AFPM machine is obtained as shown in Fig. 6.5. The rotational angle θ and the angular speed ω are sensed by the rotary encoder, while the axial displacement from the equilibrium point along z-axis direction is detected by the non-contact eddy-current displacement sensor. The speed ω is then compared with its command ω^*. The speed error between ω^* and ω is amplified by the PI controller to generate the current reference i_q^*. In a similar manner, the error $z^* - z$ is regulated by the PID controller to obtain the current command $\tilde{i}_{cd}^*$. The *d*-axis current command can then be obtained using (4.38) and (4.49). Space vector modulation technique [168] is applied to control a voltage source

inverter to supply three-phase pulse width modulation voltages as calculated by the controllers to feed the machine.

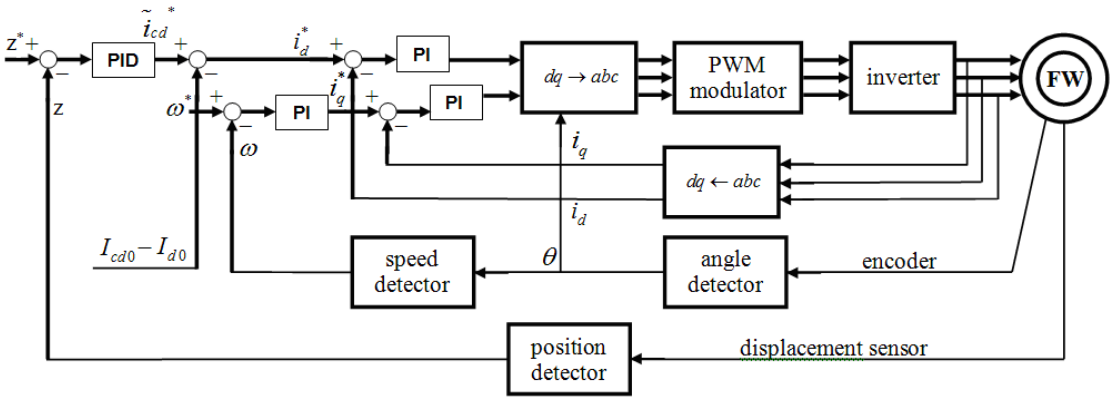

Fig. 6.5 Control system block diagram

6.3.4 Simulation results

6.3.4.1. At rated current

The simulation is performed to test the feasibility of the control scheme designed for this AFPM machine. The parameters of the machine are shown in Table 6.1. The flywheel-rotor is simulated to accelerate and decelerate which corresponds with the energy charging and discharging respectively. Stator currents are maintained at the rated values during the transient period of charging and discharging period.

Table 6.1 Parameters of the machine

Number of stator windings, N_s	208 turns
Moment of inertia, J	49 kg.cm^2
Phase resistance, R	4.67 Ω
d and q inductance, $L_d \approx L_q$	26.8 mH
Mass of flywheel-rotor, M	3.15 kg
Equivalent upper air-gap, g_{10}	2.877 mm
Equivalent lower air-gap, g_{20}	2.763 mm
Number of pole pair, P	2

The simulation results are shown in Fig. 6.6. Fig. 6.6(a) shows the speed of the flywheel-rotor, which is controlled to speed up linearly to 3,000 *rpm* (314.2 *rad/s*) since starting. The speed is constant after reaching the reference speed. This is the period of energy charging and storage. When the reference speed is changed to 1,000 *rpm* (104.7 *rad/s*), the speed slows down linearly to this reference value. This shows the discharge period of the flywheel. It indicates that the charge and discharge process of the flywheel can be successfully realized. The energy profile corresponding with the mentioned periods is shown in Fig. 6.6(b).

The energy stored in the flywheel when it is operating at 314.2 *rad/s* is:

$$E = \frac{1}{2} J \omega_r^2 = 241.87 \, Joules \tag{6.10}$$

The discharge energy when the speed decreases to 104.7 *rad/s* is:

$$\Delta E = \frac{1}{2} J (\omega_{r1}^2 - \omega_{r2}^2) = 215.01 \;\; Joules \tag{6.11}$$

The upper speed of the AFPM machine is limited at a half of its rated speed, at 3,000rpm, for the convenience in comparison with the experiments later on. For this low-speed prototype, the stored energy as mentioned above is relatively low. However, this does not affect on the feasibility study of the proposed AFPM machine design for FESS applications and the validity of the derived mathematic model.

Axial variation of the rotor is shown in Fig. 6.6(c). The position of the rotor is stabilized at the equilibrium point with the fluctuation range of 10^{-6} m, which is within the range of the air-gap length of $9x10^{-4}$ m. Fig. 6.6(d) and (e) are the simulation diagrams of levitation force and electromagnetic torque respectively. The force is almost equal to that due to the gravity. When the speed remains constant at 3,000 rpm and 1,000 rpm, the torque is almost zero as this is the steady state of machine. The two modes of the machine, motoring and generating, are reflected by the torque diagram. The torque is positive in the motoring mode when the machine is accelerated; and when the machine is decelerated, the value of torque becomes negative. So the proposed AFPM machine is capable of responding according to the request of the controller.

The diagrams of the *d-q* currents are shown in Fig. 6.6 (f). It is seen that the displacement and speed of the rotor of the above-mentioned periods are well controlled by i_d and i_q respectively. This is in accordance to the analysis of the mathematical model.

The three-phase currents in stator windings during the charging to standby period of are shown in Fig. 6.6 (g). Rated current is maintained in this period to speed up the rotor to its reference speed. This current becomes small when rotor goes into the steady state at 3,000 rpm. A sudden change in currents is seen when the machine is changed from the standby mode to the discharging mode. They are zoomed in as shown in Fig. 6.6 (h).

From the simulations, it is seen that the proposed machine can be well-controlled. The

three important modes of FESS applications, charging, standby and discharging, can be well handled by the proposed AFPM machine. This confirms the obtained mathematical model of this machine in Chapter 4. It is therefore feasible to develop a compact flywheel energy storage system based on the proposed AFPM machine.

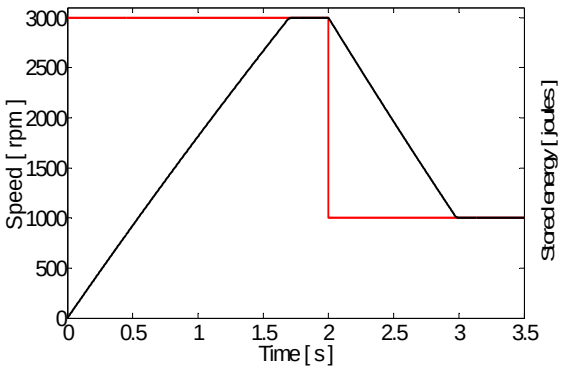

(a) Speed

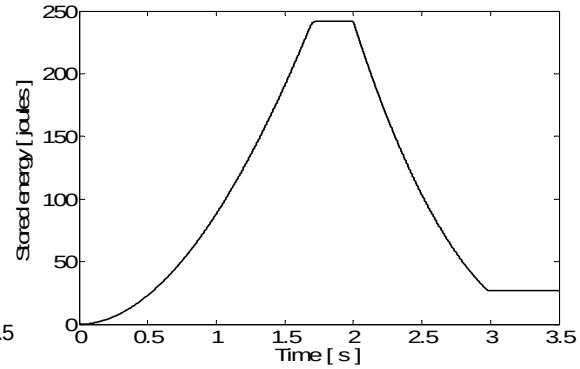

(b) Stored energy

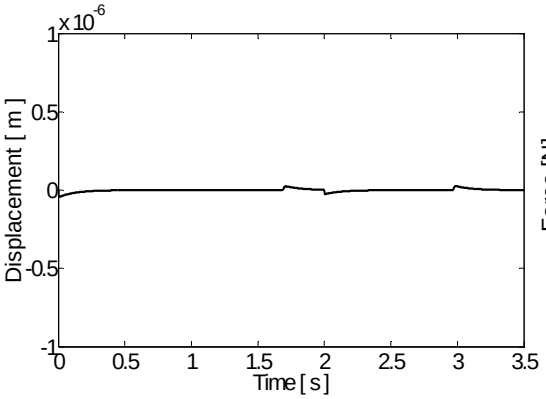

(c) Axial displacement

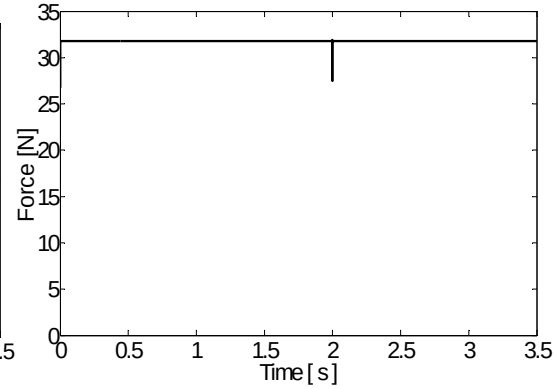

(d) Axial force

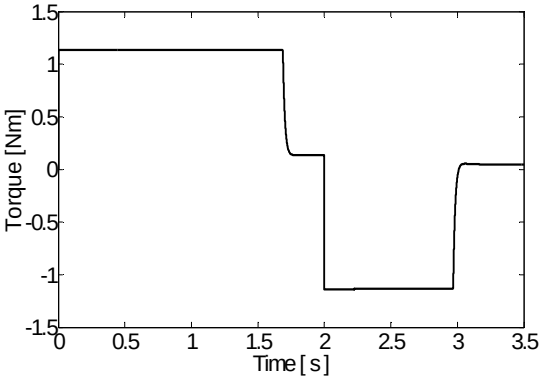

(e) Electromagnetic torque

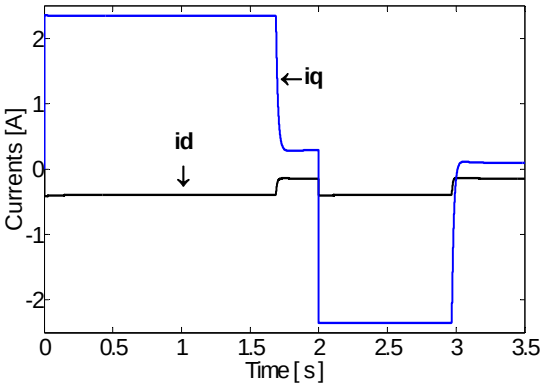

(f) i_d and i_q

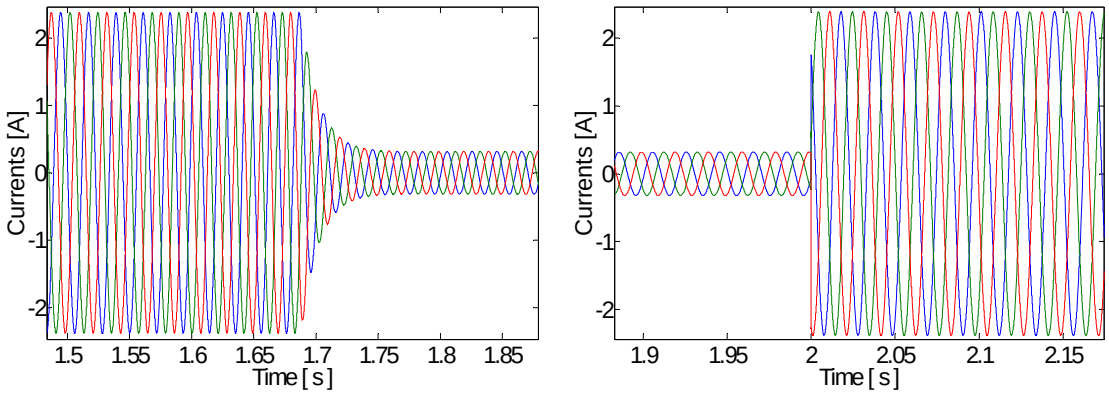

(g) Currents in charging mode (h) Currents in discharging mode

Fig. 6.6 Simulation results of the machine operating at rated currents

6.3.4.2. Fast charge and fast discharge of energy at over-rated current

Fast acceleration and fast deceleration of the machine correspond with the fast charge and fast discharge of the FESS. In order to study this fast-response characteristic of the machine, the stator winding currents can be controlled at the over-rated values. In the following simulation, the stator winding currents are maintained at about 2 times of rated value in the transient periods of the machine.

Fig. 6.7 shows the simulation results of the above-mentioned case. The simulation results are quite similar to those obtained at rated stator winding currents. However, the main differences are in the currents as shown in Fig. 6.7 (e-h). During the transient period of the machine, the stator winding currents are maintained at 5 amps. The over-rated current gives a double torque value which enables the fast charge and fast discharge of the energy. In short periods of time, the applied-currents can be maintained at higher values than the ratings because the temperature rise in the machine, especially in the stator windings, is slower than the change in currents. Therefore during transient periods, the machine can operate at a higher power than its rating. The simulation has shown another specific feature of the proposed machine. It is valuable to exploit this characteristic in the FESS applications.

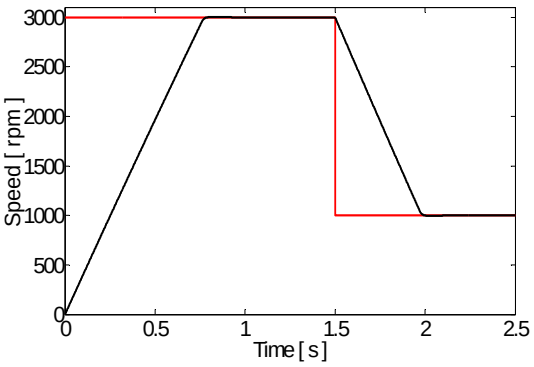

(a) Speed

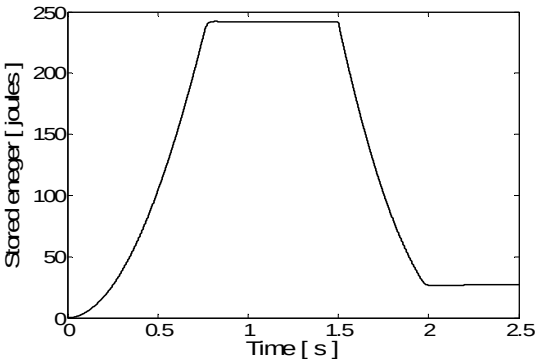

(b) Stored energy

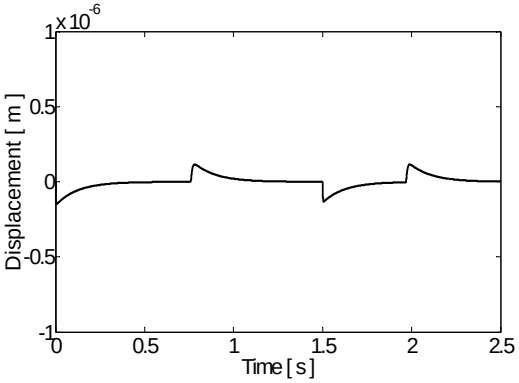

(c) Axial displacement

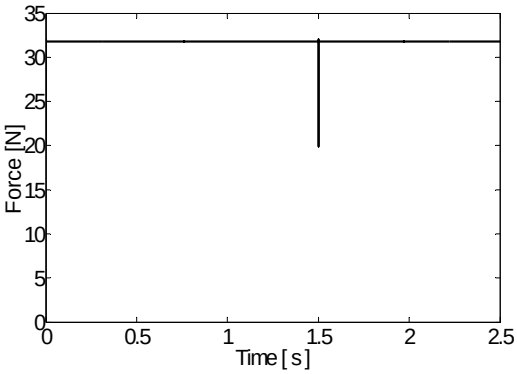

(d) Axial force

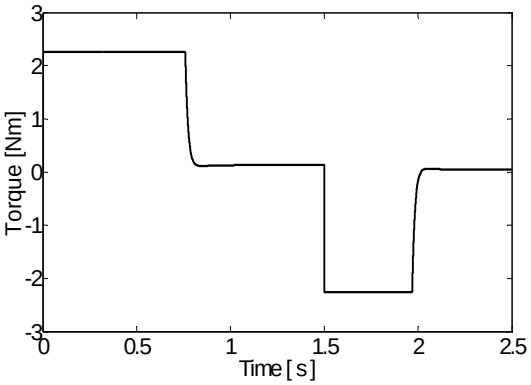

(e) Electromagnetic torque

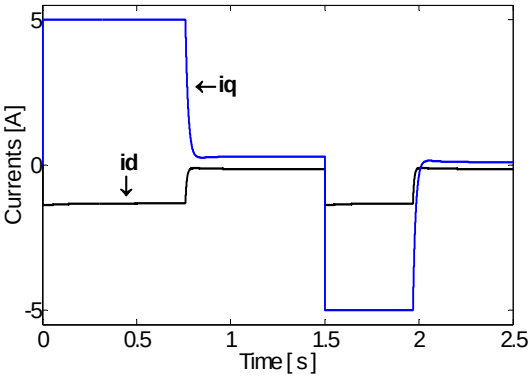

(f) i_d and i_q

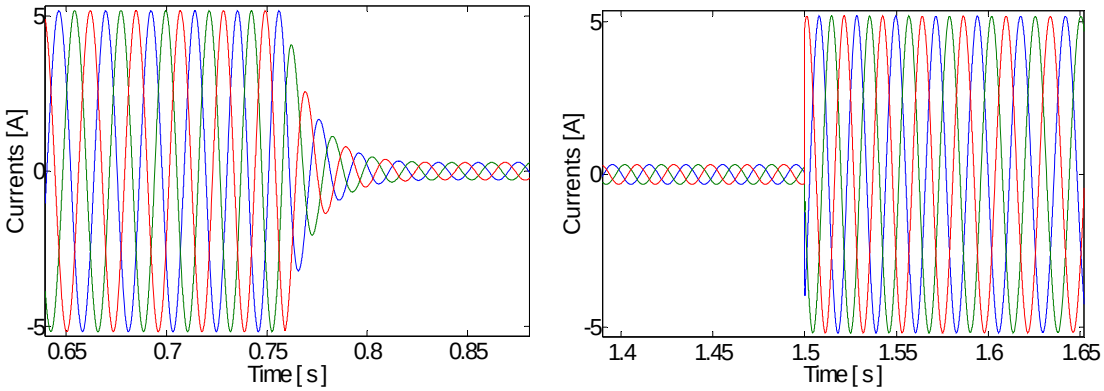

(g) Currents in charging mode (h) Currents in discharging mode

Fig. 6.7 Simulation results of the machine operating at over-rated currents

6.4 Position sensorless control of the dual air-gap AFPM machine

Field-oriented or vector control has been used for the electrical machine drives in FESS applications [17, 20, 169]. Definitely the continuous rotor-position information is required in such control scheme. In this case, encoders are often used to detect the rotor position. Therefore the system operation is totally dependent on the rotary encoders. However, the presence of encoder presents several drawbacks in FESS applications, such as growing the system cost, increasing the overall weight, and making the system inactive if the encoders fail. Hence, it is desirable to eliminate this sensor in such systems.

Several sensorless control schemes for electric machine drives have been proposed [170-180]. Position estimation based on high-frequency (HF) signal injection [173-175], uses the saliency property of the PMSM. Solutions at standstill and low speeds can be fulfilled by HF signal injection method, but as the speed increases, its performance severely reduce. Furthermore, accurate measurements of the machine parameters are required. The extended Kalman filter (EKF) method [176, 177] can give recursive optimum state estimation for PMSM using terminal signals that may be polluted by noise. But this sensorless-control scheme requires high computation

involving in vector and matrix operations. Moreover, to avoid instability noise covariance matrices and initial values for the algorithm have to be carefully chosen in this scheme. Literatures [178-180] propose the rotor position estimation basing on induced voltage (back-EMF). These estimators with explicit compensation for nonlinear properties, parameter variation, and disturbance work well in wide speed range.

In this part, the position-sensorless field-oriented control of the proposed AFPM machine for FESS is presented. The approach is based on the estimation of the machine induced voltage with the help of measured stator currents and reference voltages. Based on sliding mode observer, the rotor position can be accurately estimated. High performance of the system based on this position sensorless control algorithm is then demonstrated.

6.4.1 Sliding mode observer and stability analysis

6.4.1.1. Sliding mode observer

In stationary reference frame, the dynamic equations of the AFPM machine can be expressed in the matrix form as:

$$\dot{\vec{i}}_s = A \cdot \vec{i}_s + B \cdot (\vec{v}_s - \vec{e}_s) \tag{6.12}$$

where

$$A = \begin{bmatrix} \frac{-R_s}{L_s} & 0 \\ 0 & \frac{-R_s}{L_s} \end{bmatrix}, \quad B = \begin{bmatrix} \frac{1}{L_s} & 0 \\ 0 & \frac{1}{L_s} \end{bmatrix}$$

$$\vec{i}_s = \begin{bmatrix} i_{\alpha s} \\ i_{\beta s} \end{bmatrix}, \quad \vec{v}_s = \begin{bmatrix} v_{\alpha s} \\ v_{\beta s} \end{bmatrix}, \quad \vec{e}_s = \begin{bmatrix} e_{\alpha s} \\ e_{\beta s} \end{bmatrix} = \omega_r \cdot K_m \cdot \begin{bmatrix} -\sin(\theta_r) \\ \cos(\theta_r) \end{bmatrix}$$

with R_s , L_s and K_m referring to the stator resistance, inductance and back-electromotive force constant, respectively.

The sliding mode observer presented here uses only the electrical equation of the machine. The equation of the sliding mode observer is:

$$\dot{\hat{\vec{i}}}_s = A \cdot \hat{\vec{i}}_s + B \cdot \left[\vec{v}_s - l.sign\left(\bar{i}_s \right) \right] \tag{6.13}$$

where l is a constant observer gain, $\bar{i}_s = \hat{\vec{i}}_s - \vec{i}_s$, $\bar{i}_s = \begin{bmatrix} \bar{i}_{\alpha s} \\ \bar{i}_{\beta s} \end{bmatrix}$, and $\hat{\vec{i}}_s = \begin{bmatrix} \hat{i}_{\alpha s} \\ \hat{i}_{\beta s} \end{bmatrix}$.

From (6.12) and (6.13), the dynamic error equation for estimated currents can be obtained as:

$$\dot{\bar{i}}_s = A \cdot \bar{i}_s + B \cdot \left(\vec{e}_s - l.sign\left(\bar{i}_s \right) \right) \tag{6.14}$$

Choose the sliding surface $S = \begin{bmatrix} s_{\alpha s} \\ s_{\beta s} \end{bmatrix} = \begin{bmatrix} \bar{i}_{\alpha s} \\ \bar{i}_{\beta s} \end{bmatrix}$. When the estimation error trajectories reach the sliding surface, i.e., $S = 0$, obviously, estimated currents will eventually converge to their actual values.

If switching gain l is large enough to guarantee

$$S \cdot \dot{S} < 0 \tag{6.15}$$

The sliding mode exists, the following equation is obtained:

$$\vec{e}_s = \begin{bmatrix} e_{\alpha s} \\ e_{\beta s} \end{bmatrix} = \begin{bmatrix} l \cdot sign(\bar{i}_{\alpha s}) \\ l \cdot sign(\bar{i}_{\beta s}) \end{bmatrix} \tag{6.16}$$

It is clear that the information of estimated back-EMF can be obtained from equivalent control $e_{\alpha s}$, $e_{\beta s}$. Estimated back-EMF is obtained by the low pass filter (LPF) as shown in (6.17)

$$\begin{bmatrix} \hat{e}_{\alpha s} \\ \hat{e}_{\beta s} \end{bmatrix} = \begin{bmatrix} \dfrac{\omega_{cutoff}}{s+\omega_{cutoff}} e_{\alpha s} \\ \dfrac{\omega_{cutoff}}{s+\omega_{cutoff}} e_{\beta s} \end{bmatrix} \tag{6.17}$$

The angular position $\hat{\theta}_r$ and speed $\hat{\omega}_r$ can be estimated as:

$$\hat{\theta}_r = -\tan^{-1}\left(\frac{e_{\alpha s}}{e_{\beta s}}\right) \tag{6.18}$$

$$\hat{\omega}_r = \frac{\sqrt{e_{\alpha s}^2 + e_{\beta s}^2}}{K_m} \tag{6.19}$$

The actual angle can be obtained by adding $\hat{\theta}_r$ with a compensated angle $\Delta\theta$, the overall sliding mode observer diagram is illustrated in Fig. 6.8:

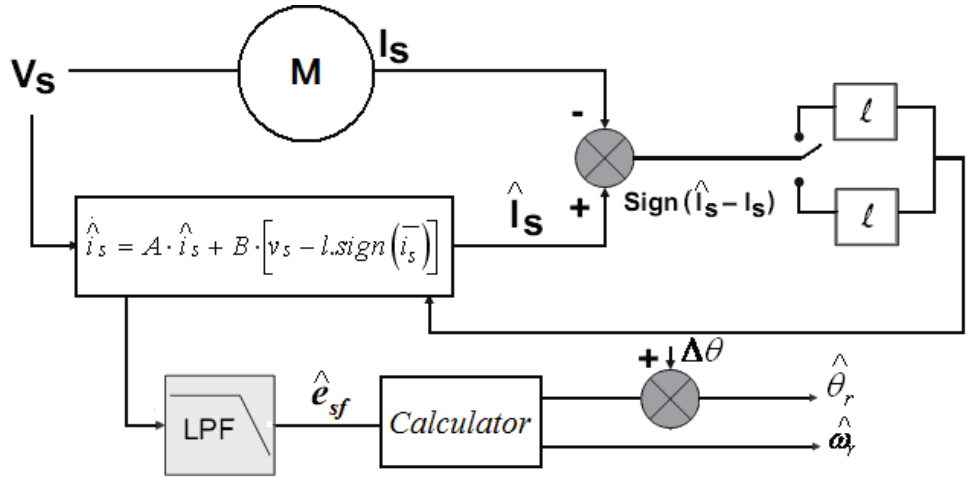

Fig. 6.8 Sliding mode observer

6.4.1.2. Stability analysis

Define a Lyapunov candidate function as follow:

$$V = \frac{1}{2}\left[\bar{i}_s^{T} \cdot \bar{i}_s\right] > 0 \tag{6.20}$$

Differentiating (6.20) with respect to time, $\dot{V}$ is obtained as:

$$\dot{V} = \bar{i}_s^{T} \cdot \bar{i}_s \tag{6.21}$$

To ensure the stability of the observer, $\dot{V}$ as shown in (6.21) is necessary to be negative. From this requirement, the condition to obtain the stability is:

$$\begin{aligned}\dot{V} &= \bar{i}_s^{T} \cdot A \cdot \bar{i}_s + \bar{i}_s^{T} \cdot B \cdot e_s - l \cdot \bar{i}_s^{T} \cdot B \cdot sign\left[\bar{i}_s\right] < 0 \\ &= \bar{i}_s^{T} \cdot A \cdot \bar{i}_s + \bar{i}_s^{T} \cdot B \cdot e_s - \frac{l}{L_s}\left\{\left|\bar{i}_\alpha\right| + \left|\bar{i}_\beta\right|\right\} < 0\end{aligned}$$

$$\Rightarrow l > L_s \frac{\bar{i}_s^{T} \cdot A \cdot \bar{i}_s + \bar{i}_s^{T} \cdot B \cdot e_s}{\left|\bar{i}_\alpha\right| + \left|\bar{i}_\beta\right|} \tag{6.22}$$

6.4.2 Position sensorless control scheme

Based on rotor-flux oriented vector control [181], *d*- and *q*-axis current of the AFPM machine can be decoupled and controlled separately. From (6.1) and (6.7), it can be seen that torque and force can be used to control the machine speed and axial levitation independently. The overall position sensorless control diagram for the proposed machine is shown in Fig. 6.9. Information of the rotor angle is estimated from the stator currents and voltage reference. Similar to the case using a rotary encoder for rotor angle above, the PID controllers are used to control the speed, the axial displacement the *d*- and *q*-axis currents, respectively.

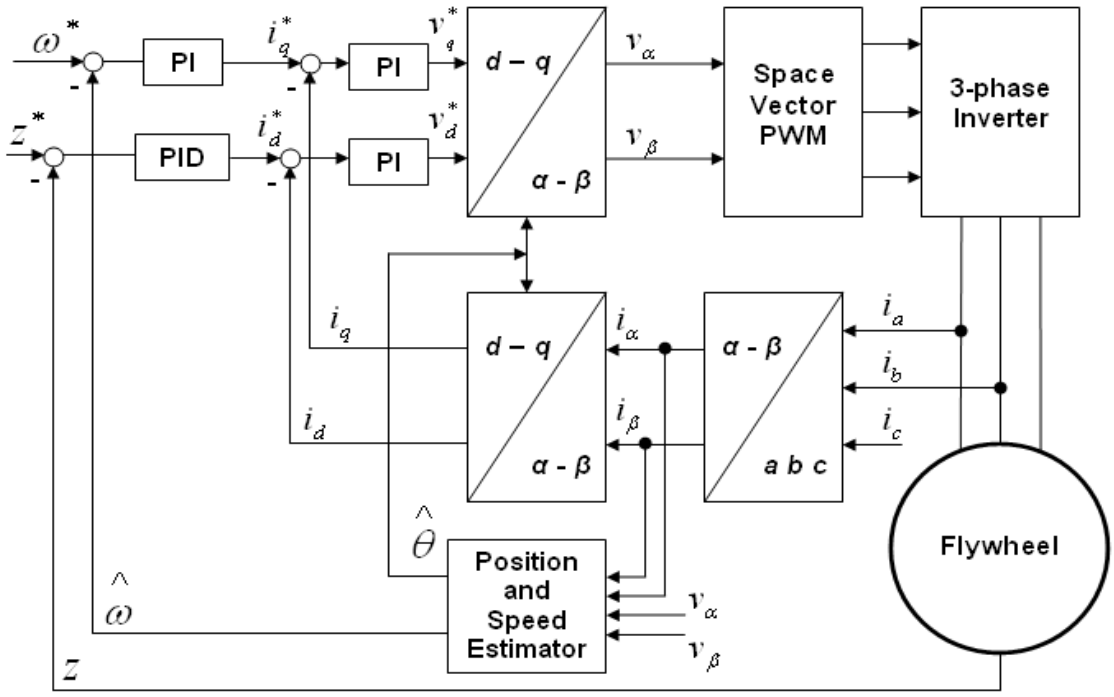

Fig. 6.9 Control system diagram

6.4.3 Simulation results

Fig. 6.10 (a) and (b) shows the simulation results when machine is running at 1,000 rpm and 3,000 rpm respectively. In the two cases, the waveforms of the estimated and real rotor position angle almost overlap together with very small errors.

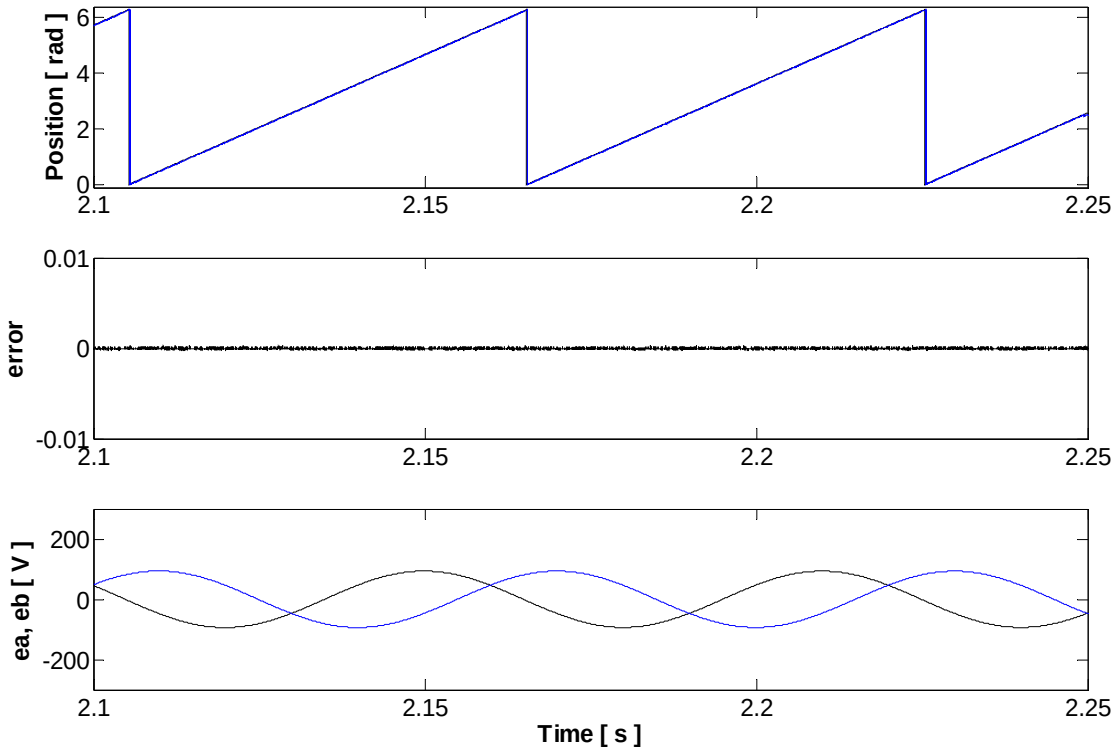

(a) Simulation results at 1,000 rpm

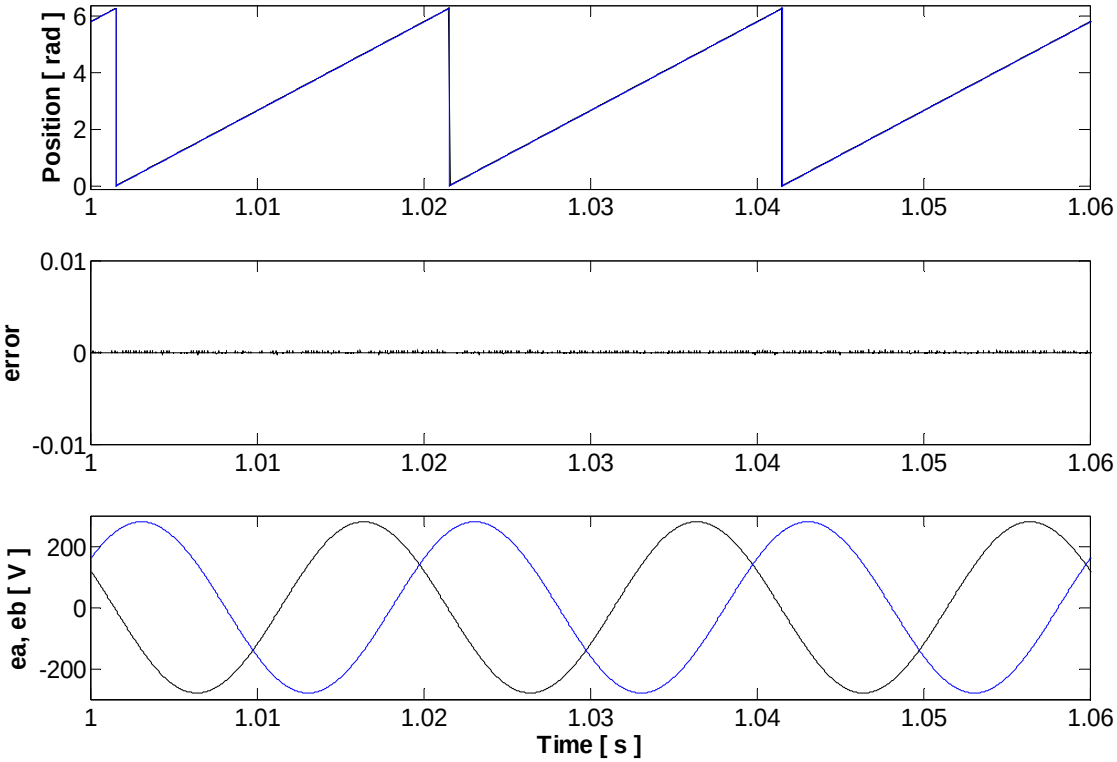

(b) Simulation results at 3,000 rpm

Fig. 6.10 Estimated and actual position (top), position error (second, in *rad*) and phase a& b back-EMF (bottom): (a) at 1,000 rpm, (b) at 3,000 rpm.

In following simulation, the machine is controlled to accelerate for charging and decelerate for discharging the energy respectively. Stator currents are controlled to maintain at the overrated-value in transient period for fast acceleration and fast deceleration of the machine. The simulation results are shown in Fig. 6.11. From the results, it is seen that the charge and discharge of this machine in the FESS can be performed successfully. As the simulation results are quite similar to which of rotary-encoder-based control scheme, detail descriptions of the figures are not repeated.

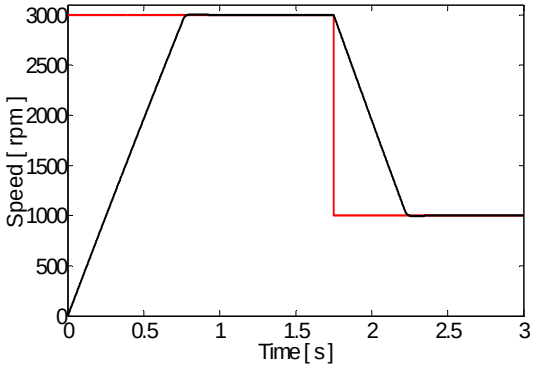

(a) Speed

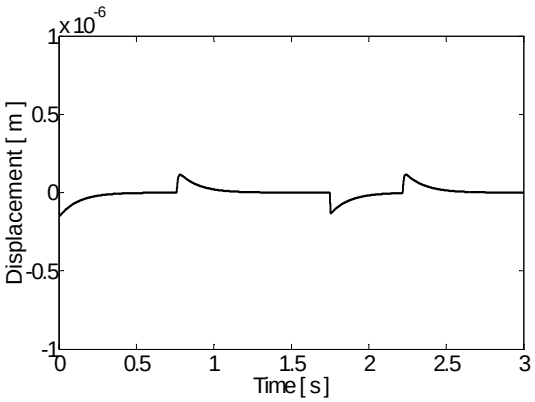

(b) Axial displacement

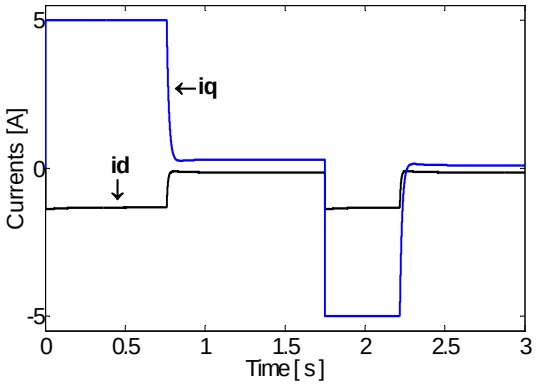

(c) i_d and i_q

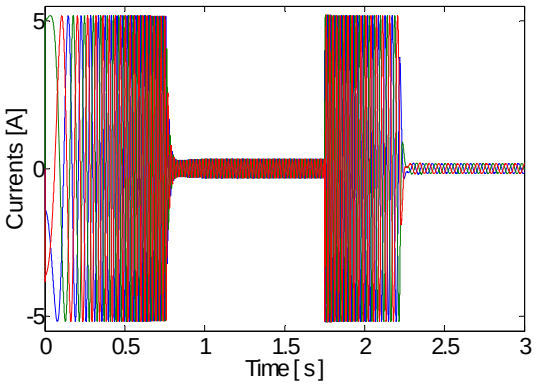

(d) 3-phase currents

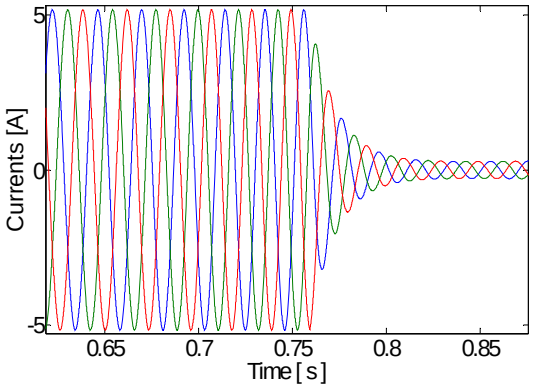

(e) Charging mode

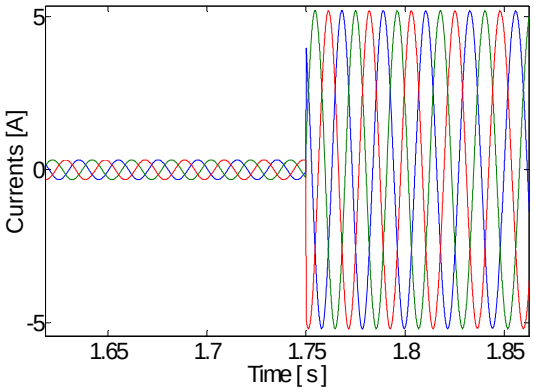

(f) Discharging mode

Fig. 6.11 Simulation results

The obtained simulation results show that the proposed machine can perform well its task in the FESS. Fast charging and discharging of the flywheel based on the proposed machine has been demonstrated; both speed and axial displacement are simultaneously supervised under the position-sensorless control scheme. It is valuable to mention that position-sensorless control scheme can eliminate the hassle of rotary encoder, remove the possibility of encoder failure in the system, reduce overall cost and increase the reliability. Therefore, this enhances the overall performance of the FESS.

6.5 Conclusions

This chapter has presented the design and simulation studies of the control system for the proposed AFPM machine. Simulation results have shown the feasibility in control of the proposed machine based on its mathematical model.

The position-sensorless control approach for the AFPM machine has been demonstrated. Distinct feature of the machine for fast charge and fast discharge of energy has also been presented under position-sensorless control scheme, which eliminates the hassle of rotary encoder, reduces overall cost and increases the system reliability. It is therefore feasible to perform the experimental setup and tests on the fabricated machine prototypes. This will be discussed in the next chapter.

CHAPTER 7 EXPERIMENTAL IMPLEMENTATION AND ANALYSIS OF DUAL AIR-GAP AFPM MACHINE PROTOTYPES

7.1 The dual air-gap AFPM machine prototypes

For further investigation and verification of the proposed machine concept, the dual air-gap AFPM machine prototypes with $q = 2$ and $q = 1.5$ slots/pole/phase have been fabricated and tested. Fig. 7.1 (a) shows the stator core of the machine without windings. The stator with windings is illustrated in Fig. 7.1(b) and stators with $q = 2$ and $q = 1.5$ are also shown in Fig. 7.1 (c) and (d) respectively. The rotor with non-skew and skew magnet configuration is shown in Fig. 7.2. The rotor is supported by a conventional ball bearing system.

(a) Stator core

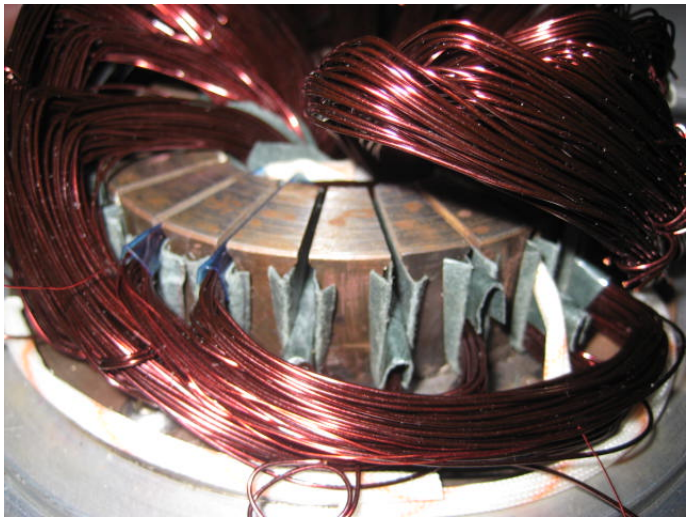

(b) Stator core with windings

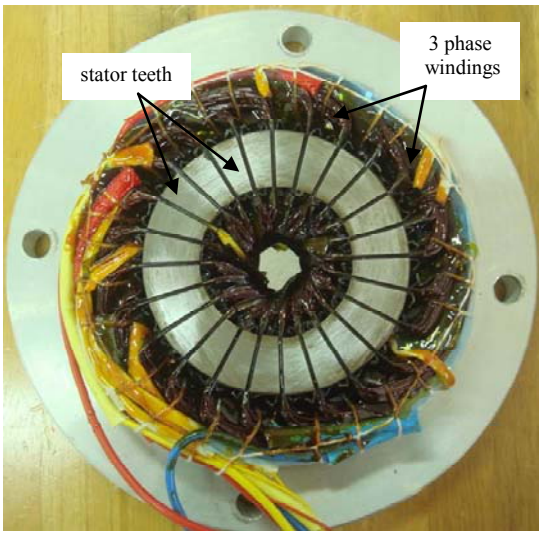

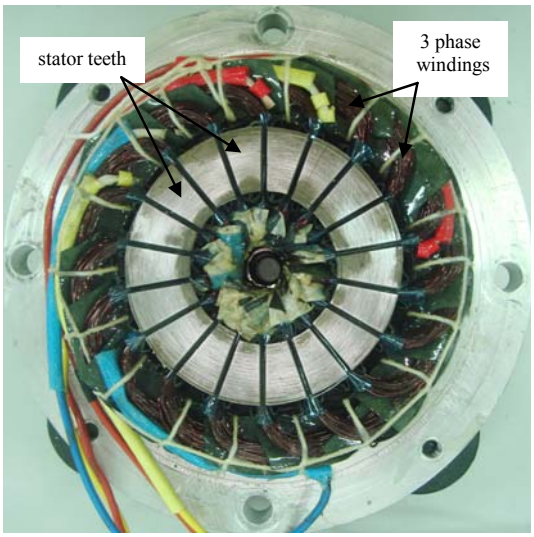

(c) Stator core with windings (q = 2) (d) Stator core with windings (q = 1.5)

Fig. 7.1 Stator core and windings

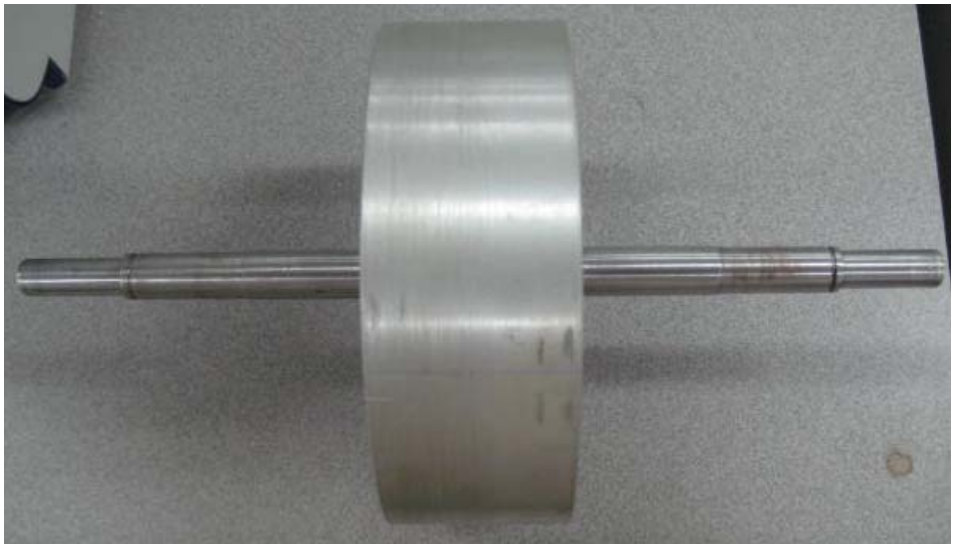

(a) Rotor and shaft

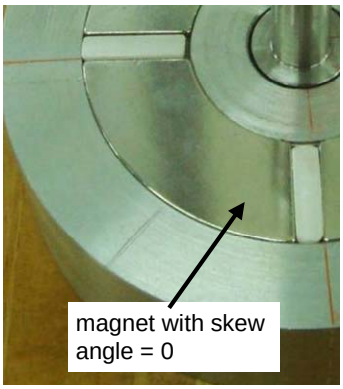

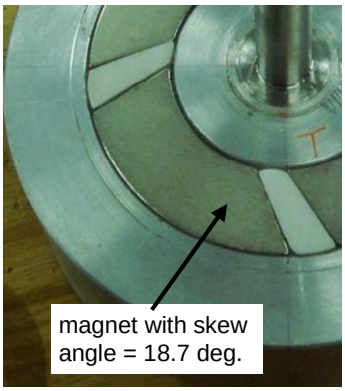

(b) Rotor with non-skewed PM(c) Rotor with skewed PM

Fig. 7.2 Rotor with non-skew and skew magnets

As the focus of the experiments is on the AFPM machine performance, the rotor was not fitted with a composite material flywheel rim. The full pictures of the machines with $q = 2$ and $q = 1.5$ slots/pole/phase are also shown in Fig. 7.3 and Fig. 7.4.

Fig. 7.3 Machine prototype with q = 2 slots/pole/phase

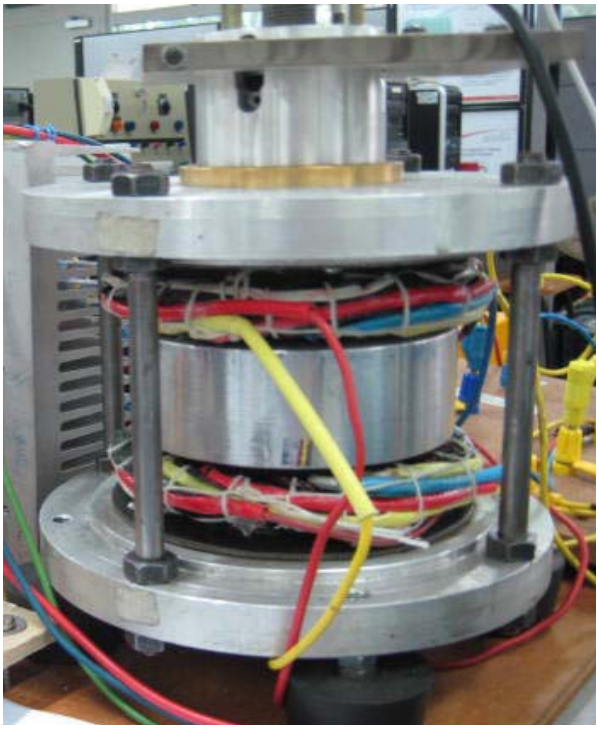

Fig. 7.4 Machine prototype with q = 1.5 slots/pole/phase

7.2 Experimental system set-up and control

The hardware system consists of three main parts: CPU joint with DSP control card, power electronic inverter and the machine prototypes.

7.2.1 DSPACE 1103 card

The DSP-1103 PPC controller card consists of Motorola Power PC 640e/333 MHz main processor and Texas instruments TMS320F240/40 MHz slave subsystem with powerful features, such as 16 Channels of 16-bit ADC, 4 channels of 12-bit ADC, 8 channels of 14-bit DAC, 6 channels of digital input incremental encoder subsystem and 4 channels of 8-bit digital I/O ports. In the control system for the machine prototypes, it is employed as the controller to perform analogue to digital and digital to analogue conversion, calculation, and PWM signal generation. The DSP controller card has real-time interface (RTI) with MATLAB/SIMULINK and it is installed on a host computer. The simulation diagram and control algorithm are downloaded to the Dspace Control Desk Software to implement the controller in real time mode.

7.2.2 Power electronic inverter and driver board

To drive the machine prototypes, a three-phase bridge inverter has been built from six IGBTs (three IGBT modules - Semikron SKM 50GB 123D). These six IGBTs of the inverter are switched on and off by the regulated voltages of +15V and -5V respectively. Six gate drive opto-couplers (HCPL 3120) are used to build the isolated driving circuit for the inverter. A customized transformer is used to provide the isolated supply voltage for the driving circuit. The inverter can supply 90kVA apparent power and up to 20 kHz switching frequency. The detail of the driving circuit is shown in the Appendix.

7.2.3 Configuration design of the DSP-based control

The DSP-based control system for the machine prototypes is shown in Fig. 7.5. The angular position of the rotor is detected by the DSP from the pulse signals given by the encoder. Differential calculation of the angular position gives the rotational speed information to the DSP. It is compared with the speed command value and the difference is amplified to the desired value i_q^* by the speed regulator. Current and voltage transducers are used to sense the stator currents, bus currents and voltages of the inverter. The eddy-current sensor is used to measure the displacement of the rotor along axial axis. All the sensing analogue signals are converted into digital values and sent to the DSPACE 1103 board. Digital value of axial displacement is compared with its reference and the displacement error is then sent to the displacement regulator which generates the command i_d^* after that. The currents are then regulated by the current regulators which generate V_d^* and V_q^* values. Space vector modulation technique is used to generate the PWM control signals to drive the inverter to energize the machine.

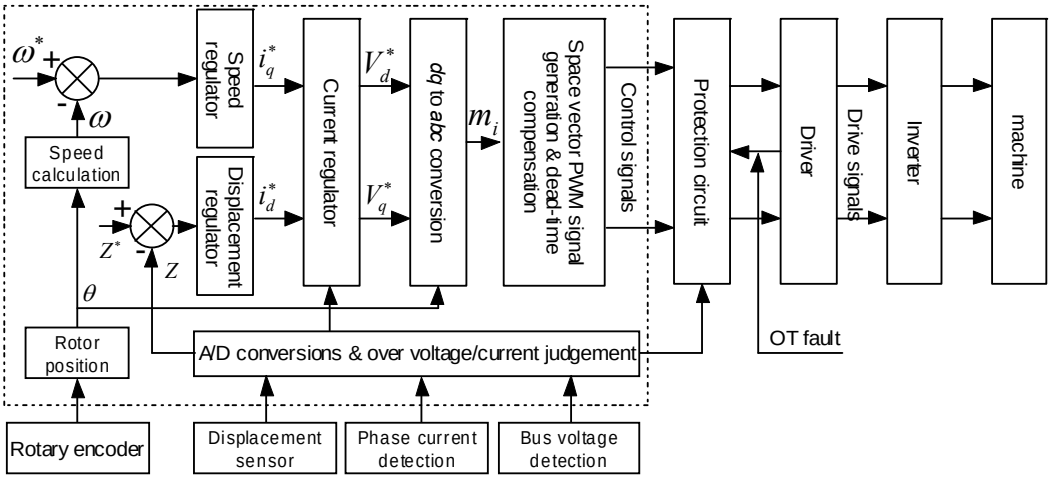

Fig. 7.5 DSP-based control system

7.2.4 System set-up

The test system schematic used in the experiments is shown in Fig. 7.6. The system includes the machine prototype, the power electronic converter for the 3-phase windings and the DSP-based controller. The actual picture of the system set-up is shown in Fig. 7.7.

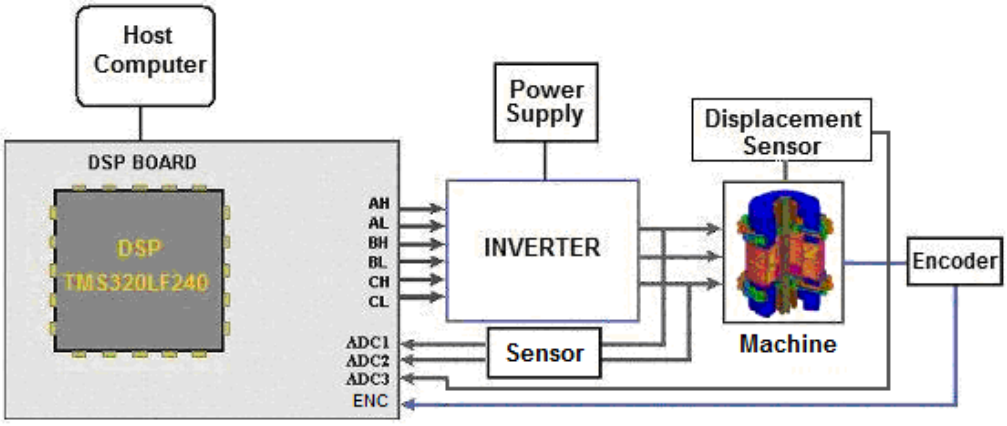

Fig. 7.6 Control system diagram

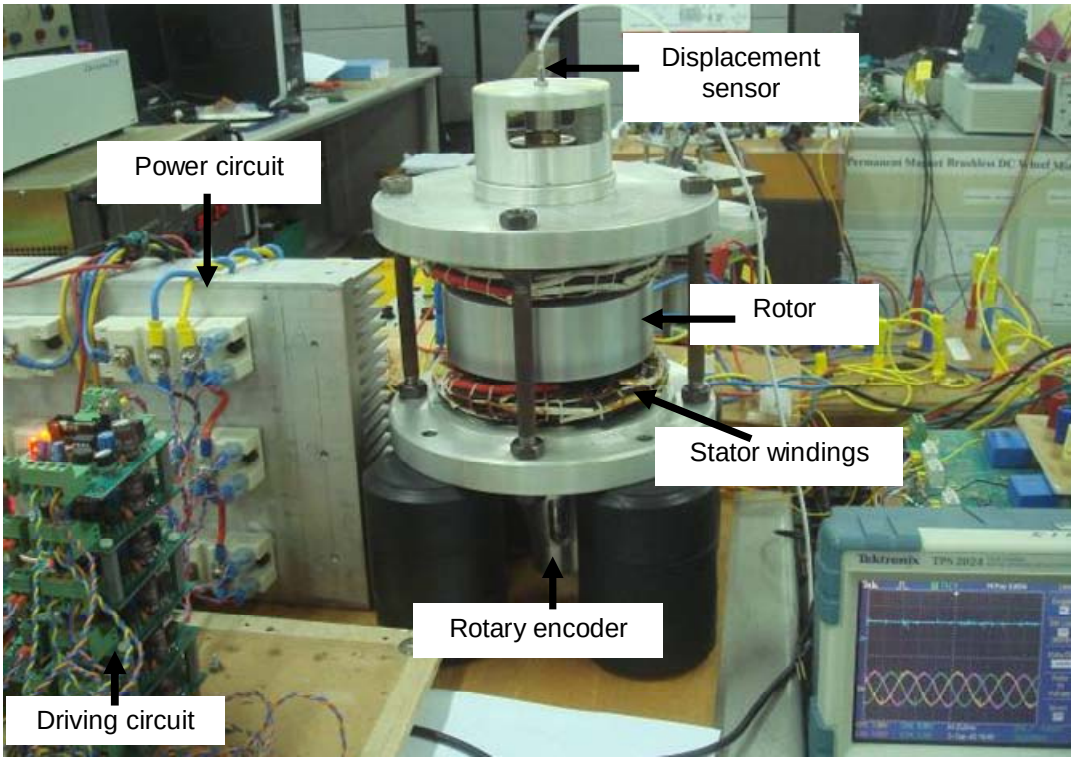

Fig. 7.7 Overall view of the test system

7.2.5 Instruments used in the set-up

The devices used in the system are as follows:

- DSPACE 1103 PPC controller board,
- Incremental encoder Kubler Co. 05.2400.1122.1024,
- Displacement sensor Eddy-current type Micro-Epsilon Co. DT110-T,
- DC power supply 6035A system power supply,
- Torque sensor Magtrol HD-810-8NA with control interface M6200, the set-up with torque sensor is illustrated in Fig. 7.8.

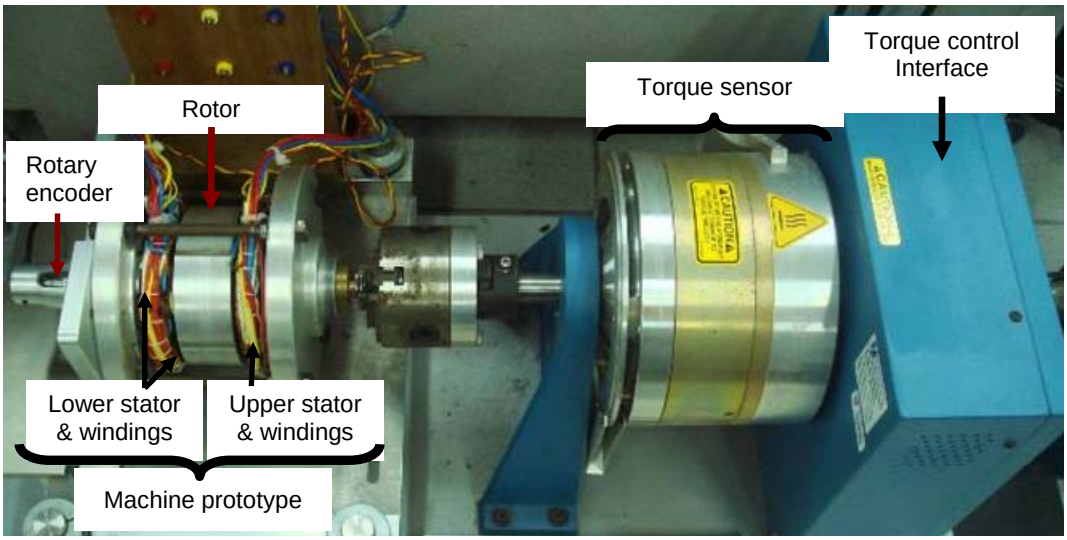

Fig. 7.8 Test set-up in the laboratory

7.3 Experimental work

The aim of the experimental work is to investigate and verify the proposed machine concept. In this part, the results obtained from the measurements on the machine prototype with $q = 2$ slots/pole/phase are presented.

7.3.1 Cogging torque

The machine prototype is controlled to run in no-load condition in low speed zone. The cogging torque variation at low rpm for a few seconds is obtained. Using the rated torque as the base value, the FEA and experimental results of the cogging torque are illustrated in Fig. 7.9. From the cogging torque profiles, it is experimentally verified that magnetic skew results in a reduction of 87% in cogging torque. The close agreement between FEA and experimental results also validates the use of FEA in the optimization of the AFPM machine design, especially in magnetic skew technique for cogging torque reduction.

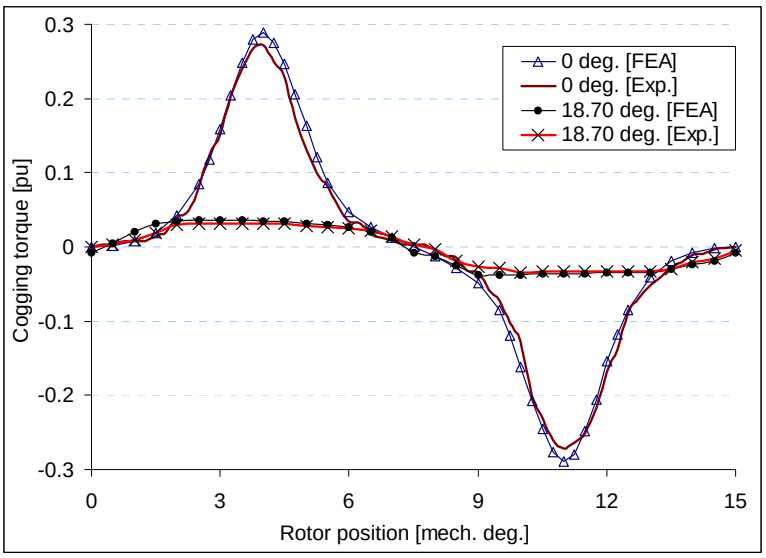

Fig. 7.9 Cogging torque

7.3.2 Air-gap flux

As it is not feasible to install a load cell for axial force measurement, the air-gap flux is measured to test for axial force controllability of the machine prototype. The following tests are performed on the machine with 18.7-degree skewed magnets. A span search coil is placed in the stator teeth to measure the value of one pole air-gap flux, as shown in Fig. 7.10. First, the *d*-axis is aligned with the search coil and the rotor is locked; then a single-phase voltage of 50Hz is applied to the stator windings

which are connected as shown in Fig. 7.11. By this alignment a stator magnetomotive force is applied directly to *d*-axis of the rotor. By varying the supply current, induced voltages in search coil are measured. Using numerical integration the air-gap flux per pole is calculated.

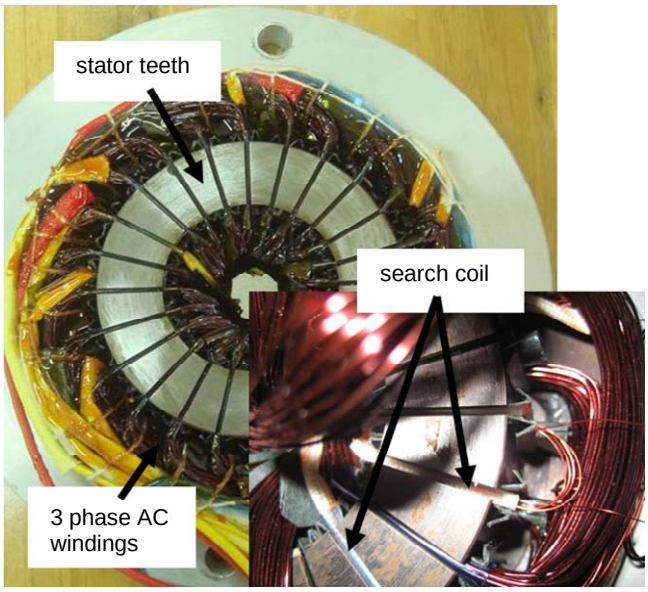

Fig. 7.10 Stator, windings and search coil

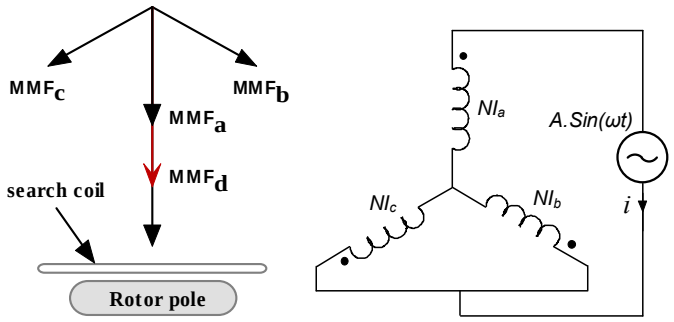

Fig. 7.11 Locked rotor test.

By operating the machine in no-load generator mode, induced voltages in the search coil are measured. The voltage obtained in this case is only generated by PM excitation flux because there is no armature reaction flux. The air-gap flux is derived from the voltage waveform. The resultant air-gap flux components are depicted in Fig. 7.12. The total air-gap flux can be controlled by i_d within the range of $\pm 15\%$. This demonstrates the axial force controllability of this machine as discussed previous

chapters.

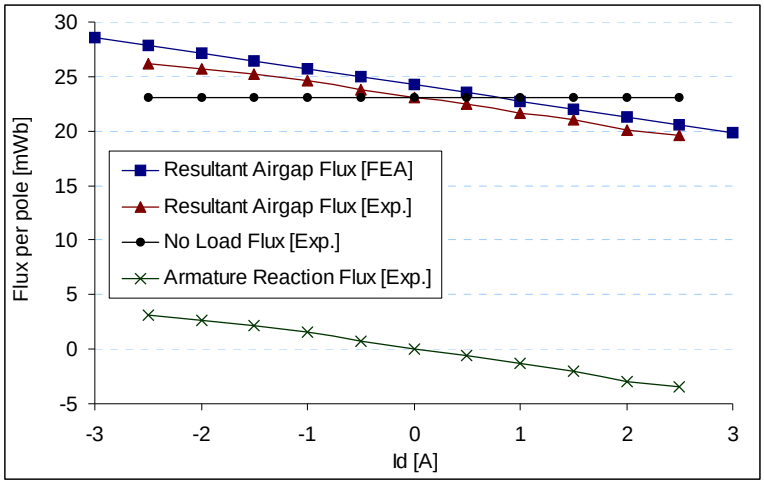

Fig. 7.12 Air-gap flux versus i_d

7.3.3 Inductance profile and induced voltage

In order to measure the *d*- or *q*-axis inductance of the machine, the rotor is aligned along the *d*- and *q*-axis of the machine respectively. The AC excitation is applied to the stator windings in such a manner that only *d*- or *q*-axis was energized. Voltage and current values are recorded and based on these values, the *d*- and *q*-axis inductances are calculated. The *d*- and *q*-axis inductances are illustrated in Fig. 7.13.

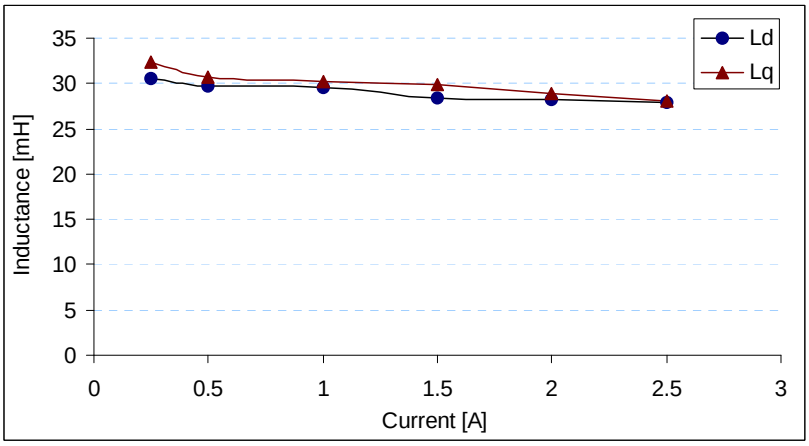

Fig. 7.13 *d*- and *q*-axis inductances

Induced voltage is measured when running the machine at 3,000 rpm. Close

agreement was found between the predicted and measured no-load induced voltage waveform, as depicted in Fig. 7.14.

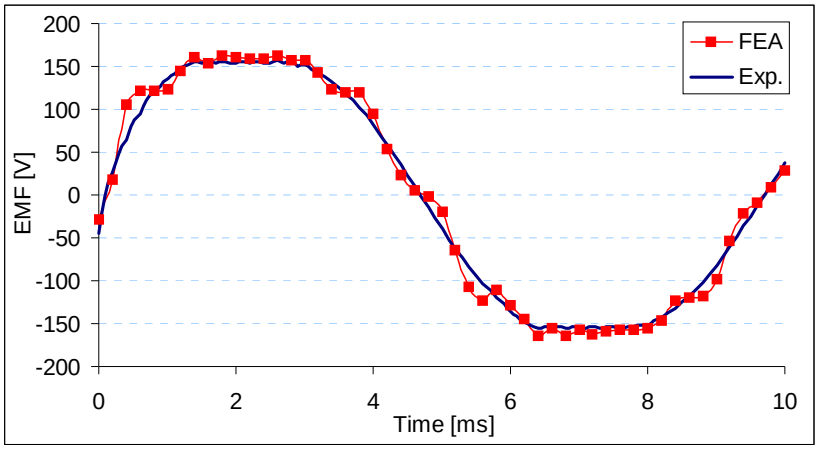

Fig. 7.14 Induced voltage

7.3.4 Torque versus i_q

In this test, the results from experimental measurements on torque and i_q are obtained. In order to test the torque characteristic of this machine, a torque sensor was set up. The torque is controlled by regulating i_q and keeping $i_d = 0$. By varying the load applied to the machine, i_q values were recorded. The profile of torque versus i_q is shown in Fig. 7.15. As seen from the plot, a quasi-linear relationship of torque and i_q is confirmed. Predicted torque is about 7.5% larger than the measured value. Although there is a small difference between the measured and simulated results, it can be concluded that 3D-FEA gives accurate predictions.

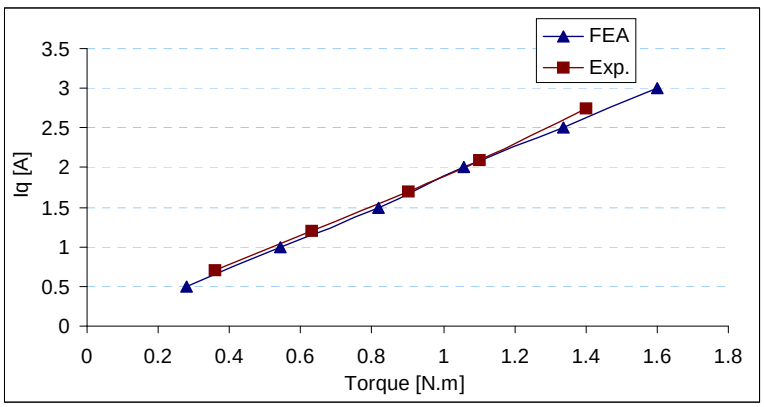

Fig. 7.15 Torque versus i_q

7.3.5 Evaluation of power losses

The aim of this experiment is to evaluate the proposed machine in terms of its potential to reduce axial bearing stress and power loss by controlling the net axial force to counter the gravitational force acting on the rotor. Four configurations of the machine are evaluated in FESS standby mode condition.

Case 1: the machine being driven by the upper stator only;

Case 2: the machine being driven by the lower stator only;

Case 3: the machine being driven by both stators but without active axial force control; and

Case 4: the machine being driven by both stators with active axial force control.

Losses of these four configurations of the AFPM machine at various rotor speeds are illustrated in Fig. 7.16. It can be seen from the plot that losses of the machine in cases 1 and 2 are nearly the same and are about 4 times larger than in cases 3 and 4. The higher losses when operated as single air-gap machine is due to the axial force stress on the bearings. This axial stress in much less when the machine operated as dual air-gap AFPM machine because the rotor weight is largely balanced by the net axial force in the machine. This axial stress is further reduced when active axial force control is applied, as in case 4. It is seen that the losses in case 4 are up to 12.5% smaller than case 3 in the tested speed range.

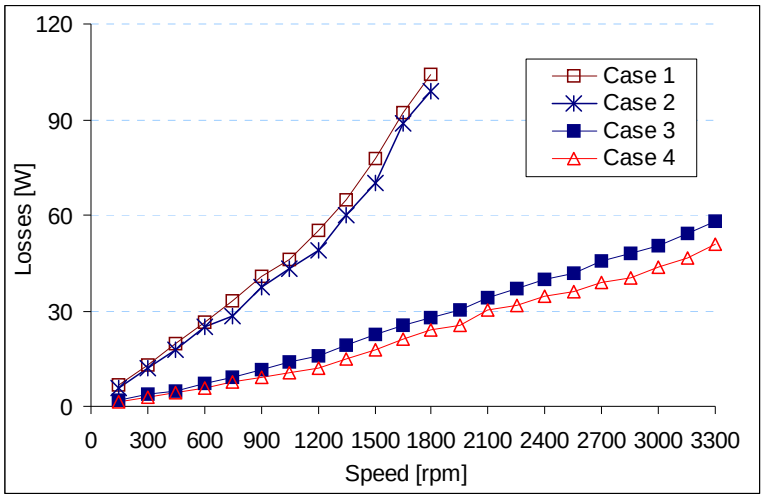

Fig. 7.16 Losses in different configurations of the machine

7.3.6 Comparison of dual air-gap AFPM machines with fractional and integral slot per pole

In this section, the two dual air-gap AFPM machines with $q = 1.5$ (machine 1) and $q = 2$ slots/pole/phase (machine 2) are analyzed, tested and compared. For convenience in comparison, the FEA results presented in Chapter 5 and experimental results are plotted in common diagrams in this part.

7.3.6.1. Torques

Taking the rated torque of the machine with integral slot per pole ($q=2$) as the base value, the FEA and experimental results of the cogging torque are illustrated in Fig. 7.17.

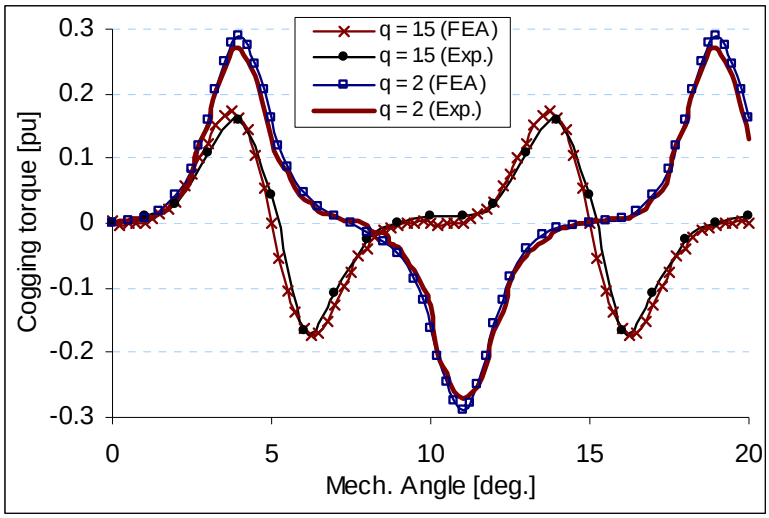

Fig. 7.17 Cogging toque of the two machines with non-skew PMs

From the cogging torque profiles, it is shown that the cogging torque frequency of machine with $q = 1.5$ is higher than that of machine with $q = 2$. It is also seen that cogging torque amplitude of machine with $q = 1.5$ is 40.7% less than that of machine with $q = 2$; this bodes well with the theory applied in the conventional PM machine as in (7.1) and (7.2) [182]:

The number of cogging torque cycles per slot pitch depends on the least common multiple (*LCM*) of the number of stator slots Q and the number of poles $2P$, as follows:

$$N_{per-pitch} = \frac{LCM\{Q, 2P\}}{Q} \tag{7.1}$$

For the conventional radial flux permanent magnet machine, it has been shown in [156] that, the smaller the greatest common divisor (GCD) of Q and $2P$, then the smaller will be the amplitude of the cogging torque ($A_{cogging}$):

$$A_{cogging} = function\left(GCD\{Q, 2P\}\right) \tag{7.2}$$

The close agreement between FEA and experimental results has been found, this validates the use of FEA in the design and analysis of the AFPM machines.

7.3.6.2. Machine losses

Effect of both space and time harmonics on the machine losses has been analyzed and experimentally verified. Fig. 7.18 shows the obtained results of the two machines at 1,500 and 3,000 rpm respectively. FEA and experimental results are both plotted in a diagram. It is seen that more losses are found in machine 1 than in machine 2.

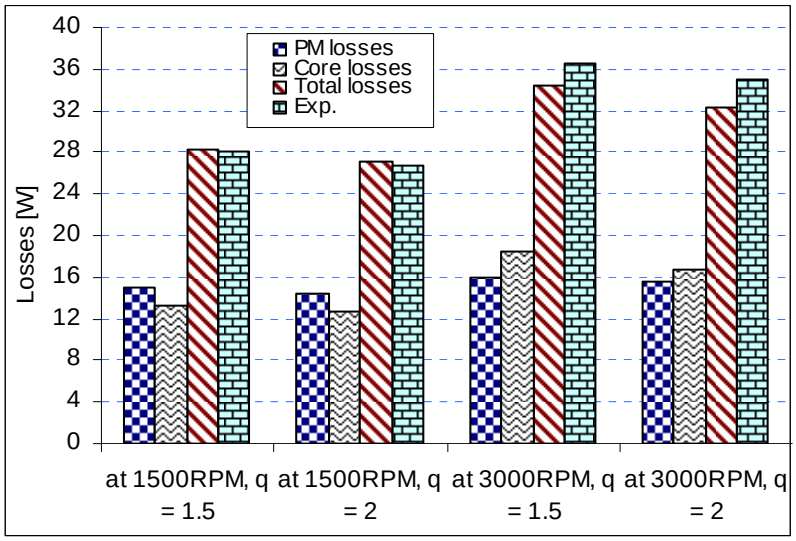

Fig. 7.18 Losses of the machine with *q = 2* and *q = 1.5*

The losses in the magnets are caused by the eddy-currents which tend to distribute at the side of the magnets. This loss can be explained as follows [182]:

The eddy-current loss in the magnet is calculated as:

$$\Delta P_{PM} = \frac{\pi}{2}\frac{\gamma B_m^2}{\mu}\frac{sh\gamma - \sin\gamma}{ch\gamma - \cos\gamma} \times f \tag{7.3}$$

where:

$$\gamma = \sqrt{\frac{\omega\sigma\mu d^2}{2}} = \sqrt{\pi\sigma\mu f d^2} \tag{7.4}$$

B_m is the peak induction, μ is the permeability of the magnet, σ is the magnet resistivity, d is the magnet dimension and $\omega = 2\pi f$ is the frequency of the applied field.

Skin depth of eddy-current flow is:

$$\delta = \sqrt{\frac{2}{\omega\sigma\mu}} \tag{7.5}$$

At low frequency $\gamma << 1$ $(d << \delta)$, loss per cycle becomes:

$$\Delta P_{PM} \cong \frac{\pi^2}{6}\sigma d^2 B_m^2 f^2 \tag{7.6}$$

At high frequency $\gamma >> 1$ $(d >> \delta)$, loss per cycle becomes:

$$\Delta P_{PM} \cong \frac{\pi^{3/2}}{2}\sqrt{\frac{\sigma}{\mu}} d B_m^2 f^{1/2} \tag{7.7}$$

It is seen that the PM losses are comparable with the iron-core losses in the two machines. And it can be also derived from the loss profile that time harmonics give more significant losses in the magnets than the space harmonics do.

7.3.7 Control of the dual air-gap AFPM machines

Performance test of this AFPM machine is performed by the closed loop control of speed and axial displacement as discussed in Chapter 6. The pulse width modulation frequency and sampling time used in this experiment is 20KHz and 50 μsec respectively. The actual testing speed was limited at 3,000 rpm due to the experimental setup's rotor-dynamics. In order that machine can be fast accelerated and decelerated in short period, stator current is controlled at the over-rated value (about 2 times of its rated). The machine is controlled to speed up from 1,000 to 3,000 rpm and then slowed down to 1,000 rpm which reflects charging and discharging periods accordingly. All the data was captured and displayed in dSPACE ControlDesk by a personal computer. The experimental results of the above-mentioned periods are shown in Fig. 7.19.

Fig. 7.19(a, b) show the speed response and axial displacement of the rotor. Speed is well managed by i_q while axial displacement is well controlled at the equilibrium point by regulating i_d, Fig. 7.19 (e). The accelerating period is zoomed in and shown in Fig. 7.19(b). It takes about 0.48sec for the rotor to reach its reference speed. Fig. 7.19(c) shows the speed response of the rotor in the discharging period. It takes about the same time for decelerating to 1,000 rpm. i_q is controlled according to speed command, as shown in Fig. 7.19 (f).

The q-axis current, i_q of ± 5 Amperes is maintained during the acceleration and deceleration for fast charge and fast discharge of the kinetic energy, respectively. The three phase currents in period of charging and discharging mode are shown in Fig. 7.19(g, h). A small stator current is maintained during steady state of the machine. Therefore the machine has small losses in idling mode.

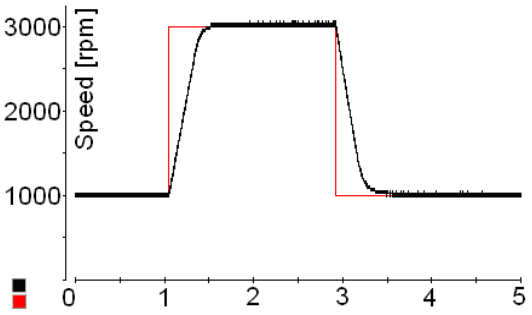

(a) Speed vs. time(s)

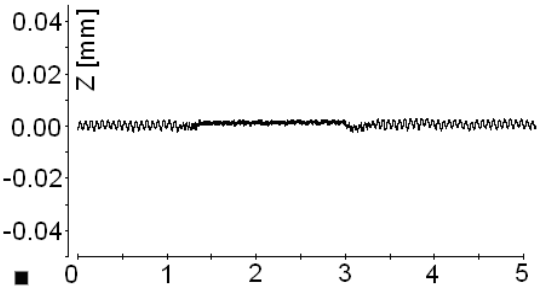

(b) Axial displacement vs. time(s)

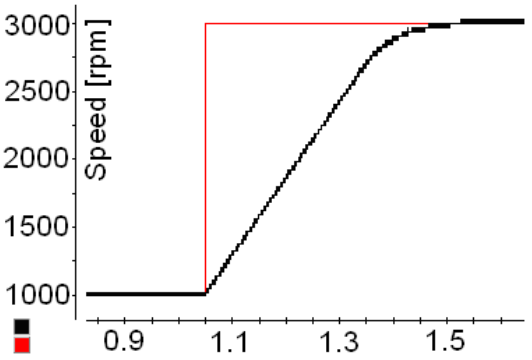

(c) Speed vs. time(s) response in charging mode

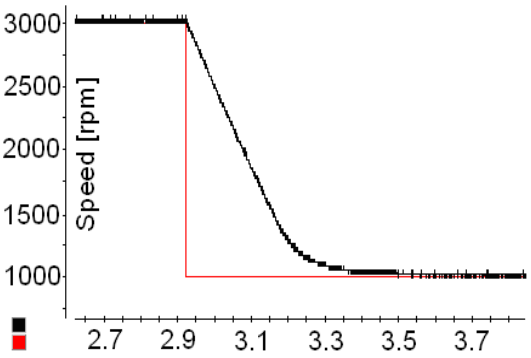

(d)Speed vs. time(s) response in discharging mode

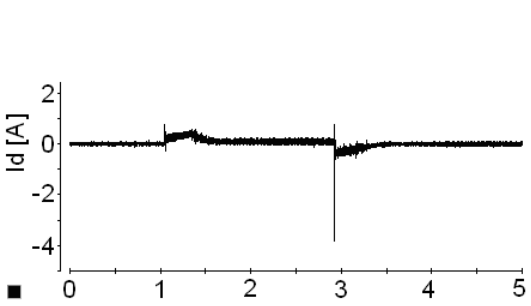

(e) i_d vs. time(s)

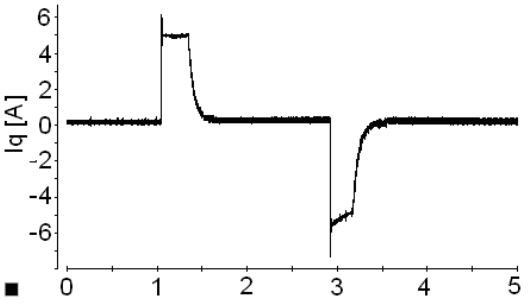

(f) i_q vs. time(s)

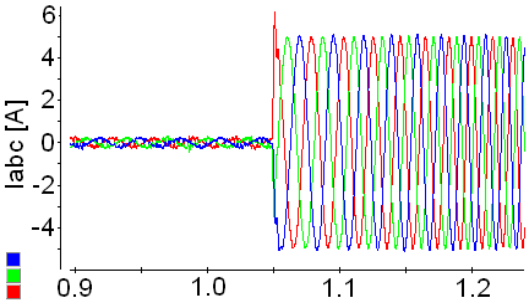

(g) Currents vs. time(s) in charging mode

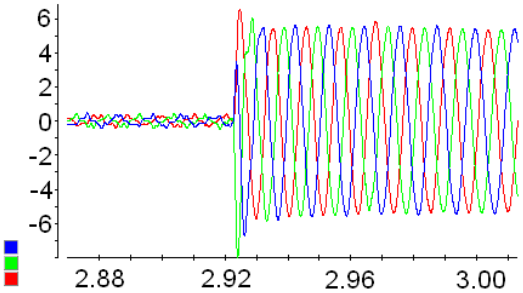

(h) Currents vs. time(s) in discharging mode

Fig. 7.19 Experimental results in charge/discharge mode

From the experimental results, it can be seen that the AFPM machine can be well controlled in all three fundamental modes of the FESS: charge, standby and discharge. This validates the derived mathematical model for this machine in Chapter 4. Temperature rise in the machine is slower than the change in current, so during transient period the current can be maintained at higher value than its rating; this allows the machine to perform its fast charge and discharge tasks. The requirement of fast charge or fast discharge of energy can be totally fulfilled by operating the machine under over-rated power condition in short periods. Thanks to this characteristic, the FESS can be considered as a potential candidate for applications with fast charge and/or fast discharge of energy.

7.3.8 Position sensorless control of the dual air-gap AFPM machines

The following experiment is also performed with the pulse width modulation frequency of 20KHz and sampling time of 50 μsec. The measured and estimated position when the rotor operates at 1,000rpm and 3,000rpm respectively are obtained and shown in Fig. 7.20. It is seen that the estimated and measured position are well matched with very small errors (in radian) for both cases.

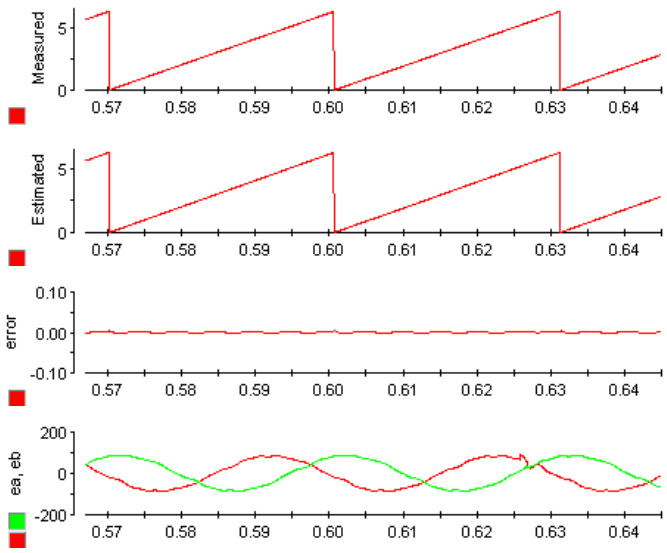

(a) At 1,000 rpm

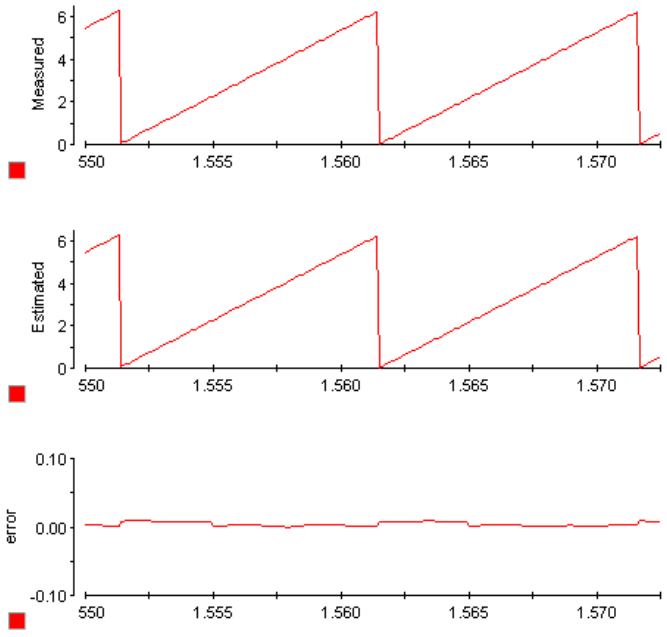

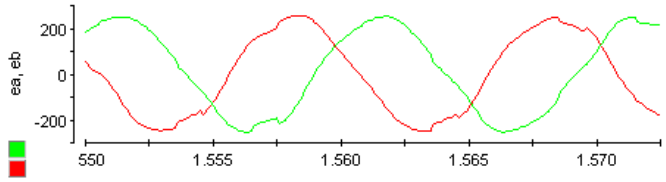

(b) At 3,000 rpm

Fig. 7.20 From top to bottom: Actual position, estimated position, position error (rad) and phase a & b back-EMF (V): (a) at 1,000 rpm, (b) at 3,000 rpm.

The performance test of this AFPM machine has also been performed using the closed loop control of speed and axial displacement. The obtained results are shown in Fig. 7.21.

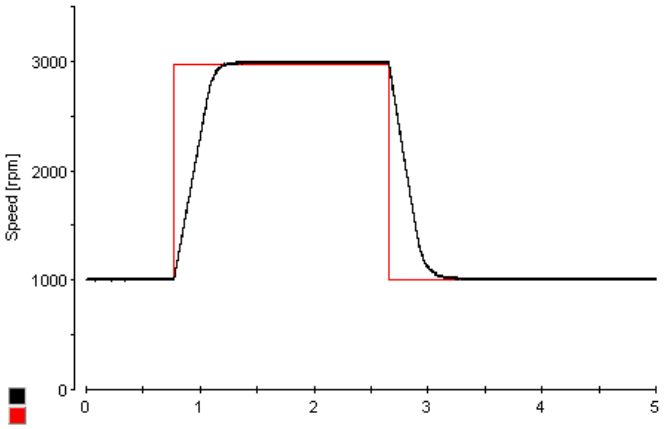

(a) Speed vs. time(s)

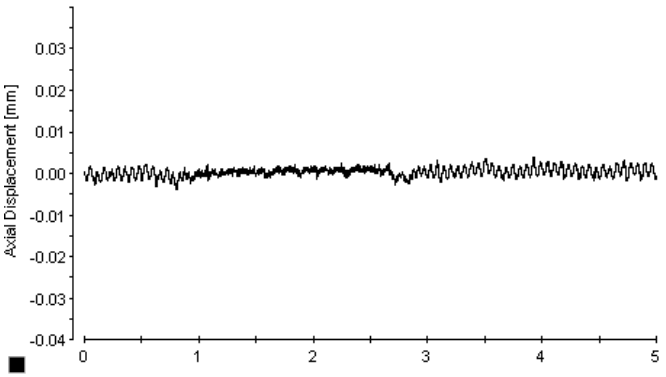

(b) Axial displacement vs. time(s)

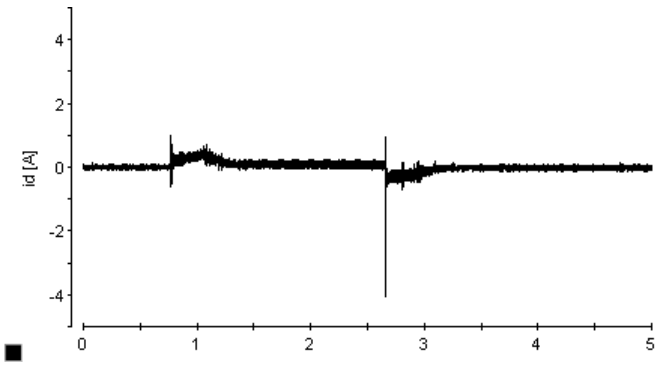

(c) i_d vs. time(s)

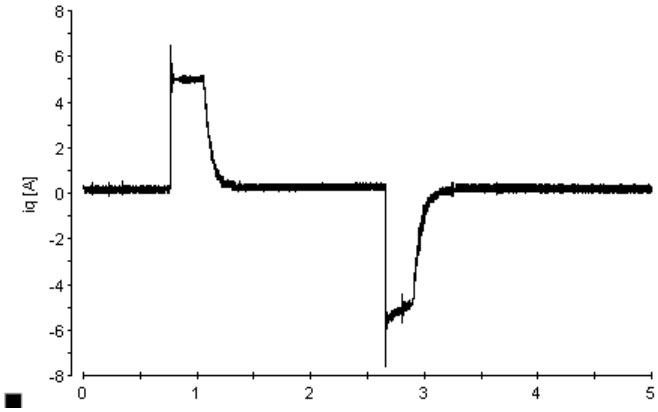

(d) i_q vs. time(s)

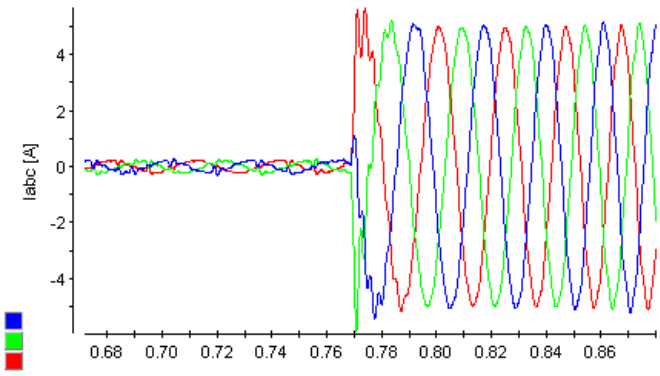

(e) Currents vs. time(s) in charging mode

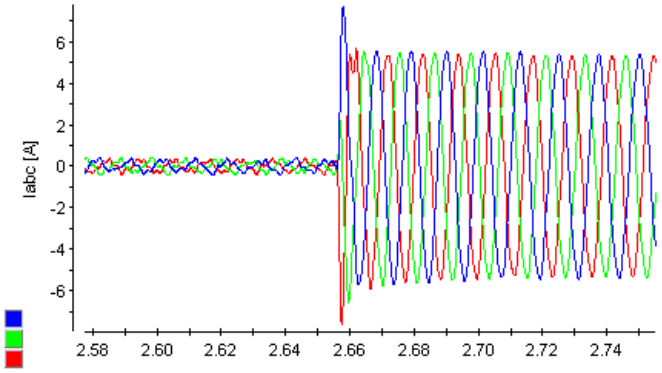

(f) Currents vs. time(s) in discharging mode

Fig. 7.21 Experimental results under position-sensorless control scheme

From the experimental results, it is seen that machine can be successfully controlled under the position-sensorless scheme. The fast charge and fast discharge of energy of the FESS based on the proposed machine is achieved. Position of the rotor can be well estimated by the sliding mode observer. It is valuable to mention that the elimination of rotary encoder in the system helps reduce the overall cost and increase the reliability of the whole system.

7.4 Conclusions

This chapter has presented the test set-up and the measurements of the proposed dual air-gap AFPM machine prototypes. The design and analysis of the dual air-gap AFPM machines have been verified by close agreements found between the predicted and measured quantities such as: cogging torques, air-gap flux, inductances, induced voltages, and electromagnetic torques. Performance of the machines under both position sensored and sensorless schemes has also been studied experimentally. Distinct feature of this AFPM machine in FESS applications: fast charge and fast discharge of energy has been confirmed by the close agreements between the simulation and experimental results.

CHAPTER 8 CONCLUSIONS, CONTRIBUTIONS AND RECOMMENDATIONS

The overall goal of this thesis has been to contribute to the design, analysis and control of a novel axial flux permanent magnet machine suitable for application in flywheel energy storage system. The conclusions are drawn and after that the recommendations are given in this chapter.

8.1 Conclusions

The study which is summarized by this thesis has presented a review of energy storage systems, particularly the flywheel energy storage systems; the design of a compact and efficient FESS based on dual air-gap AFPM machine; the modeling of the proposed AFPM machine; the FEM analysis of this machine; the development of control system for the proposed AFPM; and the experimental implementation and analysis of the machine prototypes.

The axial flux permanent magnet configuration has been selected to use in FESS application as it has a distinct feature which can be exploited in FESS application: its axial force can be controlled to counter the gravitational force acting on the rotor if the axis of rotation is in the vertical orientation. The dual air-gap AFPM machine has been adopted as the motor/generator component responsible for the three fundamental operation modes in the FESS: charging, standby and discharge. The machine is composed of two separate single air-gap AFPM machines, has two sets of three-phase stator windings but requires only a single power converter which supplies power for control of both axial force and electromagnetic torque. The application of the proposed machine in FESS is realized by orientating

its axial direction vertically and having its double-sided rotor to be the core of the flywheel. The availability of axial force control helps to minimize the vertical bearing force to improve the efficiency of the FESS.

Analytical equations and 3D-FEM used in the design of this machine has been summarized by the design procedure described in Chapter 3. The design of the dual air-gap AFPM machine has been optimized for high efficiency, zero fundamental frequency rotor losses, low cogging torque and improved back-EMF waveforms.

The mathematical model for the proposed dual air-gap AFPM machine has been developed in Chapter 4. Modeling of this special machine has been built based on the basic theory of AC electrical machines. The machine equations have been also obtained in rotor-reference frame to facilitate its control. The electromagnetic torques and axial forces have been derived based on co-energy method. After that the equations of speed and axial displacement of the rotor were obtained thereafter. As the model is a non-linear multi-variable system, linearization has been used to facilitate the implementation of the control system.

Due to the special geometry of the machines, the 3D FEA has been employed for the design and analysis, including their electromagnetic torques, axial forces and losses of the proposed machine. The analysis has been performed for the dual air-gap axial flux permanent magnets machines with $q = 2$ and $q = 1.5$ slots/pole/phase respectively. Effects of rotor PM skew angle on the torque and the axial force of the machine have been studied. It is found that an optimum skew angle is effective in reducing the overall cogging torque with negligible effect on the static axial force. The latter is crucial and it is exploited to minimize axial bearing stress in the FESS application described in Chapter 5. The performance of the machine has also been studied by 3D-FEM and experimentally verified.

The development of the control system for the proposed AFPM machine has been presented in Chapter 6. Simulation results obtained have shown the feasibility in

control of the proposed machine based on its mathematical model. The position sensorless control approach has also demonstrated. Distinct feature of the machine for fast charge and fast discharge of energy in FESS has also been shown under position-sensorless control scheme.

The test set-up and also the measurements of the performance of the proposed dual air-gap AFPM machine prototypes have been performed and presented in Chapter 7. The design and analysis of the dual air-gap AFPM machines have been verified by close agreements found between the predicted and measured quantities such as: cogging torques, air-gap flux, inductances, induced voltages, and electromagnetic torques. Performance of the machines for FESS applications has also studied experimentally. Distinct feature of the machine in FESS applications: fast charge and fast discharge of energy has been verified by close correspondences of the experimental results with the simulations.

8.2 Contributions

The main contributions of this thesis can be summarized in four parts as follows:

a. Review of flywheel energy storage technology with the focus on the major research directions in FESS undertaken in universities and industries, the current status of flywheel energy storage technology, the obstacles faced by FESS industries, the present research and development activities, the potential future applications of FESS and comparison of FESS with other energy storage systems

b. Design and analysis of a novel dual air-gap axial flux permanent magnet machine optimized for use in FESS applications

c. Modeling and control of the proposed dual air-gap axial flux permanent magnet machine

d. Implementation of the proposed AFPM machine, experimental study of the

machine prototypes and comparison between experimental results and simulations.

8.3 Recommendations

Although the principles, design and control of the dual air-gap AFPM machine have been explored in this thesis, there exist many areas that need to be explored in the future studies. Future researches are recommended in the following areas:

8.3.1 Advanced control of the dual air-gap AFPM machine

Model predictive control (MPC) of this dual air-gap AFPM machine is recommended as MPC system can pre-calculate the system behaviour and provide more satisfactory tracking response than conventional PID control. This advanced control approach for this machine has been "half-way" done in [183], however the control variables were limited to i_d and i_q due to the deficiency of current processor used in this project. Therefore, in order to implement this advance control of this machine for all four important control variables: ω (speed), z (axial displacement), i_d and i_q simultaneously, simplifying the control algorithm together with utilizing an advance processor is suggested.

8.3.2 Dynamic control of the dual air-gap AFPM machine

Study of dynamic performance of the machine under various transient conditions is one of important and interesting themes for dual air-gap AFPM machine. Transient behaviour of the machine drive needs to be investigated especially under over-rated condition of the machine. Therefore a complete transient simulation program including power electronic inverter, control and non-linear model of the machine is recommended. The dynamic response of the machine needs to be studied with the help of finite element analysis model for more accurate levels where the saturation and field effects can be included.

8.3.3 High speed dual air-gap AFPM machine for the FESS

For the feasibility verification purpose, the dual air-gap AFPM machine proposed in this thesis is designed to operate at low speed. However a high speed dual air-gap AFPM based on the proposed AFPM machine is highly recommended. With higher speed operation the machine will be shrunk in size; the applied FESS will store much more energy and be more compact. Taking safety criteria into consideration, a solid housing is required to dissipate radial kinetic energy from the rotor fragments in case of rotor failure. In order to reduce the windage loss and increase the system efficiency, using vacuum chamber is a must. Other security options such as on-line health monitoring system that supervises rotor imbalance or rim geometry as detected by proximity sensors can also be considered. Further study of the high speed machine in this aspect is also necessary.

8.3.4 Halback array permanent magnet rotor machine

To enhance the performance of the machine the permanent magnets can be arranged so that the magnetomotive force is approximately sinusoidal. Such arrangement is known as Halback. The AFPM machine using Halback array PM arrangement is expected to have advantages as:

- More sinusoidal MMF hence reduce space harmonics,
- Higher power efficiency due to the factor of fundamental field is higher than in conventional PM arrangement.

8.3.5 Slotless dual air-gap AFPM machine for the FESS

Slotless machine has advantages in comparison with slotted-type machine such as:

- Ideally no cogging torque then no vibration and noise;

- No issue with the teeth saturation due to no slot;
- Less axial length of the stator than the slotted type; and
- Less complexity in manufacturing than slotted machine

With the mentioned advantages, the slotless dual air-gap AFPM machine is expected to have no cogging torque, no vibration and noise, no teeth saturation, and easy in manufacturing. However it is also noted that slotless type will have large air-gap, and less robust winding structure.

BIBLIOGRAPHY

[1] R. Hebner, J. Beno, A. Walls, and M. J. Riezenman, "Flywheel batteries come around again," *IEEE Spectrum,* vol. 39, no. 4, pp. 46-51, 2002.

[2] R. Cardenas*, et al.*, "Power Smoothing Using a Flywheel Driven by a Switched Reluctance Machine," *IEEE Transactions on Industrial Electronics,* vol. 53, no. 4, pp. 1086-1093, 2006.

[3] X.-D. Sun, K.-H. Koh, B.-G. Yu, and M. Matsui, "Fuzzy-Logic-Based V/f Control of an Induction Motor for a DC Grid Power-Leveling System Using Flywheel Energy Storage Equipment," *IEEE Transactions on Industrial Electronics* vol. 56, no. 8, pp. 3161-3168, 2009.

[4] B. Wang and G. Venkataramanan, "Dynamic Voltage Restorer Utilizing a Matrix Converter and Flywheel Energy Storage," *IEEE Transactions on Industry Applications,* vol. 45, no. 1, pp. 222 - 231, 2009.

[5] H. Mitsuda, A. Inoue, B. Nakaya, and M. Komori, "Improvement of Energy Storage Flywheel System With SMB and PMB and Its Performances," *IEEE Transactions on Applied Superconductivity,* vol. 19, no. 3, pp. 2091 - 2094, 2009.

[6] F. N. Werfel*, et al.*, "Towards High-Capacity HTS Flywheel Systems," *IEEE Transactions on Applied Superconductivity,* vol. 20, no. 4, pp. 2272-2275, August 2010.

[7] L. Bakay, M. Dubois, P. Viarouge, and J. Ruel, "Losses in hybrid and active magnetic bearings applied to Long Term Flywheel Energy Storage," *5th IET International Conference on Power Electronics, Machines and Drives (PEMD), Brighton, Unitied Kingdom,* April 2010.

[8] K. Sitapati and R. Krishnan, "Performance comparisons of radial and axial field, permanent-magnet, brushless machines," *IEEE Transactions on Industry Applications,* vol. 37, no. 5, pp. 1219-1226, 2001.

[9] A. Cavagnino, M. Lazzari, F. Profumo, and A. Tenconi, "A comparison between the axial flux and the radial flux structures for PM synchronous motors," *IEEE Transactions on Industry Applications,* vol. 38, no. 6, pp. 1517-1524, 2002.

[10] M. Aydin, S. Huang, and T. A. Lipo, "Torque Quality and Comparison of Internal and External Rotor Axial Flux Surface-Magnet Disc Machines," *IEEE Transactions on Industrial Electronics,* vol. 53, no. 3, pp. 822-830, 2006.

[11] M. Aydin, S. Huang, and T. A. Lipo, "Design, Analysis and Control of a Hybrid Field Controlled Axial Flux Permanent Magnet Motor," *IEEE Transactions on Industrial Electronics,* vol. 57, no. 1, pp. 78 - 87, 2010.

[12] C.-T. Liu, T.-S. Chiang, J. F. D. Zamora, and S.-C. Lin, "Field-oriented control evaluations of a single-sided permanent magnet axial-flux motor for an electric vehicle," *IEEE Transactions on Magnetics,* vol. 39, no. 5, pp. 3280 - 3282, 2003.

[13] F. Marignetti, V. D. Colli, and Y. Coia, "Design of Axial Flux PM Synchronous Machines Through 3-D Coupled Electromagnetic Thermal and Fluid-Dynamical Finite-Element Analysis," *IEEE Transactions on Industrial Electronics,* vol. 55, no. 10, pp. 3591-3601, 2008.

[14] T.-S. Kwon, S.-K. Sul, L. Alberti, and N. Bianchi, "Design and control of an axial-flux machine for a wide flux-weakening operation region," *IEEE Transactions on Industry Applications,* vol. 45, no. 4, pp. 1258-1266, 2009.

[15] J. H. Choi, J. H. Kim, D. H. Kim, and Y. S. Baek, "Design and Parametric Analysis of Axial Flux PM Motors With Minimized Cogging Torque," *IEEE Transactions on Magnetics,* vol. 45, no. 6, June 2009.

[16] D. A. Gonzalez-Lopez, J. A. Tapia, R. Wallace, and A. Valenzuela, "Design and Test of an Axial Flux Permanent-Magnet Machine With Field Control Capability," *IEEE Transactions on Magnetics,* vol. 44, no. 9, pp. 2168 - 2173, 2008.

[17] T. D. Nguyen, K. J. Tseng, S. Zhang, and H. T. Nguyen, "On The Modeling and Control of a Novel Flywheel Energy Storage System," *IEEE International Symposium on Industrial Electronics, Bari, Italy,* July - 2010.

[18] J. R. Hull*, et al.*, "High Rotational-Rate Rotor With High-Temperature Superconducting Bearings," *IEEE Transactions on applied superconductivity,* vol. 19, no. 3, pp. 2078 - 2082, 2009.

[19] D. A. Christopher and R. Beach, "Flywheel technology development program for aerospace applications," *IEEE Aerospace and Electronic Systems Magazine,* vol. 13, pp. 9-14, 1998.

[20] B. H. Kenny, P. E. Kascak, R. Jansen, T. Dever, and W. Santiago, "Control of a high-speed flywheel system for energy storage in space applications," *IEEE Transactions on Industry Applications,* vol. 41, no. 4, pp. 1029 - 1038, 2005

[21] M. A. Pichot*, et al.*, "Active magnetic bearings for energy storage systems for combat vehicles," *10th Electromagnetic Launch Technology (EML) Symposium,* 2001.

[22] M. E. F. Kasarda, "Overview of active magnetic bearing technology and applications," *Shock and Vibration Digest,* vol. 32, pp. 91-99, 2000.

[23] M. Nosaka*, et al.*, "Improvement of Durability of Hybrid Ceramic Ball Bearings in Liquid Hydrogen at 3 Million DN (120,000 rpm)," *Tribology Online,* vol. 5, no. 1, pp. 60-70, Feb 2010.

[24] S. Ginter*, et al.*, "Spacecraft energy storage systems," *IEEE Aerospace and Electronic Systems Magazine,* vol. 13, no. 5, pp. 27-32, 1998.

[25] Beacon-Power, "Smart Energy Matrix 20 MW Frequency Regulation Plant," *http://www.beaconpower.com/,* 2009.

[26] R. Moser, J. Sandtner, and H. Bleuler, "Optimization of Repulsive Passive Magnetic Bearings,"

IEEE Transactions on Magnetics, vol. 42, no. 8, pp. 2038 - 2042, 2006.

[27] A. V. Filatov and E. H. Maslen, "Passive Magnetic Bearing for Flywheel Energy Storage Systems," *IEEE Transactions on Magnetics,* vol. 37, no. 6, pp. 3913-3924, 2001.

[28] T. Ohji, S. C. Mukhopadhyay, M. Iwahara, and S. Yamada, "Performance of Repulsive Type Magnetic Bearing System Under Nonuniform Magnetization of Permanent Magnet," *IEEE Transactions on Magnetics,* vol. 36, no. 5, 2000.

[29] J. Fang and J. Sun, "New permanent magnet biased radial magnetic bearing in magnetic suspending flywheel application," *Beijing Hangkong Hangtian Daxue Xuebao/Journal of Beijing University of Aeronautics and Astronautics,* vol. 32, no. 11, pp. 1304-1307, 2006.

[30] Y. Y. Kang, "Energy Storage Systems in Distribution Systems," *Final year project report, Nanyang Technological University,* 2008.

[31] S. R. Holm, "Modelling and optimization of a permanent magnet machine in a flywheel," *PhD Thesis - Technische Universiteit Delft,* 2003.

[32] "Flywheel based UPS, Vycon," http://www.vyconenergy.com/.

[33] F. J. M. Thoolen, *PhD Thesis - Development of an Advanced High Speed Flywheel Energy Storage System, Technische Universiteit Eindhoven,* 1993.

[34] "Uninterruptible Power Supply, Active Power," http://www.activepower.com/.

[35] "Urenco Power Technologies Ltd.," http://www.urenco.com/.

[36] S. O. Siems, W. R. Canders, H. Walter, and J. Bock, "Superconducting magnetic bearings for a 2 MW/10 kW h class energy storage flywheel system," *Superconductor Science and Technology,* vol. 17, no. 5, pp. S229-S233, 2004.

[37] T. Ichihara, *et al.*, "Application of superconducting magnetic bearings to a 10 kWh-class flywheel energy storage system," *IEEE Transactions on Applied Superconductivity,* vol. 15, no. 2 PART II, pp. 2245-2248, 2005.

[38] N. Koshizuka, "R&D of superconducting bearing technologies for flywheel energy storage systems," *Physica C: Superconductivity and its Applications,* vol. 445-448, no. 1-2, pp. 1103-1108, 2006.

[39] M. Strasik, *et al.*, "Design, fabrication, and test of a 5-kWh/100-kW flywheel energy storage utilizing a high-temperature superconducting bearing," *IEEE Transactions on Applied Superconductivity,* vol. 17, no. 2, pp. 2133-2137, 2007.

[40] F. N. Werfel, *et al.*, "A compact HTS 5 kWh/250 kW flywheel energy storage system," *IEEE Transactions on Applied Superconductivity,* vol. 17, no. 2, pp. 2138-2141, 2007.

[41] F. N. Werfel, *et al.*, "250 kW flywheel with HTS magnetic bearing for industrial use," *Journal of*

Physics: Conference Series, vol. 97, no. 1, 2008.

[42] Q. He, H. Liu, Y. Zhang, J. Ye, and Q. Niu, "The characteristics of hybrid ceramic ball bearing for high-speed spindle " *International Conference on Mechatronics and Automation, (ICMA 2009),* pp. 2489 - 2494, 2009.

[43] L. Sibley, "Patented Flywheel Energy Storage System," *A report of Tribology Systems Inc, Warminster PA 18974, USA,* 2010.

[44] M. Strasik*, et al.*, "Design, fabrication, and test of a 5-kWh/100-kW flywheel energy storage utilizing a high-temperature superconducting bearing," *IEEE transactions on applied superconductivity,* vol. 17, no. 2, pp. 2133–2137, 2007.

[45] "Argonne National Laboratory," http://www.anl.gov/.

[46] U. Floegel-Delor*, et al.*, "Fabrication of HTS bearings with ton load performance," *IEEE Transactions on Applied Superconductivity,* vol. 17, no. 2, pp. 2142-2145, 2007.

[47] A. Ruddell, "Investigation on Storage Technologies for Intermittent Renewable Energies: Evaluation and recommended R&D strategy," *Storage Technology Report, CCLRC-Rutherford Appleton Laboratory,* June 2003.

[48] D. W. Swett and J. G. I. Blanche, "Flywheel charging module for energy storage used in electromagnetic aircraft launch system," *Magnetics, IEEE Transactions on,* vol. 41, no. 1, pp. 525-528, 2005.

[49] R. G. Lawrence, K. L. Craven, and G. D. Nichols, "Flywheel UPS," *IEEE Industry Applications Magazine,* vol. 9, pp. 44-50, 2003.

[50] O. Saito, G. Kuwata, and S. Saito, "Development of the flywheel for uninterruptible power supply," *Transactions of the Japan Society of Mechanical Engineers, Part C,* vol. 76, no. 769, pp. 2255-2261 2010.

[51] M. L. Lazarewicz and T. M. Ryan, "Integration of flywheel-based energy storage for frequency regulation in deregulated markets," *IEEE PES General Meeting,* 2010.

[52] J. Cleary, M. L. Lazarewicz, L. J. Nelson, R. Rounds, and J. Arsenault, "Interconnection study: 5MW of Beacon power flywheels on 23 kV line - Tyngsboro, MA " *IEEE Conference on Innovative Technologies for an Efficient and Reliable Electricity Supply, CITRES,* pp. 285-291 2010.

[53] P. Fairley, "Flywheels keep the grid in tune," *Spectrum, IEEE,* vol. 48, no. 7, pp. 16-18, 2011.

[54] M. M. Flynn, McMullen, P., Solis, O., "High-speed flywheel and motor drive operation for energy recovery in a mobile gantry crane," *Conference Proceedings - IEEE Applied Power Electronics Conference and Exposition - APEC,* pp. 1151-1157, 2007.

[55] B. Johansson, "Reduction of network peak power and power swing demand in mine hoist applications," *Hoist and Haul 2010 - Proceedings of the International Conference on Hoisting and Haulage,* pp. 111-118, 2010.

[56] R. T. J. Beno, and R. Hebner, "Flywheel batteries for vehicles," *Proceedings of the 2002 Workshop on Autonomous Underwater Vehicles, San Antonio, TX, United States,* Jun 20-21 2002.

[57] P. P. Acarnley*, et al.*, "Design principles for a flywheel energy store for road vehicles," *IEEE Transactions on Industry Applications,* vol. 32, pp. 1402-1408, 1996.

[58] J. He, G. Ao, J. Guo, Z. Chen, and L. Yang, "Hybrid electric vehicle with flywheel energy storage system," *WSEAS Transactions on Systems,* vol. 8, no. 5, pp. 638-648, 2009.

[59] J. G. Bitterly, "Flywheel technology: past, present, and 21st century projections," *IEEE Aerospace and Electronic Systems Magazine,,* vol. 13, pp. 13-16, 1998.

[60] V. Babuska, S. M. Beatty, B. J. DeBlonk, and J. L. Fausz, "A review of technology developments in flywheel attitude control and energy transmission systems," *IEEE Aerospace Conference Proceedings,* vol. 4, pp. 2784-2800, 2004.

[61] W. Wang, "Design of high speed flywheel motor/generator for aerospace applications," *PhD Thesis - The Pennsylvania State University,* 2004.

[62] W. Wang, H. Hofmann, and C. E. Bakis, "Ultrahigh speed permanent magnet motor/generator for aerospace flywheel energy storage applications," *IEEE International Conference on Electric Machines and Drives,* pp. 1494-1500, 2005.

[63] D. Hockney*, et al.*, "Extreme energy density flywheel energy storage system for space applications," *6th International Energy Conversion Engineering Conference, IECEC,* 2008.

[64] J. R. Sears, "The next generation of energy storage technology," *Proceeding 26th Annual International Telecommunication Energy Conference,* pp. 218-222, Sep. 2004.

[65] P. V. d. Bossche*, et al.*, "An assessment of sustainable battery technology," *Journal of power sources,* vol. 162, no. 2, pp. 913-919, 2006.

[66] "Electric Storage Association," http://www.electricitystorage.org.

[67] R. B. Schainker, "Executive overview- energy storage options for a sustainable energy future," *IEEE PES General Meeting,* pp. 2309 - 2314 2004.

[68] A. Oudalov, D. Chartouni, and C. Ohler, "Optimizing a Battery Energy Storage System for Primary Frequency Control," *IEEE Transactions on Power Systems,* vol. 22, pp. 1259 – 1266, 2007.

[69] L. Sang-Seung, K. Young-Min, P. Jong-Keun, M. Seung-Il, and Y. Yong-Tae, "Compressed Air

Energy Storage Units for Power Generation and DSM in Korea," *IEEE Power Engineering Society General Meeting,* pp. 1-6, 2007.

[70] J. M. Iocca, A. C. Kelsall, and R. W. Potts, "Compressed air energy storage, an alternative to pumped hydro," *Power Engineering,* vol. 90, pp. 30-33, 1986.

[71] R. B. Schainker and M. Nakhamkin, "Compressed-air energy storage (CAES):overview, performance and cost data for 25 MW and 220 MW plants," *IEEE Transactions on Power Apparatus and Systems,* vol. PAS-104, pp. 791-795, 1985.

[72] S. Lemofouet and A. Rufer, "A Hybrid Energy Storage System Based on Compressed Air and Supercapacitors With Maximum Efficiency Point Tracking (MEPT)," *IEEE Transactions on Industrial Electronics,* vol. 53, no. 4, pp. 1105 – 1115, 2006.

[73] T. Bossmann, A. Bouscayrol, P. Barrade, S. Lemoufouet, and A. Rufer, "Energetic Macroscopic Representation of a hybrid storage system based on supercapacitors and compressed air," *IEEE International Symposium on Industrial Electronics,* pp. 2691 – 2696, 2007.

[74] J. M. Carrasco, "Power-Electronic Systems for the Grid Integration of Renewable Energy Sources- A Survey," *IEEE Trans on Ind. Electro.,* pp. 1002- 1016, 2006.

[75] J. R. Sears, "TEX: The next generation of energy storage technology," *Proc. 26th Annual Int. Telecom. Energy Conf.,* pp. 218–222, 2004.

[76] "Environmental Science Division, Department of Energy, USA," http://www.ead.anl.gov/index.cfm.

[77] K. Thiel, "Energy storage utilizing water power," *Int. J. Hydropower & Dams,* vol. 2, pp. 61-64, 1995.

[78] A. Bocquel and J. Janning, "Analysis of a 300 MW variable speed drive for pump-storage plant applications," *European Conference on Power Electronics and Applications,* 2005.

[79] S. Schoenung, "Energy storage systems cost update: a study for the DOE Energy Storage Systems Program," *Sandia National Laboratories, Albuquerque, New Mexico 87185 and Livermore, California 94550, USA,* April 2011.

[80] "International Power First Hydro, UK," http://www.fhc.co.uk/.

[81] M. Urata and T. Murayama, "Superconducting Energy Storage Systems," *Nihon Enerugi Gakkaishi/Journal of the Japan Institute of Energy,* vol. 81, pp. 799-810, 2002.

[82] W. Buckles and W. V. Hassenzahl, "Superconducting magnetic energy storage," *IEEE Power Engineering Review,* vol. 20, pp. 16-20, 2000.

[83] W. Hassenzahl, "Superconducting magnetic energy storage," *Applied Superconductivity Conference,* 1988.

[84] H. Makinen, R. Mikkonen, and J. T. Eriksson, "Availability analysis of a 100 kWh superconducting magnetic energy storage," *Proceedings of the 13th International Conference on Magnet Technology,* 1994.

[85] e. a. A. Friedman, "Superconducting magnetic energy storage device operating at liquid nitrogen temperatures," *Cryogenics,* vol. 39, 1999.

[86] "American Superconductor, USA," http://www.amsc.com/.

[87] H. Spath and K. P. Becker, "Energy storage by capacitors," *European Transactions on Electrical Power,* vol. 12, pp. 211-216, 2002.

[88] T. Peppel and E. Al, "Elimination of high power delivery rates by energy storage in super-capacitors," *European Conference Power Electronics and Applications, Dresden, Germany.,* 2005.

[89] R. K. a. M. Carlen, "Principles and applications of electrochemical capacitors," *Electrochimica Acta,* vol. 45, pp. 2483-2498, 2000.

[90] "Library of Congress Home, USA," http://www.loc.gov.

[91] C. Zhang and K. J. Tseng, "A Novel Flywheel Energy Storage System with Partially-Self-Bearing Flywheel-Rotor," *IEEE Trans on Energy Conversion,* vol. 22, no. 2, pp. 477 – 487, 2007.

[92] H. Ibrahim, A. Ilinca, and J. Perron, "Energy storage systems—Characteristics and comparisons," *Science Direct,* pp. 1221–1250, 2008.

[93] A. F. Fischbach, "The future of fuel cells," *Electrical Construction and Maintenance,* vol. 104, pp. 26-32, 2005.

[94] J. V. Mierlo, P. V. d. Bossche, and G. Maggetto, "Models of energy sources for EV and HEV: Fuel cells, batteries, ultracapacitors, flywheels and engine-generators," *Journal of power sources,* vol. 128, pp. 76-89, 2004.

[95] H. Ibrahim, A. Ilinca, and J. Perron, "Energy storage systems-Characteristics and comparisons," *Renewable and Sustainable Energy Reviews,* vol. 12, no. 5, pp. 1221-1250, 2008.

[96] H. Chen, T. N. Cong, W. Yang, C. Tan, and Y. Li, "Progress in electrical energy storage system: A critical review," *Progress in Natural Science,* no. 19, pp. 291–312, 2009.

[97] David Connolly,
"A review of energy storage technologies for the integration of fluctuating renewable energy "
Tech. rep. Limerick University, Oct. 2010.

[98] S. Vazquez, S. M. Lukic, E. Galvan, L. G. Franquelo, and J. M. Carrasco, "Energy Storage Systems for Transport and Grid Applications," *Industrial Electronics, IEEE Transactions on,* vol.

57, no. 12, pp. 3881-3895, 2010.

[99] M. Beaudin, H. Zareipour, A. Schellenberglabe, and W. Rosehart, "Energy storage for mitigating the variability of renewable electricity sources: An updated review," *Energy for Sustainable Development,* vol. 14, pp. 302–314, Sep. 2010.

[100] "Emerging Energy Storage Technologies in Europe," *Rapport Frost & Sullivan,* 2003.

[101] M. Henley, "Grid-scale Energy Storage Technology Opportunities," *Boeing Research & Technology / Boeing Energy, The Boeing Company,* Aug. 2010.

[102] T. D. Nguyen, K.-J. Tseng, S. Zhang, and H. T. Nguyen, "A Novel Axial Flux Permanent Magnet Machine for Flywheel Energy Storage System: Design and Analysis," *IEEE Transactions on Industrial Electronics,* no. 99, 2010.

[103] B. Bose, "Motion control with induction motors," *Power Electronics and Variable Frequency Drives:Technology and Applications,* pp. 209 - 276 1996.

[104] P. J. Lawrenson, J. M. Stephenson, N. N. Fulton, P. T. Blenkinsop, and J. Corda, "Variable-speed switched reluctance motors," *Electric Power Applications, IEE Proceedings B,* vol. 127, no. 4, pp. 253-265, 1980.

[105] W. F. Ray*, et al.*, "High-Performance Switched Reluctance Brushless Drives," *Industry Applications, IEEE Transactions on,* vol. IA-22, no. 4, pp. 722-730, 1986.

[106] H. H. Moghbelli and M. H. Rashid, "Performance review of the switched reluctance motor drives," in *Circuits and Systems, 1991., Proceedings of the 34th Midwest Symposium on*, 1991, pp. 162-165 vol.1.

[107] P. Vas and W. Drury, "Electrical machines and drives: present and future," in *Electrotechnical Conference, 1996. MELECON '96., 8th Mediterranean*, 1996, pp. 67-74 vol.1.

[108] S. Jebarani Evangeline and S. Suresh Kumar, "Torque Ripple Minimization of switched reluctance drives - A survey," in *Power Electronics, Machines and Drives (PEMD 2010), 5th IET International Conference on*, 2010, pp. 1-6.

[109] X. D. Xue, K. W. E. Cheng, and S. L. Ho, "Optimization and Evaluation of Torque-Sharing Functions for Torque Ripple Minimization in Switched Reluctance Motor Drives," *Power Electronics, IEEE Transactions on,* vol. 24, no. 9, pp. 2076-2090, 2009.

[110] R. Krishnan and P. Vijayraghavan, "State of the art: acoustic noise in switched reluctance motor drives," in *Industrial Electronics Society, 1998. IECON '98. Proceedings of the 24th Annual Conference of the IEEE*, 1998, pp. 929-934 vol.2.

[111] T. Matsuo, "Design and Control of a Synchronous Reluctance Motor Drive," *Ph.D. Thesis, University of Wisconsin-Madison,* May, 1994.

[112] J.-D. Park, C. Kalev, and H. F. Hofmann, "Control of High-Speed Solid-Rotor Synchronous Reluctance Motor/Generator for Flywheel-Based Uninterruptible Power Supplies," *IEEE Transactions on Industrial Electronics,* vol. 55, no. 8, pp. 3038 - 3046, Aug. 2008

[113] H. Hofmann and S. R. Sanders, ""Synchronous reluctance motor/alternator for

flywheel energy storage systems," " *Power Electronics in Transportation, Dearborn, MI, USA,* 24-25 Oct. 1996.

[114] T. J. E. Miller, A. Hutton, C. Cossar, and D. A. Staton, "Design of a synchronous reluctance motor drive," *Industry Applications, IEEE Transactions on,* vol. 27, no. 4, pp. 741-749, 1991.

[115] A. Binder and T. Schneider, "Permanent magnet synchronous generators for regenerative energy conversion - a survey," in *Power Electronics and Applications, 2005 European Conference on*, 2005, pp. 10 pp.-P.10.

[116] W. S. Leung and J. C. C. Chan, "A New Design Approach for Axial-Field Electrical Machines," *Power Apparatus and Systems, IEEE Transactions on,* vol. PAS-99, no. 4, pp. 1679-1685, 1980.

[117] J. R. Bumby and R. Martin, "Axial-flux permanent-magnet air-cored generator for small-scale wind turbines," *Electric Power Applications, IEE Proceedings -,* vol. 152, no. 5, pp. 1065-1075, 2005.

[118] T. F. Chan and L. L. Lai, "An Axial-Flux Permanent-Magnet Synchronous Generator for a Direct-Coupled Wind-Turbine System," *Energy Conversion, IEEE Transactions on,* vol. 22, no. 1, pp. 86-94, 2007.

[119] C. Boccaletti, P. Di Felice, L. Petrucci, and E. Santini, "Parametric analysis of axial flux wind generators focused on total harmonic distortion evaluation," *Renewable Power Generation, IET,* vol. 5, no. 2, pp. 148-159, 2011.

[120] A. Di Gerlando, G. Foglia, M. F. Iacchetti, and R. Perini, "Axial Flux PM Machines With Concentrated Armature Windings: Design Analysis and Test Validation of Wind Energy Generators," *Industrial Electronics, IEEE Transactions on,* vol. 58, no. 9, pp. 3795-3805, 2011.

[121] L. Mingyao, H. Li, L. Xin, Z. Xuming, and Z. Q. Zhu, "A Novel Axial Field Flux-Switching Permanent Magnet Wind Power Generator," *Magnetics, IEEE Transactions on,* vol. 47, no. 10, pp. 4457-4460, 2011.

[122] P. R. Upadhyay, K. R. Rajagopal, and B. P. Singh, "Design of a compact winding for an axial-flux permanent-magnet brushless DC motor used in an electric two-wheeler," *Magnetics, IEEE Transactions on,* vol. 40, no. 4, pp. 2026-2028, 2004.

[123] Y. Yee-Pien, L. Yih-Ping, and C. Cheng-Huei, "Design and control of axial-flux brushless DC wheel motors for electric Vehicles-part I: multiobjective optimal design and analysis," *Magnetics, IEEE Transactions on,* vol. 40, no. 4, pp. 1873-1882, 2004.

[124] P. Zheng*, et al.*, "Evaluation of the magnetic coupling degree and performance of an axial-axial flux compound-structure permanent-magnet synchronous machine used for hybrid electric vehicles," *Journal of Applied Physics,* vol. 103, no. 7, pp. 07F113-07F113-3, 2008.

[125] N. P. Shah, A. D. Hirzel, and C. Baekhyun, "Transmissionless Selectively Aligned Surface-Permanent-Magnet BLDC Motor in Hybrid Electric Vehicles," *Industrial Electronics, IEEE Transactions on,* vol. 57, no. 2, pp. 669-677, 2010.

[126] O. Wallmark, P. Kjellqvist, and F. Meier, "Analysis of Axial Leakage in High-Speed Slotless PM Motors for Industrial Hand Tools," *Industry Applications, IEEE Transactions on,* vol. 45, no. 5, pp. 1815-1820, 2009.

[127] C. Anyuan, R. Nilssen, and A. Nysveen, "Performance Comparisons Among Radial-Flux, Multistage Axial-Flux, and Three-Phase Transverse-Flux PM Machines for Downhole Applications," *Industry Applications, IEEE Transactions on,* vol. 46, no. 2, pp. 779-789, 2010.

[128] Y. Guo-Jhih, H. Liang-Yi, W. Jing-Hui, T. Mi-Ching, and W. Xin-Yi, "Axial-Flux Permanent Magnet Brushless Motor for Slim Vortex Pumps," *Magnetics, IEEE Transactions on,* vol. 45, no. 10, pp. 4732-4735, 2009.

[129] S. Jung-Moo, R. Se-Hyun, K. Joo-Han, C. Jun-Hyuk, and J. In-Soung, "Design of axial flux permanent magnet brushless DC motor for robot joint module," in *Power Electronics Conference (IPEC), 2010 International*, 2010, pp. 1336-1340.

[130] F. Caricchi, F. Maradei, G. D. Donato, and F. G. Capponi, "Axial-Flux Permanent Magnet Generator for Induction Heating Gen-sets," *IEEE Transactions on Industrial Electronics,* 2009.

[131] F. Caricchi, F. Crescimbini, and O. Honorati, "Low-cost compact permanent magnet machine for adjustable-speed pump application," *Industry Applications, IEEE Transactions on,* vol. 34, no. 1, pp. 109-116, 1998.

[132] A. Yuejun, L. Guoming, W. Peng, W. Hongliang, and M. Zhaojun, "Magnetic force analysis and experiment of novel permanent magnet axial thrust balance structure in canned motor pump," in *Advanced Computer Control (ICACC), 2010 2nd International Conference on*, 2010, pp. 396-398.

[133] Z. Zhang, F. Profumo, and A. Tenconi, "Axial flux versus radial flux PM motors," *in Proc. SPEEDAM, Capri, Italy,* pp. A4-19-A4-25, 1996.

[134] R. Qu, "Design and analysis of dual-rotor, radial-flux, toroidallywound, surface-mounted PM machines," *Ph.D. Thesis, University of Wisconsin-Madison,* Aug. 2002.

[135] J. F. Eastham*, et al.*, "Novel axial flux machine for aircraft drive: design and modeling," *Magnetics, IEEE Transactions on,* vol. 38, no. 5, pp. 3003-3005, 2002.

[136] F. Profumo, A. Tenconi, M. Cerchio, J. F. Eastham, and P. C. Coles, "Axial flux plastic multi-disc brushless PM motors: performance assessment," in *Applied Power Electronics*

Conference and Exposition, 2004. APEC '04. Nineteenth Annual IEEE, 2004, pp. 1117-1123 vol.2.

[137] X. Wang and K. Xiao, "Analysis for magnetic field in the air gap of the wheel multi-disc coreless permanent magnet synchronous motor," in *Electrical Machines and Systems, 2009. ICEMS 2009. International Conference on*, 2009, pp. 1-4.

[138] T. S. El-Hasan, P. C. K. Luk, F. S. Bhinder, and M. S. Ebaid, "Modular design of high-speed permanent-magnet axial-flux generators," *Magnetics, IEEE Transactions on,* vol. 36, no. 5, pp. 3558-3561, 2000.

[139] W. Fei, P. C. K. Luk, and T. S. El-Hasan, "Rotor Integrity Design for a High-Speed Modular Air-Cored Axial-Flux Permanent-Magnet Generator," *Industrial Electronics, IEEE Transactions on,* vol. 58, no. 9, pp. 3848-3858, 2011.

[140] J. F. Gieras, R.-J. Wang, and M. J. Kamper, "Axial Flux Permanent Magnet Brushless Machines," *Kluwer Academic Publishers,* 2005.

[141] S. Gair, J. F. Eastham, and F. Profumo, "Permanent magnet brushless d.c. drives for electric vehicles," *Conference on Electric Machines and Power Electronics ACEMP'95, Kusadasi, Turkey,* pp. 638-643, 1995.

[142] E. Spooner, B. Chalmers, and M. M. El-Missiry, "A Compact brushless d.c. machine," *Electric Drives Symposium EDS'90, Capri, Italy,* pp. 239-243, 1990.

[143] M. Lukaniszyn, R. Wrobel, A. Mendrela, and R. Drzewoski, "Towards optimization of the disk-type brushless d.c. motor by changing the stator core structure," *International Conference on on Electric Machine ICEM'2000,* pp. 1357-1360, 2000.

[144] Z. Zhong and T. Lipo, "Improvements in EMC performance of inverter-fed motor drives," *IEEE Transactions on Industry Applications,* vol. 31, no. 6, pp. 1247-1256, 1995.

[145] A. K. Sawhney, "A Course in Electrical Machine Design," *Dhanpat Rai & Sons,* 1987.

[146] A. Parviainen, "Design Of Axial-Flux Permanent-Magnet Low-Speed Machines And Performance Comparison Between Radial-Flux And Axial-Flux Machines," *Ph.D. Thesis Lappeenranta University of Technology,* 2005.

[147] F. Sahin, A. M. Tuckey, and A. J. A. Vandenput, "Design, development and testing of a high-speed axial-flux permanent-magnet machine," *Thirty-Sixth IAS Annual Meeting, IEEE Industry Applications Conference,* vol. 3, pp. 1640 - 1647, 2001.

[148] A. S. Holmes, G. Hong, and K. R. Pullen, "Axial Flux Permanent Magnet Machines for Micropower Generation," *Journal of Microelectromechanical Systems,* vol. 14, no. 1, pp. 54 - 62, Feb. 2005.

[149] J. K. Hendershot and T. J. E. Miller, "Design of Brushless Permanent Magnet Motor," *Clagna*

Physics Publishing and Clarendon Press, Oxford, 1994.

[150] D. C. Hanselman, "Brushless Permanent Magnet Motor Design," *Second Edition, MacGraw-Hill,* March 2003.

[151] A. E. Fitzgerald, C. J. Kingsley, and S. D. Umans, "Electric Machinery, Sixth Edition," *McGraw-Hill Higher Education,* 2003.

[152] P. C. Krouse, O. Wasynczuk, and S. D. Sudhoff, "Analysis of Electrical Machinery and Drive System," *Piscataway, NJ: IEEE Press,* 2004.

[153] S. J. Salon, "Finite Element Analysis of Electrical Machines," *Kluwer Academic Publishers,* 1995.

[154] N. Bianchi, "Electrical Machine Analysis Using Finite Elements," *Talor & Francis,* 2005.

[155] J. P. A. Bastos and N. Sadowski, "Electromagnetic Modeling by Finite Element Methods," *Marcel Dekker Inc.,* 2003.

[156] Z. Q. Zhu and D. Howe, "Influence of design parameters on cogging torque in permanent magnet machines," *IEEE Trans on Energy Conversion,* vol. 15, no. 4, pp. 407–412, Dec. 2000.

[157] M. Nakano, H. Kometani, and M. Kawamura, "A study on eddy-current losses in rotors of surface permanent magnet synchronous machines," *IEEE Transactions on Industry Applications,* vol. 42, no. 2, pp. 429 - 435, Mar. 2006.

[158] J. Wang, K. Atallah, R. Chin, W. M. Arshad, and H. Lendenmann, "Rotor Eddy-Current Loss in Permanent-Magnet Brushless AC Machines," *IEEE Transactions on Magnetics,* vol. 46, no. 7, pp. 2701 - 2707, July 2010.

[159] S.-H. Han, T. M. Jahns, and Z. Q. Zhu, "Analysis of Rotor Core Eddy-Current Losses in Interior Permanent-Magnet Synchronous Machines," *IEEE Trans. on Industry Applications,* vol. 46, no. 1, pp. 196 - 205, 2010.

[160] N. Mohan, T. M. Undeland, and W. P. Robbins, "Power Electronics: Converters, Applications, and Design," *John Wiley & Sons,* 2003.

[161] "Ansoft Maxwell 3D Electromagnetic and Electromechanical Analysis," *Ansoft Corporation, Pittsburgh, PA 15219,* 2009.

[162] M. P. Kazmierkowski and L. Malesani, "Current control techniques for three-phase voltage-source pwm converters: A survey," *IEEE Transactions on Industrial Electronics,* vol. 45, no. 5, pp. 691-703, 1998.

[163] D. C. Lee and Y. S. Kim, "Control of single-phase-to-three-phase AC/DC/AC PWM converters for induction motor drives," *IEEE Transactions on Industrial Electronics,* vol. 54, no. 2, pp. 797-804, 2007.

[164] K. M. Rahman, M. Rezwan Khan, M. A. Choudhury, and M. A. Rahman, "Variable-band hysteresis current controllers for PWM voltage-source inverters," *IEEE Transactions on Power Electronics,* vol. 12, no. 6, pp. 964-970, 1997.

[165] K. H. Kim and M. J. Youn, "A simple and robust digital current control technique of a PM synchronous motor using time delay control approach," *IEEE Transactions on Power Electronics,* vol. 16, no. 1, pp. 72-82, 2001.

[166] W. C. Lee, T. K. Lee, and D. S. Hyun, "Comparison of single-sensor current control in the DC link for three-phase voltage-source PWM converters," *IEEE Transactions on Industrial Electronics,* vol. 48, no. 3, pp. 491-505, 2001.

[167] S. H. Ko, S. R. Lee, H. Dehbonei, and C. V. Nayar, "Application of voltage- and current-controlled voltage source inverters for distributed generation systems," *IEEE Transactions on Energy Conversion,* vol. 21, no. 3, pp. 782-792, 2006.

[168] B. K. Bose, "Modern power electronics and AC drives," *Prentice Hall,* 2002.

[169] R. Cardenas, R. Pena, G. Asher, and J. Clare, "Power smoothing in wind generation systems using a sensorless vector controlled induction Machine driving a flywheel," *IEEE Transaction on Energy Conversion,* vol. 19, no. 1, pp. 206 - 216 2004.

[170] G. Pellegrino, P. Guglielmi, E. Armando, and R. Bojoi, "Self-Commissioning Algorithm for Inverter Non-Linearity Compensation in Sensorless Induction Motor Drives," *IEEE Transactions on Industry Applications,* vol. PP, no. 99, 2010.

[171] K. Geldhof, A. V. d. Bossche, and J. Melkebeek, "Rotor Position Estimation of Switched Reluctance Motors Based on Damped Voltage Resonance," *IEEE Transactions on Industrial Electronics,* vol. PP, no. 99, 2009.

[172] D. D. Reigosa, P. Garcia, F. Briz, D. Raca, and R. D. Lorenz, "Modeling and Adaptive Decoupling of High-Frequency Resistance and Temperature Effects in Carrier-Based Sensorless Control of PM Synchronous Machines," *IEEE Transactions on Industrial Electronics,* vol. 46, no. 1, pp. 139 - 149 2010.

[173] G.-D. Andreescu, C. I. Pitic, F. Blaabjerg, and I. Boldea, "Combined flux observer with signal injection enhancement for wide speed range sensorless direct torque control of IPMSM drives," *IEEE Transactions on Energy Conversion,* vol. 23, no. 2, pp. 393–402, Jun. 2008.

[174] Q. Gao, G. Asher, and M. Sumner, "Sensorless position and speed control of induction motors using high-frequency injection and without offline precommissioning," *IEEE Transactions on Industrial Electronics,* vol. 54, no. 5, pp. 2474–2481, Oct. 2007.

[175] I. Boldea*, et al.*, "DTFC-SVM motion sensorless control of a PM-assisted reluctance synchronous machine as starter-alternator for hybrid vehicles, vol. 21, no. 3, pp. , ," *IEEE Trans. Power Electron.,* vol. 21, no. 3, pp. 711–719, 2006.

[176] M. Barut, S. Bogosyan, and M. Gokasan, "Experimental evaluation of braided EKF for sensorless control of induction motors," *IEEE Transactions on Industrial Electronics,* vol. 55, no. 2, pp. 620–632, 2008.

[177] M. Barut, S. Bogosyan, and M. Gokasan, "Speed-sensorless estimation for induction motors using extended Kalman filters," *IEEE Trans. Ind. Electron.,* vol. 54, no. 1, pp. 272–280, 2007.

[178] M. F. Rahman, M. E. Haque, L. Tang, and L. Zhong, "Problems associated with the direct torque control of an interior permanent magnet synchronous motor drive and their remedies," *IEEE Transactions on Industrial Electronics,* vol. 51, no. 4, pp. 799–809, Aug. 2004.

[179] B. Nahid-Mobarakeh, F. Meibody-Tabar, and F.-M. Sargos, "Back EMF estimation-based sensorless control of PMSM: Robustness with respect to measurement errors and inverter irregularities," *IEEE Transactions on Industrial Electronics,* vol. 43, no. 2, pp. 485–494, 2007.

[180] D. Cascadei, G. Serra, A. Stefani, A. Tani, and L. Zarri, "DTC drives for wide speed range applications using a robust flux-weakening algorithm," *IEEE Trans. Ind. Electron.,* vol. 54, no. 5, pp. 2451–2461, 2007.

[181] P. Vas, "Sensorless vector and direct torque control," *Oxford University Press,* 1998.

[182] T. D. Nguyen and K. J. Tseng, "Comparison of Axial Flux Permanent Magnet Machines with Fractional and Integral Slot per Pole," *IEEE Power Engineering Society General Meeting,* 2011 (accepted for publication).

[183] T. D. Nguyen and K. J. Tseng, "Control of a Dual-airgap Axial Flux Permanent Magnet Machine for Flywheel Energy Storage System: A Model Predictive Control Approach," *Australian Journal of Electrical & Electronics Engineering,* 2012 (in press).

APPENDICES

Appendix A:

Preliminary design of the AFPM machine with q = 2 slots / pole / phase

Description and equations		Reference
A.1 Main dimensions		
Power of the machine	$S = 1000$ [VA]	
Frequency	$f = 200$ [Hz]	
Number of phases	$m = 3$	
Number of pole pairs	$p = 2$	
Rotor velocity	$n_s = \frac{f}{p}$ [r.p.s]	
Distribution winding factor	$k_{w1} = 0.95$	
Air gap flux density	$B_{mg} = 0.6$ [T]	
Inner-to-outer PM radius	$k_d = 1/\sqrt{3}$	
EMF-to- phase voltage ratio	$\varepsilon = 0.98$	
Stator line current density	$A_m = 10000$ [A/m]	
Outer diameter	$D_o = \sqrt[3]{\frac{4\varepsilon S}{\pi^2 n_s k_{w1} \alpha_M B_{mg} A_m (1+k_d)(1-k^2{}_d)\sin\left(\frac{\alpha_M \pi}{2}\right)}} = 0.088$ [m]	(3.84)
Choose	$D_o = 0.09$ [m]	
Inner diameter	$D_i = D_o / \sqrt{3} = 0.052$ [m]	
Operation temperature of PM	$\vartheta_{PM} = 100\left[{}^0C\right]$	
Temperature coefficients of PM	$\alpha_B = -0.095$	
	$\alpha_H = -0.64$	

Remanent magnetic flux at 20^0C $\quad B_{r20} = 1.26\,[\mathrm{T}]$

Coercive force at 20^0C $\quad H_C = 965000\ [\mathrm{A/m}]$

Remanent magnetic flux at 100^0C

$$B_{r100} = B_{r20}\left[1+\frac{\alpha_B}{100}\left(\vartheta_{PM}-20\right)\right]\ [\mathrm{T}]$$

Coercive force at 100^0C

$$H_{c100} = H_{c20}\left[1+\frac{\alpha_H}{100}\left(\vartheta_{PM}-20\right)\right]\ [\mathrm{A/m}]$$

Physical air gap $\quad g_0 = 0.0009\ [\mathrm{m}]$

Carter factor $\quad k_C = 1.1$

Equivalent air gap $\quad g' = k_C g_0$

Relative recoil magnet permeability

$$\mu_{rrec,100} = \frac{B_{r100}}{\mu_0 H_{C100}}$$

Length of PM of upper rotor $\quad l_{M1} \approx \dfrac{\mu_{rrec} B_{mg} g'}{B_{r100} - B_{mg}}\ [\mathrm{m}]$ (3.11)

Choose $\quad l_{M1} = 0.002\ [\mathrm{m}]$

Total weigh of rotating part $\quad M_{rotor} = 3.15\ [\mathrm{kg}]$

$$g = 9.81\left[m/s^2\right]$$

Peak value of air-gap flux density of the lower half

$$B_{mg2} = \sqrt{B_{mg1}^2 - \frac{8\mu_0 g M_{rotor}}{\pi\alpha_M\left(D_o^2 - D_i^2\right)}}$$ (3.14)

Length of PM of lower rotor $\quad l_{M2} \approx \dfrac{\mu_{rrec} B_{mg2} g'}{B_{r100} - B_{mg2}}\ [\mathrm{m}]$ (3.15)

Choose $\quad l_{M2} = 0.00187\ [\mathrm{m}]$

Number of turns of stator windings for each machine's half is chosen as

$$N_1 = N_2 \approx \frac{\sqrt{2}V}{2\pi n_s B_{mg1}\alpha_M D_o^2\left(1-k_d^2\right)\sin\left(\dfrac{\pi\alpha_M}{2}\right)}$$ (3.76)

Choose $\quad N_1 = N_2 = 208\ [\mathrm{turns}]$

Choose flux density in rotor yoke

$$B_{rot,y} = 1.1\ [\mathrm{T}]$$

Rotor length $\quad l_{rot} = \dfrac{\alpha_M B_{mg1}\pi D_o}{4pB_{rot,y}}$

Choose rotor length $\quad l_{rot} = 0.02\ [\mathrm{m}]$

Choose flux density in stator yoke $\quad B_{s,y} = 1.2\ [\mathrm{T}]$

Lamination stacking factor $k_{st} = 0.95$

Length of stator yoke $w_{bi} = \dfrac{\alpha_M B_{mg1} \pi D_o}{4 p B_{s,y} k_{st}}$ (3.53)

Choose length of stator yoke $w_{bi} = 0.018$ [m]

Choose number of slots $Q = 24$

The number of slots per pole $N_{sm} = \dfrac{Q}{2p}$

Choose flux density in stator tooth $B_{s,t} = 1.4$ [T]

The required minimum narrow tooth $w_{tbi} = \dfrac{\alpha_M \pi B_{mg1} D_i}{2 p B_{s,y} k_{st} N_{sm}}$ (3.55)

The maximum width of slot $w_{sb} = \dfrac{\pi D_i}{Q} - w_{tbi}$ (3.56)

Choose the width of slot $w_{sb} = 0.035$ [m]

The rectangular semi-open slot as shown in Fig. 3.14:

$w_s = 0.0015$ [m]

$d_1 = 0.0015$ [m]

$d_2 = 0.0015$ [m]

$d_3 = 0.0200$ [m]

The length of stator $l_S = d_1 + d_2 + d_3 + w_{bi}$

A.2 Stator winding design

Phase voltage $V = 240$ V

The phase current $I_a = \dfrac{S_{in}}{3V}$

Taking a current density of 5 [A/m^2]

$J_a = 5$ [A/m^2]

The required diameter of stator winding

$$d_{sw} = \sqrt{\frac{4 I_a}{\pi J_a}}$$

Choose $d_{sw} = 0.00063$ [m]

The winding is double-layer type as shown in Fig. 3.17. The number of slots per pole per phase is:

$$q = \frac{Q}{2pm} \quad (3.62)$$

The number of turns per coil $N_{sl} = \dfrac{N_1}{pq} = \dfrac{N_1 m}{Q}$ (3.64)

Taking the number of turns per coil as

$N_{sl} = 26$

The total cross section of number of copper turns in a slot:

$$A_{cu} = 2 N_{sl} \frac{\pi d_{st}^2}{4}$$

Check the space factor

$$spf_S = \frac{A_{cu}}{w_{sb} d_3} = 0.31$$

Space factor satisfies the practical requirement if $spf_s \le 0.4$

Average slot pitch $\tau_{S,avg} = \frac{\pi D}{Q} = \frac{\pi (D_o - D_i)}{2Q}$

Carter factor

$$k_C = \frac{\tau_{s,avg}}{\tau_{s,avg} - \gamma w_s} \quad (3.58)$$

The approximated equivalent air-gap length $g' = k_C g_0$ (3.57)

The number of slots per pole per phase $q = \frac{Q}{2pm}$ (3.62)

The coil pitch-to-pole pitch ratio is $\beta = \frac{w_c(r)}{\tau(r)} = \frac{5*2p}{Q} = 0.833$ (3.67)

The distribution factor ($M = 3$) $k_{d1} = \frac{\sin(\pi / 2m_1)}{q \sin[\pi / (2m_1 q)]}$ (3.69)

The pitch factor $k_{p1} = \sin\left(\beta \frac{\pi}{2}\right)$ (3.70)

The winding factor $k_{w1} = k_{d1} k_{p1} = 0.933$ (3.68)

A.3 Calculating electrical parameter

Specific slot leakage permeance

$$\lambda_{l,s} = \frac{3\beta + 1}{4}\left(\frac{d_3}{3w_{sb}} + \frac{2d_2}{w_s + w_{sb}} + \frac{d_1}{w_s}\right) \quad (3.89)$$

The length of inner connection of each turn

$$l_{l,in} = 0.9 \frac{\pi D_i}{2} \sin\left(\frac{\beta\pi}{p}\right) \quad (3.94)$$

The length of outer connection of each turn

$$l_{l,out} = 0.9 \frac{\pi D_o}{2} \sin\left(\frac{\beta\pi}{p}\right) \quad (3.95)$$

Specific leakage permeances of inner and outer connections

$$\lambda_{l,ein} = \lambda_{l,eout} = 0.1q \quad (3.93)$$

The stator leakage reactance

$$X_l = 4\pi f \mu_0 \frac{N_1^2}{pq}\left[\frac{(D_o - D_i)}{2}\lambda_{ls} + l_{l,in}\lambda_{l,ein} + l_{l,out}\lambda_{l,eout}\right] \quad (3.88)$$

The mutual reactances for upper stator and lower stator (3.87)

$$X_{up,a} = m_1 \mu_0 f \left(\frac{N_1 k_{w1}}{p} \right)^2 \frac{\left(D_o^2 - D_i^2 \right)}{2 g_{up,equ}}$$

$$X_{low,a} = m_1 \mu_0 f \left(\frac{N_1 k_{w1}}{p} \right)^2 \frac{\left(D_o^2 - D_i^2 \right)}{2 g_{low,equ}}$$

where

$$g_{up,equ} = g_0 k_C + \frac{l_{M1}}{\mu_{rrec}}$$

$$g_{low,equ} = g_0 k_C + \frac{l_{M2}}{\mu_{rrec}}$$

The synchronous reactance,

$$X_{up,s} = X_{up,a} + X_l \qquad (3.86)$$

$$X_{low,s} = X_{low,a} + X_l$$

The average length of turn

$$l_{1av} = D_o - D_i + l_{1in} + l_{1out} \qquad (3.100)$$

The resistivity of the armature conductor at operating temperature

$$\rho_{cu,20} = 0.01724 * 10^{-6}$$

$$\alpha_{cu} = 0.00393$$

$$\vartheta_1 = 100^0 C$$

$$\rho_{cu,1} = \rho_{cu,20} \left[1 + \alpha_{cu20} \left(\vartheta_1 - 20 \right) \right] \qquad (3.97)$$

Taking $a_w = 1,\ a_p = 1$

The cross section area of a copper conductor

$$s_a = \frac{\pi d_{st}^2}{4}$$

The armature winding resistance per phase for the d.c. current

$$R_{1dc} = \frac{N_1 l_{1av}}{a_p a_w s_a} \rho_{cu,1} \qquad (3.96)$$

The skin depth of the conductor in free space

$$\chi = \sqrt{\frac{2}{\omega \mu_0 \sigma_{cu,1}}} = \sqrt{\frac{\rho_{cu,1}}{\pi f \mu_0}} \qquad (3.102)$$

The phase resistance

$$R_1 = R_{1,dc} \left[1 + \frac{1}{9} \left(\frac{d_3 d_{st}}{\chi^2} \right)^2 \right] \qquad (3.101)$$

A.4 Calculating air-gap flux density

Permeances for main and leakage fluxes

By taking $l_M = l_{M1}$ for upper stator and $l_M = l_{M2}$ for lower stator, the air gap permeance components are calculated as:

$$G_{g1} = \mu_0 \frac{\pi \alpha_M (D_o^2 - D_i^2)}{8pg'} \tag{3.22}$$

$$G_{g2} = 0.52\mu_0 \frac{D_o - D_i}{2} \tag{3.23}$$

$$G_{g3} = \frac{3.26\alpha_M}{2p} \mu_0 \left(\frac{D_i}{2} + \frac{g}{4} \right) \tag{3.24}$$

$$G_{g4} = \frac{3.26\alpha_M}{2p} \mu_0 \left(\frac{D_o}{2} + \frac{g}{4} \right) \tag{3.25}$$

$$G_{up,g5} = \frac{2\alpha_M}{2p} \mu_0 \left(D_i + g \right) \ln \left(1 + \frac{l_{M1}}{g} \right)$$
$$G_{low,g5} = \frac{2\alpha_M}{2p} \mu_0 \left(D_i + g \right) \ln \left(1 + \frac{l_{M2}}{g} \right) \tag{3.26}$$

$$G_{up,g6} = \frac{2\alpha_M}{2p} \mu_0 \left(D_o + g \right) \ln \left(1 + \frac{l_{M1}}{g} \right)$$
$$G_{low,g6} = \frac{2\alpha_M}{2p} \mu_0 \left(D_o + g \right) \ln \left(1 + \frac{l_{M2}}{g} \right) \tag{3.27}$$

$$G_{up,g7} = \mu_0 \frac{2\left(D_o - D_i \right)}{2\pi} \ln \left(1 + \frac{l_{M1}}{2g} \right)$$
$$G_{low,g7} = \mu_0 \frac{2\left(D_o - D_i \right)}{2\pi} \ln \left(1 + \frac{l_{M2}}{2g} \right) \tag{3.28}$$

$$G_{g8} = 0.308\mu_0 g \tag{3.29}$$

$$G_{up,g9} = \mu_0 \frac{l_{M1}}{4}$$
$$G_{low,g9} = \mu_0 \frac{l_{M2}}{4} \tag{3.30}$$

The air gap permeance of upper stator and lower stator

$$G_{up,g} = G_{g1} + 2(G_{g2} + G_{up,g7}) + G_{g3} + G_{g4} + G_{up,g5} + G_{up,g6} + 4(G_{g8} + G_{up,g9})$$
$$G_{low,g} = G_{g1} + 2(G_{g2} + G_{low,g7}) + G_{g3} + G_{g4} + G_{low,g5} + G_{low,g6} + 4(G_{g8} + G_{low,g9}) \tag{3.21}$$

The permeance leakage flux components:

$$G_{up,10} = \frac{3.26\alpha_M}{2p} \mu_0 \left(\frac{D_i}{2} + \frac{l_{M1}}{8} \right)$$
$$G_{low,10} = \frac{3.26\alpha_M}{2p} \mu_0 \left(\frac{D_i}{2} + \frac{l_{M2}}{8} \right) \tag{3.32}$$

$$G_{upg11} = \frac{3.26\alpha_M}{2p} \mu_0 \left(\frac{D_o}{2} + \frac{l_{M1}}{8} \right)$$
$$G_{lowg11} = \frac{3.26\alpha_M}{2p} \mu_0 \left(\frac{D_o}{2} + \frac{l_{M2}}{8} \right) \tag{3.33}$$

$$G_{g12} = 0.52\mu_0 \left(\frac{D_o - D_i}{2} \right) \quad (3.34)$$

$$G_{up\,g13} = 0.308\mu_0 \frac{l_{M1}}{2}$$
$$G_{low\,g13} = 0.308\mu_0 \frac{l_{M2}}{2} \quad (3.35)$$

The permeance leakage flux of the upper and lower stator respectively

$$G_{up,lM} = G_{up,10} + G_{up,11} + 2G_{12} + 4G_{up,13}$$
$$G_{low,lM} = G_{low,10} + G_{low,11} + 2G_{12} + 4G_{low,13}$$

The PM leakage flux coefficient of the upper and lower stator respectively

$$\sigma_{up\,lM} = 1 + \frac{G_{up\,lM}}{G_{up,g}}$$
$$\sigma_{low\,lM} = 1 + \frac{G_{low\,lM}}{G_{low,g}} \quad (3.36)$$

The magnet permeance of the upper and lower stator respectively

$$G_{up,m} = \frac{\alpha_M \pi \mu_{rrec} \mu_0}{8pl_{M1}} \left(D_o^2 - D_i^2 \right)$$
$$G_{low,m} = \frac{\alpha_M \pi \mu_{rrec} \mu_0}{8pl_{M2}} \left(D_o^2 - D_i^2 \right)$$

The peak value of flux density of upper and lower stator respectively

$$B_{up,mg} = \frac{G_{up,g}}{2G_{up,lM} + G_{up,m} + G_{up,g}} B_r$$
$$B_{low,mg} = \frac{G_{low,g}}{2G_{low,lM} + G_{low,m} + G_{low,g}} B_r \quad (3.17)$$

A.5 Losses and efficiency

Stator winding losses

The winding losses of the upper and lower stator

$$\Delta P_{up,1w} = \Delta P_{low,1w} = mI_a^2 R_1 = 15.77 \text{ [W]} \quad (3.110)$$

Friction loss

Velocity of motor [r.p.m]

$$n = \frac{n_S}{60}$$

The diameter of rotor shaft [145]:

$$d_{sh}[m] = 0.0055 \sqrt[3]{\frac{P_{out}[W]}{n[rpm]}}$$

Select $d_{sh} = 0.02$ [m]

Length of shaft $l_{sh} = 0.16$ [m]

The diameter in bearings

$$d_{shb,} \approx \frac{2}{3} d_{sh}$$

Select $d_{sh,b} = 0.012$ [m]

The outer diameter of the rim attached on rotor

Select $D_{r,o} = 0.124$ [m]

$\gamma_{Al} = 2700$ [kg/m^3]: density of aluminium.

$\gamma_{Fe} = 7860$ [kg/m^3]: density of rotor shaft

Mass of shaft $$m_{sh} \approx \frac{\pi d_{sh}^2}{4} l_{sh}\, \gamma_{Fe}$$

Mass of rotor

$$m_r = 2\frac{\pi\left(D_o^2 - D_i^2\right)}{4} l_{rot}\gamma_{Fe} + \frac{\pi\gamma_{Al}}{4}\left[(D_i^2 - d_{sh}^2) + (D_{r,o}^2 - D_o^2)\right] \quad (3.105)$$

Select $k_{fb} = 2$, the friction loss is

$$\Delta P_{fr} = 0.06 k_{fb}(m_r + m_{sh})n \quad (3.103)$$

Windage loss

$\mu = 1.8 * 10^{-5}$

$$c_f = \frac{3.87}{\sqrt{\frac{2\pi\rho\, n\, D_{r,o}^2}{4\mu}}} \quad (3.124)$$

$$\rho = 1.2$$

$$\Delta P_{wind} = \frac{1}{2} c_f \rho \left(2\pi n\right)^3 \left[\left(\frac{D_{r,o}}{2}\right)^5 - \left(\frac{d_{sh}}{2}\right)^5\right] \quad (3.123)$$

Mechanical loss $$\Delta P_{mech} = \Delta P_{fr} + \Delta P_{wind} = 15.74 \text{ [W]} \quad (3.125)$$

Losses in the permanent magnet

Fundamental frequency of the magnet flux because of the stator slot opening

$$f_{sl} = Qpn_s$$

with $$g_{eq} = g_0 k_C + \frac{l_{M1}}{\mu_{rrec}}$$

$$\beta_{sl} = 0.5\left(1 - \frac{1}{\sqrt{1 + \left(\frac{w_s}{g_{eq}}\right)^2}}\right)$$

$$\Gamma = \frac{2w_s Q}{\pi\left(D_o + D_i\right)}$$

$$a_{sl} = \frac{4}{\pi}\left(0.5 + \frac{\Gamma^2}{0.78 - 2\Gamma^2}\right)\sin(1.6\pi\,\Gamma)$$

$$B_{avg} = \alpha_M B_{up,mg}$$

$$B_{sl} = a_{sl}\beta_{sl}k_C B_{avg}$$

$$\sigma_{PM} = 0.7*10^6 \text{ [S/m]}$$

$$\beta_1 = \frac{4Q}{D_o + D_i} \quad (3.115)$$

$$k = \sqrt{\frac{2\pi\, f_{sl}\mu_0\mu_{rrec}\sigma_{PM}}{2}} \quad (3.116)$$

$$\alpha_1 = (1+j)k \quad (3.114)$$

$$k_z = 1 + \frac{\pi(D_o + D_i)}{2Q(D_o - D_i)} \quad (3.113)$$

$$a_R = \frac{1}{\sqrt{2}}\sqrt{\sqrt{4 + \left(\frac{\beta_1}{k}\right)^4} + \left(\frac{\beta_1}{k}\right)^2} \quad (3.112)$$

losses in the permanent magnet are

$$\Delta P_{up,PM} \approx \Delta P_{low,PM} = \frac{1}{2}a_R k_z \frac{|\alpha_1|^2}{\beta_1^2}\left(\frac{B_{sl}}{\mu_0\mu_{rrec}}\right)^2 \frac{k}{\sigma_{PM}}\alpha_M \frac{\pi}{4}\left(D_o^2 - D_i^2\right) = 16.43 \text{ [W]} \quad (3.111)$$

Rotor core losses

The surface of the rotor disc

$$S_{Fe} = \frac{\pi}{4}\left(D_o^2 - D_i^2\right) \quad (3.118)$$

Electric conductivity of steel

$\sigma_{Fe} = 4.5*10^6$ [S/m]

Relative magnetic permeability of the rotor steel $\mu_r = 300$

Select $a_{R1} = 1.4$, $a_{X1} = 0.8$

$$a_{RFe} = \left[\sqrt{4a_{R1}^2 a_{X1}^2 + \left(a_{R1}^2 - a_{X1}^2 + \frac{\beta_1^2}{k^2}\right)^2} + a_{R1}^2 - a_{X1}^2 + \frac{\beta_1^2}{k^2}\right]^{1/2} \quad (3.119)$$

Rotor core losses in the solid steel

$$\Delta P_{up,2FE} \approx \Delta P_{low,2FE} = \frac{1}{2}a_{RFe}k_Z \frac{|\alpha_1|^2}{\beta_1^2}\left(\frac{B_{sl}}{\mu_0\mu_r}\right)^2 \frac{k}{\sigma_{Fe}}S_{Fe} = 1.98\ 10^{-4} \text{ [W]} \quad (3.117)$$

Stator core losses

Select

$k_{adt} = 1.8$

$k_{ady} = 3$

$\Delta P_{1/50}$ =0.54 [W/kg]

The total area of the teeth

$$S_{\Sigma,t} = \left[\frac{\pi(D_o^2 - D_i^2)}{4} - Qw_{sb} \frac{D_o - D_i}{2} \right] \quad (3.106)$$

The mass of the teeth

$$m_{1,t} = \gamma_{Fe}(d_1 + d_2 + d_3)S_{\Sigma,t} \quad (3.105)$$

The mass of the stator yoke

$$m_{1y} = \gamma_{Fe} w_{bi} \frac{\pi\left(D_o^2 - D_i^2\right)}{4} \quad (3.107)$$

The magnetic flux per pole

$$\varphi_{up,f1} = \frac{1}{2p}\alpha_M B_{up,mg} \sin\left(\frac{\alpha_M \pi}{2}\right) D_o^2 \left(1 - k_d^2\right)$$
$$\varphi_{low,f1} = \frac{1}{2p}\alpha_M B_{low,mg} \sin\left(\frac{\alpha_M \pi}{2}\right) D_o^2 \left(1 - k_d^2\right) \quad (3.72)$$

The magnet flux density in a tooth

$$B_{up,1r} = \frac{\varphi_{up,f1}}{S_{\Sigma,t}}$$
$$B_{low,1r} = \frac{\varphi_{low,f1}}{S_{\Sigma,t}} \quad (3.108)$$

The magnet flux density in the yoke

$$B_{up,1y} = \frac{\varphi_{up,f1}}{w_{bi}\left(D_o - D_i\right)}$$
$$B_{low,1y} = \frac{\varphi_{low,f1}}{w_{bi}\left(D_o - D_i\right)} \quad (3.109)$$

Stator core losses

$$\Delta P_{up,1Fe} = \Delta p_{1/50} \left(\frac{f}{50}\right)^{4/3} \left(k_{adt} B_{up,1t}^{\ 2} m_{1t} + k_{ady} B_{up,1y}^{\ 2} m_{1y}\right) = 7.15 \text{ [W]}$$
$$\Delta P_{low,1Fe} = \Delta p_{1/50} \left(\frac{f}{50}\right)^{4/3} \left(k_{adt} B_{low,1t}^{\ 2} m_{1t} + k_{ady} B_{low,1y}^{\ 2} m_{1y}\right) = 6.81 \text{ [W]} \quad (3.104)$$

The total losses in the AFPM machine

$$\Delta P = \Delta P_{mech} + 2\Delta P_{1w} + \Delta P_{up,1Fe} + \Delta P_{low,1Fe} + 2\Delta P_{up,2,Fe} + 2\Delta P_{up,PM}$$
$$= 94.11 \text{ [W]} \quad (3.126)$$

Electromagnet torque of each machine half:

$$T_{m,up} = 2pm_1 N_1 k_{w1} \phi_{up,f1} I_a$$
$$T_{m,low} = 2pm_1 N_1 k_{w1} \phi_{low,f1} I_a \quad (3.127)$$

The output power

$$P_{out} = \left(T_{m,up} + T_{m,low}\right) 2\pi n_s - (\Delta P_{mech} + 2\Delta P_{up,2,Fe} + 2\Delta P_{up,PM}) = 781 \text{ [W]} \quad (3.129)$$

Efficiency of the AFPM

$$\eta = \frac{P_{out}}{P_{out} + \Delta P} = 89.25 \text{ [\%]} \quad (3.130)$$

Appendix B:

Modeling of Dual-Airgap AFPM machine in Matlab programming

```
#define S_FUNCTION_LEVEL 2
#define S_FUNCTION_NAME  DualAirgapAFPMMachine
#define Rs1_IDX 0 /* upper half of the machine*/
#define GetRs1(S) ssGetSFcnParam(S,Rs1_IDX)
#define Ns1_IDX 1 /* lower half of the machine*/
#define GetNs1(S) ssGetSFcnParam(S,Ns1_IDX)
#define Mmf1_IDX 2
#define Mmf2_IDX 3
#define GetMmf1(S) ssGetSFcnParam(S,Mmf1_IDX)
#define GetMmf2(S) ssGetSFcnParam(S,Mmf2_IDX)
#define RotorParam_IDX 4
#define GetRotorParam(S) ssGetSFcnParam(S,RotorParam_IDX)
#define NPARAM 5
#define NSTATE 6
#define u0(index)  (*uPtrs0[index])

#define PI  (3.141593)
#define Miu0 (1.2566e-6)
#define i_d0 (0.0)

/* Need to include simstruc.h for the definition of the SimStruct and
 * its associated macro definitions.   */
#include "simstruc.h"
#include "math.h"
#include "stdlib.h"

real_T Rs, Ns, Mmf1, Mmf2, J, Ff, P, Ri, Ro, G01, G02, M;
real_T Ud, Uq;

/* begin s-function method */
#define MDL_CHECK_PARAMETERS
#if defined(MDL_CHECK_PARAMETERS) && defined(MATLAB_MEX_FILE)
  /* Function: mdlCheckParameters
   * Abstract: Validate our parameters to verify if they are okay. */
  static void mdlCheckParameters(SimStruct *S)
  {
     /* Check 1st parameter: Stator resistance of motor1 (Ohm) */
     {
        if (!mxIsDouble(GetRs1(S)) ||
           mxGetNumberOfElements(GetRs1(S)) != 1) {
           ssSetErrorStatus(S,"1st parameter to S-function must be a "
                       "scalar \" Stator resistance (Ohm)\" ");
           return;
        }
     }
     /* Check 2nd parameter: WingdingNumbers of motor1 */
     {
        if (!mxIsDouble(GetNs1(S)) ||
           mxGetNumberOfElements(GetNs1(S)) != 1) {
           ssSetErrorStatus(S,"2nd parameter to S-function must be a "
                       "scalar  \"Stator Winding Numbers \" ");
           return;
        }
     }
```

```
    /* Check 3rd parameter: Magnetomative Force induced by magnets (Wb) of motor1  */
    {
       if (!mxIsDouble(GetMmf1(S)) ||
          mxGetNumberOfElements(GetMmf1(S)) != 1) {
          ssSetErrorStatus(S,"3rd parameter to S-function must be a "
                     "scalar \"Magnetomactive Force (Ampere Turns)\" ");
          return;
       }
    }
    /* Check 4th parameter: Inertia, friction factor
    and pairs of poles, Radius and GapLength[J(kg*m^2) F(N*m*s) p Ri(m) Ro(m) g0(m) M (kg)] */
    {
       if (!mxIsDouble(GetRotorParam(S)) ||
          mxGetNumberOfElements(GetRotorParam(S)) != 1) {
          ssSetErrorStatus(S,"4th parameter to S-function must be a "
                     "vector with 7 element\" J, F, poles, innerRadius, outerRadius, GapLength, M\" ");
          return;
       }
    }
 }
#endif /* MDL_CHECK_PARAMETERS */

/* Function: mdlInitializeSizes ===============================================
 * Abstract:
 *    The sizes information is used by Simulink to determine the S-function
 *    block's characteristics (number of inputs, outputs, states, etc.).
 */
static void mdlInitializeSizes(SimStruct *S)
{
          ssSetNumSFcnParams(S, NPARAM);          /* Number of expected parameters  is 7*/
                                                  /* they are as above definition*/
           if (ssGetNumSFcnParams(S) != ssGetSFcnParamsCount(S)) {
      /* Return if number of expected != number of actual parameters */
          ssSetErrorStatus(S,"mismatch parameters number");
           return;
   }
           ssSetNumContStates(S, NSTATE);  /* number of continous states is 8  */
                                                  /* they are: id, iq, theta, w, z, z'       */
          ssSetNumDiscStates(S, 0);  /* nubmer of discrete states is 0 */

          if (!ssSetNumInputPorts(S, 2)) return;          /* set inputPort number to 2 */
          ssSetInputPortWidth(S, 0, 3); /* 0 is the inputPort index, 3 is the width */

          ssSetInputPortWidth(S, 1, 2); /* 1 is the inputPort index, latter 1 is the width */

   /*A port has direct feedthrough if the input is used in either
    * the mdlOutputs or mdlGetTimeOfNextVarHit functions  */
          ssSetInputPortDirectFeedThrough(S, 0, 0); /* 0 is the inputport index
                                    /* and the second 0 means no feed through */
           ssSetInputPortDirectFeedThrough(S, 1, 0);
           if (!ssSetNumOutputPorts(S, 1)) return;
           ssSetOutputPortWidth(S, 0, 18);   /* number is 18 */
           ssSetNumSampleTimes(S, 1);     /* number of sample times is 1 */
           ssSetNumRWork(S, 0);  /* number of real work vector elements   */
           ssSetNumIWork(S, 0);  /* number of integer work vector elements*/
           ssSetNumPWork(S, 0);  /* number of pointer work vector elements*/
           ssSetNumModes(S, 0);  /* number of mode work vector elements   */
           ssSetNumNonsampledZCs(S, 0); /* number of nonsampled zero crossings   */
   ssSetOptions(S, 0);      /* no options */
}
```

```
/* Function: mdlInitializeSampleTimes =====================================
 * Abstract:
 *    This function is used to specify the sample time(s) for your
 *    S-function. You must register the same number of sample times as
 *    specified in ssSetNumSampleTimes.
 */
static void mdlInitializeSampleTimes(SimStruct *S)
{
            /* A continuous function th       at changes during minor integration steps */
           ssSetSampleTime(S, 0, CONTINUOUS_SAMPLE_TIME); /* 0 is the index of sample time
number as defined in above, I defined 1 */
            ssSetOffsetTime(S, 0, 0.0);  /* 0 is the index */
}

#define MDL_INITIALIZE_CONDITIONS   /* Change to #undef to remove function */
#if defined(MDL_INITIALIZE_CONDITIONS)
  /* Function: mdlInitializeConditions ====================================
   * Abstract:
   *    In this function, you should initialize the continuous and discrete
   *    states for your S-function block.  The initial states are placed
   *    in the state vector, ssGetContStates(S) or ssGetRealDiscStates(S).
   *    You can also perform any other initialization activities that your
   *    S-function may require. Note, this routine will be called at the
   *    start of simulation and if it is present in an enabled subsystem
   *    configured to reset states, it will be call when the enabled subsystem
   *    restarts execution to reset the states.
   */
  static void mdlInitializeConditions(SimStruct *S)
  {
            /* initialize the state vecotor  they are id, iq, theta ,w, z all to zero */
            int_T  i;
            real_T *x0 = ssGetContStates(S);
            for (i=0;i<NSTATE;i++)
            {
                        *x0++ =0.;
            }
  }
#endif /* MDL_INITIALIZE_CONDITIONS */

#define MDL_START  /* Change to #undef to remove function */
#if defined(MDL_START)
  /* Function: mdlStart =====================================================
   * Abstract:
   *    This function is called once at start of model execution. If you
   *    have states that should be initialized once, this is the place
   *    to do it.
   */
  static void mdlStart(SimStruct *S)
  {
  /* Get the parameter of the motor, and set to the global variables */
     real_T *Ptr;
            /* upper and lower half (1&2) parameter */
            Rs=*mxGetPr(GetRs1(S));
            Ns=*mxGetPr(GetNs1(S));
            Mmf1=*mxGetPr(GetMmf1(S));
            Mmf2=*mxGetPr(GetMmf2(S));
```

```
  /* mechanical parameters */
            Ptr=mxGetPr(GetRotorParam(S));
            J=*Ptr++;
            Ff=*Ptr++;
            P=*Ptr++;
            Ri=*Ptr++;
            Ro=*Ptr++;
            G01=*Ptr++;
            G02=*Ptr++;
            M=*Ptr;
            printf(" parameters\n Resistance = %f\n Ns = %f\n Mmf1 = %f\n Mmf2 = %f\n J = %f\n
Friction coeff. Ff = %f\n P = %f\n Ri = %f\n Ro = %f\n Go1 = %f\n Go2 = %f\n mass = %f\n", Rs, Ns,
Mmf1, Mmf2, J, Ff, P, Ri, Ro, G01, G02, M);
  }
#endif /*  MDL_START */

/* Function: mdlOutputs =======================================================
 * Abstract:
 *    In this function, you compute the outputs of your S-function
 *    block. Generally outputs are placed in the output vector, ssGetY(S).
 */
static void mdlOutputs(SimStruct *S, int_T tid)
{
            real_T *y = ssGetOutputPortRealSignal(S,0);  /* output */
             real_T *x = ssGetContStates(S);          /* continous state */
            InputRealPtrsType  uPtrs0=ssGetInputPortRealSignalPtrs(S, 0);/*input port0*/
            real_T F1;
            real_T F2;
            real_T thetae;
            real_T id, k, k1, k2, k3, f_linear, i_cd0;

  /* output:          0-2: Stator line currents ia1,ib1,ic1(A)
   *                                                  3-4: Stator currents id1,iq1(A)
   *                                                  5-6: Stator voltages Ud1, Uq1(V)
            7: Electromagnetic torque Te1 (N*m)
            8: Electromagnetic force   Fs1 (N)
                                    9:     Rotor electrical speed We (rad/s)
            10:     Rotor electrical angle theta_e (deg)
                                    11:   Electromagnetic torque Te (N*m)
            12: Electromagnetic force F (N)
            13: Position Displacement z
            14: z'
        */
  /* id=x[0], iq=x[1], theta=x[2], w=x[3], z=x[4], z'=x[5] */

            thetae=x[2]*P;

            y[0]=x[0]*cos(thetae)-x[1]*sin(thetae);
            y[1]=x[0]*cos(thetae-2.*PI/3.)-x[1]*sin(thetae-2.*PI/3.);
            y[2]=x[0]*cos(thetae+2.*PI/3.)-x[1]*sin(thetae+2.*PI/3.);

            y[3]=x[0];  /* id */
            y[4]=x[1];  /* iq */

            y[5]=Ud;  /* ud */
            y[6]=Uq;  /* uq */

            y[7]=(3.0*Miu0*PI*(Ro*Ro-Ri*Ri)*Ns/(16.0*P)) *(Mmf1/(G01-x[4])+Mmf2/(G02+x[4]))
*x[1];  /*Te, gap = go - z */
```

```
            k = Miu0*PI*(Ro*Ro - Ri*Ri)/(16.0*P*P);

            k1 = k* (
(Mmf1*Mmf1+2.5*Ns*Mmf1*i_d0+1.5*Ns*Ns*(i_d0*i_d0+x[1]*x[1]))/(G01*G01)-
(Mmf2*Mmf2+2.5*Ns*Mmf2*i_d0+1.5*Ns*Ns*(i_d0*i_d0+x[1]*x[1]))/(G02*G02) );

            k2 = -k* ( (Mmf1*Mmf1+2.5*Ns*Mmf1*i_d0 +
1.5*Ns*Ns*(i_d0*i_d0+x[1]*x[1]))/(G01*G01*G01) +
(Mmf2*Mmf2+2.5*Ns*Mmf2*i_d0+1.5*Ns*Ns*(i_d0*i_d0+x[1]*x[1]))/(G02*G02*G02) );

            k3 = k* ( (2.5*Ns*Mmf1+3.0*Ns*Ns*i_d0)/(G01*G01)-
(2.5*Ns*Mmf2+3.0*Ns*Ns*i_d0)/(G02*G02) );
            i_cd0 == (k1-M*9.81)/k3;
            f_linear == ( k1+k2*x[4]+k3*(x[0]-i_d0) );

      /* Fs = F1 - F2 */
            F1 = (Miu0*PI*(Ro*Ro-Ri*Ri)/((G01-x[4])*(G01-x[4]))/16.0*P*P)*
(Mmf1*Mmf1+2.5*Ns*Mmf1*x[0]+1.5*Ns*Ns*(x[0]*x[0]+x[1]*x[1]));
            F2 = (Miu0*PI*(Ro*Ro-Ri*Ri)/((G02+x[4])*(G02+x[4]))/16.0*P*P)*
(Mmf2*Mmf2+2.5*Ns*Mmf2*x[0]+1.5*Ns*Ns*(x[0]*x[0]+x[1]*x[1]));

            y[8]= F1 - F2;
            y[9]=x[3]*P;
            y[10]=thetae;
            y[11]=y[7];
            y[12]=y[8];
            y[13]=x[4];
            y[14]=i_cd0;
            y[15]=k1;
            y[16]=k2;
            y[17]=k3;
}
 #define MDL_UPDATE  /* Change to #undef to remove function */
 #if defined(MDL_UPDATE)
  /* Function: mdlUpdate ======================================================
   * Abstract:
   *    This function is called once for every major integration time step.
   *    Discrete states are tyPIcally updated here, but this function is useful
   *    for performing any tasks that should only take place once per
   *    integration step.
   */
  static void mdlUpdate(SimStruct *S, int_T tid)
  {
/*                      can't calculate Ud and Uq here because when debug in matlab, if use this
     method, ud an uq always be 0 and never call this function. */
  }
#endif /* MDL_UPDATE */

#define MDL_DERIVATIVES  /* Change to #undef to remove function : chuyen thanh #undef de bo
function can bo*/
#if defined(MDL_DERIVATIVES)
  /* Function: mdlDerivatives =================================================
   * Abstract:
   *    In this function, you compute the S-function block's derivatives.
   *    The derivatives are placed in the derivative vector, ssGetdX(S).
   */
static void mdlDerivatives(SimStruct *S)
{
            real_T            *xdot   = ssGetdX(S);
            real_T            *x    = ssGetContStates(S);
```

```
        InputRealPtrsType uPtrs0 = ssGetInputPortRealSignalPtrs(S,0); /* uabc1 */
        InputRealPtrsType uPtrs1 = ssGetInputPortRealSignalPtrs(S,1);  /* Tmech */   /*Fnoise*/

        real_T *y = ssGetOutputPortRealSignal(S,0);  /* output */
        real_T thetae;    /* electrical angular velocity */
        real_T id;

   /* index         0     1     2       3           4    5
            x:    id1   iq1   thetar  wr      z    z'
            x':   id1'  iq1'  wr      wr'     z'   z'' */

        thetae=x[2]*P;

        Ud=2./3.*(u0(0)*cos(thetae)+u0(1)*cos(thetae-2./3.*PI)+u0(2)*cos(thetae+2./3.*PI));
        Uq=-2./3.*(u0(0)*sin(thetae)+u0(1)*sin(thetae-2./3.*PI)+u0(2)*sin(thetae+2./3.*PI));

   /* id1=x[0], iq1=x[1], theta=x[2], w=x[3], z=x[4], z'=x[5] */
   /* xdot[0]:  id1' */
        xdot[0]=16.*P*P*(G01- x[4])*(Ud-Rs*x[0])/(3.*Miu0*PI*(Ro*Ro-
Ri*Ri)*Ns*Ns)+P*x[3]*x[1];

   /* xdot[1]:  iq1' */
   xdot[1]=16.*P*P*(G01- x[4])*(Uq-Rs*x[1])/(3.*Miu0*PI*(Ro*Ro-Ri*Ri)*Ns*Ns)-P*x[3]*x[0]-
2./3.*Mmf1*P*x[3]/Ns;

   /* xdot[2]:  wr=thetar' */
        xdot[2]=x[3];

   /* xdot[3]:  wr'   y[11]=Te, x[3]=wr, */
   xdot[3]=(y[11]-Ff*x[3]-(*uPtrs1[0]))/J;

   /* xdot[4]: z'  x[4]=z  */
   xdot[4]=x[5];

   /* xdot[5]: z'' x[5]=z' */
   xdot[5]=(y[12]+(*uPtrs1[1]))/M - 9.81;

}
#endif /* MDL_DERIVATIVES */

/* Function: mdlTerminate =====================================================
 * Abstract:
 *    In this function, you should perform any actions that are necessary
 *    at the termination of a simulation.  For example, if memory was
 *    allocated in mdlStart, this is the place to free it.
 */
static void mdlTerminate(SimStruct *S)
{
}

#ifdef  MATLAB_MEX_FILE    /* Is this file being comPIled as a MEX-file? */
#include "simulink.c"      /* MEX-file interface mechanism */
#else
#include "cg_sfun.h"       /* Code generation registration function */
#endif
```

Appendix C:

Driving circuit for Voltage Source Inverter

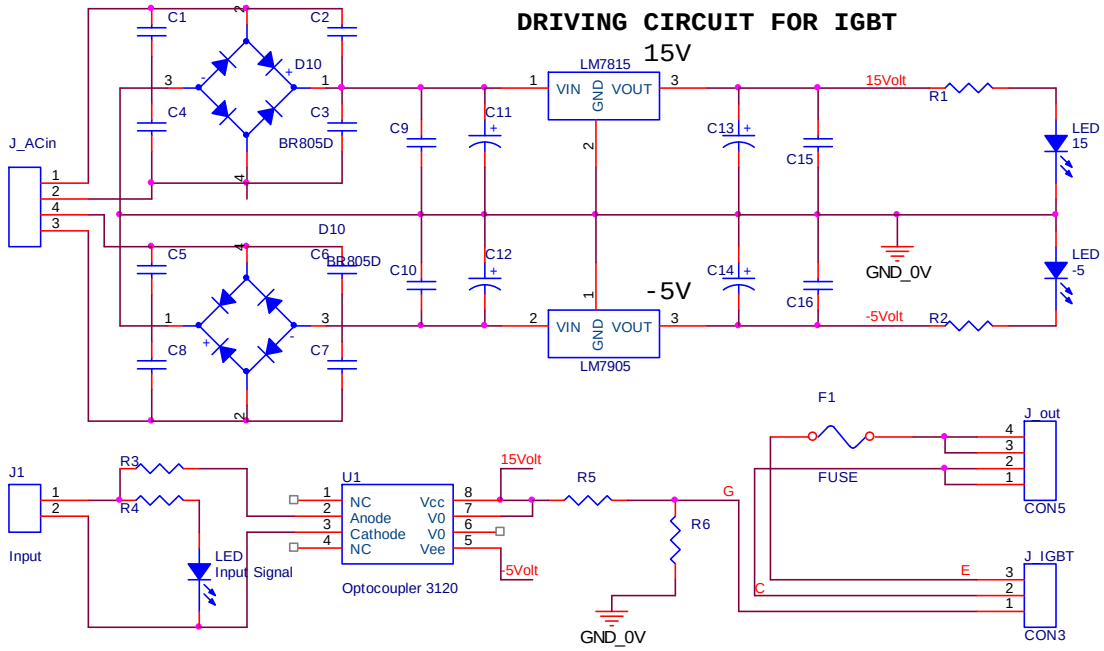

Fig. C.1. Schematic of driving circuit for IGBTs

Fig. C.2. Driving circuit for single IGBT

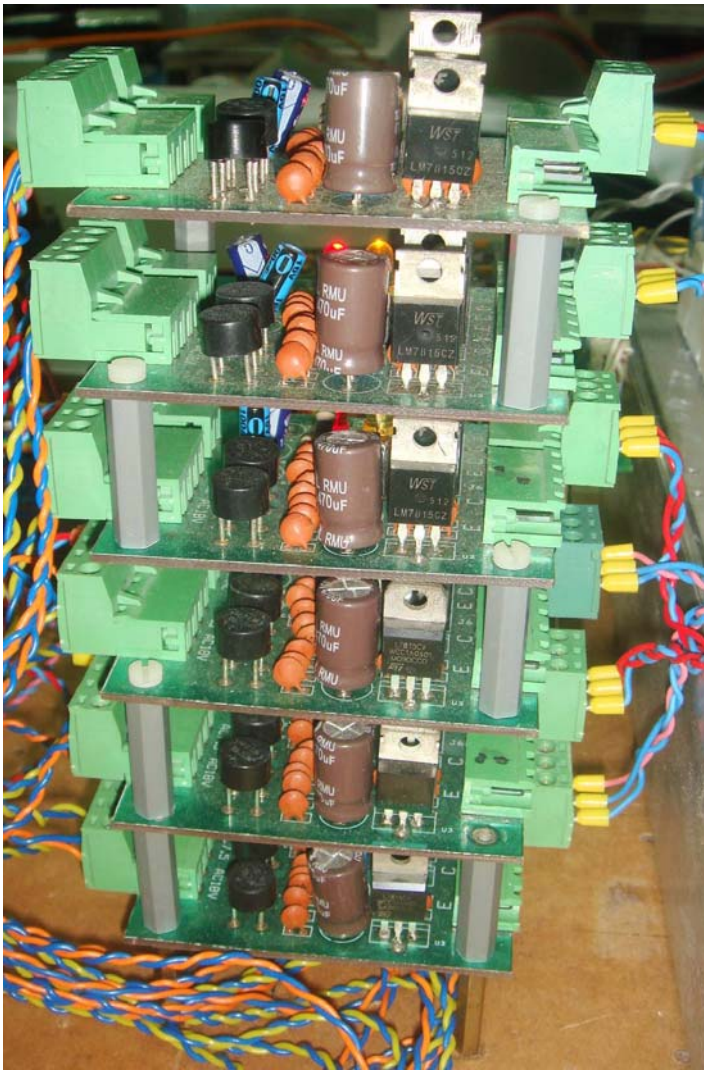

Fig. C.3. Driving circuits for three-phase voltage source inverter

Appendix D:

Real-time control programs

D.1. Program for Vector Control of the Dual-airgap AFPM Machine using a rotary encoder

```
#include <Brtenv.h>          /* basic real-time environment */
#include <Ctrl.h>

/* variables for communication with Slave DSP */
Int16 task_id = 0;              /* communication channel */
Int16 index = -1;               /* slave DSP command index */
Int16 error ;

/* variables for execution time measurement */
Float64   exec_time, Vdclink, ia, ic, ib, Tuning;
int       index_inc;

/* parameters for PWM initialization */
Float64 pwm_period = T_S;                    /* PWM period */
Float64 deadband = 0.0e-6;                   /* deadband period */
/* parameters for PWM initialization */
Float64 sync_pos = SLVDSP1103_PWM3_SYNC_CENT;

/*-------------------------------------------------------------------------*/
//#define DT 1e-4                            /* 100 us simulation step size */
/*---------------------------------timerA----------------------------------*/

/* variables for execution time profiling */
UInt16 scale_value = 0;                      /* set the scaling of timerA */
/* adjust values for timer0 */
Float64 timerA_period = T_S;
/*-------------------------------------------------------------------------*/

/*---------------------------------Encoder---------------------------------*/
/* variables for ControlDesk */
/* position and velocity of Encoder channel 1 and 7         *
 * flag for index found                                     */
Float64 inc_pos_an, inc_vel_an, inc_pos_dig, inc_vel_dig;
Int32 ind_found;                 /* Use Int32 instead of Int16 for .trc !!*/

/*-------------------------------------------------------------------------*/

/*-------------------------------------------------------------------------*/
void isr_timerA(void)
{
  ds1103_begin_isr_timerA();
//  RTLIB_TIC_START();             /* start time measurement */
  host_service(1, 0);            /* ControlDesk service */

/**********************Rotor Position and Speed Acquisition************************/
   psn_init = psn_init1*PI/180.0;
   /*read with highest resolution, 1/4 line */

   //Use channel 6;
   inc64 = ds1103_inc_counter_rd(6);
```

```
  inc_k = inc64.high;
  eps_m1 = eps_m1+(double)(inc_k - inc_k1)*PI2/4096.0;

  angle_limit(eps_m1);
  eps_m = eps_m1 + psn_init;

  angle_limit(eps_m);

  /*calculate electrical angle between the rotor and stator */
  eps_rs = Pp * eps_m;
  angle_limit(eps_rs);

  eps_rs_k = eps_m1-PI;
  if ((eps_rs_k<eps_rs_k1-PI) || (eps_rs_k>eps_rs_k1+PI)){}
  else  {ch_eps_rs = eps_rs_k - eps_rs_k1;}
  eps_rs_k1 = eps_rs_k;

  speed_w =  2.0 * ch_eps_rs / T_S;
  fol(speed_w, speed_w_fol, fol_speed);
  speed_spd = speed_w * 60.0 / (PI2 * Pp);
  fol(speed_spd, speed_spd_fol, fol_spd);
  inc_k1 = inc_k;

/*--------------------------------End of Encoder--------------------------------*/

/**************************DC Bus Voltage and Current
Acquisition************************/

  /*V_DC measurement*/
  ds1103_adc_mux(1);
  ds1103_adc_delayed_start(DS1103_ADC1);  //delay 2us not 1us
  V_DC = 217.2886*ds1103_adc_read_ch(1)+4.4157;
  Vdclink = V_DC;
  /* get phase currents from ADCs */
  ds1103_adc_start(DS1103_ADC2 | DS1103_ADC3 | DS1103_ADC4);
  i_abc.a = -20*ds1103_adc_read_ch(5)-0.11463380;
  i_abc.b = -20*ds1103_adc_read_ch(9)-0.1296338;
  i_abc.c = -i_abc.a - i_abc.b;

  z = ds1103_adc_read_ch(13)-0.4109+0.01784+Tuning;
  fol_z.K1 = (2.0*T_z-T_S)/(2.0*T_z+T_S);
  fol_z.K2 = T_S/(2.0*T_z+T_S);
  fol(z, z_w_fol, fol_z);

  ia=i_abc.a;
  ib=i_abc.b;
  ic=i_abc.c;
  /* convert phase currents to stator current vector */
  fc3_2_spec(i_abc,i_ab);

  sincos(eps_rs,trig_fct);
  vr_neg(i_ab,trig_fct,i_dq);
  id=i_dq.d;
  iq=i_dq.q;
  i_alpha = i_ab.alpha;
  i_beta = i_ab.beta;

iq_max = 5;
id_max = 2.34;
```

```
//-----------------------------------PI Speed Controller---------------------------------/

  count++;
  if (count >= 5)
  {
            count = 0;

            u_error_spd = speed_ref- speed_w_fol;
            u_error_p = Kp_spd*u_error_spd;
            u_error_i = Ki_spd*u_error_spd+K_anti_spd*(iq_ref-u_out_spd)+u_error_i;

            if (u_error_i >= iq_max) { u_error_i = iq_max;}
            if (u_error_i <=-iq_max) { u_error_i =-iq_max;}

    u_out_spd=u_error_p+u_error_i;
    iq_ref=u_out_spd;

    if (iq_ref >= iq_max) { iq_ref = iq_max;}
            if (iq_ref <=-iq_max) { iq_ref =-iq_max;}
  }

//-----------------------------------PID Z-displacement Controller---------------------------------/

  count4z++;
  if (count4z >= 5)
  {
            count4z = 0;

            u_error_z = z_ref-z_w_fol;    // z_ref is z-displacement in mm
            u_error_z_p = Kp_z*u_error_z;
            u_error_z_i = Ki_z*u_error_z+K_anti_z*(id_ref-u_out_z)+u_error_z_i;
            if (u_error_z_i >= id_max) { u_error_z_i = id_max;}
            if (u_error_z_i <=-id_max) { u_error_z_i =-id_max;}
            u_error_z_d = Kd_z*u_error_z;

        u_out_z=u_error_z_p+u_error_z_i+ u_error_z_d;
        id_ref=u_out_z;

    if (id_ref >= id_max) { id_ref = id_max;}
            if (id_ref <=-id_max) { id_ref =-id_max;}
  }
//-----------------------------------End of Z-displacement Controller----------------------------/

theta_e=theta_est+pos;
angle_limit(theta_e);

//-----------------------------------PI Current Controllers---------------------------------/

//id controller
  id_error =id_ref-i_d_est;
  id_error_p = Kp_d*id_error;
  id_error_i = Ki_d*id_error+id_error_i+K_anti_d*(vd_ref-vd_out);

  if (id_error_i >= 0.866*V_DC) { id_error_i = 0.866*V_DC;}
  if (id_error_i <=-0.866*V_DC) { id_error_i =-0.866*V_DC;}

  vd_out=id_error_p+id_error_i;//-speed_w_fol*Lq*iq;
  vd_ref=vd_out;

  if (vd_ref >= 0.866*V_DC) { vd_ref = 0.866*V_DC;}
```

```
  if (vd_ref <=-0.866*V_DC) { vd_ref =-0.866*V_DC;}

  //iq controller
  iq_error =iq_ref-i_q_est;
  iq_error_p = Kp_q*iq_error;
  iq_error_i = Ki_q*iq_error+iq_error_i+K_anti_q*(vq_ref-vq_out);

  if (iq_error_i >= 0.866*V_DC) { iq_error_i = 0.866*V_DC;}
            if (iq_error_i <=-0.866*V_DC) { iq_error_i =-0.866*V_DC;}

  vq_out=iq_error_p+iq_error_i;//+speed_w_fol*(FLUXM+Ld*id);
  vq_ref=vq_out;

  if (vq_ref >= 0.866*V_DC) { vq_ref = 0.866*V_DC;}
            if (vq_ref <=-0.866*V_DC) { vq_ref =-0.866*V_DC;}

//-----------------------------------Park's Transformation---------------------------------/

U_alpha=vd_out*cos(theta_e)-vq_out*sin(theta_e);
U_beta =vq_out*cos(theta_e)+vd_out*sin(theta_e);
  //-----------------------------------SVM---------------------------------

  theta_v=atan2(U_beta,U_alpha);

  if(theta_v<0) {theta=theta_v+2*PI;}
    else        {theta=theta_v;}

  if(theta>=0 && theta<PI/3)            {sector=1;   theta=theta;}
  else if(theta>=PI/3 && theta<2*PI/3)   {sector=2;   theta=theta-PI/3;}
  else if(theta>=2*PI/3 && theta<PI)     {sector=3;   theta=theta-2*PI/3;}
  else if(theta>=PI && theta<4*PI/3)     {sector=4;   theta=theta-PI;}
  else if(theta>=4*PI/3 && theta<5*PI/3) {sector=5;   theta=theta-4*PI/3;}
  else                                   {sector=6;   theta=theta-5*PI/3;}
  V_mag = sqrt(U_alpha * U_alpha + U_beta * U_beta);
  V_lim = V_DC*0.866/sin(2*PI/3-theta);

  if(V_mag>=V_lim)
    {Ua=V_lim*cos(theta_v);   t1=pwm_period*V_lim/V_DC/0.866*sin(PI/3-theta);
     Ub=V_lim*sin(theta_v);   t2=pwm_period*V_lim/V_DC/0.866*sin(theta);}
  else
    {Ua=V_mag*cos(theta_v);   t1=pwm_period*V_mag/V_DC/0.866*sin(PI/3-theta);
     Ub=V_mag*sin(theta_v);   t2=pwm_period*V_mag/V_DC/0.866*sin(theta);}

 /*****************************************************************************/

//  exec_time = RTLIB_TIC_READ();
  ds1103_end_isr_timerA();
}


/* interrupt service routine for PWM sync interrupt */
void PWM_sync_interrupt(void)
{
  /* write PWM3 duty cycle to slave DSP and test for error */
   error = ds1103_slave_dsp_pwm3sv_duty_write(task_id, index, sector, t1, t2);
   if ( error != DSCOMDEF_NO_ERROR)
   {
     write_PWM3sv_error=1;
   }
}
```

```
main()
{
   /* basic initialization of DS1103 */
   init();
/*********************************************************/
  /* input signal for channel 6 via TTL */
//  ds1103_inc_init(6, DS1103_INC_CH6_RS422);            // input signal RS422
  ds1103_inc_init(6, DS1103_INC_CH6_32BIT);           // Channel 6: 32-bit resolution
  ds1103_inc_set_idxmode(6, DS1103_INC_RESETONIDX);    // Reset on index
//  ds1103_inc_set_idxmode(6, DS1103_INC_NO_RESETONIDX);  // No reset on index

 /* init incremental encoder channel 6   */
  index_inc = 0;
  while (index_inc == 0) {
     index_inc = ds1103_inc_index_read(6, DS1103_INC_IDX_NOT_SET);
  }

  ds1103_inc_counter_clear(6);  // clear the encoder channel counter
/*****************************************************************************/

/*****************************************************************************/
   /* initialization of slave DSP communication */
   ds1103_slave_dsp_communication_init();

   /* init and start of 3-phase PWMSV generation on slave DSP */
   ds1103_slave_dsp_pwm3sv_init(task_id, pwm_period, sector, t1, t2, deadband, sync_pos);
   ds1103_slave_dsp_pwm3_start(task_id);

   /* registration of PWM duty cycle update command */
   ds1103_slave_dsp_pwm3sv_duty_write_register(task_id, &index);

   /* initialization of PWM sync interrupt */
   ds1103_set_interrupt_vector(DS1103_INT_SLAVE_DSP_PWM,
     (DS1103_Int_Handler_Type) &PWM_sync_interrupt,
     SAVE_REGS_ON);
   ds1103_enable_hardware_int(DS1103_INT_SLAVE_DSP_PWM);
   RTLIB_INT_ENABLE();
/*****************************************************************************/
/* initialize ctrol param. */
    varinit();
/* periodic event with TimerA */
    ds1103_start_isr_timerA(timerA_period, isr_timerA);
   /* Background tasks */
   while(1)
   {
     RTLIB_BACKGROUND_SERVICE();   /* ControlDesk service */
   }
}
   /*****************************************************************************/
```

D.2. Program for Position Sensorless Control of the Dual-airgap AFPM Machine

```
#include <Brtenv.h>          /* basic real-time environment */
#include <Ctrl.h>

/* variables for communication with Slave DSP */
Int16 task_id = 0;              /* communication channel */
Int16 index = -1;               /* slave DSP command index */
Int16 error ;

/* variables for execution time measurement */
Float64   exec_time, Vdclink,ia,ic,ib, Tuning;
int       index_inc;

/* parameters for PWM initialization */
Float64 pwm_period = T_S;                    /* PWM period */
Float64 deadband = 0.0e-6;                   /* deadband period */
/* parameters for PWM initialization */
Float64 sync_pos = SLVDSP1103_PWM3_SYNC_CENT;

/*---------------------------------timerA-----------------------------------*/

/* variables for execution time profiling */
UInt16 scale_value = 0;                      /* set the scaling of timerA */
/* adjust values for timer0 */
Float64 timerA_period = T_S;
/*--------------------------------------------------------------------------*/

/*---------------------------------Encoder----------------------------------*/
/* variables for ControlDesk */
/* position and velocity of Encoder channel 1 and 7        *
 * flag for index found                                    */
Float64 inc_pos_an, inc_vel_an, inc_pos_dig, inc_vel_dig;
Int32 ind_found;                 /* Use Int32 instead of Int16 for .trc !!*/

/*--------------------------------------------------------------------------*/
void isr_timerA(void)
{
  ds1103_begin_isr_timerA();
  host_service(1, 0);            /* ControlDesk service */

/**********************Rotor Position and Speed Acquisition**************************/
   psn_init = psn_init1*PI/180.0;
   /*read with highest resolution, 1/4 line */

   //Use channel 6;
   inc64 = ds1103_inc_counter_rd(6);
   inc_k = inc64.high;

   eps_m1 = eps_m1+(double)(inc_k - inc_k1)*PI2/4096.0;

   angle_limit(eps_m1);
   eps_m = eps_m1 + psn_init;

   angle_limit(eps_m);

   /*calculate electrical angle between the rotor and stator */
   eps_rs = Pp * eps_m;
   angle_limit(eps_rs);
```

```
  eps_rs_k = eps_m1-PI;
  if ((eps_rs_k<eps_rs_k1-PI) || (eps_rs_k>eps_rs_k1+PI)){}
  else  {ch_eps_rs = eps_rs_k - eps_rs_k1;}
  eps_rs_k1 = eps_rs_k;

  speed_w =  2.0 * ch_eps_rs / T_S;
  fol(speed_w, speed_w_fol, fol_speed);
  speed_spd = speed_w * 60.0 / (PI2 * Pp);
  fol(speed_spd, speed_spd_fol, fol_spd);
  inc_k1 = inc_k;

/*-------------------------------End of Encoder-------------------------------*/

/*************************DC Bus Voltage and Current
Acquisition************************/

 /*V_DC measurement*/
 ds1103_adc_mux(1);
 ds1103_adc_delayed_start(DS1103_ADC1);  //delay 2us
 V_DC = 217.2886*ds1103_adc_read_ch(1)+4.4157;
 Vdclink = V_DC;

 /* get phase currents from ADCs */
 ds1103_adc_start(DS1103_ADC2 | DS1103_ADC3 | DS1103_ADC4);
 i_abc.a = -20*ds1103_adc_read_ch(5)-0.11463380;
 i_abc.b = -20*ds1103_adc_read_ch(9)-0.1296338;
 i_abc.c = -i_abc.a - i_abc.b;

 z = ds1103_adc_read_ch(13)-0.4109+0.01784+Tuning;
 fol_z.K1 = (2.0*T_z-T_S)/(2.0*T_z+T_S);
 fol_z.K2 = T_S/(2.0*T_z+T_S);
 fol(z, z_w_fol, fol_z);

 ia=i_abc.a;
 ib=i_abc.b;
 ic=i_abc.c;
 /* convert phase currents to stator current vector */
 fc3_2_spec(i_abc,i_ab);

 sincos(eps_rs,trig_fct);
 vr_neg(i_ab,trig_fct,i_dq);
 id=i_dq.d;
 iq=i_dq.q;
 i_alpha = i_ab.alpha;
 i_beta = i_ab.beta;

/***************Forward Voltage Drop & Dead-time Compensation****************/

 if (i_abc.a>=0.0)
   bicode_a=1;
 else bicode_a=0;
 if (i_abc.b>=0.0)
   bicode_b=1;
 else bicode_b=0;
 if (i_abc.c>=0.0)
   bicode_c=1;
 else bicode_c=0;

 bicode=bicode_a*4+bicode_b*2+bicode_c;
 dtime=(deadband-t_on_off)/pwm_period;
```

```
 Vdead=(V_DC-0.0*2.0/3.0)*dtime;

 switch(bicode)
  {
   case 1: vfd_d = 2.0/3.0*Vce*(-1.0); vfd_q =-2.0/3.0*Vce*0.866*2.0;    vdt_d=Vdead*(-1.0);
vdt_q=-Vdead*0.866*2.0;  break;             /* v1(100) */
   case 2: vfd_d = 2.0/3.0*Vce*(-1.0); vfd_q =2.0/3.0*Vce*0.866*2.0;     vdt_d=Vdead*(-1.0);
vdt_q= Vdead*0.866*2.0;  break;             /* v2(110) */
   case 3: vfd_d = 2.0/3.0*Vce*(-2.0); vfd_q = 0.0;                      vdt_d=Vdead*(-2.0);  vdt_q=0.0;
break;             /* v3(010) */
   case 4: vfd_d = 2.0/3.0*Vce*2.0;    vfd_q = 0.0;                     vdt_d=Vdead*2.0;     vdt_q=0.0;
break;             /* v4(011) */
   case 5: vfd_d = 2.0/3.0*Vce*1.0;    vfd_q =-2.0/3.0*Vce*0.866*2.0;    vdt_d=Vdead*1.0;
vdt_q= -Vdead*0.866*2.0; break;             /* v5(001) */
   case 6: vfd_d = 2.0/3.0*Vce*1.0;    vfd_q =2.0/3.0*Vce*0.866*2.0;     vdt_d=Vdead*1.0;
vdt_q= Vdead*0.866*2.0;  break;             /* v6(101) */
  }

  v_alpha = Ua-vdt_d-vfd_d;
  v_beta = Ub-vdt_q-vfd_q;

  count_init++;
   if (count_init <= 1)
   {
     flux_alpha_old = FLUXM * trig_fct.cos;
     flux_beta_old  = FLUXM * trig_fct.sin;
   }

   count_init = 2;
  //Stator Flux Estimation
  flux_alpha = flux_alpha + (v_alpha - i_alpha*Rs + v_alpha_comp) * T_S;
  flux_beta = flux_beta + (v_beta - i_beta*Rs + v_beta_comp) * T_S;

  /*Active Flux*/
  flux_a_alpha = flux_alpha - Lq*i_alpha;
  flux_a_beta = flux_beta - Lq*i_beta;

  /*Rotor Position Estimation*/
  theta_est = atan2(flux_a_beta,flux_a_alpha);
  angle_limit(theta_est);

  flux_d_est = flux_alpha*cos(theta_est) + flux_beta*sin(theta_est);
  flux_q_est = -flux_alpha*sin(theta_est) + flux_beta*cos(theta_est);

  id_est = (flux_d_est-FLUXM)/Ld;
  iq_est = flux_q_est/Lq;

  i_alpha_est=id_est*cos(theta_est)-iq_est*sin(theta_est);
  i_beta_est =iq_est*cos(theta_est)+id_est*sin(theta_est);

  i_alpha_error = i_alpha - i_alpha_est;
  v_alpha_comp= Kp_current*i_alpha_error;

  if (v_alpha_comp >= 10) { v_alpha_comp = 10;}
  if (v_alpha_comp <=-10) { v_alpha_comp =-10;}

  i_alpha_error = i_beta - i_beta_est;
  v_beta_comp= Kp_current*i_beta_error;

  if (v_beta_comp >= 10) { v_beta_comp = 10;}
```

```
  if (v_beta_comp <=-10) { v_beta_comp =-10;}

  torque_est = 3.0/2.0 * Pp * (flux_alpha * i_ab.beta - flux_beta * i_ab.alpha);
  flux_est = sqrt(flux_alpha * flux_alpha + flux_beta * flux_beta);

  theta_s = atan2(flux_beta,flux_alpha);

/*****************************Rotor Speed Estimator*********************************/

  /* Estimation of speed */
  ch_theta=(theta_est - theta_est_o)/2.0;
  theta_est_o = theta_est;

  if (fabs(speed_ref)<150.0)
  {
    if (fabs(ch_theta)>0.05 ) {ch_theta = ch_theta_o;}
  }

  if (fabs(speed_ref)>=150.0)
  {
    if (fabs(ch_theta)>0.4 ) {ch_theta = ch_theta_o;}
  }

  ch_theta_o = ch_theta;

  //estimated electrical speed in rad/s
  fol_sp.K1 = (2.0*T_spd-T_S)/(2.0*T_spd+T_S);
  fol_sp.K2 = T_S/(2.0*T_spd+T_S);
  fol(ch_theta, ch_theta_f, fol_sp);
  w_est_f = 2.0 * ch_theta_f/ T_S;

/*******************************************************************************/
iq_max = 5;
id_max = 2.34;

//-----------------------------------PI Speed Controller----------------------------------/
  count++;
  if (count >= 5)
  {
            count = 0;

            u_error_spd = speed_ref-w_est_f;
            u_error_p = Kp_spd*u_error_spd;
            u_error_i = Ki_spd*u_error_spd+K_anti_spd*(iq_ref-u_out_spd)+u_error_i;

            if (u_error_i >= iq_max) { u_error_i = iq_max;}
            if (u_error_i <=-iq_max) { u_error_i =-iq_max;}

            u_out_spd=u_error_p+u_error_i;
            iq_ref=u_out_spd;

            if (iq_ref >= iq_max) { iq_ref = iq_max;}
            if (iq_ref <=-iq_max) { iq_ref =-iq_max;}
  }
```

```
//-----------------------------------PID Z-displacement Controller---------------------------------/
  count4z++;
  if (count4z >= 5)
  {
            count4z = 0;
            u_error_z = z_ref-z_w_fol;
            u_error_z_p = Kp_z*u_error_z;
            u_error_z_i = Ki_z*u_error_z+K_anti_z*(id_ref-u_out_z)+u_error_z_i;
            if (u_error_z_i >= id_max) { u_error_z_i = id_max;}
            if (u_error_z_i <=-id_max) { u_error_z_i =-id_max;}
            u_error_z_d = Kd_z*u_error_z;

    u_out_z=u_error_z_p+u_error_z_i+ u_error_z_d;
    id_ref=u_out_z;

    if (id_ref >= id_max) { id_ref = id_max;}
            if (id_ref <=-id_max) { id_ref =-id_max;}
  }
 //-----------------------------------End of Z-displacement Controller-----------------------------/

theta_e=theta_est+pos;
angle_limit(theta_e);

i_d_est = i_alpha*cos(theta_e) + i_beta*sin(theta_e);
 i_q_est = -i_alpha*sin(theta_e) + i_beta*cos(theta_e);
//-----------------------------------PI Current Controllers---------------------------------/

//id controller
  id_error =id_ref-i_d_est;
  id_error_p = Kp_d*id_error;
  id_error_i = Ki_d*id_error+id_error_i+K_anti_d*(vd_ref-vd_out);

  if (id_error_i >= 0.866*V_DC) { id_error_i = 0.866*V_DC;}
  if (id_error_i <=-0.866*V_DC) { id_error_i =-0.866*V_DC;}

  vd_out=id_error_p+id_error_i;//-speed_w_fol*Lq*iq;
  vd_ref=vd_out;

  if (vd_ref >= 0.866*V_DC) { vd_ref = 0.866*V_DC;}
  if (vd_ref <=-0.866*V_DC) { vd_ref =-0.866*V_DC;}

  //iq controller
  iq_error =iq_ref-i_q_est;
  iq_error_p = Kp_q*iq_error;
  iq_error_i = Ki_q*iq_error+iq_error_i+K_anti_q*(vq_ref-vq_out);

  if (iq_error_i >= 0.866*V_DC) { iq_error_i = 0.866*V_DC;}
  if (iq_error_i <=-0.866*V_DC) { iq_error_i =-0.866*V_DC;}

  vq_out=iq_error_p+iq_error_i;//+speed_w_fol*(FLUXM+Ld*id);
  vq_ref=vq_out;

  if (vq_ref >= 0.866*V_DC) { vq_ref = 0.866*V_DC;}
  if (vq_ref <=-0.866*V_DC) { vq_ref =-0.866*V_DC;}

//-----------------------------------Park's Transformation---------------------------------/
 U_alpha=vd_out*cos(theta_e)-vq_out*sin(theta_e);
 U_beta =vq_out*cos(theta_e)+vd_out*sin(theta_e);
```

```
//-----------------------------------SVM---------------------------------

  theta_v=atan2(U_beta,U_alpha);
  if(theta_v<0) {theta=theta_v+2*PI;}
  else       {theta=theta_v;}
  if(theta>=0 && theta<PI/3)                  {sector=1;   theta=theta;}
  else if(theta>=PI/3 && theta<2*PI/3)       {sector=2;   theta=theta-PI/3;}
  else if(theta>=2*PI/3 && theta<PI)         {sector=3;   theta=theta-2*PI/3;}
  else if(theta>=PI && theta<4*PI/3)         {sector=4;   theta=theta-PI;}
  else if(theta>=4*PI/3 && theta<5*PI/3)     {sector=5;   theta=theta-4*PI/3;}
  else                                       {sector=6;   theta=theta-5*PI/3;}
  V_mag = sqrt(U_alpha * U_alpha + U_beta * U_beta);
  V_lim = V_DC*0.866/sin(2*PI/3-theta);

  if(V_mag>=V_lim)
    {Ua=V_lim*cos(theta_v);   t1=pwm_period*V_lim/V_DC/0.866*sin(PI/3-theta);
     Ub=V_lim*sin(theta_v);   t2=pwm_period*V_lim/V_DC/0.866*sin(theta);}
  else
    {Ua=V_mag*cos(theta_v);   t1=pwm_period*V_mag/V_DC/0.866*sin(PI/3-theta);
     Ub=V_mag*sin(theta_v);   t2=pwm_period*V_mag/V_DC/0.866*sin(theta);}

 /*************************************************************************/

//  exec_time = RTLIB_TIC_READ();
  ds1103_end_isr_timerA();
}


/* interrupt service routine for PWM sync interrupt */
void PWM_sync_interrupt(void)
{
  /* write PWM3 duty cycle to slave DSP and test for error */
   error = ds1103_slave_dsp_pwm3sv_duty_write(task_id, index, sector, t1, t2);
   if ( error != DSCOMDEF_NO_ERROR)
   {
     write_PWM3sv_error=1;
   }
}

main()
{
   /* basic initialization of DS1103 */
   init();
/*********************************************************/
 /* input signal for channel 6 via TTL */
  ds1103_inc_init(6, DS1103_INC_CH6_32BIT);           // Channel 6: 32-bit resolution
  ds1103_inc_set_idxmode(6, DS1103_INC_RESETONIDX);    // Reset on index

 /* init incremental encoder channel 6   */
  index_inc = 0;
  while (index_inc == 0) {
     index_inc = ds1103_inc_index_read(6, DS1103_INC_IDX_NOT_SET);
  }

  ds1103_inc_counter_clear(6);  // clear the encoder channel counter
/*************************************************************************/
   /* initialization of slave DSP communication */
   ds1103_slave_dsp_communication_init();

   /* init and start of 3-phase PWMSV generation on slave DSP */
```

```
  ds1103_slave_dsp_pwm3sv_init(task_id, pwm_period, sector, t1, t2, deadband, sync_pos);
  ds1103_slave_dsp_pwm3_start(task_id);

  /* registration of PWM duty cycle update command */
  ds1103_slave_dsp_pwm3sv_duty_write_register(task_id, &index);

  /* initialization of PWM sync interrupt */
  ds1103_set_interrupt_vector(DS1103_INT_SLAVE_DSP_PWM,
    (DS1103_Int_Handler_Type) &PWM_sync_interrupt,
    SAVE_REGS_ON);
  ds1103_enable_hardware_int(DS1103_INT_SLAVE_DSP_PWM);
  RTLIB_INT_ENABLE();
/*****************************************************************************/
/* initialize ctrol param. */
   varinit();
/* periodic event with TimerA */
   ds1103_start_isr_timerA(timerA_period, isr_timerA);
   //ds1103_start_isr_timerA(scale_value, timerA_period, isr_timerA);
  /* Background tasks */
  while(1)
  {
    RTLIB_BACKGROUND_SERVICE();   /* ControlDesk service */
  }
}
  /*****************************************************************************/
```

Appendix E:

List of Publications

[1]. **T. D. Nguyen**, K.-J. Tseng, S. Zhang, and H. T. Nguyen, "A Novel Axial Flux Permanent-Magnet Machine for Flywheel Energy Storage System: Design and Analysis," *Industrial Electronics, IEEE Transactions on*, vol. 58, no. 9, pp. 3784-3794, 2011.

[2]. **T. D. Nguyen** and K. J. Tseng, "Control of a Dual-airgap Axial Flux Permanent Magnet Machine for Flywheel Energy Storage System: A Model Predictive Control Approach," *Australian Journal of Electrical & Electronics Engineering*, 2012 (in press).

[3]. **T. D. Nguyen**, K. J. Tseng, and S. Zhang, "Loss Study of a Novel Axial Flux Permanent Magnet Machine," *Australian Journal of Electrical and Electronics Engineering*, 2012 (in press).

[4]. **T.D. Nguyen**, G. Foo, K. J. Tseng, and D. M. Vilathgamuwa, "Modeling and Sensorless Direct Torque and Flux Control of a Dual-Airgap Axial Flux Permanent Magnet Machine with Field Weakening Operation," *Mechatronics, IEEE Transactions on*, 2011 (revised & submitted).

[5]. **T. D. Nguyen**, G. Foo, K. J. Tseng, and D. M. Vilathgamuwa, "Modeling and Position-Sensorless Control of a Dual-Airgap Axial Flux Permanent Magnet Machine for Flywheel Energy Storage System," *Journal of Power Electronics*, 2011 (revised & submitted).

[6]. Z. Shao, T. King-Jet, D. M. Vilathgamuwa, **T. D. Nguyen**, and W. Xiao-Yu, "Design of a Robust Grid Interface System for PMSG-Based Wind Turbine Generators," *Industrial Electronics, IEEE Transactions on*, vol. 58, no. 1, pp. 316-328, 2011.

[7]. **T. D. Nguyen** and K. J. Tseng, "Loss Study of a Novel Axial Flux Permanent Magnet Machine," IEEE International Electric Machines and Drives (IEMDC), 2011.

[8]. **T.D. Nguyen**, K.J. Tseng, S. Zhang, H.T.Nguyen, "Position Sensorless Control of a Novel Flywheel Energy Storage System," The 9th International Power and Energy Conference IPEC 2010.

[9]. **T.D. Nguyen**, K.J. Tseng, S. Zhang, H.T.Nguyen, "Model Predictive Control of a Novel Axial Flux Permanent Magnet Machine for Flywheel Energy Storage System," The 9th International Power and Energy Conference (IPEC), Singapore, 2010.

[10]. **T.D. Nguyen**, K.J. Tseng, S. Zhang, H.T.Nguyen, "On The Modeling and Control of a Novel Flywheel Energy Storage System," IEEE International Symposium on Industrial Electronics (ISIE), Bari, Italy, July 2010.

[11]. C. Zhang, **T.D. Nguyen**, K.J. Tseng, S. Zhang. "Stiffness Analysis and Levitation Force Control of the Active Magnetic Bearing for a Partially-Self-Bearing Flywheel System." 2nd IEEE International Conference on Sustainable Energy Technologies, ICSET 2010

[12]. C. Zhang, K.J. Tseng, **T.D. Nguyen**, S. Zhang. "Analysis and Comparison of Axial Flux PM Synchronous Motor and Induction Motor." The 9th International Power and Energy Conference IPEC 2010.

[13]. C. Zhang, K.J. Tseng, **T.D. Nguyen**, S. Zhang. "Design and Loss Analysis of A High Speed Flywheel Energy Storage System Based on Axial-Flux Flywheel-Rotor Electric Machines." The 9th International Power and Energy Conference IPEC 2010.

[14]. K.J. Tseng and **T.D. Nguyen**, "A Green and Clean Flywheel Energy Storage System: Design, Analysis and Control," The 2nd Annual Workshop on Energy Research, Singapore, June, 2010.

[15]. **T.D. Nguyen**, K.J. Tseng, S. Zhang, H.T.Nguyen, "Control of a Novel Flywheel Energy Storage System for Renewable Energy Applications." The 2nd AUN/SEED-Net Regional Conference on New/Renewable Energy, Thailand, Jan 2010.

[16]. S. Zhang, K.J. Tseng, **T.D. Nguyen**, "Novel Three-Phase AC-AC Z-Source Converters Using Matrix Converter Theory", IEEE Energy Conversion Congress and Exposition (ECCE), pp. 3063 - 3070, Sept. 2009.

[17]. S. Zhang, K.J. Tseng, **T.D. Nguyen**, “Modeling of AC-AC Matrix Converter for Wind Energy Conversion System”, 4th IEEE Conference on Industrial Electronics and Applications (ICIEA), pp. 184 – 191, 2009.

[18]. K.J. Tseng, **T.D. Nguyen** and H.T. Nguyen, "Low-maintenance Flywheel Energy Storage Devices," The 1st Annual Workshop on Energy Research, Singapore, June, 2009.

[19]. **T.D. Nguyen**, K.J. Tseng, S. Zhang, C. Zhang, "A Flywheel Cell for Energy Storage System." IEEE International Conference on Sustainable Energy Technologies (ICSET), pp. 214 - 219, 2008.

[20]. **T.D. Nguyen**, K.J. Tseng, H.T.Nguyen, "A Flywheel Energy Storage Cell Based on Axial Flux Permanent Magnet Machine." IET, BETNET - The Biopolis, Singapore, 2008.

[21]. SS. Choi, KJ. Tseng, DM. Vilathgamuwa, **T.D. Nguyen**, "Energy Storage Systems in Distributed Generation Schemes." IEEE Power Engineering Society General Meeting, pp. 01 - 08, 2008.

[22]. S. Zhang, K.J. Tseng, **T.D.Nguyen**, “WRIG based wind conversion system excited by matrix converter with current control strategy”, IEEE International Conference on Sustainable Energy Technologies (ICSET), pp. 203 - 208, 2008.